LEDs and Doped Polymer Light Guides for Efficient Illumination and Colour Engineering

by
Christine Anne Deller

B.Sc(Hons). (University of Technology) 2001

A dissertation submitted for the requirements for the degree of

Doctor of Philosophy

in

Applied Physics

FACULTY OF SCIENCE

UNIVERSITY of TECHNOLOGY SYDNEY

2005

Certificate of Authorship/Originality

I certify that the work in this thesis has not previously been submitted for a degree, nor has it been submitted as part of requirements for a degree except as fully acknowledged within the text.

I also certify that the thesis has been written by me. Any help that I have received in my research work and in the preparation of the thesis itself has been acknowledged. In addition, I certify that all information sources and literature used are indicated in the thesis.

_____

C. A. Deller

June 2005

Acknowledgments

Professor Geoff Smith was my supervisor throughout the duration of this project. He suggested the basic concepts of this research work, and imparted some theoretical knowledge. He suggested the importance of investigating the variation of refractive index with wavelength in TRIMM systems. He also provided editing assistance and suggestions during the writing of this thesis.

Jim Franklin derived the theory of deviation of a TRIMM sphere, and assisted with the basic concepts of spherical trigonometry and probability functions. He also suggested the method for measuring TRIMM concentration in matrix materials, and the method for measuring 'luminous flux half angle' of the LEDs.

All of the experimental and simulated results presented in this thesis are my own work.

I developed all computer programs, using Mathematica®software. This was no small feat since I had previously received very little relevant training, having attempted only short, rudimentary programming exercises. I therefore do not claim that the coding style is the most elegant that has ever been written.

Tony Hoggard provided the use of his (higher speed) PCs and printers for running of some computer simulations. The staff of the Applied Physics Department at UTS were always supportive and helpful. My children Simone, Stacey, Bethany and Brendan, and husband Rick gave me leave of absence, especially to attend an overseas conference.

My husband Richard Pope gave me much emotional and practical support, and kept encouraging me to "get that PhD finished".

My mother gave invaluable support, especially during my undergraduate degree when the children were younger and I was a sole parent. She lived to attend my Honours graduation ceremony, and to see me hooked up with a nice bloke. She did not live to see me married on 25th January 2004, or to see me complete my PhD. Fay Hoggard passed away on 3rd April 2003. I miss you Mum.

Preface

Parts of this Thesis have appeared in the following articles, published in Journals and Conference Proceedings:

C. A. Deller, G. B. Smith, J. Franklin, "Colour mixing LEDs with short microsphere doped acrylic rods", *Optics Express*, **12** (15), 3327-3333, 2004.

J. C. Jonsson, G. B. Smith, C. Deller, A. Roos, "Directional and angle-resolved optical scattering of high-performance translucent polymer sheets for energy efficient lighting and skylights", *Applied Optics* **44** (14), 2745-2754, 2005.

C. A. Deller, G. B. Smith, J. B. Franklin, "Uniform white light distribution with low loss from coloured LEDs using polymer doped polymer mixing rods", *in Proceedings of SPIE Vol. 5530: Fourth International Conference on Solid State Lighting*, 231-240, 2004

C A Deller, J B Franklin, G B Smith, "Monte Carlo ray tracing in particle-doped light guides", *accepted for publication in Journal of Lighting Research and Technology.*

C. A. Deller, J. Franklin, "Optimising the length of doped polymer light mixers", in *Proceedings of the Australian Institute of Physics 16th Biennial congress*, 84-87, 2005.

C. Deller, G. B. Smith, J. Franklin, E. Joseph, "The integration of forward light transport and lateral illumination of polymer optical fibre", in *Proceedings of the Australian Institute of Physics 15th Biennial congress*, Vol 5192, 307-309, Causal Productions, Sydney, 2002.

Table of Contents

Glossary of Symbols and Acronyms

(X, Y, Z)	direction cosines of a ray
(x_0, y_0, z_0)	Cartesian coordinates of the starting point of a ray, or the starting point for propagation in a new ray direction
(x_1, y_1, z_1)	next interaction point of a ray (particle or guide wall)
(X_i, Y_i, Z_i)	CIE tristimulus values
(x_i, y_i, z_i)	CIE colour coordinates for a pixel of the output light distribution
$(x_{LED}, y_{LED}, z_{LED})$	CIE colour coordinates for a LED
a	axial particle number (the number of particles intercepted by a straight line drawn through a TRIMM-doped light guide, parallel to the optic axis)
CCD	charge coupled device
CCT	colour correlated temperature
CIE	Commission Internationale de L'Eclairage
CRI	colour rendering index
EPA	1-ethoxy-2-propyl acetate
ESEM	environmental scanning electron microscope
F	exponential decrease of side-scattered output light with distance along a TRIMM-doped light guide
$f(\delta)$	the probability density distribution of the deviation $\delta(h)$
h	impact ratio, $h = H/r$. h is independent of sphere radius.
H	perpendicular separation distance (of a ray impacting a sphere) from the parallel ray passing through a sphere's centre ($H = r$-λ at the geometric limit)

HID	high intensity discharge (lamp)
i	projection of l' onto the x-y plane
I	light intensity (or in some cases, luminance)
IR	infra-red
l	propagation length of a ray between two particular particles
L	Length of a light guide (generally in cm)
LCD	liquid crystal display
LED	light-emitting diode
l'	length from a particle to the light guide wall, if the wall is intercepted before the following particle is reached
m	relative refractive index (usually the ratio of particle refractive index to that of the matrix in which the particles are dispersed)
m_f	mass fraction (of spheres in a matrix)
MMA	methylmethacrylate (monomer)
NA	numerical aperture (of a light guide)
n_i	refractive index of component i, such as TRIMM sphere or light guide matrix
p	average path length travelled by a ray between particle interactions
$P(h)$	the integrated probability density distribution (for unit TRIMM sphere radius)
$P(\theta)$	cumulative probability density function (for empirical LED source models)
PMMA	polymethylmethacrylate
POF	(flexible) polymer optical fibre
r	radial distance of (x_0, y_0, z_0) from the z-axis in the x-y plane (ray tracing context)
r	particle radius (e.g. of a TRIMM sphere)
R	radius of a cylindrical light guide
R	Fresnel reflectance

RGB	red, green, blue
RI	refractive index
$S(\lambda)$	spectral power distribution (of a LED)
SPD	spectral power distribution
SRF	source radial fraction (position of a LED at the entrance end of a mixing rod, relative to the optical axis the rod)
T	transmittance
TIR	total internal reflection
TRIMM	transparent refractive index matched micro-particles
UTS	University of Technology Sydney
UV	ultraviolet
V_f	volume fraction (of particles in a matrix)
$\bar{\Sigma}$	mean half-cone angular spread of light in the cross-sectional plane of a light guide
α	reflection angle of a ray from the light guide wall in the x-y plane (ray tracing context)
α	linear particle density (number of particles per metre intercepted by a straight line drawn through a TRIMM-doped light guide, parallel to the optic axis)
χ	'glancing angle' between a ray and the wall of a cylindrical light guide
χ_n	angle between a ray and the normal to the light guide wall
δ	semi-cone angular component of a ray's deviation, relative to the previous direction of the ray
$\bar{\delta}$	mean deviation angle of the probability density distribution of the deviation $f(\delta)$
δ_{geom}	deviation angle at the geometric limit

δ_m	median deviation angle of the probability density distribution of the deviation $f(\delta)$
$\delta(h)$	general expression for deviation angle of a ray impacting a TRIMM sphere, in terms of the impact ratio h
ε_1	azimuth component of a ray deviation
ε_2	difference (in angle) between ϕ_2 and ϕ_1
ϕ	azimuth component of a ray rotated about the z-axis, with $\phi = 0$ at the x-axis
ϕ_1	initial ϕ component of a ray (within a light guide)
ϕ_2	ϕ component of a ray after angular deviation by a particle
$\phi_{reflect}$	new ϕ direction after reflection from the light guide wall
ϕ_t	ϕ in the translated reference frame (rotated by τ)
ϕ_{tr}	reflected ϕ in the translated reference frame
γ	angle between r and the x-axis
φ	azimuth angle of a ray relative to the plane containing both r and the z-axis
λ	wavelength of light
m	difference of the relative refractive index m from 1
θ	semi-cone angle of a ray with the z-axis (light guide axis) within the matrix of the light guide
θ_1	initial θ direction of a ray (within a light guide)
θ_2	θ direction of a ray after angular deviation by a particle
θ_s	angle-of-incidence of a ray impacting a TRIMM sphere
τ	angle between R and the x-axis

List of Figures and Tables

Abstract

This project involves the study of optical properties of polymers doped with TRIMM (transparent refractive index matched micro-particles), and their uses in light guides. The refractive index difference between dopant and host material is small (<0.02), so forward transmittance is high, and losses due to backscattering are negligible. Flexible polymer optical fibre (POF) and polymethylmethacrylate (PMMA) rods are being incorporated into an increasing range of lighting and light mixing applications. For energy efficient mixing of red, green and blue (RGB) light-emitting diodes (LEDs) to produce white light and a range of other colours, light is transmitted from the end of a light guide ("end-light"). A major problem here is solved, namely the achievement of uniform illumination, simultaneously with low losses from scattering. Light output from RGB LEDs is shown to be completely mixed by short TRIMM-doped light guides. Alternatively, long lengths of TRIMM-doped POF can be used for "side-light". The concentration of TRIMM for these is chosen such that light is emitted from the side walls of the guide to give even illumination along its length.

A geometrical method of ray tracing in particle-doped rectangular and cylindrical light guides is derived, and Monte Carlo ray tracing simulations performed for undoped and TRIMM-doped light guides. The evolution of the distribution of ray angles, internal and external to a light guide, with propagation distance are studied. Computer simulations of angular distribution of light emitted from the wall of POF agree with measurements performed using a photogoniometer.

Simulations and measurements of light output intensity and colour from RGB LED arrays when projected from the end of a mixing rod, are also presented. Colour calculations agree with photometric measurements of RGB LED output from clear and TRIMM-doped PMMA mixing rods. Results of transmittance measurements and computer simulations show that light losses are almost entirely due to Fresnel reflectance from the entrance and exit surfaces of the rods.

Photogoniometer measurements of the angular distribution of light from LEDs are used as a basis for LED source models used in ray tracing simulations. Results of an investiga-

tion comparing the effect of using a smoothed LED source model instead of measurement-based models on simulated light output distributions are presented. The light output from LEDs can have sudden peaks in intensity at certain angles, resulting in distinctive patterns with clear colour separation, after mixing in clear polymer mixing rods. These caustic patterns are eliminated by using TRIMM-doped mixing rods, with a transmittance of ~90% after Fresnel losses, which can be readily reduced.

Introduction

Motivation for this work

Polymer light guides are being employed in an ever increasing range of lighting applications. They can be used to transport light from a source point to a target; a useful property when it is desirable to have the light source some distance from the target zone. Examples are swimming pool lights, and refrigerator lighting. Light guides are increasingly being employed to combine red, green and blue light; in data projectors (Krijn *et al.* 2004), backlit displays (Martynov *et al.* 2003) and for general illumination (Zhao *et al.* 2002). Light guides are available in a wide range of lengths, diameters, and cross-sectional shapes. Rectangular and circular cross-sections were studied in this work.

Until recently, polymer optical fibres (POF) have been used primarily for communications. Large core polymer optical fibre first became commercially available in 1986, and manufacturing techniques improved such that they had become a viable alternative for lighting by 1996 (Whitaker *et al.* 1997). The problems to be addressed for illumination using POF are quite different to those for communications. When the author commenced the research reported in this thesis, there was no published literature showing systematic evaluation of the interaction of white light with POF (Narendran *et al.* 2000). Light guides used for illumination often have a polychromatic light source, and the colour output has to appear white and aesthetically pleasing. It is important that light attenuation does not vary significantly across the wavelength range of the incident light, or there will be a visible colour shift. Some colour shift is inevitable in any light guide, as small defects in the material scatter blue light more than red. This means that white light will appear yellow after propagating a certain distance along a guide: the length at which this occurs is a function of the optical quality of the polymer. For example, the flexible POF studied in this work could initially transport light up to ~10 m without significant visible 'yellowing'. Now, after improvements to fibre quality, there is no visible colour shift in fibre lengths of ~30 m of transport. Until recently, the light sources for flexible polymer light guides generally consisted of a lamp/reflector/condenser combination, collectively referred to as an 'illuminator' (Davenport *et al.* 1998). Generally, high input flux is necessary, input coupling efficiencies are low, and output light distributions vary with different illumina-

tors for a particular fibre (Narendran *et al.* 1998). Light emitting diodes (LEDs) are a suitable alternative light source as they are small in size, energy efficient, and more directional than traditional lamps (Decker 2000). Their use is rapidly expanding, they are constantly growing in brightness, and costs are falling. Widespread increased use of LEDs will therefore lead to a more widespread use of polymer fibre.

The research described in this thesis centres around TRIMM (transparent refractive index matched micro-particles) dispersed in polymer light guides. As the acronym TRIMM suggests, the dopant particles are micrometer-sized (average diameter ≈35 μm), do not absorb visible light and have a refractive index close to that of the host polymer. The particles are cross-linked PMMA, and can be dispersed in the matrix material before polymerisation, as they have greater resistance to chemical attack than conventional acrylates.

Initially, TRIMM systems in large core flexible POF were studied, using a commercially available illuminator as a light source. TRIMM is incorporated into the fibre during polymerisation, with a view to producing energy efficient 'side-light' in long, continuous lengths. This fibre could be an alternative to fluorescent lights, with the added advantage of variable length. The TRIMM spheres deviate light by a small amount with each ray interaction, with low backscatter, resulting in an integration of forward transport of light and gradual leakage of light out of the side walls of the fibre. A significant amount of energy is wasted due to inefficient coupling of the illuminator source light into the POF. This is mainly due to the etendúe mismatch between the illuminator and the fibre, exacerbated by the lower index cladding surrounding the fibre core (Irvin *et al.* 1991, Sillyman *et al.* 2004).

TRIMM-doped guides are suitable as mixing rods for red, green and blue (RGB) LEDs, thus creating polychromatic light for illumination, as the angular intensity distributions of each of the coloured LEDs can be blended to produce output light that is smooth in both colour and intensity. Since the light loss via transmission through the walls is low, the output from these guides, which have a relatively low concentration of dopant particles, is referred to as 'end-light'. Complete mixing is achieved with a shorter length of a TRIMM-doped rod, compared to an equivalent undoped rod. This is because the TRIMM-doped rod does not rely solely on total internal reflection for light mixing, as the TRIMM particles also deviate the rays. PMMA can be used as the matrix material for these RGB LED mixing rods, as they do not need to be flexible. This means that a lower

index protective outer cladding is not required, and the half-cone acceptance angle of incident light is a full 90° for TRIMM-doped PMMA rods.

Another method of obtaining white light from LEDs is the conversion of some of the emission from a blue or UV LED chip to light of a longer wavelength using phosphors. These 'phosphor-white' LEDs suffer reduced efficiency due to energy loss caused by Stokes' shift (Zukauskas *et al.* 2002). Energy efficiency of phosphor white LEDs exceed those of incandescent lights by at least a factor of 2 (Pelka *et al.* 2003) but they suffer yellowing over time due to photo-degradation of the phosphor (Narendran *et al.* 2004). The main obstacle to combining light from RGB LEDs has been attaining a uniform illuminance and colour at the output. This requires a uniform spread of rays from all of the source distributions, in both angle and space. Up until now this problem has been tackled by the addition of diffusers (Zhao *et al.* 2002, Sales *et al.* 2004) which commonly cause large additional light losses due to backscattering, and/or have high manufacturing costs. TRIMM addresses this by deviating rays by a small angle with each particle interaction, whilst retaining forward transport, thus smoothing out inhomogeneities in the source distributions with very little light loss. Hence RGB colour mixing with TRIMM-doped polymer rods is a more favourable alternative to phosphor-white LEDs.

Thesis structure

The thesis is structured as follows:

- Chapter 1 is essentially a literature review of the technological background of light guides and sources used for illumination.
- Chapter 2 gives the theoretical physics background relevant to TRIMM systems in the context of particle scattering.
- Chapter 3 describes the experimental measurements of the optical properties of TRIMM particles and matrix materials.
- Chapter 4 presents a general Monte Carlo ray tracing method for light guides with particles randomly dispersed in a matrix material, with particular reference to cylindrical geometries.
- Chapter 5 describes the measurements of the beam patterns of various LEDs, highlighting their differences, and outlines the development of source models for use in efficient ray tracing simulations.

- Chapter 6 reports the methods and results of experimental and simulated RGB LED colour mixing, comparing the use of clear PMMA rods with TRIMM-doped PMMA systems.
- Chapter 7 shows how the uniformity of output light distributions from TRIMM mixers are affected by variation of key parameters.
- Chapter 8 discusses angular distributions of light exiting light guides via the side walls, and the significance of Fresnel reflection on these distributions, mainly from a modelling perspective.
- Chapter 9 reports the initial experimental investigations of TRIMM incorporated in flexible polymer optical fibre (POF).
- Chapter 10 consists of conclusions and suggestions for further work.

1 Technology Background

1.1 Light guides for illumination

There are several different types of light guides that are used for illumination purposes. Hollow light pipes include mirror light pipes, and prism light guides. Propagation in prism light guides is by total internal reflection (TIR) from the outer surface of the light guide wall (Whitehead 1982). Reflection losses are high, however, at 0.02 per reflection, primarily due to skew rays precessing around the guide (see Figure 1-1 for an illustration of skew rays), and additional losses at the light guide seams (Whitehead 1998). Solid core light guides include large core polymer optical fibres (POF), and solid unclad 'rods' (often PMMA). The POF consist of acrylates and plasticisers cast in a cladding material of lower refractive index. Propagation along the light guide is by TIR. Originally, light guides were used to transport source light to the application point at the opposite end of the guide; in other words, simply to transport light directly from one place to another. Later, techniques were developed to 'leak' the light out via the guide walls along the length of the light guide. In this way, the light guide becomes a side-scattering secondary light source.

1.1.1 Daylighting

Mirror light pipes have been used for daylighting. A major issue is the minimisation of the number of reflections per unit length, as reflection losses are high, and can give strong variations in the spectral properties of the transmitted light with angle of incidence of radiation (Swift *et al.* 1995). Hence the most effective mirror light pipes are short, with a small length to diameter aspect ratio (Oakley *et al.* 2000), although these restrictions can be lessened by refracting the light in at steeper angles (Edmonds *et al.* 1995). Otherwise, automatic tracking has to be employed to follow the sun's path during the day, or seasonal adjustments made by maintenance staff (Littlefair 1989). There is also a problem with heat transmission, although this can be reduced by using dichroic materials (Littlefair 1989).

A more recent study has reported the use of PMMA rods for daylighting. The rods are unclad, and so have an acceptance angle of 90°. As the light is propagated by TIR, the loss per wall reflection is very low. This means that a greater number of reflections per unit length is acceptable for PMMA rods, compared to mirror light pipes. As a result, similar transmittance of daylight was obtained for PMMA rods with aspect ratio 6 times larger, and collector area 36 times smaller, than mirror light pipes (Callow *et al.* 2003). PMMA rods also have the advantage of lowering the heat load introduced into a building.

1.1.2 Large core polymer optical fibres

The numerical aperture (NA) of a fibre is defined as $\sqrt{n_{core}{}^2 - n_{clad}{}^2}$ where n_{core} and n_{clad} are the refractive indices of the core and cladding materials, respectively. The maximum acceptance angle for a meridonal ray is $\sin\theta_{max} = \frac{1}{n_0}NA$, where n_0 is the refractive index of the surrounding medium, which is usually air. All non-meridional rays are skew rays (the path of a skew ray is shown in Figure 1-1). Skew rays may be propagated if their incidence angle is greater than θ_{max} when they strike any point on the entrance face except for the fibre axis (Dugas *et al.* 1987, Cozannet *et al.* 1975). For example, a typical POF with $n_{core} = 1.48$ and $n_{clad} = 1.33$ has $\theta_{max} = 40.5°$ for meridional rays. A ray of high skewness striking the input face at a distance of $R/2$ from the guide axis, where R is the radius of the light guide, has $\theta_{max} = 47.7°$, and a ray striking $0.75R$ from the axis has $\theta_{max} = 78.7°$. Further reference to theory of light propagation in optical fibres can be found in the literature (Allan 1973, Marcou 1997, Irvin *et al.* 1991).

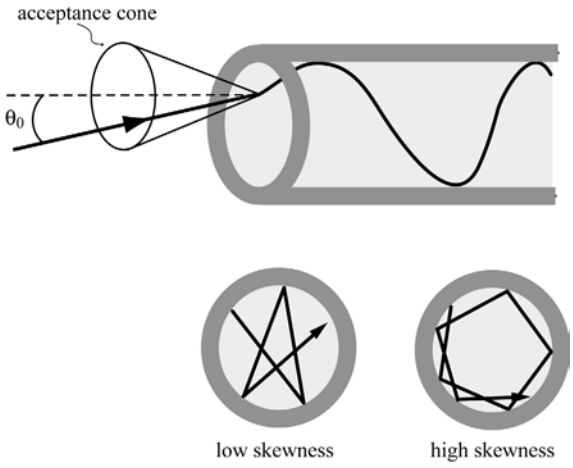

Figure 1-1. Injection and transmission of light in POF. The grey region is the cladding.

A propagation model for meridional light rays in POF which considers absorption and number of reflections per unit length of fibre is given in Narendran *et al.* 2000. Blue light is lost by Rayleigh scattering, due to microscopic variations around the average material density and composition related fluctuations in the refractive index on a scale that is small compared to the wavelength. Long wavelengths are lost primarily to molecular absorption, and so some fibres exhibit a colour shift towards green over long transmission lengths. Attenuation with wavelength for typical POF material has been documented (Narendran *et al.* 2000, Poppendieck 1998). Irregularities in fibre geometry can cause additional losses, so attention to minimising these factors is paramount to obtaining POF that will transport polychromatic light over long distances without noticeable colour shift. The primary attenuation factors are scattering and absorption in the core material, incomplete reflection and small-scale irregularities at the core/cladding interface, and ray deflections from bends. Propagation characteristics are therefore a function of wavelength, skewness and axial angle. The role of ray skewness in transmission characteristics is often neglected in a simple discussion of NA and acceptance values (Irvin *et al.* 1991). It is important to avoid bends in the initial section of the POF (where the light source is coupled) as bend losses there are much greater, due to many high angle initial rays (Saraiji *et al.* 1996).

As was previously mentioned, POF was originally used for communications applications. The advent of large core polymer fibres meant they could be used for illumination, but the issues are different to those in communications, which transmits in the near infra-red range (Saraiji *et al.* 1996). For light, transmittance needs to be maximised, and be uniform, across the entire visible light range. To achieve this, POF needs to be manufactured with chemicals that are highly purified, and the cladding must be tight around the core throughout the fibre, or the results can be inconsistent from optic to optic when the fibre is manipulated (Whitaker *et al.* 1997). This was also found from personal experience early in this research project. An early paper reported that the interface roughness between core and cladding can cause losses comparable to the bulk losses (Remillard *et al.* 1992). This further illustrates the importance of obtaining intimate contact between core and cladding, if high levels of light transport are to be achieved.

The light loss increases as input angle increases for all fibre diameters, although the highest loss for every angle was found for smallest diameter fibres (Narendran *et al.* 2000). This is an important point to consider when using light sources with a high spread of

angles incident on the fibre. High angle incident rays are more likely to propagate as skew rays, so the longer path length can potentially cause a greater colour shift. It is partly because of this that POF transmission and attenuation measurements reported by manufacturers can be misleading, especially if characterised at a single wavelength (Poppendieck 1998). For a particular fibre these properties must be suited to the source characteristics, such as the illuminator, reflector spectral characteristics, incident angle and fibre diameter. Light loss is commonly reported without any reference to spectral changes (Biermann *et al.* 1998), colour shift therefore not being considered. POF characteristics vary between types of fibres: the most significant observable difference between POF types is in their blue attenuation (Poppendieck 1998), which relates ultimately to the optical quality and production methods of the fibre.

1.1.3 Applications of POF

Advantages of using POF for lighting purposes include:

- they do not conduct heat or electrical current
- they do not transmit UV or IR radiation
- they can be installed in hard-to-reach locations
- a single lamp can illuminate several fixtures
- bulbs can be changed without scaffolding

In spite of these advantages, in 1997 it was predicted that fibre optic lighting may never replace conventional light sources, mainly due to fibre cost, coupling efficiency from lamps, POF quality and low efficacy of general purpose lamps (Barreneche 1997). These conclusions were drawn prior to the development of high brightness LEDs, and their capacity as light sources for coupling into POF had not been realised. Side-light was simply ordinary POF enclosed by a PVC sleeve. A history of POF and the associated focussing optics used for the sources, and the development of fibre technology has been reported (Davenport *et al.* 1998).

In the automotive industry, POF is useful for areas that are difficult to access, and costs can be reduced considerably compared with conventional alternatives. A 20W halogen lamp, located inside the vehicle and therefore free from shock and moisture, can feed light to 30 POFs. The POF replaces the incandescent lamp, copper wires, socket, lamp housing

and sealants required for an external application such as lighting a door handle (Saddlers 2001).

1.1.4 PMMA light guides

PMMA light guides are favoured because absorption of PMMA for visible light is low (Crist *et al.* 1980), making them ideal for highly efficient light transport. Absorption losses are mainly due to the C-H bond vibrations, and there are some losses due to Rayleigh scattering. A typical absorption spectrum for PMMA is given in many sources, including (Biermann *et al.* 1998, Kaino *et al.* 1982, 1983).

If the acceptance angle of a light guide is maximised, then so is the throughput from a given source. The acceptance angle for an unclad guide in air is equal to 90° for an index of refraction > $\sqrt{2}$. PMMA unclad rods are useful as short light guides, as, in addition to their high NA, they do not suffer the losses due to bends and cladding that POF do. Unclad PMMA rods were used for the RGB colour mixing in this project.

1.2 Light source colour and efficiency

1.2.1 Correlated Colour Temperature (CCT)

The correlated colour temperature (CCT) of a light source is the absolute temperature of a black body radiator corresponding to the closest possible colour match with the source. An incandescent light bulb has a CCT of ~2800 K, classed as 'warm' or yellowish-white. A CCT of 9000 K appears bluish-white, and 'daylight', defined as a combination of sun-light and clear sky, is around 6500 K (Murdoch 1985).

1.2.2 Colour Rendering Index (CRI)

Colour rendering index (CRI) has been defined as a measure of the degree to which the perceived object's colours illuminated by a test source conform to those of the same object illuminated by a standard test source (Narendran *et al.* 2002). The highest CRI obtainable is 100 (CIE Publication No.13.3 1995). There is no unique spectrum for a particular chromaticity, so the CRI of a particular perceived colour can vary depending on the combined spectrum of the individual RGB sources (Mueller-Mach *et al.* 2000). The perceived colour shift when an object is illuminated first by one source then another is a combination of the actual chromaticity shift, and the changes in adaptation of the observer (Murdoch 1985). The actual chromaticity shift can be measured, but it is difficult to account for human adaptation mathematically. The CRI is currently the only internation-

ally agreed metric for colour rendering evaluation, but is known to have deficiencies, particularly for the mixing of 3 different coloured LEDs (Ohno 2004).

1.2.3 Luminous efficacy

Radiant flux Φ_e is equal to the total power (in watts) of electromagnetic radiation emitted or received. The unit of luminous flux, the lumen, can be defined as the luminous flux associated with a radiant flux of 1/683 W at a wavelength of 555 nm in air (Cayless *et al.* 1983). If the total luminous flux over the visible wavelength range is Φ_v, a measure of the ability of radiation to produce visible sensation can be expressed as

$$K = \frac{\Phi_v}{\Phi_e} \tag{1-1}$$

where K is the luminous efficacy of radiation. The luminous efficacy of a light source with total power input W watts, η_v, is given by

$$\eta_v = \frac{\Phi_v}{W} \tag{1-2}$$

In considering efficacy, the entire lighting system needs to be included. Total efficacy of a lamp can be lower than that of the source, due to the effect of light distributors such as diffusers and luminaires. For example, a prism light guide luminaire, designed as an alternative for a fluorescent light in 1998, was quoted as having 40% of the light leaving the lamp going to useful light output (Whitehead 1998, Saxe *et al.* 1986). This is the efficacy of the luminaire, not of the lamp.

Further definitions and explanations regarding radiometric concepts can be found in texts such as Driscoll *et al.* 1978, Wyszecki *et al.* 2000.

1.3 LEDs

1.3.1 Advantages and applications

Light emitting diodes (LEDs) have many advantages over traditional light sources, including vibration and shock resistance, small size, low voltage, long lifetime (at least 75,000 hours compared to ~1000-5000 hours for an incandescent light and 40,000 hours for a fluorescent light), rapid on-off switching, and efficiency of producing coloured light (Green *et al.* 2003).

It is widely believed that LED technology will be the next evolution in lighting, and that the use of LEDs will come to dominate most lighting systems over the next 20 years

(Pelka *et al.* 2003, Grossman 2000). According to data from Hewlett-Packard, in the 3 decades since the invention of the LED, each decade has seen a light emission factor increase of 30 times (Decker 2000). It is predicted that lighting industry research will advance LED development to the point where it will usurp 10% -50% of the lighting market by 2025, depending on government funding. The LED market now has the potential to replace the incandescent market when costs are reduced; LED spot and flood lamps are already being manufactured as direct replacements for incandescents. LEDs are also being packaged as light sources, for example brake lights, as well as discrete packages (Knisley 2002, Budimir 2004).

Key factors in the recent prolification of LEDs and developments of their use for lighting are the energy savings and low maintenance costs. Lighting accounts for ~20% of electricity consumption in the USA (Savage 2000). A red traffic light that is powered by LEDs uses 15W, compared with 120W for a traditional light. Due to the long life of LEDs, the need for replacements is infrequent, drastically reducing maintenance costs and inconvenience to traffic. Furthermore, if a single LED in an array fails, the lamp does not cease to operate. Another example is the recent lighting of the Vincent Thomas Bridge, at the Port of Los Angeles. Each LED fixture is a cluster of 410 5mm LEDs, and requires 20W, giving light output equivalent of a 150W incandescent bulb. Furthermore, the system is powered by a 5.4 kW solar photovoltaic array. As a result of such accomplishments, interest in the possibilities offered by LEDs is growing in the wider architectural and design community (Broehl 2005). LEDs also show promise for replacing neon lighting, because of their energy efficiency, they can produce vivid colours without needing lossy filters, and rapid on-off cycling (Knisley 2003). Some of the systems developed in this project can be used as neon replacement.

The hand-held market for LEDs has also soared recently. 40% of LED sales are consumed by mobile phones and personal data assistant markets. Liquid crystal display and backlighting applications are also developing (Pelka *et al.* 2003).

1.3.2 Light extraction

The LED packaging greatly influences the luminous intensity and the viewing angle of the LED. (The viewing angle is the angle over which the pattern of radiated light is at least half of its peak value.) The reflector shape, lens shape and distance between the lens and chip all contribute to the final beam pattern (Morrison 2000). A barrier to light extraction

is TIR of the light emitted from the chip and from the lens surface. The light has to be extracted from the semiconductor chip, and then from the package. Trapped light as a consequence of TIR occurs in both cases. Geometric chip shaping can minimise this (Wall 2000), but there is a trade-off between high light extraction efficiency and low beam divergence (Bockstaele *et al.* 1999). It was recently reported that the best AlInGaP LEDs (red and amber) convert 40-50% of electrons sent into their p-n junctions directly into useful light output, and the best InGaN LEDs (UV, blue, green, white) convert 25-30% of electrons into useful light (Pelka *et al.* 2003).

1.3.3 Disadvantages

Different types of LEDs may have wide variability in their beam patterns, particularly between differing colours. Batches of LEDs are categorised into many 'bins' of colour and intensity, due to the difficulty of replicating LEDs with closely matching output characteristics. Furthermore, LEDs of a particular bin are not always available (Green *et al.* 2003). They also exhibit temperature dependence of colour and intensity, and are not readily compatible with household AC voltage outlets.

Green LEDs in particular have been reported to have a shift of emission wavelength with drive current density, a stronger temperature dependence of spectral shape and variations of light output with temperature. One group even suggested an alternative phosphor conversion of blue to green, at the expense of conversion losses (Mueller-Mach *et al.* 2002).

With all the advantages of LEDs, the photometric levels are currently still too low for some applications, such as coupling into light guides where high brightness is required, unless arrays and concentrating and focussing optics are employed (Garcia-Botella *et al.* 2000).

1.3.4 Phosphor white LEDs

Phosphor-white LEDs consist of a blue (or UV) LED with a phosphor coating (usually yttrium-aluminium garnet, or YAG) in the encapsulant to convert some of the light to a longer wavelength. Since the 'white' is produced by only blue and yellow wavelengths, the colour rendering is poor in the red (Green *et al.* 2003, Savage 2000). Colour properties can be improved by the addition of a 2nd or 3rd phosphor, at the expense of additional energy loss with the Stokes' shifts, although it is difficult to find the right combination of phosphors to do this. Mueller-Mach reported a conversion efficiency of ~70% for phosphors, although the variation between types is large (Mueller-Mach *et al.* 2000). GELcore

increased the ability of their phosphors to absorb energy by a factor of 100 (Talbot 2003) but the inherent losses due to the down conversion cannot be avoided.

The main barriers to the large scale replacement of lamps by LEDs is the difficulty in making white LEDs both efficient and cost-effective (Craford *et al.* 2001). In terms of lumens per dollar, white LEDs are still ~100 times more expensive than incandescent lights, and the efficiencies are well below that for coloured LEDs (Green *et al.* 2003). Commonly available phosphor-white LEDs have luminous efficacies of around 20-40 lumens per Watt. In November 2004 Cree inc. announced a phosphor white LED product with a luminous efficacy of up to 60 lm/W, with a typical value of 45 lm/W, which they claimed to be the highest commercial brightness in the industry (Cree inc 2004). Coloured LEDs have typical luminous efficacies of ~30 lm/W, depending on the LED.

Phosphor white LED lamps are not suitable as direct replacement for incandescents due to high initial cost, low power efficiency, poor colour rendering index and variation in correlated colour temperature. MR16 arrays have been found to have a variation of 3000 K across the output beam (Brown *et al.* 2004). Other problems with phosphor white LEDs is that the epoxy encapsulant and phosphor degrades due to heat, accelerating the light depreciation. Studies show that the life time for white LEDs is ~10,000 hours, compared to 50-100,000 hours for coloured LEDs (Narendran *et al.* 2001, 2004). Colour variation between similar LEDs is reported to be of the order of 10-12 MacAdam ellipses (MacAdam 1942, Narendran *et al.* 2001). One study investigated the possibility of rectifying this problem, while improving the colour rendering index, by the use of coloured filters to change the colour correlated temperature (You 2004). The efficiency of the filters ranged from 54-90% for 16 filters, the average being 79%; this is in addition to the inherent loss from the phosphor. It was stated in the same study that an alternative way to alter the colour is to add a coloured LED to create a warmer colour. “Means to mix the colors to make it appear uniform in color exist. However it usually introduces a considerable energy loss.” (You 2004). The aim of the research presented in this thesis was to obtain tuneable white light with high energy efficiency and low light loss, whilst gaining an understanding of the physics of TRIMM systems. Since this has been achieved, many of the problems outlined above have now been solved.

1.4 White by RGB; uniform illuminance and colour mixing

1.4.1 Mixing rods and uniform illuminance

"A mixing rod is a long light pipe used to homogenise light output." (Irving 2003). The output light from a mixing rod can contain caustics, as a result of the combination of angular variations in the source distribution, and light guide geometry. Long lengths are necessary for 'clear' light guides that rely on TIR only, to smooth irregularities in the output pattern. Reducing the length, and hence cost and weight of these mixing rods, is desirable when used in modern compact applications, such as digital data projectors. There are many such situations where homogeneous spatial and angular mixing of light is required; both for single sources and for coloured sources. If used in inspection lighting for medical and dental purposes, for example, it is required that a light guide give uniform output illumination in addition to transporting the light from the source to the application point.

Two cross-sectional shapes are commonly used for mixing rods: square and circular. A clear square guide gives better spatial uniformity at the output end than a circular guide, but a circular guide has better angular uniformity (Cassarly *et al.* 1995). If uniformity of illuminance is desired at the output surface of a mixing rod, a square cross-sectional shape is often preferable. A recent report describes the use of a square optical mixer as a solar concentrator, collecting light reflected from a primary collecting dish, then transporting it to a target array of photovoltaic cells (Winston *et al.* 2004). It was claimed that a square mixing rod gives better spatial uniformity of illuminance at the exit face than a circular rod. It is important to consider, however, that if the target plane to be illuminated is located at some distance from the exit end of the mixing rod, then *angular* uniformity at the exit face is necessary in order to obtain uniform illuminance across the target plane.

One method of homogenising the light in angular space, that is, mixing rays of high and low skewness to remove caustics, is to use microstructured surfaces. The effect of microstructured pyramids on output illumination and colour was examined using Monte Carlo methods (Leutz *et al.* 2003). Good mixing was reported, but reflection losses were not considered.

1.4.2 White light by combining RGB sources

One problem with RGB LEDs is that each colour responds differently to temperature variations (Morrison 2000) and operates with a different drive voltage. The lumen depreciation also varies between different coloured LEDs. One study, published in 2001, studied

the lumen depreciation of red, blue, green and white LEDs after operation at a drive current of 20 mA for nearly 6000 hours. The light output at the end of the experiment, relative to the light output at the beginning, was 91% for the red, 85% for the green, 68% for the blue, and 52% for the white LED. These difficulties can be overcome by optical feedback, i.e. automatically adjusting the duty cycles of the LEDs to compensate for variations in luminous output over time (Martynov *et al.* 2003, Perduijn *et al.* 2000). The electronics of these feedback systems can be optimised to save power and maximise efficiency (Latvala 2003).

An advantage of combining RGB LEDs to create white light is the ability to spectrally tune the output. Spectral drift with age can be corrected by changing the applied current manually (Grossman 2000) if automatic optical feedback is not incorporated. RGB LEDs are favoured for projection systems because coloured filters are not needed, the start up is cold, and either white colour or larger colour space is achieved (Lee *et al.* 2004). The barrier to combining light from red, green and blue LEDs has been the difficulty in mixing the colours efficiently with good uniformity and control of illumination and colour (Craford *et al.* 2001). Diffusers have been used to obtain uniform output from RGB LED in imaging devices (Hancock *et al.* 2004). TRIMM mixers offer a low light loss preferable alternative to traditional diffusers.

One research group has produced microstructured diffusers for colour mixing in angular space, using Fresnel lenses, TIR lenses and Fresnel mirrors (Benítez *et al.* 2004). Another approach is Kinoform diffusers (also known as holographic, light-shaping or tailored micro diffusers) (Pelka *et al.* 2003). The main function of these types of devices is to homogenise and distribute light within some angular space. They are, however, expensive and complicated to construct. Similarly, engineered diffusers™ are comprised of many individually designed microlenses to attain a particular illumination pattern (Sales *et al.* 2004). It has been stated that the addition of a diffuser when combining the light from RGB LEDs cannot completely eliminate the colour banding around the perifery of the white, mixed region (Sales *et al.* 2004). This has also been observed using TRIMM-doped mixing rods with RGB LEDs in this project.

1.4.3 RGB LED applications

RGB LEDs are now being used in portable devices such as mobile phones (Latvala 2003), backlit LCD screens (Grossman 2000, Martynov *et al.* 2003, Perduijn *et al.* 2000), and

projectors (Keuper *et al.* 2004, Li *et al.* 2004). A RGB LED illuminator for pocket-sized projectors recently reported a 40 lumen output, resulting in 15 lumens out of the projector. This is comparable to the brightness of a laptop when illuminating a screen area with a 15 inch diagonal (Keuper *et al.* 2004). An advantage of using RGB LEDs in projectors is the vivid colours at peak brightness levels. Traditional systems suffer desaturation of colours and energy losses, associated with colour wheels and filters (Keuper *et al.* 2004).

An important consideration in selection of LEDs for RGB colour mixing is the colour rending index (CRI). Studies based on human preference have shown that RGB LED light sources with low CRI are often preferred over phosphor-white LEDs with high CRI, and over halogen and incandescent lamps, for certain indoor and outdoor lighting applications (Narendran *et al.* 2002, Shakir *et al.* 2002). This indicates that the CRI of a light source may not be as crucial to acceptable illumination as once believed.

RGB LED colour mixing also has a potential application for car headlights. Most people are accustomed to halogen and HID headlights, which have low CCT. Colour mixing technology can be employed to overcome the colour degradation and colour difference problems associated with phosphor-based white LEDs (Van Derlofske *et al.* 2002). An additional advantage is the facility for colour adaptation to suit dry conditions, night time or fog.

1.5 Lamps and reflectors

Primary lamp characteristics include luminous efficacy, life, lumen depreciation, colour and brightness. Common types of lamps include the incandescent, tungsten-halogen, discharge lamps, sodium, mercury, fluorescent and metal halide. An overview of these lamps and their operating principles can be found in (Pritchard 1985).

Metal halide lamps have been popular for use as headlights, due to high luminance and high efficacy (Cassarly *et al.* 1997) and are now being produced in smaller packages, 3.35 inches long for example (Knisley 2003). Fluorescent lamps have developed their efficiency over 65 years, to 6 times that of the incandescent lamp, at 80 lm/W. In 2003 it was reported that incandescent and halogens annually produce 16% of the total electrically generated light output in the USA, but consume 42% of the total energy used for lighting (Pelka *et al.* 2003). This is disproportionate: obviously high efficacy light sources are needed. Neither incandescent or fluorescent lighting systems can compete with the combination of non-imaging optics and/or microstructures coupled with LED light sources.

1.5.1 Lamp reflectors and coupling

The common lamp reflector shapes are spherical, parabolic (for light collimating), and elliptical (for light focussing). The fundamental question of light collection is how to direct a set of rays with angular divergence θ_{max} distributed over an entrance aperture, into the smallest possible entrance aperture in an efficient manner (Winston 1970). The limiting factor of light collection is the étendue; the product of the diameter and acceptance angle of the target aperture. The classical method for lamp reflector design that maximises étendue coupling is to model an extended filament, and reflect once for the furthermost edge rays (Rabl *et al.* 1994, Doyle *et al.* 1999).

Significant coupling losses can be caused from skewness mismatch between source and target. There is a trade-off between maximum efficiency and maximum concentration. The upper theoretical limit for flux-transfer efficiency is 46.8% for cylindrical systems, although it can be increased to 75.1% by breaking the rotational symmetry of the reflector, using a star-shaped cross-section (Ries 1997, Shatz *et al.* 1997). Recently, a dual paraboloid reflector has been designed to couple light from an arc lamp into light guides with reduced étendue and conservation of source brightness (Li *et al.* 2004). The disadvantage is that the retroreflector reduces the efficiency of the system to 60-80%.

1.6 Source coupling into light guides

1.6.1 Lamps

When coupling light from a lamp into a light guide, it is desirable to collect as much light as possible from the lamp, and focus this light onto as small area as possible to maximise transmission through the guide. Sources used for illumination purposes emit light in all directions and are large relative to the light guide. This makes coupling hard to achieve (Saraiji *et al.* 1996). When coupling a single source into more than one fibre, it is desirable to split the light efficiently to avoid unnecessary losses due to gaps between packed fibres. The distribution of light onto each fibre end needs to be uniform, to ensure that output from each fibre will appear uniform. This is particularly important in the case of headlights. 'Multi-focus' optical systems, where the collection optics create spatially separated spots have been designed to minimise packing fraction losses (Cassarly *et al.* 1996). Other multi-focus systems have been designed by arranging light guides around a light source. Étendue restraints pose limits to the collection efficiency: 50-75% of the source light can be recovered. The higher figure is possible only for 2D designs; for example, grouping concentrators around a long linear light source (Feuermann *et al.* 1998). One

design, in an attempt to collect all of the available light from a lamp, has an array of lenses designed in various shapes to fit together like tiles on a sphere. The efficiency obtained was 53%, with an estimated 17% loss due to gaps and mounting hardware (Mathis 1997).

1.6.2 POF illuminators

Lamps that have high power densities inherent to small active radiating regions, such as conventional metal-halide, halogen and xenon lamps, are suitable for use in POF illuminators (Feuermann *et al.* 1998). A problem with most commercially available POF illuminators is that they are designed to perform optimally with only one type of fibre. This also causes a problem with fibre specifications.

Improving the performance of an illuminator involves increasing the system efficacy, (defined as the luminous flux available for transport at the illuminator port per watt of input power) and, when coupling into multiple fibres, increasing the uniformity and constancy of the beam pattern and colour across the face of the fibres (Biermann *et al.* 1998, Narendran *et al.* 1998). In the case of side scattering guides, the source brightness, angular distribution, and light pipe parameters must be optimised to maximise the amount of light travelling down the light guide (Sillyman *et al.* 2004).

Ultimately, light cannot be sufficiently concentrated into the phase space of both angle and position. If a beam is concentrated spatially, it is decollimated with respect to its angular distribution (Cassarly *et al.* 1997, Kan *et al.* 2000). It is therefore advantageous to have a light source that is small compared to the cross-section of the light guide. LEDs coupled into light guides are therefore a valuable contribution to energy efficient lighting.

1.6.3 Coupling LEDs into light guides

Methods are being developed to couple LED light into various types of light guides, for uses such as side-scattered illumination, projectors, and combining RGB to create white light for general illumination. Techniques that have been suggested to couple an array of LEDs into light guides include lenslet arrays (Irving 2003), bulb-shaped couplers (Lazarus *et al.* 2001), and cylindrical mirrors (Martynov *et al.* 2003). These methods are costly to produce, and /or involve light losses. If a LED is coupled directly into a light guide, generally some sort of diffuser system is needed to uniformly extract the light. A right angle coupler with a diffuse reflector has been suggested, to aid mixing (Van Derlofske 2001). TRIMM-doped mixing rods pose a solution to this problem, without the losses associated with reflectors. TRIMM mixers are also cheap to produce. As image panel

sizes are becoming smaller for microdisplay based projectors and televisions, more efficient coupling from the source to the image panel is becoming mandatory (Li *et al.* 2003).

1.7 Side-scattering light guides

1.7.1 POF side-scattering

A side-scattering technique that has been used for flexible polymer optical fibres involves cutting of notches in the fibre wall. Sta-Flex Linear Emitting Fibre (LEF™) employs a computer program that calculates the sequence, depth and dimensions of the cuts along a fibre wall (Whitaker *et al.* 1997, Sillyman *et al.* 2004). The spacing of the notches is engineered so that the output light patterns overlap. This exit light is directional, however, as the notches are cut in the wall following a line parallel to the guide axis. It has been suggested that, due to the high mechanical processing capability of POF, 'micro-mirrors' could be formed by cutting, metal deposition and refilling of notches along the wall to produce sidelight (Li *et al.* 1996). These sorts of processes are complex and difficult.

A side scattering system of transparent PMMA micro-particles dispersed in a polymer matrix has been reported (Berthet *et al.* 2001). These doped flexible POF are similar to the TRIMM systems described in this thesis, but there are important differences. The dopant particle sizes are smaller, and the refractive index of the POF matrix lower, than for TRIMM, so there are likely to be significant scattering and diffraction effects. Light scattering intensity as a function of concentration and particle size was modelled using Mie theory, but no allowance was made for the multiple scattering which dominates the results.

1.7.2 Backlighting

As well as transporting light, light guides can be used to randomise the radiant flux over the cross-section of the guide. After many reflections, a ray's position at the exit face of the guide is randomised, but the angle of the ray with respect to the guide axis is conserved (Leutz *et al.* 2003). This leads to caustics in the output light distribution. The only way to avoid caustics, and obtain more efficient mixing, is to either break the translational symmetry of the guide, alter the path of the light rays during propagation along the light guide, or randomise the distribution at the exit face. Various methods have been employed to achieve this, especially for side-emitting light guides and backlight display panels.

A combination of microstructured surfaces, mirrors, and microlenses, has been modelled to out-couple light out to produce a side-emitting light pipe (Teijido *et al.* 1996). A

common approach uses scattering paint or diffusers, where the area of deposited diffuser material increases with distance along a light guide, in order to control the uniformity of the side-scattered output (Whitehead 1998, Teijido *et al.* 1996). Deposition of such materials directly onto the surface is not possible with light guides with low refractive index cladding. These techniques are also not easily adapted for mass production. Approaches to obtain even distribution from backlight by complicated light guide geometries are also impractical (Zhao *et al.* 2003).

A "highly scattering optical transmission" (HSOT) polymer has been reported for backlighting panels. It consists of silicone particles (average diameter 0.75 μm) in PMMA. An even distribution of light was obtained on the top face of the backlight by optimising the particle size and internal particle concentration (Okumura *et al.* 2003), but needed a wedge-shaped light guide design.

2 Background Theory

This chapter begins with a brief description of relevant scattering theory, and then treats TRIMM particles in this context. The theory of ray deviation for a single TRIMM sphere is described, then the mean deviation of a TRIMM sphere is extended to applications of multiple TRIMM scattering.

2.1 Single particle scattering

Light scattering by a particle can be viewed as the superposition of the energy radiated by an array of electric and magnetic multipoles (Kerker 1965). The scattering pattern resulting from multiple particles can be obtained by summing the intensities and phases of the single particle patterns. The exact solution of single particle scattering can be given by Mie theory (Mie 1908). However, simplifications and approximations of Mie theory can be appropriate in certain cases. Alternative treatments of scattering can be made for different size regimes (Figure 2-1).

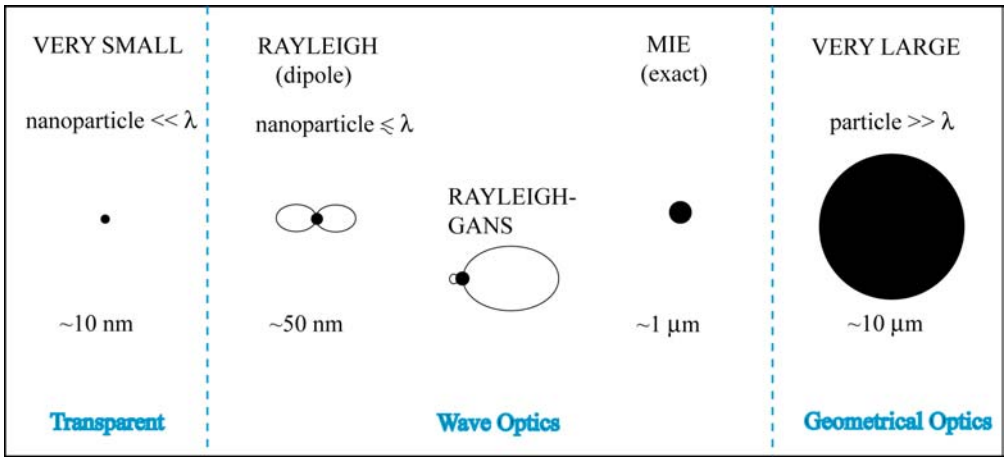

Figure 2-1. Scattering regimes for the visible electromagnetic spectrum, for increasing particle size

Nanometre-sized particles, which are tiny compared to the wavelength of light, are transparent (apart from absorption) when dispersed in a clear polymer (Smith *et al.* 2002). Scattering by particles that are small compared to the wavelength can be described by Rayleigh scattering. Rayleigh-Gans scattering applies where the size of the particle is

comparable to the wavelength. For particles that are huge compared to the incident wavelength, geometrical optics can be applied.

2.1.1 Rayleigh scattering

Particles that are small compared to the wavelength (λ) are effectively enveloped by the incident radiation. Each particle can be considered as a dielectric sphere suspended in a uniform electromagnetic field. The electric component of the surrounding field induces a dipole in each particle, and so secondary waves are radiated in all directions. Thus for very small particles, the incident radiation is scattered in equal amounts in forward and reverse directions (Kerker 1969).

A standard form of the Rayleigh equation is

$$Q_{sca} = \frac{8}{3}(kr)^4 \left| \frac{m^2 - 1}{m^2 + 1} \right|^2 \qquad \textbf{(2-1)}$$

Q_{sca} is the scattering efficiency factor, $k = \frac{2\pi}{\lambda}$ and m is the relative refractive index of that of the particle to that of the surrounding medium (Kerker 1969).

2.1.2 Rayleigh-Gans scattering

Particles that are of a size comparable to the wavelength may be treated using Rayleigh-Gans scattering. In contrast to Rayleigh scattering, where the incident wave causes a single dipole, multipoles are induced within the particle in Rayleigh-Gans scattering. Consequently, in this domain forward scattering greatly exceeds the backscattering. The parameter $x = \frac{2\pi r}{\lambda}$, which relates the size of a particle to the incident wavelength, lies in the range $0.2 \geq x \geq 10$ in the Rayleigh-Gans domain (van de Hulst 1981). The backscattering of radiation is somewhat smaller than the forward scattering even at the lower limit of $x = 0.2$, and with increasing x this asymmetry becomes more pronounced. For the larger values of x in this domain, the concentration of light towards $\theta = 0°$ becomes very great. For $x = 10$, for a total calculated scattering cross-section of 194.0, 193.7 is in the forward hemisphere (Ryde *et al.* 1931).

A condition for Rayleigh-Gans scattering is that, in addition to $\frac{2\pi r}{\lambda}$ being small, the phase shift of the ray upon travelling through the particle along a diameter, $\rho = \frac{4\pi r}{\lambda}(m - 1)$, must also be small (van de Hulst 1981). This means that a range of $r \ll \frac{\lambda}{(m - 1)}$ applies.

2.1.3 Very large spheres

Mie theory can be expressed as the exact result of the combined effects of the geometrical optics pattern, and the diffraction pattern around the edges of a sphere. The scattering can be thought of as a combination of the Fraunhofer scattered pattern, and the rays undergoing reflections and refractions upon striking a sphere (Kerker 1965, van de Hulst 1981).

If the size of a particle is increased from small (with respect to the wavelength) to large, the reflection and refraction scattering pattern increasingly approaches that of geometric optics, and the diffraction pattern is compressed into a narrow lobe around the forward direction. From the part of the incident wave which hits the sphere, a narrow beam can be isolated which is much smaller than the sphere radius. This is called a 'ray' in geometrical optics. The difference between rays incident on a particle and rays passing the particle can be clearly differentiated, and rays hitting different parts of the sphere's surface can be clearly distinguished, for particles that are ~20 times greater than the wavelength. Hence if the particle is sufficiently large, geometrical optics, or ray optics, can be adopted as an alternative to the rigorous Mie theory (van de Hulst 1981). A detailed comparison of geometrical optics scattered light patterns with those obtained using Mie theory was made for spherical transparent particles within a diameter range of 1-100 μm (Ungut *et al.* 1980). For particles with diameters of >10 μm and for forward scattering angles of 0-20°, the average percent least squares error between geometric optics and Mie theory calculations was reported to be of the order of 10%. The diffraction part of the scattered pattern is insignificant in the geometrical limit; ray optics gives the same pattern as the exact result, except for grazing rays, for $x > 15$.

2.1.4 Spheres with relative refractive index close to 1

Scattering by a particle is dependent on the fact that its refractive index differs from the surrounding medium; that is, the relative refractive index (m) of the sphere to the matrix material differs from 1. If this difference of relative refractive index from 1 is μ, then

$$m = 1 + \mu \tag{2–2}$$

then if $\mu = 0$ there is no scattering, and for μ close to 0 the scattering is small.

μ can be positive or negative. In practical terms the scattering pattern is the same whether the spheres have a greater or smaller refractive index than the host material.

2.2 Single particle scattering: TRIMM spheres

Transparent refractive index matched micro-particles (TRIMM) are very large compared to the wavelength of visible light, having a mean particle diameter of about 35 μm. The particles are dispersed within a matrix of similar refractive index, so μ is small ($\mu = 0.0114$ for TRIMM in PMMA, and $\mu = 0.0182$ for TRIMM in flexible optical fibre matrix).

As discussed in Section 2.1.3, rays can be clearly differentiated striking different parts of the surface of a sphere which is greater than ~20 times the wavelength. For TRIMM spheres, this corresponds to a size range of 8-14 μm over the visible light wavelength range of $400 < \lambda < 700$ nm. Most TRIMM spheres fall within the diameter range of 15-50 μm, which is well within the domain of geometrical optics. Thus the angular deviation of a ray encountering a TRIMM particle is not dependent on the actual size of the TRIMM particle, but rather depends only on the value of μ.

A small fraction of TRIMM spheres (<1%) fall in the diameter range of 5 μm or less, so one should ask, what is the lower size limit at which geometrical optics can be justifiably applied for TRIMM systems? The upper end of the Rayleigh-Gans domain is one indicator of this limit. For visible light, and with $x = 10$, which is the upper size limit in the Rayleigh-Gans domain (Section 2.1.2), a particle diameter of ≈ 2 μm is obtained. This corresponds to a very small fraction of TRIMM spheres encountered. In the Rayleigh-Gans domain, forward scattering greatly exceeds backscatter, so even in this small limit back-scattering arising from a single induced dipole, as occurs for very small spheres, is inapplicable. Any significant back-reflectance is due to Fresnel reflection. An alternative-sphere size limit for geometrical optics treatment is discussed in Section 2.2.3, where the geometrical limit is defined as a ray striking a sphere at a distance of one wavelength from the sphere's edge.

2.2.1 Fresnel reflection from a TRIMM sphere

Since TRIMM spheres are large and can be treated using geometrical optics, the reflection and refraction of rays incident upon a sphere will now be considered. The refractive index of TRIMM is closely matched to that of the matrix material; that is, μ is very small, so internally reflected rays within the particle are insignificant. Only incident, reflected, and transmitted refracted rays with respect to the sphere outer surface need to be considered.

Due to the large size of the particles, Fresnel reflection is the only type of back reflectance to merit serious consideration.

A ray can impact a TRIMM sphere at various points on its surface. A ray travelling in a pre-defined direction will impact a TRIMM sphere at a certain angle-of-incidence θ_s, which is dependent upon H, the perpendicular separation distance from the parallel ray passing through the sphere's centre. The impact ratio h is defined as $h = \frac{H}{r}$, and is thus independent of sphere radius r. So the angle of incidence will be 0° at $h = 0$ (normal incidence), and 90° at $h = 1$, when it strikes 'grazing incidence', at a tangent to the sphere (refer Figure 2-2).

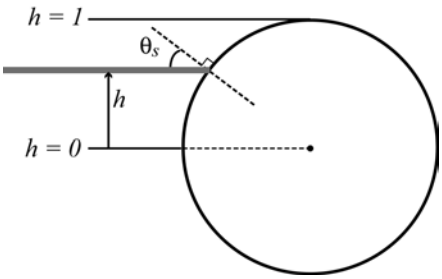

Figure 2-2. Angle of incidence of a ray with a sphere, related to the impact distance h.

Fresnel reflectance curves of a ray impacting a TRIMM sphere at varying angles-of-incidence are shown in Figure 2-3. Figure 2-3(a) shows the reflectance for the averaged parallel and perpendicular polarisation states, for the two types of TRIMM systems studied. A PMMA matrix gives $\mu = 0.0114$ (lower curve), and a flexible polymer optical fibre (POF) matrix gives $\mu = 0.0182$ (upper curve). Figure 2-3(b) shows the reflectance curves for the perpendicular, parallel and averaged initial polarisation states for $\mu = 0.0114$.

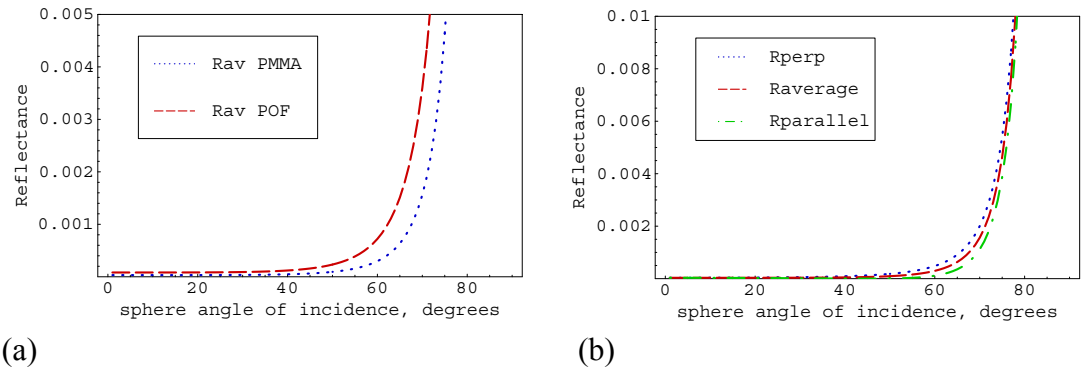

Figure 2-3. (a) Fresnel reflectance (average of parallel and perpendicular polarisation states) from a TRIMM sphere vs angle of incidence with a sphere's surface. Curves are shown for PMMA matrix ($\mu = 0.0114$) and flexible polymer optical fibre (POF) matrix ($\mu = 0.0182$). (b) Fresnel reflectance curves for $\mu = 0.0114$.

For normal incidence, that is $\theta_s = 0$ and $h = 0$, Fresnel reflectance can be approximated as

$$R = \left(\frac{n_2 - n_1}{n_2 + n_1}\right)^2 = \left(\frac{m-1}{m+1}\right)^2 = \frac{\mu^2}{(\mu+2)^2} \sim \frac{\mu^2}{4} \qquad \textbf{(2-3)}$$

since $\mu^2 \ll 0.001$.

The median value of h, the radial fraction of contact of a ray with a sphere at the median point, is $\frac{1}{\sqrt{2}}$. The angle-of-incidence of the ray with the sphere at this point is 45°. The Fresnel reflection for the median value of h, at $\mu = 0.0114$, is $R_{\perp} = 1.26 \times 10^{-4}$, $R_{\parallel} = 1.58 \times 10^{-8}$ giving $R_{average} = 6.29 \times 10^{-5}$. To obtain an incident light loss of 0.5% in system of TRIMM in PMMA, each ray would have to strike ~ 80 particles. It should be noted that some of this reflectance would be in a sideways direction, which is helpful for TRIMM when used in side-light applications. For end-light applications, such as for the short rods used in RGB LED colour mixing, the number of spheres struck during transmission through the rod, and hence the Fresnel back-reflectance due to the particles, does not significantly contribute to overall losses. The only case where the back-scattered loss from TRIMM spheres may reach 1% or higher would occur in very long flexible fibres where high numbers of particles (> 200) may be encountered.

2.2.2 Ray deviation by a TRIMM sphere

A simple theory based on geometrical optics was developed for rays incident on TRIMM spheres, in order to develop ray tracing models, and to assist in understanding and predicting light distributions inside and outside of TRIMM-doped light guides.

Every time a ray strikes a TRIMM particle, upon transmission there is an angular deviation, δ(shown in Figure 2-4). As described previously, the ray deviation can be described in terms of geometrical optics because the size of the particle is large compared to the wavelength. The ratio h, which determines the incident angle of the ray with the sphere surface, is randomly determined for each interaction of a ray with a TRIMM sphere, to give uniform probability of impact point. Internal reflections within the sphere are neglected, since the Fresnel reflection is very small, as discussed in Section 2.2.1. During ray tracing simulations, the new direction for the deviated ray is calculated after each particle interaction, using 3D spherical geometry. This will be discussed in Chapter 4.

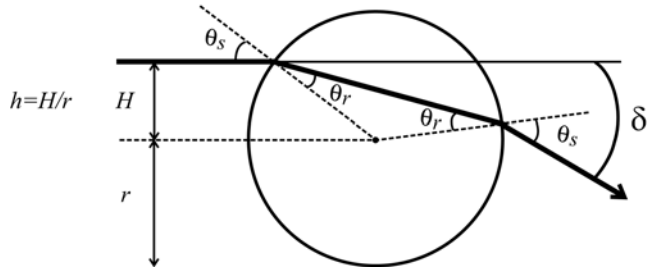

Figure 2-4. Angular deviation of a ray when it strikes a TRIMM sphere. Note that δ is actually a 3 dimensional change in ray direction.

2.2.2.1 Deviation formula derivation

A ray of light incident on a sphere of radius r enters at a point that is distance H from the optic axis (Figure 2-4). The derivation of total deviation angle, δ, can be made to be independent of sphere radius by expressing the impact point as $h = \frac{H}{r}$. The ray is refracted when entering the sphere, according to Snell's Law, so that

$$n_{matrix} \sin\theta_s = n_{sphere} \sin\theta_r \qquad \textbf{(2-4)}$$

The total angular deviation, δ, can be expressed as $2(\theta_s - \theta_r)$, so

$$\theta_r = \theta_s - \frac{\delta}{2} \qquad \textbf{(2-5)}$$

It can be seen from Figure 2-4 that

$$h = \sin\theta_s \qquad \textbf{(2-6)}$$

so combining eqn 2-4, eqn 2-5, eqn 2-6 and eqn 2-2 gives:

$$\delta(h) = 2\left[\sin^{-1}(h) - \sin^{-1}\left(\frac{h}{\mu}\right)\right] \qquad \textbf{(2-7)}$$

which is a general expression for deviation angle of a ray impacting on a large TRIMM sphere.

In the geometric limit the single particle scattering pattern depends only on μ, and is independent of sphere size, since δ depends only on h and μ (eqn 2-7). Figure 2-5 shows the relationship of deviation angle δ with the impact parameter h, for the two values of μ studied in this work.

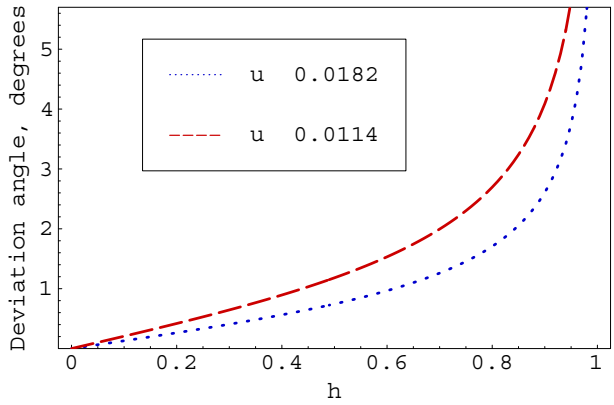

Figure 2-5. Ray deviation angle by a single sphere, as a function of the sphere impact point h (calculated using eqn 2-7) for $\mu = 0.0114$ and $\mu = 0.0182$)

2.2.3 Deviation formula and the geometric limit

For a sphere of radius r and light of wavelength λ, the ray deviation at the geometric limit, δ_{geom}, occurs at $h = 1 - \frac{\lambda}{r}$ (i.e. at $H = r - \lambda$, one wavelength from the sphere's edge), and is given by

$$\delta_{geom} = 2\left[\sin^{-1}\left(1 - \frac{\lambda}{r}\right) - \sin^{-1}\left(\frac{1 - \frac{\lambda}{r}}{1 + \mu}\right)\right] \qquad \textbf{(2-8)}$$

So for TRIMM-doped PMMA rods, with cross-linked PMMA spheres in a PMMA matrix, $\mu = 0.0114$ at $\lambda = 590$ nm, giving $\delta_{geom} = 4.5^{o}$. For TRIMM spheres in a POF matrix, $\mu = 0.0182$, giving $\delta_{geom} = 6.9^{o}$.

The geometrical limit for TRIMM spheres in PMMA, at the average size of $r = 17$ µm, corresponds to $h = 0.966$. That means that only ~ 3% of sphere deviations in a simulation are outside of this limit. At the geometric limit, $\theta_s = 75^{o}$and $R_{average} \approx 0.005$.

Estimates of the size limit to which geometrical optics can be applied for TRIMM were made in Section 2.2. Another approach, using the deviation formula for a TRIMM sphere, is to find the value of h at the geometrical limit, defined as one wavelength away from the sphere's edge, for various sphere sizes. This was done for $\lambda = 590$ nm applying eqn 2-8 over a range of r, using eqn 2-7 to obtain the corresponding values of h. The results are shown in Figure 2-6(a). The h values can be correlated with the angle-of-incidence of a ray on a sphere surface (see Figure 2-6(b)). It can be seen that a sphere with diameter > 10 µm has $h > 0.9$ at the geometric limit, which corresponds to a sphere incidence angle

of ~ 65°. Below this diameter, the value of *h* at the geometrical limit begins to fall rapidly, but geometrical optics still holds for near-normal incidence angles.

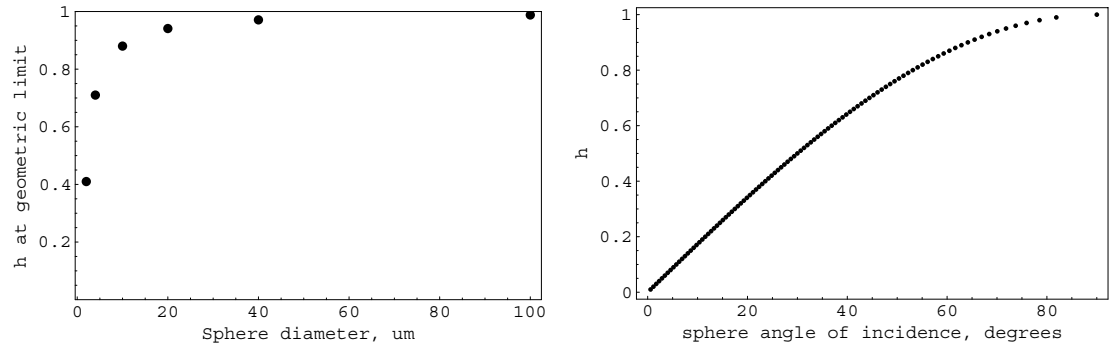

Figure 2-6. (a) impact parameter *h* at the geometric limit, defined as one wavelength's distance from the sphere's edge, for λ = 590 nm, for various values of sphere diameter. (b) correlation between *h* and the angle-of-incidence of a ray with the surface of a sphere.

The geometrical limit size estimate results obtained using the method just described agrees with the estimate made using $r > 20\lambda$ at the beginning of this section. In both cases, the geometric limit for TRIMM spheres is 10 μm for all but grazing angles of incidence. For the 2 μm Rayleigh-Gans limit estimated, it can be seen from Figure 2-6 that the geometrical optics is valid for 0 < h < 0.41, which corresponds to $0 < \theta_s < 24°$.

2.2.4 Effect of varying μ on distribution of deviation angles

The impact point of a ray with a sphere is determined randomly with each sphere interaction in a ray tracing simulation; *h* is selected by taking the square root of a random number between 0 and 1. The median value of *h*, the radial fraction of contact of a ray with a sphere, is $\frac{1}{\sqrt{2}}$. Substituting this into eqn 2-7 the median deviation angle, δ_m, is thus

$$\delta_m = 2\mu \qquad \textbf{(2-9)}$$

For the TRIMM-doped PMMA rods, $\mu = 0.0114$, so $\delta_m = 1.3°$. For TRIMM in POF, $\mu = 0.0182$, giving $\delta_m = 2.1°$.

The effect of changing the sphere-to-matrix relative refractive index ratio *m*, and therefore μ, on deviation angle frequency distribution is shown in Figure . Figure (a) has been generated with $\mu = 0.0114$. It can be seen that the greatest number of deviations are ≈ 1-2°. Figure (b) has $\mu = 0.0182$. It can be seen that, in addition to δ_m increasing with increasing μ, there is a significant increase in higher angle ray deviation events. This is an important factor to consider when designing TRIMM systems, as higher values of μ for a particular

TRIMM concentration will result in higher losses out of the walls of the light guide. This may be useful or may need to be countered depending on the application.

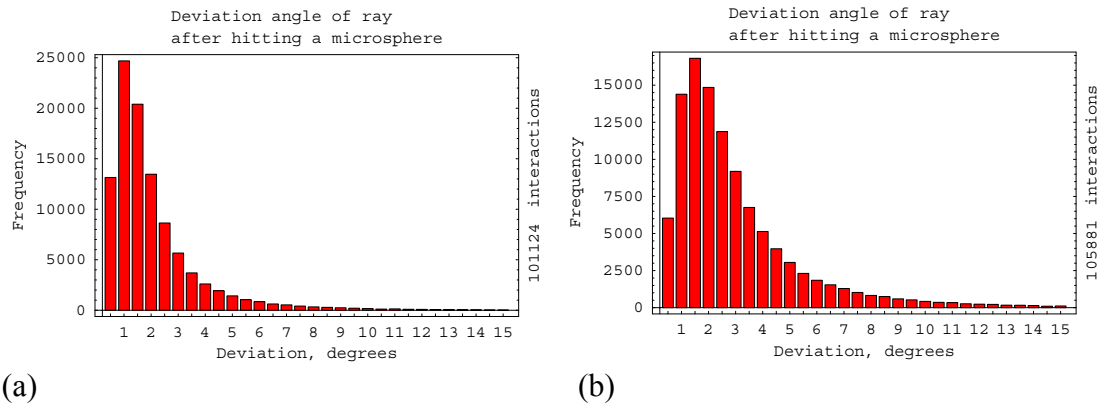

(a) (b)

Figure 2-7. Frequency of deviation angles upon encountering a TRIMM particle, for (a) $\mu = 1.011$ (b) $\mu = 1.018$. Distributions were obtained using computer ray tracing simulations.

2.2.5 Derivation of the probability density distribution of the deviation

The probability density distribution of the deviation, $f(\delta)$, is shown (unnormalised) as derived from Monte Carlo modelling in Figure . It can also be calculated analytically.

The integrated probability density $P(h) = \frac{\pi h^2}{\pi r^2}$, thus for a unit TRIMM sphere radius, is

$$P(h) = h^2 = \int_0^{\partial h} f(\delta)\partial\delta \qquad \textbf{(2-10)}$$

Therefore

$$f(\delta) = \frac{\partial P}{\partial \delta} = \frac{\partial P}{\partial h} \cdot \frac{\partial h}{\partial \delta} = \frac{h}{\frac{1}{\sqrt{1-h^2}} - \frac{1}{\sqrt{(1+\mu)^2 - h^2}}} \qquad \textbf{(2-11)}$$

Figure 2-8 shows $f(\delta)$ as calculated using eqn 2-10 and eqn 2-7, and $f(\delta)$ as derived using Monte Carlo data shown in Figure (a), for $\mu = 0.0114$.

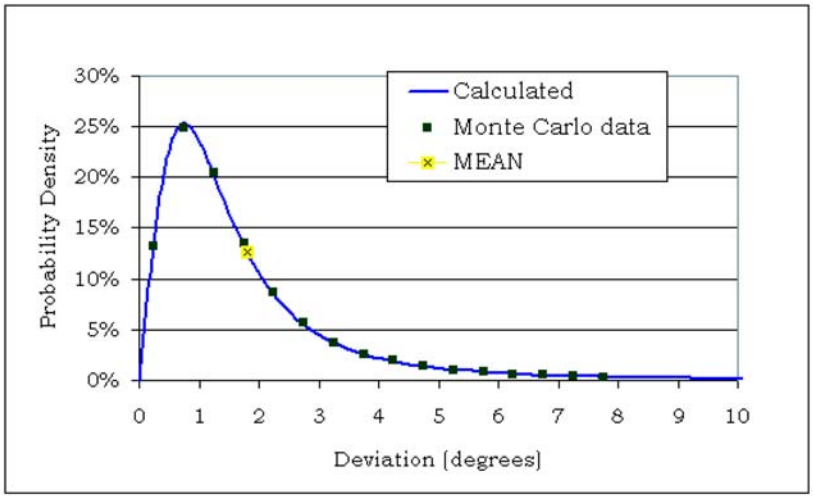

Figure 2-8. The probability density distribution of the deviation, $f(\delta)$, for $\mu = 0.0114$. $\bar{\delta}$ is marked with an x.

2.2.6 Mean ray deviation by a single sphere

In order to calculate the mean deviation, $\bar{\delta}$, it is noted that the probability of an incident ray having a fractional radial contact value in the interval h to $h+\partial h$ is $2\pi h \partial h$ (Figure 2-9).

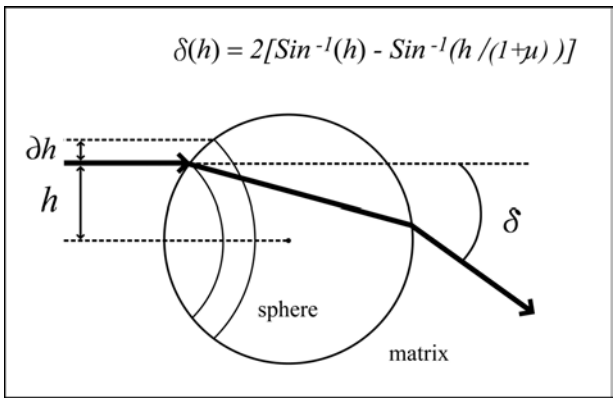

Figure 2-9. Angular deviation of a single ray striking a TRIMM sphere of unit radius.

Thus the mean deviation of a ray striking a single sphere is

$$\bar{\delta} = \frac{\int_0^1 \delta(h) 2\pi h \partial h}{\int_0^1 2\pi h \partial h} = 4 \int_0^1 h \left[\sin^{-1}(h) - \sin^{-1}\left(\frac{h}{1+\mu}\right) \right] \partial h \qquad \textbf{(2-12)}$$

Figure 2-10(a) shows the variation of $\bar{\delta}$ with μ, as evaluated using eqn 2-12. Figure 2-10(b) shows this variation when $\bar{\delta}$ is expressed as a multiple of μ.

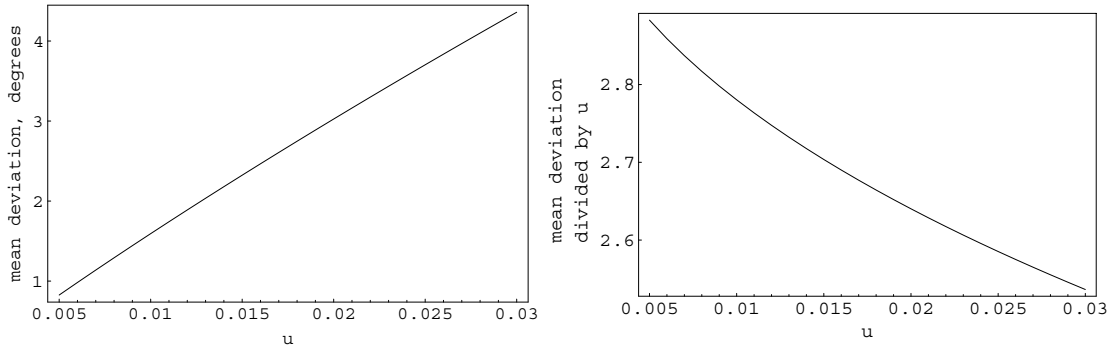

(a) (b)

Figure 2-10. a) Variation of mean deviation, $\bar{\delta}$ with μ, as per eqn 2-12. b) Variation of $\bar{\delta}$ with μ, when $\bar{\delta}$ is expressed as a multiple of μ.

Table 2-1 shows a summary of the ray deviation angle statistics for a single TRIMM sphere in the two host matrix materials studied, as calculated using eqn 2-9, eqn 2-12 and eqn 2-8.

Table 2-1. Summary of deviation statistics for the TRIMM materials studied (λ = 590 nm).

material	n_{matrix}	n_{TRIMM}	μ	δ_{median}	$\bar{\delta}$	$\delta_{geom\ limit}$
TRIMM in PMMA	1.49	1.507	0.0114	1.3°	1.8°	4.5°
TRIMM in POF	1.48	1.507	0.0182	2.1°	2.8°	6.9°

2.3 Multiple TRIMM spheres

The transmittance pattern of light passing through a matrix containing many spheres can be obtained by multiple ray tracing. Each ray encounters several spheres as it is traced through the light guide using a Monte Carlo method. Phase effects are not considered in the ray tracing modelling, as phase differences are averaged out by even a small spread in particle size (Ungut *et al.* 1980). The size spread of TRIMM particles is considerable, and additionally, the particles are randomly dispersed throughout the matrix material. Displacements of particles relative to each other and changes in scattering angle will randomise these phase effects. Thus in this case, transmitted intensities can be added directly to obtain an averaged result without including phase.

2.3.1 Angular spread of light after multiple interactions

The value of μ is fixed by the properties of the TRIMM and matrix combination. The deviation distribution of a single particle is dependent only on μ. The scattered intensity distribution for a single sphere in limit of small μ with large sphere radius, as given by van der Hulst, can be expressed in terms of peak value *i(0)* measured at $\delta = 0$ (Smith *et al.* 2003)

$$i(\delta) = i(0)\left[\frac{1}{1 + (\delta^2/(4\mu^2))}\right] \qquad \textbf{(2-13)}$$

It can be seen from eqn 2-13 that, since μ is small, $i(\delta)$ is small. For light of parallel incidence, a significant spread of exit angles is obtained only upon interaction with several spheres. Since μ is fixed for a particular system, the output light distribution can be altered by changing the TRIMM concentration or sample thickness, i.e. by controlling the number of ray/particle interactions.

2.3.1.1 Angular spread estimate using TRIMM deviation formulae

A ray's path along a TRIMM mixer, as it deviates with every sphere interaction, can be described as a random walk. Each time a ray passes through a micro-sphere it is deviated by a small angle, δ. Multiple interactions will tend to randomly deviate the ray.

The distribution of light exiting a mixing rod will be a convolution of the source emission function with the point-spread function of the propagating light. As a preliminary estimate of the total angular spread of rays reaching the end of a TRIMM mixer, consider the propagation of rays entering a rod at normal incidence.

Consider a straight line drawn through a light guide of length *L*, parallel to the optic axis. The number of TRIMM spheres intercepted by this line is defined as the axial particle number, *a*, of the light guide. The corresponding number of particles per metre is defined as the linear particle density, α; thus,

$$a = \alpha L \qquad \textbf{(2-14)}$$

Because $\bar{\delta}$ is small, for rays reaching the guide end, the total length of the ray path, *P*, is approximately equal to the mixing rod length, *L*. The ray undergoes approximately *a* interactions of average deviation $\bar{\delta}$, so the Central Limit Theorem suggests that the mean half cone angular spread, $\bar{\Sigma}$, of light in the cross-sectional plane when it reaches the end of a TRIMM doped rod can be approximated by

$$\bar{\Sigma} \approx \bar{\delta}\sqrt{a} \qquad \textbf{(2-15)}$$

as shown in Figure 2-11.

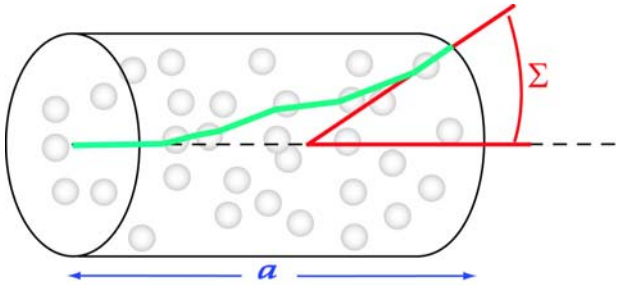

Figure 2-11. half-cone angular spread, Σ, for a single ray launched at normal incidence after propagating through a TRIMM-doped rod with axial particle number, a.

Now the probability distribution of deviation by a single sphere is such that there will be a number of events with a deviation significantly higher than $\bar{\delta}$ (Figure 2-8). In addition, the number of particle interactions per ray is actually greater than a, since $P > L$. It is also desirable to derive a model in terms of μ rather than $\bar{\delta}$, for design convenience. Evaluation of eqn 2-12 shows that $\bar{\delta}$, when expressed as a multiple of μ varies slowly with μ, so, as a rough approximation, $\bar{\delta} \approx constant \times \mu$ (see Figure 2-10).

Taking these simplifications into account, a closer approximation to the mean half cone angular spread $\bar{\Sigma}$ than eqn 2-15 can be obtained by modelling a best fit for a independent additions of deviations (given by eqn 2-7and eqn 2-10)

$$\bar{\Sigma} \approx k\mu a^{p} \qquad \textbf{(2-16)}$$

by adjusting k and p until optimisation is reached. This was performed with an optimisation range of $0.01 < \mu < 0.02$ and $50 < a < 130$ chosen, to match the typical experimental range of these parameters. The optimised fit for eqn 2-16 is

$$\bar{\Sigma} \approx 3.39\mu a^{0.514} \qquad \textbf{(2-17)}$$

The error in the sum of the squares of the residuals varied from 1.1% - 6.2% over the optimised range of μ and a.

2.3.1.2 Example: Critical Length of TRIMM-doped rods

A convenient parameter for TRIMM mixer design is the critical length, L_{crit}. This is defined as the length, for a given μ and α, where $\bar{\Sigma}$ is equal to θ_{crit}, the ray angle with respect to the rod axis where rays will escape out of the walls due to the critical condition.

For a guide of refractive index n_{matrix} with square walls, or for meridional rays in a circular light guide, $\theta_{crit} = \frac{\pi}{2} - \sin^{-1}\left(\frac{1}{n_{matrix}}\right)$, assuming the medium outside the mixer is air. From eqn 2-15 it can be seen that the critical length, assuming a Guassian distribution of $\bar{\delta}$, is

$$L_{crit} = \frac{\theta_{crit}^{2}}{\alpha(\bar{\delta})^{2}} \qquad \textbf{(2-18)}$$

From eqn 2-18 and eqn 2-17 a general formula for the critical length can be derived:

$$L_{crit} = \frac{\theta_{crit}^{1.946}}{\alpha(3.39\mu)^{1.946}} \qquad \textbf{(2-19)}$$

Equation 2-19 is a rough estimate of the critical length, due to the following factors:

- only meridional rays are considered;
- As α increases, the actual number of particles encountered per ray is increasingly greater than a, since $P > L$;
- $\bar{\delta}$ is not a constant multiple of μ
- eqn 2-19 is not optimised for $a > 130$.

Figure 2-12(a) shows a plot of critical length vs TRIMM concentration, according to eqn 2-19, for $\mu = 0.0114$ and $\mu = 0.0182$.

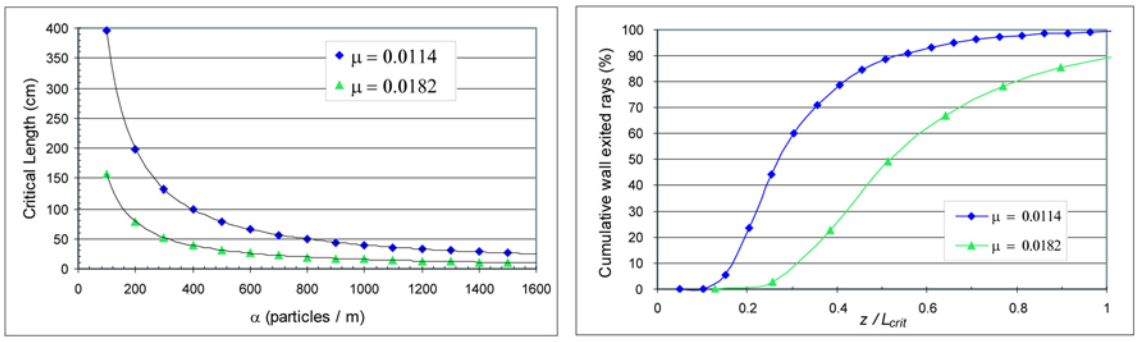

Figure 2-12. a) Critical length vs TRIMM linear particle density α for $\mu = 0.0114$ and $\mu = 0.0182$. b) Monte Carlo modelled wall exited rays as a function of z/L_{crit} (fraction of total guide length), for $\alpha = 2000$, for the same two μ values.

As an example, for a set concentration of $\alpha = 2000$ TRIMM particles per metre, critical lengths can be calculated using two values of μ. For $\mu = 0.0114$, $a \approx 400$ (from eqn 2-14),

and L_{crit} = 19.7 cm. For μ = 0.0182, $a \approx 160$, and L_{crit} = 7.8 cm. Monte Carlo ray tracing for 100,000 rays was performed for each system using a light guide with a 2 cm square cross-section, with $L \sim L_{crit}$. Figure 2-12(b) shows the percentage of initially launched rays that have exited through the walls as a function of fraction of critical length. Figure 2-13(a) and Figure 2-13(b) show ray traces (100 rays) for each system.

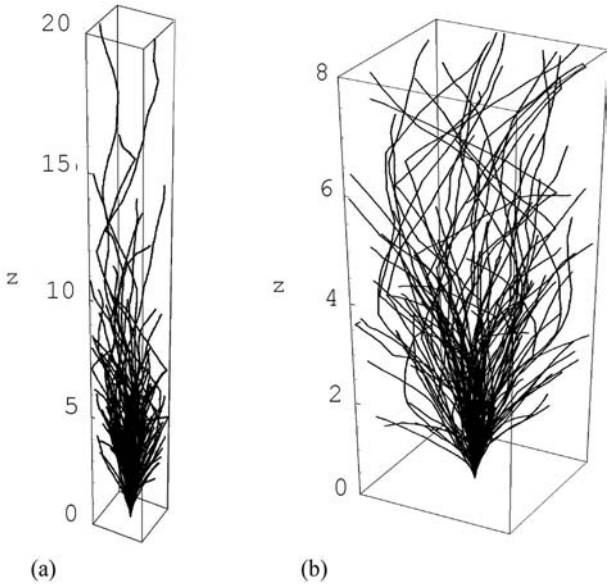

Figure 2-13. a) Ray trace for μ = 0.0114. b) Ray trace for μ = 0.0182. (α = 2000).

The purpose of modelling a critical length is to aid in the choice of optimum parameters when designing TRIMM rod light mixers. It would be useful to have an equation to estimate, for example, the length required to have 50% of the light reaching the end of the light guide. For μ = 0.0182, this length is $\sim L_{crit}/2$ (from Figure 2-12(b)). The corresponding critical length for μ = 0.0114 is overestimated by using eqn 2-19; this is not surprising, since Figure 2-12(b) has $a = 400$, which is much greater than the upper optimisation limit of a = 130. However, the model described here can serve as a rough design estimate, especially if a is optimised over the appropriate range, and for lower concentrations of TRIMM, since $P>>L$ for high TRIMM concentrations.

It should also be remembered that this simplified propagation model has been considered for rays at normal incidence. $\bar{\Sigma}$ is spread about the incident ray direction, and should be convolved with the source angular distribution for actual light sources.

3 TRIMM micro-spheres and matrix materials: measurements

3.1 Introduction

Transparent refractive index matched micro-particles (TRIMM) are so named because there is only a small refractive index difference between the dopant particles and the matrix polymer. TRIMM are often referred to as 'spheres', partly due to their shape, but also because the theory of ray deviation described in Section 2.2 assumes that the particles are spherical. The relative refractive index, $m = n_{TRIMM} / n_{matrix}$ (where n_{TRIMM} is the refractive index of the spheres and n_{matrix} is that of the matrix material) can be usefully described by its difference from one; $m = 1+\mu$. So

$$\mu = (n_{TRIMM}/n_{matrix}) - 1 = m - 1 \qquad \textbf{(3-1)}$$

In TRIMM systems $\mu << 0.1$ and the particle size is large compared to the wavelength of light. The deviation angle of a light ray intersecting a TRIMM particle is small, and back reflectance is $\approx \mu^2/4$, which is negligible. High forward light transmittance along a TRIMM-doped light guide is thus maintained, independent of the light wavelength. The average radius (r) of the spheres is > 100 times the wavelength, resulting in minimal scattering due to diffraction, so geometric optics is applicable. Small changes in n_{matrix} or n_{TRIMM} can cause large changes in μ, and thus in the angular spread and side wall transmittance of light propagating in TRIMM-doped polymers (Smith *et al.* 2003).

3.1.1 TRIMM systems studied

Two types of TRIMM-doped polymer were studied in this work:

1. TRIMM in flexible polymer optical fibre (POF), manufactured by Poly Optics Australia Ltd. For this material, $n_{matix} = 1.480$, and $n_{TRIMM} = 1.507$, giving $\mu = 0.0182$.
2. TRIMM in polymethylmethacrylate (PMMA) rods. For this material, $n_{matrix} = 1.490$, $n_{TRIMM} = 1.507$, giving $\mu = 0.0114$.

The TRIMM particles were obtained from Roehm Degussa, in Germany, in three different forms:

- Granules, ≈ 2 mm long and 1 mm in diameter. The granules consist of a high concentration of TRIMM in what was presumed to be a PMMA matrix.
- Solitary spheres, resembling a white powder when collected together. The particles are designated 'Plex 1002F' and range in size from 5-100 μm in diameter, with most falling in the range 15-40 μm.
- High TRIMM concentration diffuser sheets (Jonsson *et al.* 2005), 2.94 mm thick, designated 'Plexiglas df 238N'. These sheets are commercially available.

3.1.1.1 Doped Polymer Optical Fibre (POF)

The TRIMM-doped POF is manufactured by dissolving TRIMM granules in monomer, and casting in Teflon® tubing. The TRIMM particles are cross-linked PMMA, and are not dissolved by the monomer, in contrast to ordinary PMMA. The fibres were at first manufactured with diameters of 9 mm and 14 mm, but were later manufactured in several diameters ranging from ~ 3 mm to ~ 30 mm. Experimental work performed with these light guides is described in Chapter 9.

3.1.1.2 TRIMM-doped PMMA rods

The TRIMM-doped PMMA rods were manufactured by an extrusion process. Set proportions of TRIMM-doped granules were mixed with plain PMMA granules before extrution. Low and high TRIMM concentrations were prepared: the rods were designated '15K' and '100K', named for the concentration in ppm of TRIMM-containing granules in the extruded mix. A third concentration was unknown and designated 'A'. The diameter of these extruded rods is 12.67 mm. These rods were used as light guides to homogenise the angular distribution and colour of red, green and blue LEDs, as described in Chapter 6.

3.1.1.3 PMMA rod plus TRIMM diffuser sheet

The Plexiglas TRIMM sheets were glued to the ends of plain smooth PMMA rods. The use of these as light "mixers" is described in Chapter 6.

The remainder of this chapter describes the characterisation of TRIMM materials for modelling and experimentation. Section 3.2 describes the optical imaging of TRIMM spheres and determination of particle size. Section 3.3 describes the experimental determination of the refractive index of the TRIMM and matrix materials at a single wavelength, and the estimation of the variation of refractive indices, and hence μ, with

wavelength. Section 3.4 covers the methods of determination of TRIMM concentration in the various materials studied.

3.2 Imaging spheres and determination of particle size

3.2.1 TRIMM dispersed in matrix material

Initially, TRIMM were imaged in POF (Figure 3-1) using an Olympus BH-2 optical microscope. The Teflon® was stripped from a 9 mm fibre before imaging the particles, which were in part visible at the surface of the matrix material. The spheres were visible in a limited section of arc of the circumference of the fibre, in a strip running parallel to the long axis of the guide. It was evident that the particles had settled under gravity during polymerisation. Some 'shards' were also visible, which were presumed to have originated from sphere breakage during the production of the doped granules by extrusion.

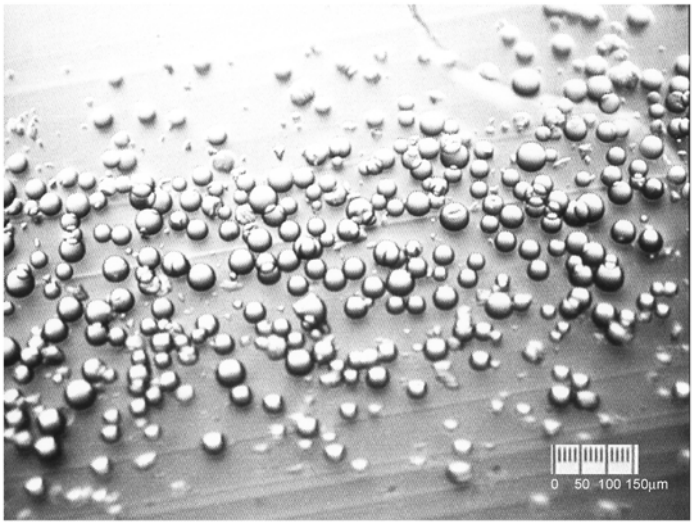

Figure 3-1. Optical micrograph of TRIMM spheres in 9 mm POF, with Teflon® jacket stripped, at the axis of maximum sphere concentration.

A micrograph of a thin slice of a TRIMM granule is shown in Figure 3-2. The proportion of shards and broken spheres appear to be about the same as for the various POF samples studied. It was concluded that there was no additional damage to the spheres during the POF manufacturing process. When the Olympus microscope stage was adjusted in a vertical direction, layers of TRIMM could be observed coming into focus, and then blurring as they moved out of the focal range as a different 'layer' came into focus. From this, a qualitative estimate was made of the concentration of TRIMM in the granules: about 30% by volume. The top and bottom surfaces of the granule slice could be identified by the

striations from polishing. Figure 3-2 shows a view focussed within the slice. The transparent nature of TRIMM is apparent, as some spheres are visible through overlying spheres. The dark outlines can be seen because the microscope was in 'transmission' mode, i.e. the light was transmitted almost undeviated through the sample, except at the edges of the spheres. In 'reflection' mode the spheres are virtually invisible, as expected due to the low value of μ.

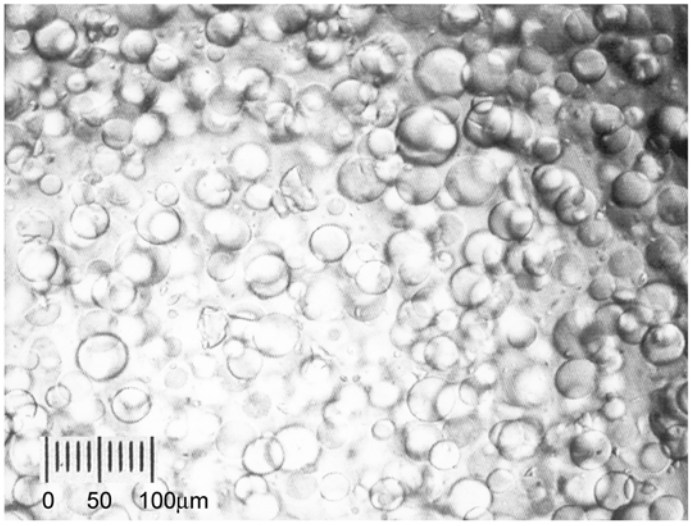

Figure 3-2. Optical micrograph of TRIMM spheres in a 'granule'.

Images were also taken of TRIMM in the PMMA rods studied. Observation of multiple cross-sections showed that the spheres are well distributed in the extruded rods.

3.2.2 Solitary TRIMM particles

3.2.2.1 TRIMM chemically isolated from granules

Initially, TRIMM were available only in granule form. It was necessary to isolate the spheres to determine their properties.

The TRIMM-containing granules were dissolved in raw MMA in a test tube, since the PMMA is soluble. A thick white residue remained undissolved along with the spheres. In contrast, when plain PMMA granules were dissolved in MMA and the solution centrifuged, no white residue was visible. The TRIMM spheres are cross-linked PMMA; it is unknown if the white residue was related to cross-linker material present in the spheres. TRIMM spheres were isolated by several iterations of pipetting undissolved granule material from the bottom of a small test tube after centrifuging. The isolated TRIMM spheres were placed on a glass slide and imaged using the Olympus microscope

(Figure 3-3). A small amount of residue is evident between some of the spheres. There were some shards present (not visible in the micrograph shown) which were deposited closer to the edges of the glass slide after being transported by the solvent.

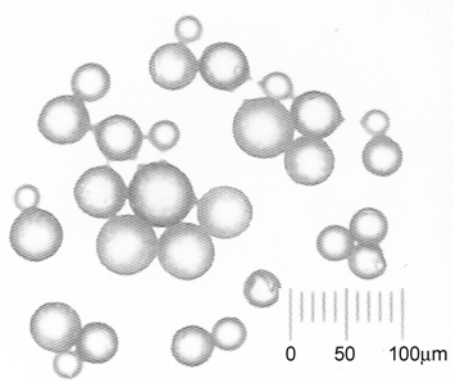

Figure 3-3. Optical microscope image of TRIMM spheres chemically isolated from granules.

3.2.2.2 Solitary TRIMM: Plex 1002F

The Plex 1002F spheres supplied by Roehm were imaged using an environmental scanning electron microscope (ESEM). Samples were mounted on an aluminium stub using carbon adhesive tape and imaged at 30 kV accelerating voltage, using the large field gaseous secondary electron detector operated at 0.9 Torr pressure and at a working distance of 10.4 mm. Micrographs are shown in Figure 3-4. It can be seen that they are close to spherical in shape; there are few oblate or broken particles.

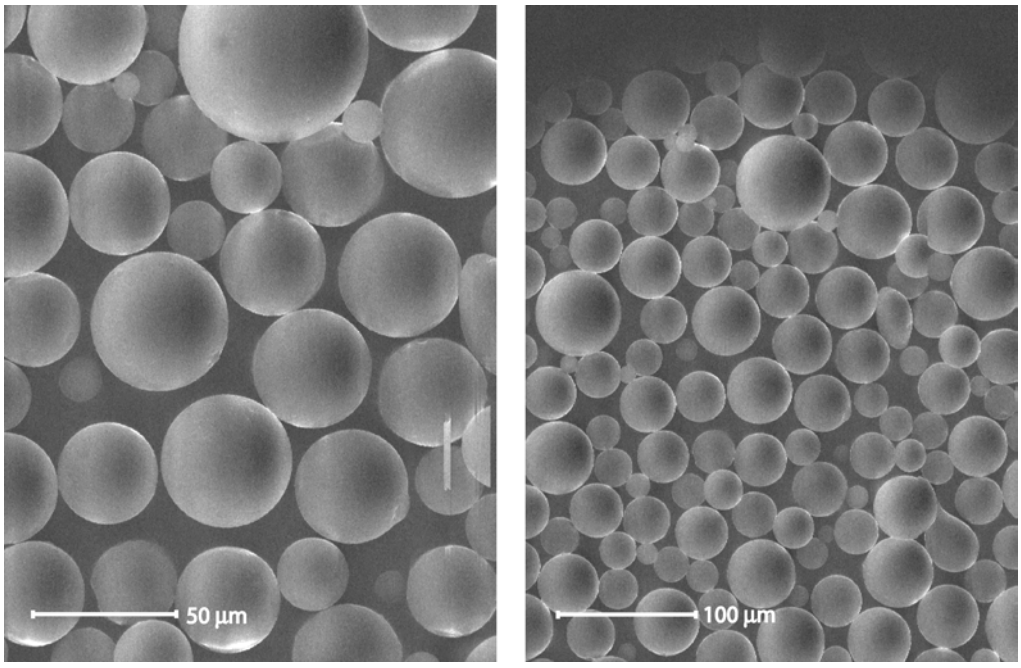

Figure 3-4. Micrographs of TRIMM Plex 1002F spheres, as imaged by an ESEM.

3.2.3 Particle size distribution of TRIMM

The particle size distribution of TRIMM was found by measuring the diameter of spheres visible on micrographs and sorting this data into 5 µm sized bins. 296 chemically isolated TRIMM, and 209 Plex 1002F TRIMM were measured. Shards and broken spheres were neglected. The resulting distributions are shown in Figure 3-5.

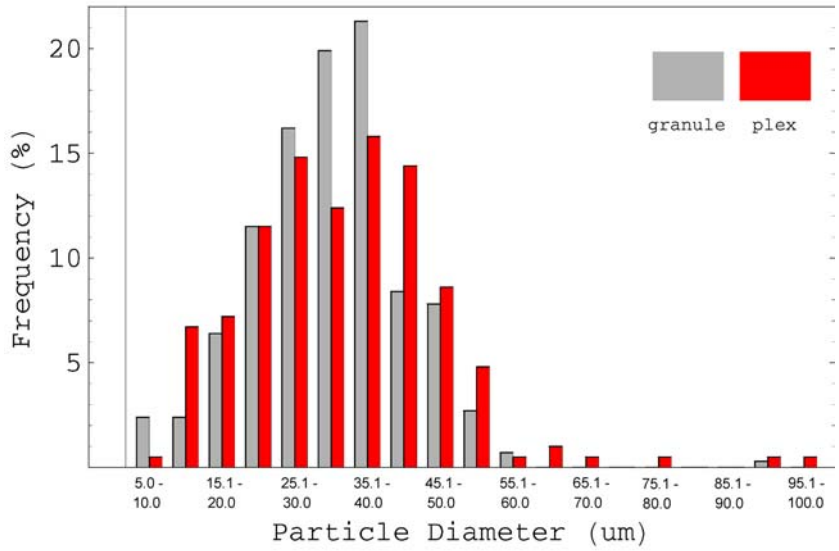

Figure 3-5. Particle size frequency distribution for 296 TRIMM spheres chemically isolated from granules, and 209 "Plex 1002F" spheres, as measured from micrographs.

Although the sample size here is insufficient for detailed statistical analysis, it can be seen that the average size of TRIMM studied is of the order of 30-35 µm in diameter. A small number of spheres approach the Rayleigh-Gans limit (Section 2.2), but most fall within the size range where geometric optics is applicable.

3.3 Experimental measurement of refractive index

3.3.1 Conventional methods

Conventional methods of refractive index measurement of polymers require flat, smooth surfaces. The refractive index of transparent solids can be found by measuring the intensity of polarized light reflected from the surface of a solid at a 45° angle of incidence. It is mandatory that the surface of the sample is perfectly smooth (Jenkins 2000). Other methods of refractive index measurement of polymers involving the polarisation of light have similar restrictions (Hemsley 1989). Ellipsometry can give refractive index values of four decimal places over the entire visible wavelength range. Ellipsometery is however an unsuitable method for TRIMM, due to their small size and spherical shape. The POF

also could not be measured using an ellipsometer, or other conventional methods, as several attempts to obtain smooth flat surfaces failed.

The POF matrix material is too soft to produce an optically smooth surface by hand polishing. Polishing undoped POF samples in a micro polisher holder containing alumina and water produced surfaces that were glassy in appearance, but were concave as a result of the released weight of the brass holders. An attempt to melt the POF surface onto a flat glass surface also failed. It was decided to measure the refractive index of the TRIMM and matrix materials using the immersion method.

3.3.2 Immersion method of refractive index measurement

The immersion method of measuring the refractive index of transparent solid objects involves putting the object into a liquid of (preferably) higher refractive index than the object, to avoid total internal reflection within the solid. Drops of a second liquid of lower refractive index than the first are added. The mixture is adjusted until the refractive index of the object and liquid are closely matched, and light rays pass through undeviated by refraction. The object thus becomes invisible to the eye. The refractive index of the matched liquid mixture is then measured.

An ellipsometer is a favoured instrument for measuring the refractive index of the immersion fluid for this work, since the refractive index can be determined over the entire visible light range at a resolution of four decimal places. In order to test the suitability of the UTS ellipsometer for liquid measurement, a sample of water was measured. Vibrations from the instrument motor disturbed the surface of the water, resulting in a 'noisy' trace. In addition, the measurements differed from literature values given for water for 3 different wavelengths (Schiebener *et al.* 1990) by 0.002. This could have been due to impurities in the water, as tap water was used. In addition, the refractive index for water is slightly temperature dependent, giving a difference of ≈ 0.001 between 20 and 30° C in the visible range (Schiebener *et al.* 1990, Robinson *et al.* 2000), and the temperature was not monitored. Due to the combination of polishing problems, instrument vibration and the uncertainties inherent from the use of the immersion method, it was finally decided to measure the immersion fluid using an Abbe refractometer. This gave the most accurate results.

3.3.3 Abbe refractometer for measuring refractive index of liquids

The Abbe refractometer measures refraction at the Sodium D line (see Appendix 1 for further information on the principles of operation of the Abbe refractometer). The Sodium

D doublet occurs at λ = 588.9950 nm and λ = 589.5924 nm (CRC, 1991), giving an average of λ = 589.3 nm.

High grade (99.5% minimum) ethanol was used to test the refractometer. Eight readings were made, using separate aliquots of the ethanol applied using a glass dropper. Four gave RI = 1.3609, two gave RI = 1.3608, and two gave RI = 1.3610. The literature value for pure ethanol is 1.3611 (CRC, 1991), which is very close to the measured value.

3.3.4 Abbe refractometer and the immersion method: experimental procedure

3.3.4.1 Selection of suitable immersion fluids

A list of liquids suitable for the determination of refractive index by the immersion method was found in the 55th edition of the CRC Handbook of Chemistry and Physics. There were several criteria to be considered in the selection of suitable liquids:

- At least two liquids of differing refractive index are required, one above and one below the refractive index of the sample to be measured.
- The selected liquids must be miscible.
- The refractive index of the selected liquids must not differ excessively. Single drops of one liquid, when added to the other, must give sufficiently small changes to the refractive index of the overall mixture. A large refractive index difference between the constituent fluids can also cause inhomogeneities within the mixture.
- The liquids must be clear. This is a requirement for measurement using the Abbe refractometer. (Many of the recommended high refractive index liquids are yellow/ brown in colour, as they contain iodine).
- They must be close together in boiling point, because the refractometer lamp heats the measured liquid.
- High grade chemicals are required. (Glycerol of unknown age used for initial testing showed refractive index variations between 1.4690 and 1.4701 over eight separate measurements: the literature value is 1.4746)
- Non-carcinogenic for safety reasons.

Chlorobenzene was selected as the higher refractive liquid, quoted as having a refractive index of 1.5241 and boiling point 132 C (CRC, 1991). A suitable candidate for the second liquid was 1,3-dichlo-propropane, with refractive index 1.4487, and boiling point 120.4 C

(CRC, 1991). Unfortunately high-grade dichloropropane proved difficult to obtain. Although not listed as an immersion fluid, 1-ethoxy-2-propyl acetate (EPA) was suggested by a colleague. The product properties information sheet quoted a refractive index of 1.405, and boiling point of 158 C.

Table 3-1 shows the chemicals selected to measure the refractive index of the TRIMM materials using the immersion method, along with a summary of relevant properties.

Table 3-1. Chemicals used for the immersion method of TRIMM and matrix materials

Immersion Fluid	*Refractive Index*	*Boiling Point (C)*	*Density*
Chlorobenzene	1.5241	132	1.1058
1-ethoxy-2-propyl acetate (EPA)	1.405	158	0.941

The refractive index of the EPA was measured twice using the Abbe refractometer: the values obtained were 1.4052 and 1.4051, which agrees with the product sheet. Chlorobenzene, obtained from the organic chemistry laboratory at the University of Technology, gave a reading of 1.5228, twice. Although this does not agree with the literature value, the label on the bottle quotes a refractive index range of 1.5222-1.5227.

The calibration of the refractometer was checked before and after each use, using high grade ethanol, chlorobenzene and EPA.

3.3.4.2 Refractive index measurement of PMMA sheet

The surface of POF was slightly altered by the immersion chemicals. Refractive index measurement of PMMA sheet was performed in order to become familiar with the practice of the immersion method using a sample that would not be subjected to attack by these chemicals.

It was found that there is a refractive index range over which the immersed object appears faint to the eye, but the point of apparent disappearance is very sharp. The PMMA sample appeared faint to the eye when immersed in a liquid of refractive index 1.520 (as measured by the refractometer). As EPA was added, the appearance changed little, until it suddenly 'disappeared' at a refractive index of 1.4901.

3.3.4.3 Refractive index measurement of POF matrix

The undoped POF material (Teflon® stripped) could not be made to be completely invisible to the eye with the immersion method, as its refractive index properties were altered

slightly by surface chemical attack. The first attempt at refractive index measurement of this material put the refractive index within the range 1.479-1.482. A chlorobenzene / EPA mixture with refractive index of 1.481 was then prepared; the edges of the sample were just barely visible, becoming slightly more visible after about one minute of immersion. A fresh piece of POF in a new solution of refractive index 1.480 appeared almost invisible. This value of 1.480 was thus taken to be the refractive index of the POF matrix material at λ = 589.3 nm.

3.3.4.4 Refractive index measurement of TRIMM spheres

The TRIMM spheres were visible in immersion fluid at the bottom of a small test tube due to edge scattering of the light. They are not dissolved by MMA, and so unlikely to affected by chemical attack. Their refractive index was measured in a similar manner as described for the POF material. They appeared very faint when immersed in a fluid of refractive index 1.5068, and were easier to see in liquid with refractive index of 1.5075. The value 1.507 was used in ray tracing modelling for the TRIMM particles at λ = 589.3 nm.

3.3.5 Uncertainties of measurement: immersion method and Abbe refractometer

The accuracy of refractive index determination of liquids is given for this instrument as ± 0.0002. There are several factors, however, which introduced additional uncertainty in the refractive index determination of the TRIMM particles and host polymers in this work.

- The determination of refractive index by the immersion method is, to some extent, subjective. The experimenter has to judge visually when the object has 'disappeared' from view, and thus the refractive index of the immersion fluid and object match.
- The minimum incremental change in refractive index of the immersion fluid mixture is a function of the drop size of the fluid being added.
- The lamp illuminating the refractometer heats up the film of fluid being measured. (This is particularly evident in the case of the high grade ethanol being used to check the calibration). For a homogenous fluid, one can constantly drizzle more fluid into the refractometer during measurement, but in the case here, a mixture of compounds differing in boiling points was being measured. In addition, the refractive index of fluids varies slightly with temperature.

- The immersion fluid reacted with the surface of the polymer in the case of the POF matrix material. This was a slow process, but will affect the refractive index measurement. This was partly compensated for by frequently removing samples and dropping new pieces into the solution.

Due to these factors, the refractive index measurements are quoted to three decimal places.

3.4 Refractive index variation with wavelength

It is important to know how the refractive index of TRIMM and matrix material varies with wavelength over the visible range, and to determine what bearing this has on their relative refractive index, and hence μ. If μ varies significantly with wavelength, then consequently the ray deviation angle function will also vary, as evidenced by eqn 2-7. This could possibly cause differences in the spatial distributions of different colours upon transmission through TRIMM material. The visual appearance of light transmittance is important in lighting, and refractive index variation with wavelength could result in colour variation of transmitted light. This is especially the case when the output is to appear 'white'.

It has already been stated that the POF matrix material could not be measured using an ellipsometer (Section 3.3.1). The TRIMM-doped PMMA rods, however, could be polished to a sufficient flatness for ellipsometer measurements. It was hoped that refractive index variation with wavelength information could be extracted from ellipsometer data using TRIMM-doped rods, as the refractometer gave information for a single wavelength only.

3.4.1 Ellipsometer measurements of TRIMM rods

The undoped PMMA was available only in granule form, and so was unsuitable for ellipsometer measurement. The low concentration (15K) TRIMM rods have a linear sphere separation of 4.0 mm (see Section 3.5.1.2). The spot size of the ellipsometer beam is ~ 1 mm in diameter when incident on a sample. The diameter of the TRIMM-doped rods is 12.67 mm. If several measurements are made of the surface of a sample on different sections of the surface, one would expect for the ellipsometer spot to either strike matrix material alone, or both matrix and a sphere. In the first case, the matrix material is measured; in the second, the readings would be somewhere between that of the matrix material and the TRIMM spheres. Probability dictates that some sample cross-sections have more

spheres exposed at the surface than others, and for these samples, there may not be any readings made of solely matrix material.

The UTS ellipsometer is an ISA UVISEL phase modulated ellipsometer. Ellipsometer readings were taken of three 15K extruded rod samples. Several measurements were made for each sample, each one at a different section of the surface. The modulator was set to 0° and the analyser to 45°. The angle of incidence was 60°. Integration time was 1000 ms and the measurements were taken at 5 nm increments. The real part of the refractive index, *n*, was calculated by the instrument software from the standard ellipsometric parameters (Azzam *et al.* 1977).

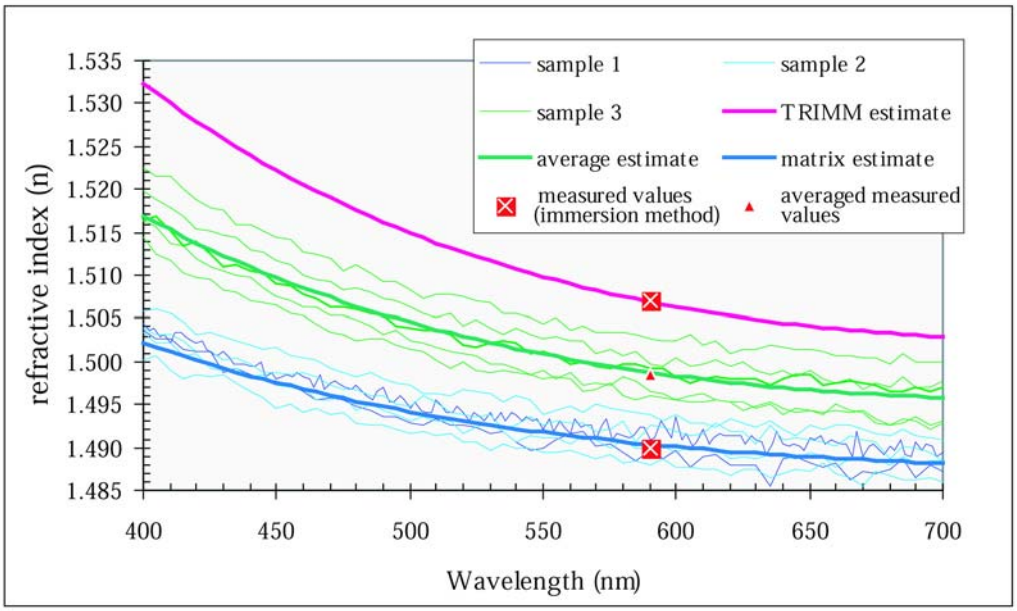

Figure 3-6. Real part of refractive index vs wavelength from ellipsometry measurements of 3 samples of '15K' TRIMM-doped PMMA rod. Modelled fits for estimates of dispersion curves for PMMA matrix, TRIMM material and average of both materials are shown as bold lines. Measured values of a PMMA sheet material and TRIMM spheres by the immersion method (described in Section 3.3.4) are also shown (crosses).

The resultant curves (several for each sample) are shown as thin lines in Figure 3-6. These curves, along with the refractive index values for TRIMM spheres and PMMA sheet measured at ≈ 590 nm by the immersion method (marked as crosses) were used to establish the dispersion curves for TRIMM and PMMA. The lower measured curves in Figure 3-6 appear to correspond to measurements of PMMA matrix material only, supported by the refractive index value of PMMA measured by the immersion method (which is the lowest cross marked on figure). Similarly, the higher measured curves appear to be an averaged value of the refractive index of the matrix and TRIMM materi-

als. Fits to the experimental data were made by adjusting the parameters E, F, G and H in the equation $n = E\left(A + \frac{F}{\lambda} + G\lambda^2\right) + H\lambda$, and are shown as thick curves in Figure 3-6. This same equation was used, along with the TRIMM refractive index value obtained from the immersion method (higher cross marked on figure) to plot a dispersion curve for the TRIMM material, following the trend of the lower two curves.

3.4.2 Variation of μ with wavelength

A curve of μ vs λ could be produced from the n_{TRIMM} and n_{matrix} fits shown in Figure 3-6. However, since the n_{TRIMM} vs wavelength dispersion curve is indirect, another technique was employed to obtain the variation of μ with wavelength for the TRIMM-doped PMMA rods, for comparison.

Transmittance measurements of all three concentrations of TRIMM-doped rods were made to obtain T vs λ. Corresponding computer simulations were performed to produce T vs μ, since the values of n_{TRIMM} and n_{matrix}, and hence μ, are easily varied in the computer programs. A curve of μ vs λ was produced by correlating T values from simulations and measurements. A description of the methods of transmittance measurement will now be given, followed by the μ vs λ curves produced from both ellipsometer and transmittance measurement methods.

3.4.2.1 LED transmittance measurements

Transmittance measurements were made of the TRIMM-doped rods using red, green and blue (RGB) LEDs as sources, to obtain data for different wavelength regions. Two groups of RGB LEDs were measured; one comprising 3 mm, and the other 5 mm lens encapsulant diameters. An Oriel 70491 integrating sphere was used to collect the output light from each LED in turn, transmitted through 10 cm and 1 cm TRIMM rod lengths. The 1 cm transmittance was used as the reference for the 10 cm measurement in each case. The measurements were made using an Ocean Optics SD2000 fibre optic spectrometer and associated software. Measurements were also taken using a BPW21 photodiode and a multimeter, for comparison.

The transmittance results were similar for both spectrophotometer and photodiode detector measurements, although in all cases the transmittance was lower than expected for TRIMM systems. There was little variation in transmittance over the wavelength range measured by the Ocean Optics spectrometer (about 50 nm bandwidth for each LED). For both groups of RGB LEDs and all three TRIMM rod concentrations, the transmittance

was lower for the green and blue LEDs than for the red. It cannot be determined from these results to what extent variations between the individual LEDs contribute to the transmittance differences. Beam patterns, and therefore source-to-light guide coupling, are unique for each LED, as will be shown in Chapter 5. For this reason, an endeavour was made to obtain spectral transmittance data using a spectrophotometer.

3.4.2.2 Spectrophotometer transmittance measurements

The UTS spectrophotometer is a custom-built instrument designed for diffuse and specular measurements using an integrating sphere, over the UV to IR range. It consists primarily of Thermo Oriel components, with a Hamamatsu UV to IR Two-color detector.

Spectrophotometer readings were taken using the same 1 cm and 10 cm length samples that had been measured using the LED sources. The rectangular source beam just fitted within the confines of each rod end. The transmittance data are shown in Figure 3-7(a).

The transmittance (T) of each of the TRIMM rods was also modelled using a ray tracing model (to be described in Chapter 4). The modelled transmittance, using $\mu = 1.0114$ at 590 nm, is much higher than the measured transmittance. Close examination revealed air bubbles and particles of dirt in the samples, particularly rod type 'A'. This causes high light loss via large angle scattering. There may also be unknown components in the TRIMM containing granules that need to be considered (the undissolved white residue mentioned in Section 3.2.2.1). Hence, the rods were not of sufficient quality to establish μ via T measurements.

Although the data obtained from the TRIMM-doped rods was not believed to be caused by the matrix material and TRIMM spheres alone, information regarding the variation of μ with λ was extracted, to compare with curves derived from the ellipsometer data. T vs μ simulation data was collected by performing ray tracing simulations with varying values of μ. The geometry of the spectrophotometer beam incident on the rods' ends was simulated in the computer models. A curve of μ vs λ was obtained by comparing measured T vs λ data (shown in Figure 3-7(a)) with the simulated T vs μ values, and equating T between the two. The resultant curve is shown in Figure 3-7(b). The values of μ are unrealistically high for the sphere-to-matrix refractive index mismatch alone, due to the effects of the impurities mentioned above. Figure 3-7(c) shows a graph of μ vs λ derived from the refractive index curves shown in Section 3-6. The shape of this curve is similar to that of Figure 3-7(b), and the μ values are within the range expected.

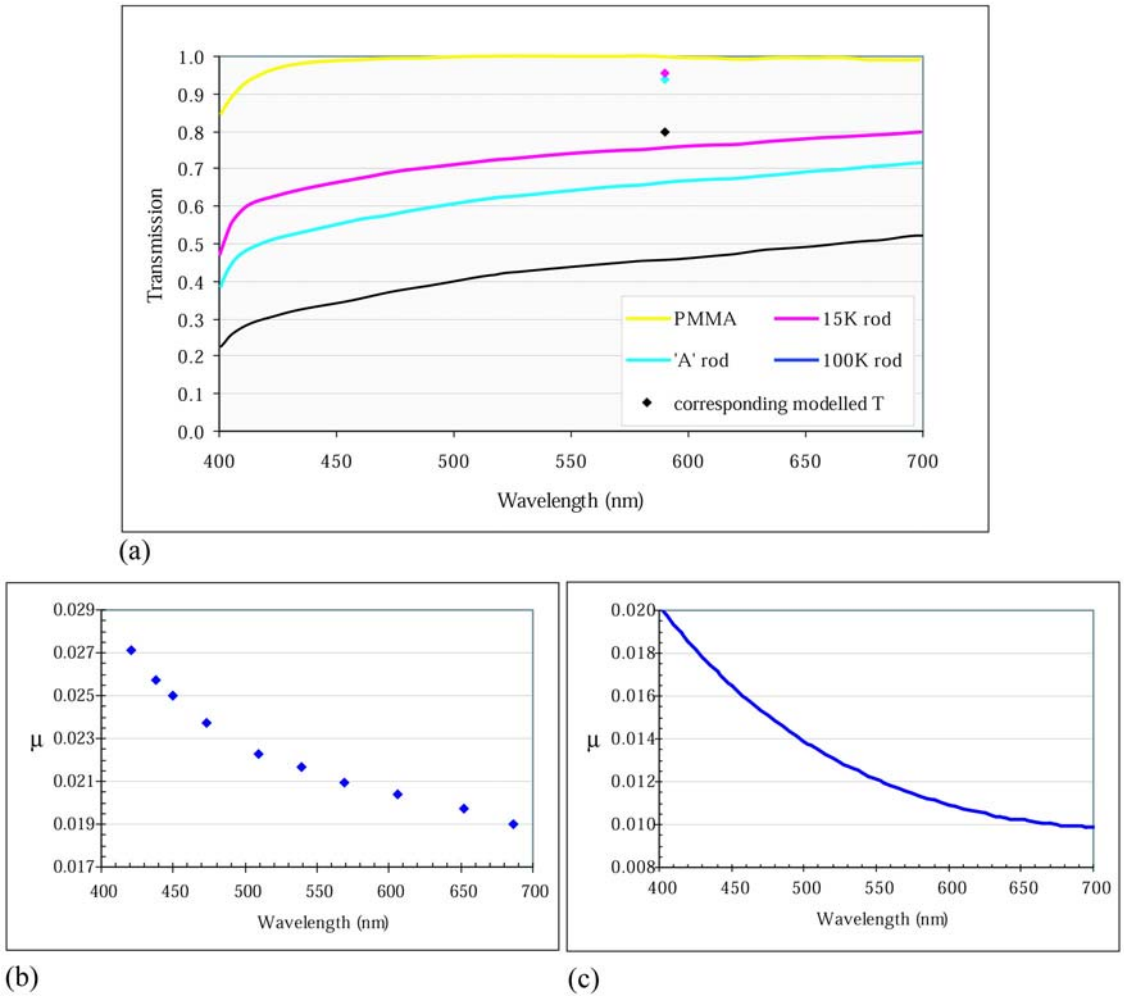

Figure 3-7. a) Transmittance measurements of 10 cm TRIMM-doped PMMA rods, normalised to a 1 cm reference, made using a spectrophotometer. Corresponding transmittance simulated for each concentration by ray tracing are shown by coloured diamonds. b) μ vs λ for 100K rod, calculated using a combination of transmittance shown in a) and ray tracing simulated transmittance results. (μ is higher than expected for TRIMM and matrix alone, due to impurities contained in the extruded rods.) c) μ vs λ as calculated from the estimated curves based on ellipsometer data shown in Figure 3-6.

3.4.2.3 Comment on μ vs λ curves

It is necessary to obtain an estimate of the variation of μ with wavelength, to ascertain its visual impact on light output from the light guides. It is acknowledged that there is a large degree of uncertainty in the derivation of the curve shown in Figure 3-7(c). In Section 7.1, simulated lighting distributions will be presented that compare the outcome of using a constant μ ($\mu = 0.0114$) with wavelength, with that of varying μ with peak LED wavelength according to Figure 3-7(c). It will be seen that varying μ has little visual impact on the output lighting distributions for the configurations studied. Thus the change of μ with wavelength, although an important point to check, turns out to have a minor effect on colour mixing distributions. Most of the key light distribution results presented in

Chapter 6 therefore use a constant value of μ, regardless of the peak wavelengths of the RGB LED sources.

3.5 TRIMM particle concentration in a light guide matrix

3.5.1 Determination of linear TRIMM particle concentration in matrix material

The number of particles encountered by a light ray along its path through a TRIMM mixer is related to the volume concentration of the particles in the matrix. For purposes of Monte Carlo computer ray tracing, it is necessary to know the mean distance between particles, p. This was not known for the TRIMM materials used, and had to be measured. In Section 2.3.1.1, the axial particle number, a, of a TRIMM-doped material was defined as the average number of particles that an undeviated ray would encounter when passing through the sample. (Here, an undeviated ray is defined as a straight line passing through the thickness of the sample.) For a sample of thickness, t, $p = t / a$. So by measuring a, p can be determined.

The probability of an undeviated ray striking a particle as it passes through a sample can be described by a Poisson distribution

$$P(x) = \frac{e^{-\sigma}\sigma^{x}}{x!} \text{ for x = 0,1,2....} \quad \textbf{(3-2)}$$

where σ is the average number of events (Wild *et al.* 1995). The probability of a ray striking zero number of particles when travelling through a sample with axial particle number a is

$$P(0) = e^{-a} = T_{spec} \quad \textbf{(3-3)}$$

where T_{spec} is the specular transmittance after correction for Fresnel reflectance occurring at the entrance and exit ends of the sample. The limit of specular transmittance measurement is the size of the detector; in this case, the aperture of the integrating sphere (see following section). Measurement of the true specular transmittance of a particular sample can be used to estimate a.

3.5.1.1 Measurement of axial particle number of TRIMM diffuser sheets

In order to measure the true specular transmittance of a particular sample, the axial particle number of the sample must be small enough to ensure a visible specular component. For $a = 6$, T_{spec} is 0.0025. The concentration of TRIMM particles in the Plexiglas diffuser sheets used is sufficiently high to necessitate measuring thin slices (< 1 mm), so slices

were cut from the main sheet using a diamond saw. To ensure optically smooth surfaces for measurement, these slices were mounted between sheets of 2 mm thick PMMA, using glycerol between each of the surfaces as a refractive index matching agent.

A helium neon laser (wavelength 633 nm) was used for the transmittance measurements that were used to calculate *a*. An advantage of using a laser is the relative ease of being able to see an transmitted undeviated, specular 'spot', indicating that the samples are sufficiently thin for axial particle measurements, as well as making alignment easier. An Oriel 70491 integrating sphere was positioned 3.8 m from the sample, and readings taken using a BPW21 photodiode at the detector port and a multimeter with a resolution of 1 μW. To estimate *a*, it is necessary to separate the specular component of transmission from the diffuse. The port size of the integrating sphere was reduced to 1 cm diameter with a cover, making the acceptance criterion for specular transmission within a cone semi-angle of 0.075^{o}. The laser beam was directed through the sample towards the integrating sphere. The component of measured transmitted intensity in the incident beam direction, I_{max}, was measured with the port of the integrating sphere in line with the undeviated beam. This is mainly the specular part of the transmitted beam, but also contains a small scattered component, $I_{scatt.}$ This was subtracted from I_{max} to obtain the specular component of measured intensity. The scattering baseline, I_{scatt}, was estimated by moving the integrating sphere 1, 2, and 3 cm to either side of the central axis, corresponding to median angular deviations of ≈ 0.15, 0.30 and 0.45 degrees, and taking intensity readings. The initial intensity I_0 was measured by directing the laser beam into the integrating sphere through the PMMA and glycerol only. The specular transmittance of the beam through the sample was then calculated by

$$T_{spec} = \frac{(I_{max} - I_{scatt})}{I_0} \qquad \textbf{(3-4)}$$

Three sets of measurements were made, using slices of sheet 0.25, 0.27 and 0.33 mm thick, to derive the linear particle concentration of TRIMM in the diffuser sheet. *a* was calculated for each sample using eqn 3-3, and from this the distance between particles *p* was calculated to be 0.075 ± 0.005 mm. The TRIMM diffuser sheet thickness is 2.94 mm, giving an axial particle number of 39 ± 3 for the Plexiglas diffuser sheet.

3.5.1.2 Axial particle number measurements of TRIMM-doped PMMA rods

The concentration of TRIMM in the extruded rods is much lower than for the diffuser sheets, so thin slices were not required. A range of lengths were cut from the rods using a lathe, with the aim of obtaining samples with *a* ranging from about 3 to 8. The samples were polished using 'wet and dry' polishing paper, and finished with Silvo® silver polish and a soft cloth.

The measurements were made in the same manner as for the diffuser sheets (Section 3.5.1.1) except that, due to their greater thickness, the samples were not mounted between sheets of PMMA and glycerol. The initial intensity I_0 was determined by directing the laser beam into the integrating sphere, and subtracting 8% from the reading to compensate for Fresnel reflection at the entrance and exit surfaces of the rods.

Table 3-2 shows the results for each of the TRIMM rod concentrations. For each set of measurements, the following values are given:

- the sample length, L;
- T_{spec} as calculated using eqn 3-4;
- a calculated using eqn 3-3;
- the mean inter-particle distance p.

The average p for each of the three TRIMM rod concentrations was used in the Monte Carlo ray tracing modelling.

Table 3-2. Measurement of axial particle number *a* for TRIMM rods

Rod sample	*L (mm)*	T_{spec}	*a*	*p (mm)*
15K	34.84	0.000328	8.02	4.34
	30.17	0.000815	7.11	4.24
	20.01	0.004679	5.36	3.73
	9.68	0.079394	2.53	3.82
				4.0 ± 0.3
A	22.53	0.00290	8.14	2.77
	6.44	0.098444	2.32	2.78
	5.88	0.104106	2.26	2.60
				2.7 ± 0.1

Table 3-2. Measurement of axial particle number *a* for TRIMM rods

Rod sample	*L (mm)*	T_{spec}	*a*	*p (mm)*
100K	4.90	0.002453	6.01	0.82
	5.33	0.000776	7.16	0.74
	3.55	0.007390	4.91	0.72
	1.88	0.074680	2.59	0.72
				0.75 ± 0.05

3.5.2 Mass fraction calculations and TRIMM concentration

The axial particle number is a necessary parameter for ray tracing modelling, but for manufacturing purposes it is useful to know what mass fraction of TRIMM-containing granules or isolated TRIMM spheres must be added to matrix material in order to obtain the desired linear particle concentration. For example, a potential customer wants a PMMA light guide of a particular length *L* to give a 50% light loss out of the guide walls at a distance L/2 from the light source end. The ray tracing computer programs are run to find the inter-particle distance *p* and the axial particle number *a* to meet the requirements. This does not tell the manufacturer directly the volume fraction of TRIMM to add to the matrix.

The refractive index ratio, and therefore the density, of the TRIMM spheres to the guide matrix is very close to one. Therefore the mass fraction (m_f) of TRIMM spheres is approximately equal to the volume fraction (V_f). The axial particle number is the number of particles encountered as one travels in a straight line parallel to the axis of the guide. To express this as a volume, a cylindrical volume with a radius equal to the radius of a TRIMM sphere is constructed (Figure 3-8).

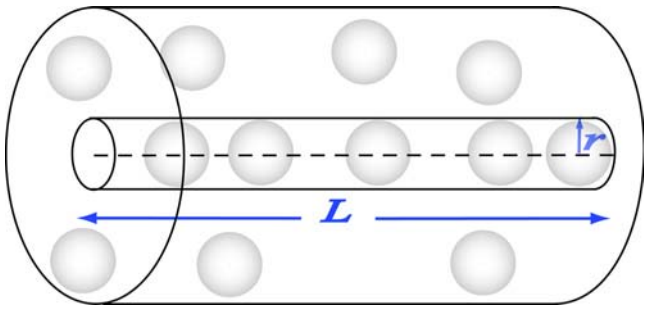

Figure 3-8. Geometry for derivation of the volume fraction of TRIMM particles in a guide

Now the volume fraction occupied by the particles is equal to the total volume of particles divided by the volume of the included cylinder, so:

$$V_f = \frac{a \times \frac{4}{3}\pi r^3}{\pi r^2 L}$$

and therefore

$$m_f = \frac{4r}{3p} \qquad \textbf{(3-5)}$$

since $a = L/p$.

Using Figure 3-5 as a guide, an average radius of $r = 17$ μm was selected to evaluate eqn 3-5. TRIMM materials can be manufactured by either adding solitary TRIMM spheres to the matrix, or by adding granules. The proportion of TRIMM in the granules is uncertain, but estimated to be 30%. The granule concentration in the TRIMM rods is also approximated for the samples used. For 100K concentration of granules in rods, the manufacturers were told to add 1 part TRIMM granules to 10 parts PMMA granules for simplicity, giving an actual granule concentration of ≈ 91K. So eqn 3-5 is expected to give a better estimate of the mass fraction of 'solitary spheres' required to give a desired linear particle concentration, than it would for the TRIMM-containing granules.

To perform a test of eqn 3-5, one could ask: for 100,000 ppm granule concentration, what path separation would be expected between spheres? Assuming that 30% of the granules are spheres, $mf = 0.03$. If $r = 17$ μm, then $p = 0.76$ mm. The axial particle measurements for 100K gave $p = 0.75$ mm (Table 3-2).

The estimate of the mass concentration of solitary spheres, and of TRIMM-containing granules, that is necessary to obtain a specified value of p, is shown graphed in Figure 3-9. Curves are calculated using eqn 3-5 with $r = 17$ μm. The concentration of TRIMM in granules is assumed to be 30%. These curves can be used to estimate the mass fraction of either solitary TRIMM spheres, or granules, to be added to a polymer matrix to obtain the desired linear particle concentration for a particular application. The upper graph in Figure 3-9 is scaled to facilitate the estimation of the TRIMM mass fraction required for high concentration systems. The lower graph is scaled to suit lower concentrations of TRIMM doping.

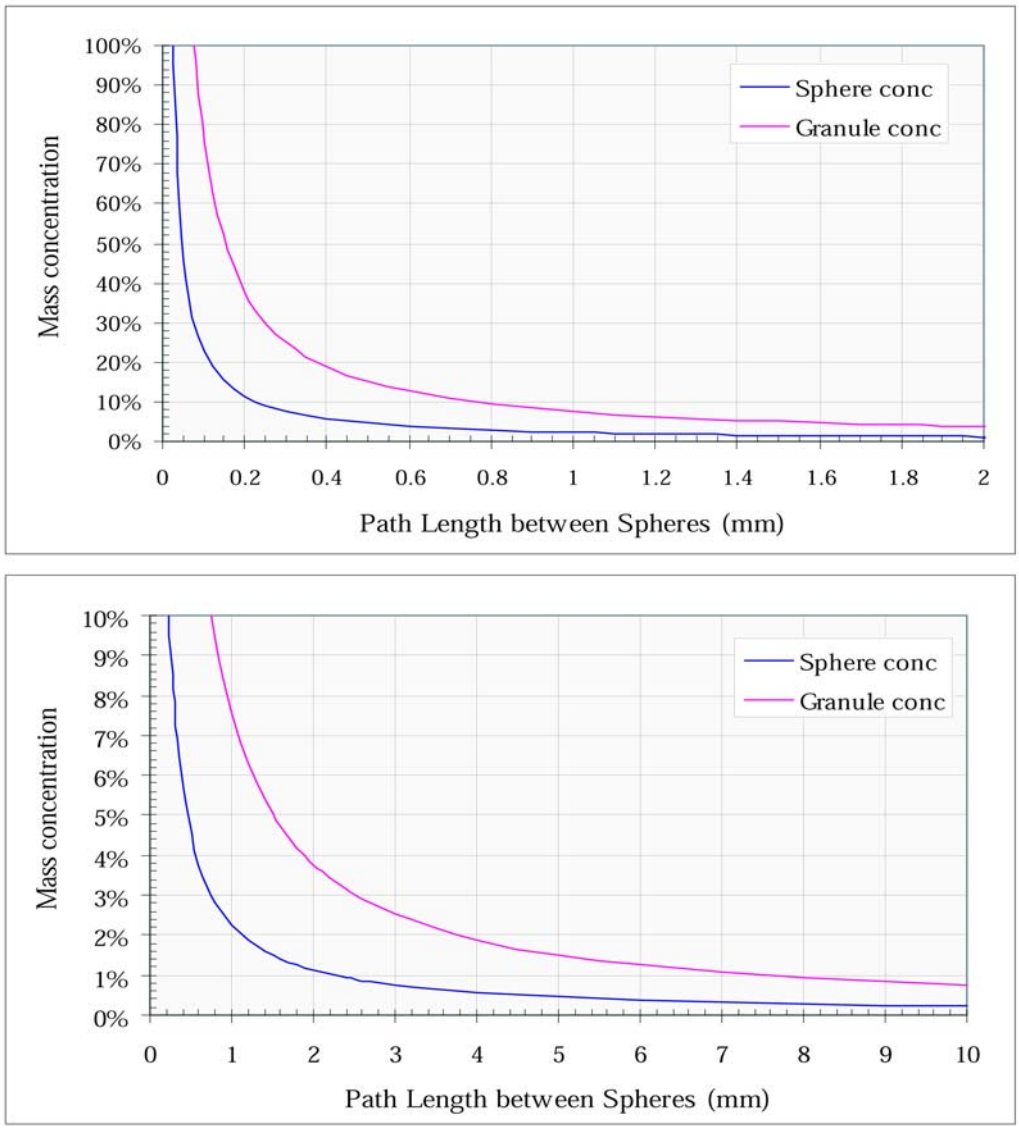

Figure 3-9. Mass concentration of TRIMM vs path length (p) between TRIMM spheres. Both graphs show the same data; the lower is scaled for low concentrations of TRIMM.

4 Monte Carlo ray tracing in particle-doped light guides

4.1 Introduction

Ray tracing simulations involving TRIMM light guides are a useful tool for studying changes in the internal and external angular distribution of light with propagation along a light guide, as well as output light patterns, mixing of coloured light sources, and loss of useful light. Commercially available non-sequential ray tracing software appear to lack the flexibility needed to simulate TRIMM systems. One package, for example, includes optical properties of pre-defined materials, and to define a different material the user needs to specify its refractive index at several different wavelengths. This information was unavailable for TRIMM materials, hence the reason for the measurements described in Section 3.3. User specified source ray patterns are not easily incorporated into the package either. In addition, each TRIMM particle must be individually specified and placed within a simulated light guide. A ray tracing program that readily incorporates ray interactions with randomly dispersed particles within a light guide matrix is not currently available, to the knowledge of the author. It was decided to develop a Monte Carlo based ray tracing program customised for simulations involving TRIMM-doped light guides.

This chapter describes a generalised system of ray tracing in cylindrical light guides when scattering particles are dispersed within the matrix material. Ray propagation geometry is defined in Section 4.2.1. In Section 4.2.2 it is shown how subsequent ray direction after particle deviation can be calculated using spherical trigonometry, using ray deviation in TRIMM-doped systems as an example. Some ray tracing systems, based on undoped guides, rely on the constancy of the ray trajectory angle with respect to the guide axis, and on light guide symmetry. In Section 4.3, aspects of previous approaches have been selected and the geometry further developed into a system suitable for ray tracing with added scatterers. In particle-doped guides, the ray/wall intercept angle also changes with ray propagation, and needs to be calculated with every wall interaction, because every

particle interaction deviates the ray. The geometrical methods employed are described in Section 4.3.2 and Section 4.3.3.

4.1.1 Background

Ray tracing simulations of illumination systems involving light guides are generally performed for undoped guides. After launch, any change in ray direction is caused by total internal reflection (TIR) from the guide wall. The angle between the fibre's optical axis and the ray does not change with propagation along the light guide. Exceptions to this include studies where scattering occurs at the ray/wall interface. Examples are incorporation of a scattering function to describe the optical reflectance properties of a material such as paint (Teijido *et al.* 1996), and geometrical scattering from structured surfaces, such as in the prism light guide (Whitehead 1982). All of the above ray tracing methods are not applicable to light guides with particles dispersed throughout the matrix material. Scattering when micro-particles are incorporated within the core of a guide have previously been described using Mie theory (Berthet *et al.* 2001) rather than by using ray tracing software. A backlighting study of a system of silicon micro-particles embedded in polymer also used Mie theory (Okumura *et al.* 2003). In the latter case, the Mie single scattering profile was employed using Monte Carlo ray tracing to simulate multiple scattering as a sequence of single scattering events. This is problematic since the single profile is extended by adjacent particles, and the simulations had to be adjusted by a coefficient that was determined by experiment.

Conventional optical design programs are not suitable for all aspects of illumination light pipe design. There is no single tool suitable for meeting requirements such as optical correctness, ease of optimisation, computer efficiency, and material and manufacturer specifications (Teijido *et al.* 1998). This is particularly the case when attempting ray tracing simulations of illumination systems with added scattering particles. For example, the mathematical function describing ray deviation (δ) with particle interaction (eqn 2-7), is applied in a statistical manner, in contrast to using a pre-defined array of spheres as optical elements. The latter is impractical for a large array. Standard ray tracing software packages have limited capabilities in applying user-defined functions to a large number of randomly dispersed separate elements. Hence Monte Carlo based ray tracing is more appropriate for simulations of TRIMM-doped light guides.

Monte Carlo ray tracing has been successfully applied to other scattering systems, such as simulations of light scattering in biological tissue (Guo *et al.* 2003) and suspension droplet light scattering (Wriedt *et al.* 2002). Similarly to TRIMM systems, each ray propagates a random distance before being deviated according to a probability distribution. Some researchers have found commercial software to be unsuitable, and alternative programs have been written to perform simulations to compare with experimental observations (Lee *et al.* 2003, Hopkins *et al.* 1999).

4.2 Ray tracing with added scatterers

4.2.1 Ray propagation geometry

Consider a light guide aligned along the z-axis, with the ray entry face positioned in the x-y plane at $z = 0$. A ray originates at point (x_0, y_0, z_0), with θ_1 semi-cone angle relative to the z-axis, and ϕ_1 azimuth component measured for rotation about the z-axis, with $\phi = 0$ at the x-axis (see Figure 4-1). The average path length, p, travelled by a ray between particle interactions is proportional to the volume concentration of particles in the light guide matrix (Section 3.5.2). The propagation length, l, between two particular particles is calculated using a Poisson distribution, so

$$l = -pLn[j] \qquad \textbf{(4-1)}$$

where j is a uniformly distributed random number between 0 and 1. The ray deviates according to a predefined function upon encounter with a particle. (The deviation function for TRIMM-doped guides was derived in Section 2.2.2, and given in eqn 2-7.) The new ray direction, relative to the light guide, is defined by θ_2 and ϕ_2. The projected intersection point (x_1, y_1, z_1) for the next particle interaction is calculated using the direction cosines (X, Y, Z).

$$\begin{aligned} X &= cos[\phi_1]sin[\theta_1] \\ Y &= sin[\phi_1]sin[\theta_1] \\ Z &= cos[\theta_1] \end{aligned} \qquad \textbf{(4-2)}$$

$$(x_1,y_1,z_1) = (x_0,y_0,z_0) + l(X,Y,Z) \qquad \textbf{(4-3)}$$

The use of statistical functions means that it is not necessary to individually specify the position of every particle within the light guide matrix.

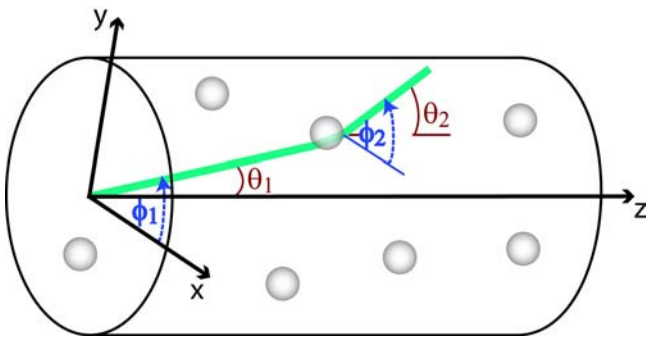

Figure 4-1. Geometry of ray propagation in a particle-doped light guide

If the point (x_1, y_1, z_1) lies outside of the light guide boundary, the intersection point with the wall or guide end is calculated. A ray intercepting the core/air boundary either exits the guide or is totally internally reflected. If the ray is reflected, the remaining path length to the next particle is calculated, and the path continues in the reflected direction until the next particle deviation. The point (x_1, y_1, z_1) is reset to (x_0, y_0, z_0), and the ray continues to propagate until it exits the light guide by refraction.

When a ray is reflected from one of the guide ends, the Z direction cosine changes sign, and the other direction cosines remain the same. This is the case for both cylindrical and rectangular guides.

Reflection from a wall of a rectangular guide is straightforward: a ray reflecting from a wall parallel to the x-axis has its Y direction cosine reversed, and a ray reflecting from a wall parallel to the y-axis has its X direction cosine reversed. The procedure for reflection from the wall of a cylindrical guide is more involved, and will be considered in Section 4.3.3. The direction of a reflected ray is defined by new θ and ϕ values calculated using the reflected direction cosines.

A generalised flow chart of the ray tracing procedure used for TRIMM systems is given in Appendix 4.

4.2.2 Defining new ray direction: spherical trigonometry

The calculation of the subsequent ray direction after encounter with a particle needs to be elucidated. The ray deviation for TRIMM particles is discussed in this section, although the procedure is relevant for other ray deviation functions.

The semi-cone angular component of a ray's deviation *(δ)* is calculated whenever a ray strikes a TRIMM sphere, as described in Chapter 2.

$$\delta = 2[sin^{-1}[h]] - sin^{-1}[h/(1+\mu)] \quad \textbf{(4-4)}$$

Initially a ray is travelling in a direction defined by θ_1, ϕ_1. It propagates for a distance l, then encounters a particle. The ray deviates with respect to the initial ray direction by an amount δ with respect to the initial ray direction. The azimuth component of deviation, $0 < \varepsilon_1 < 2\pi$, is randomly chosen. The new ray direction needs to be defined in the reference frame of the light guide, rather than the initial ray direction. That is, we need to describe the new ray direction in terms of θ_2 and ϕ_2 (see Figure 4-2). This is achieved by the use of spherical trigonometry. Using the Cosine Rule for sides for spherical triangles (see Appendix 2) θ_2 can be calculated:

$$\theta_2 = cos^{-1}[cos\,\theta_1 cos\,\delta + sin\,\theta_1 sin\,\delta cos\,\varepsilon_1] \quad \textbf{(4-5)}$$

Similarly, using the Sine Rule for spherical triangles, ε_2 (and thence ϕ_2) can be calculated.

$$\varepsilon_2 = sin^{-1}\left[\frac{sin\,\varepsilon_1 sin\,\delta}{sin\,\theta_2}\right] \quad \textbf{(4-6)}$$

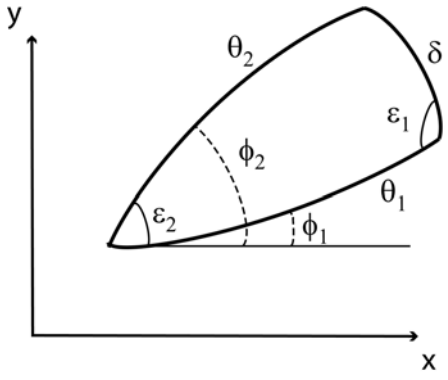

Figure 4-2. Cross-section showing the use of spherical geometry to redefine ray direction after TRIMM deviation

Care should be taken when using inverse trigonometry functions in some computer programs. For example, Mathematica® gives only one solution, always in the range $-\frac{\pi}{2} < \varepsilon_2 < \frac{\pi}{2}$, for eqn 4-6. For most ray deviations, $\delta < \theta_1$, but in a few of the cases where $\delta > \theta_1$, Mathematica® gives an incorrect solution for ε_2 due to the range constraint. A test is performed in the cases where $\delta > \theta_1$, to check the correctness of the given solution for

ε_2. This is achieved by computing $\cos[\delta_{calc}]$ using the given solution for ε_2, and comparing with $\cos[\delta]$. If $\cos\delta \neq \cos\delta_{calc}$, then the correct solution for ε_2 is selected, by subtracting the original solution from π.

4.3 Ray tracing in cylindrical guides

4.3.1 Previous methods: undoped light guides

A number of methods designed to simplify ray tracing in light guides have been documented in the literature. Generally, light guides possess translational symmetry along the *z*-axis (refer Figure 4-1) due to unchanging geometry in the *x*-*y* plane. Also, the *z*-component of ray direction, the *Z* direction cosine, is independent of the *X* and *Y* direction cosines. These properties have been utilised to follow a ray's path in two dimensions, rather than three, wherever possible. A generalised form of Snell's Law, applied to a ray's projected path onto the cross-sectional plane perpendicular to the *z*-axis, has been previously derived (Whitehead 1982). The specifics of this simplifying method cannot be applied to systems with scattering particles, but the principle of projection onto the cross-sectional plane can be applied when calculating the reflection angle of a ray from the guide wall.

In some studies of undoped light guides, the propagation of a ray is described by three parameters, θ, *r*, and φ (Mildner *et al.* 1994, Saraiji *et al.* 1996, Feuermann *et al.* 2001). These geometrical relations were derived by Mildner and Chen (Mildner *et al.* 1994). θ is the angle with the *z*-axis after refraction into the light guide. *r* is the radial distance of the entry point of the ray from the centre of the input end of the guide. φ is the azimuthal angle of the ray direction relative to the plane containing both *r* and the *z*-axis (refer Figure 4-3). In light guiding systems which do not contain scatterers, the angle θ remains unchanged as the ray undergoes TIR and propagates along the light guide (Mildner *et al.* 1994). This principle has been utilized in calculating the light flux output of a light guide in terms of the flux input, using Monte Carlo ray tracing (Saraiji *et al.* 1996). These same *r*, θ and φ parameters have been used in ray tracing studies of the role of skew rays in radiation leakage (Feuermann *et al.* 2001).

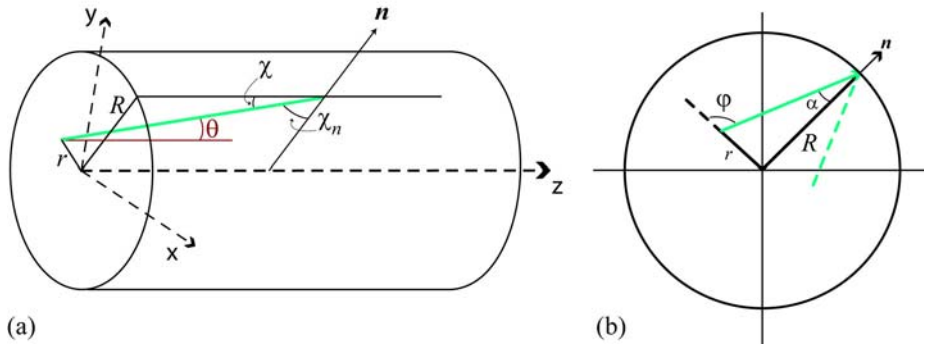

Figure 4-3. a) Geometry of a circular light guide b) projection onto *x*-*y* plane

In large core cylindrical optical fibres, such as those used for illumination purposes, the ray input position, *r*, is an important parameter affecting ray propagation. This is because the ray/wall intercept angle varies with *r*, for a particular input angle θ. The 'glancing angle' of a ray with the wall, χ (Figure 4-3(a)) was derived for a study involving the propagation of neutrons inside a cylindrical tube (Mildner *et al.* 1994). The critical angle for TIR was not relevant for the neutron study, but is needed for optical studies. An expression to calculate the angle between the ray and the cylinder wall normal (χ_n in Figure 4-3(a)) was derived later (Feuermann *et al.* 2001) to facilitate comparison with the critical angle. Also shown in Figure 4-3(b) is the reflection angle in the *x*-*y* plane, α, which will be discussed in Section 4.3.3.

4.3.2 Particle-doped cylindrical light guides: wall intercept

The geometric principles used in the previously mentioned studies (Mildner *et al.* 1994, Saraiji *et al.* 1996, Feuermann *et al.* 2001) will now be extended to include doped light guides. When scattering particles are included in a light guide, the angle at a particular point during propagation cannot be predicted solely from the launch parameters and light guide geometry. It is necessary to calculate the angle between the ray and the wall normal with each wall intercept, and compare it with the critical angle to see if TIR will occur. In this study, the parameters θ, φ and *r* are used as defined in Section 4.3.1, with the exception that *r*, the distance of (x_0, y_0, z_0) from the light guide axis in the *x*-*y* plane, is redefined with each change of ray propagation direction.

Cartesian coordinates are used to trace the path of a ray, as it is necessary to calculate each ray/particle and ray/wall interaction point. The Cartesian point (x_1, y_1, z_1) of a particle interaction is calculated using eqn 4-3, after using eqn 4-2 to define (X, Y, Z). The ray

propagation length between two particles, l, was defined in eqn 4-1. If the wall is intercepted before the particle is reached (i.e. (x_1, y_1, z_1) lies outside of the light guide) the length from the previous particle to the wall is defined as l'. The ray/wall intercept point is defined by eqn 4-3 with l' substituted for l. In other words, (x_1, y_1, z_1) is recalculated with l' substituted for l, to give the ray/wall intersection point. l' can be calculated using the intersection of a line (in this case 'ray') and a cylinder (Hopkins *et al.* 1999). Substitution of the ray (eqn 4-3, with l') into the equation of a circle leads to a quadratic in l'

$$l' = \frac{-B + \sqrt{B^2 - 4AC}}{2A} \tag{4-7}$$

where the coefficients of the quadratic are

$$\begin{aligned} A &= X^2 + Y^2 \\ B &= 2(x_0 X + y_0 Y) \\ C &= x_0^{\,2} + y_0^{\,2} - R^2 \end{aligned} \tag{4-8}$$

If the ray is reflected, the ray/wall intersection point is redefined as (x_0, y_0, z_0), the remaining path increment to the next sphere interaction point, $l - l'$, is calculated, along with a new (x_1, y_1, z_1) using the reflected direction cosines. For guides with low concentrations of added particles (i.e. the average path length p is large), consecutive wall reflections can occur before another particle is reached Multiple reflections can be accommodated by resetting the ray/wall intercept point to (x_0, y_0, z_0) after each reflection, and looping the procedure until (x_1, y_1, z_1) lies within the light guide.

4.3.3 Particle-doped cylindrical light guides: wall reflection

The calculation of the angle between a ray and the wall normal, χ_n, (shown in Figure 4-3(a)), has appeared in similar form previously (Feuermann *et al.* 2001). It is given by

$$\chi_n = \cos^{-1}\left[\sin\theta\sqrt{1 - \left(\frac{r\sin\phi}{R}\right)^2}\right] \tag{4-9}$$

χ_n is calculated at the ray/wall intercept point, and compared with the core/air critical angle. If the ray undergoes TIR, the reflection angle in the x-y plane, α, is calculated. The reflected X and Y direction cosines need to be calculated also (the Z direction cosine is unaffected by reflection from the wall).

Three angles must now be obtained in order to proceed with wall reflection calculations: φ, which is needed to calculate χ_n to test the critical condition for TIR; α, the reflection angle in the *x*-*y* plane; and the value of ϕ after reflection, $\phi_{reflect}$, needed to obtain the *X* and *Y* direction cosines of the reflected ray.

The reflected angle in the *x*-*y* plane, α, is readily calculated using the cosine rule for sides for planar triangles (see Appendix 2, and refer Figure 4-3(b) and Figure 4-4):

$$\alpha = \cos^{-1}\left[\frac{R^2 + i^2 - r^2}{2Ri}\right] \qquad \textbf{(4-10)}$$

where *i* is the projection of *l*′ onto the *x*-*y* plane.

Figure 4 shows the reflection geometry in the *x*-*y* plane, for two relative configurations of *r* and *R*. Introduced here is τ, the angle that the radial line *R* (drawn from the centre to the ray/wall intercept point) makes with the *x*-axis, and γ, the angle that is formed between *r* and the *x*-axis. ϕ is the angle between the propagating ray and the *x*-axis, as before. There are two possible configurations: Case 1, where $\tau > \gamma$, and Case 2, where $\tau < \gamma$. By geometry, φ can be calculated:

$$\varphi = \phi - \gamma \text{ (Case 1)}$$
$$\varphi = \gamma - \phi \text{ (Case 2)} \qquad \textbf{(4-11)}$$

γ is simply $\cos^{-1} x_0 / r$, and so χ_n can now be calculated using eqn 4-9. If the ray is TIR, α can be calculated using eqn 4-9.

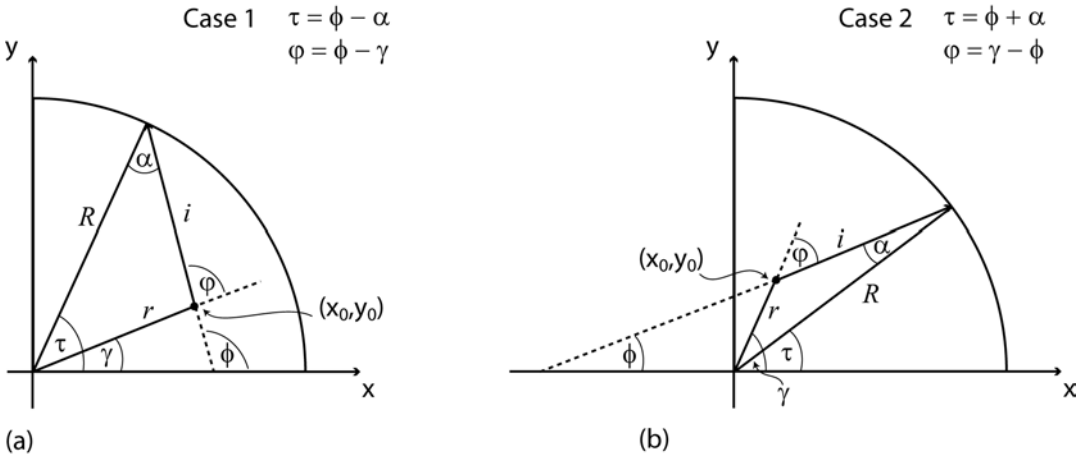

Figure 4-4. Circular reflection geometry in the *x*-*y* plane a) Case 1 b) Case 2

If the ray is reflected, new direction cosines need to be calculated. θ and Z are unchanged upon wall reflection, but ϕ, X and Y are not. One way to determine the value of $\phi_{reflect}$ is by rotation of the reference frame so that, in the new reference frame, the reflected angle is equal to the incident angle plus π. To achieve this, firstly the x-axis is rotated by the angle τ, so that it is superimposed onto R. ϕ is then translated by the same angle, giving ϕ_t. ϕ_t is reflected in the translated reference frame, to give ϕ_{tr}, simply by $\phi_{tr} = \phi_t + \pi$. Then ϕ_{tr} is rotated back to the original reference frame to obtain $\phi_{reflect}$, which is then employed to calculate the X and Y direction cosines of the reflected ray. In simplest geometric terms, this procedure simplifies to:

$$\begin{aligned} \phi_{tr} &= \pi - \alpha \text{ (Case 1)} \\ \phi_{tr} &= \pi + \alpha \text{ (Case 2)} \\ \phi_{reflect} &= \phi_{tr} + \tau \end{aligned} \qquad \textbf{(4-12)}$$

4.4 Discussion

A method of Monte Carlo ray tracing in particle-doped light guides is demonstrated in this chapter, applied to TRIMM light guides. This ray tracing method can be applied to other systems of scattering particles dispersed within a matrix. The user can define a ray deviation function for particle interaction to fit the particular conditions modelled. The average straight-line distance between particles can be calculated from the particle concentration or measured directly. The geometrical principles for reflection from a circular guide are universal. The Monte Carlo ray tracing method described here is of practical use only for relatively low concentrations of scattering particles, and relatively short light guides, because of the computational time involved. However in many cases simulations only need to be performed until the side-scattered loss reaches a steady state, and the results obtained can then be extended to systems with long guide length or high particle concentration.

5 LEDs: Measurements and source modelling for ray tracing simulations

5.1 Introduction

The LED is an appropriate light source for coupling into light-guiding optical systems, because, compared with traditional lamps, it has a directional beam and is small in size. LEDs come in many different beam patterns, and generalisations cannot be made across the various LED types (Green *et al.* 2003). This can make designing and modelling illumination systems involving LEDs difficult. The LED measurements, and corresponding source models used in computer simulations presented here are an important prelude to the following chapter on RGB LED colour mixing.

This chapter describes the methods of luminance measurement of various coloured LEDs, including those adopted for experimental and simulated colour mixing given in Chapter 6. The development of source models for computer ray tracing is also described. In Section 5.2, the differences in beam patterns between a number of 5 mm standard LEDs are examined. The angle corresponding to 50% of light output of the 5 mm LEDs, all having similar cylindrically shaped lenses with rounded ends, have been measured using an integrating sphere. Two RGB triads, designated 'Alpha' and 'Beta', were chosen from this group and used in colour mixing experiments (Section 7.3.2). For each of these LEDs, the 3D beam patterns were measured using a goniometer. 2D single line scans were also measured with the goniometer for a triad of 3 mm RGB LEDs, used as sources for colour mixing experiments with the TRIMM-doped rods (Section 7.3.1).

Section 5.3 describes the development of the LED source models used in computer simulations. Firstly an empirical LED source model, with its corresponding cumulative probability density function is developed. This was used in ray tracing simulations involving 3 mm LEDs (Section 7.4.1), where a common smoothed profile was the basis for each of the RGB source LEDs. Secondly, individual measurement based cumulative probability density functions are developed for each of the 5 mm LEDs in the Alpha and Beta groups. These are source models used in Monte Carlo ray tracing to determine the extent of the

RGB colour mixing presented in Section 7.4.2. Differences between results obtained using the common smoothed empirical source profile and the individual measurement-based profiles are described in Section 8.4.

5.1.1 Modelling of LED sources.

Accurate lighting simulations cannot be performed without accurate source models. Development of LED technologies have created an increasing market for associated illumination systems. The most important and significant source characteristics need to be identified, and accurately reproduced, for satisfactory results in illumination simulations. Methods of source modelling that are in common practice have varying degrees of accuracy. In increasing level of accuracy, these can be summarised as follows (Cassarly 2002):

1. the LED is modelled as an apodised emitter. The apodisation (variation of output in a smooth systematic way with angle) is usually derived from data supplied by the manufacturer.
2. the LED is modelled as an extended source. The angular output distribution and any spatial non-conformities are specified. The angular distribution is constrained to be the same from every point on the surface of the emittance area.
3. the LED model is based on measurement. The emitting source is scanned from all angles (using a goniometer, for example) and a source model is generated from the data (Cassarly 2002, Guo *et al.* 2003, Li *et al.* 2004). Alternatively, a multi-imaging camera with a wide dynamic range can be used. With either method, the resultant model is accurate only for the actual source scanned, and should not be used as a generic LED source.

Care should be taken when conducting goniometer measurements that the incremental angles between readings are sufficiently small. A simple cross-sectional measurement using a conventional goniometric system with an angular resolution of ~5° gives a highly inaccurate impression of the emission patterns of many LEDs (Boher *et al.* 2004).

The approach taken in the work reported in this thesis is a combination of 2 and 3 above. The source models for the LEDs were derived from data obtained by photogoniometer scanning, and modelled as an extended source. The source point for each ray in subsequent ray tracing was randomly selected from within a specified circular area.

Another common approach for modelling LED sources, using commercial ray tracing packages, is to model a 'physical representation' of the LED, complete with housing and epoxy encapsulant. Commonly a ray set representing the source is generated, to save time when Monte Carlo tracing of rays from the source through a light guide is performed (Lee *et al.* 2004). An advantage of this approach is that rays scattered back inside the LED are accounted for. A disadvantage is that the angular distribution of the source is usually matched to data supplied by the manufacturer, and may not reflect the emission characteristics of the actual LED used. If the intensity distribution thus obtained closely agrees with that specified by the manufacturer, accuracy of the source model is assumed by the user (Zhao *et al.* 2003, Van Derlofske 2001). The source intensity is usually apodised or assumed to diminish smoothly with increasing cone angle, and to be rotationally symmetric. Experimental measurements of LEDs show that this is often not the case.

Those who work closely with LEDs are familiar with the variations between them, and the associated modelling problems. Different LED profiles have bright features, such as rings and spots, at different cone angles. These bright features can have a significant effect on the projected light distribution. Upon commencement of this work, the author had not seen 3D patterns of LED angular intensity distribution showing these beam pattern differences published previously in journals. Cross-sectional profiles of various LEDs have appeared on commercial web-sites (Optical Research Associates 2004, Labsphere 2001). After the measurements described in this chapter were performed, a conference paper showing 3D LED beam patterns appeared (Boher *et al.* 2004), showing bright regions in the profiles of measured red and green LEDs. Here a Fourier optics approach and a CCD were employed to measure optical properties of various coloured LEDs with viewing angle. The importance of accounting for irregularities in beam patterns when coupling LEDs into non-diffuse systems will be discussed in Chapter 7. It is important for all those involved in lighting to be aware of this, especially when mixing different coloured LEDs.

5.1.2 Current standards and measurement problems

Standardisation of measurement for LEDs is still in its infancy. CIE's published document "Measurement of LEDs" established some guidelines for measuring LED intensity and total luminous flux (Labsphere 2001, CIE Publication No.127 1997, Miller *et al.* 2004). Therein measurement of 'Averaged LED intensity' is described. The detector is a photometer with an aperture of 1 cm^2, and there are two standard distances between the

LED and the photometer, 316 mm and 100 mm. As the name indicates, an averaged intensity is defined, and gives little indication of the beam characteristics of individual LEDs.

There are also practical difficulties encountered when measuring LEDs. The peak intensity of the LED does not always align with the mechanical axis (Miller *et al.* 2004). Goniometer measurements necessitate locating the source at the centre of rotation of the instrument. The LED is not strictly a point source, so there is some conjecture as to the exact centre of rotation. Care must be taken with calibration of photometers used for LED measurements. Photometers calibrated using a CIE lamp standard can have significant errors when measuring blue and red LEDs (Boher *et al.* 2004).

In contrast to lamp sources, a calibrated set of LEDs does not exist. The USA's National Institute of Standards and Technology (NIST) use a calibrated detector, rather than calibrated LED references. "A practical problem is that many reference LEDs of different colours and spatial distributions are required. NIST does not currently sell a calibrated set of LEDs" (Miller *et al.* 2004).

5.2 Experimental measurements

Red green and blue LEDs were purchased from retail electronic stores, with a view to building combined source triads for RGB colour mixing. Some LEDs were also supplied by Poly Optics Pty Ltd. Standard 5 mm LEDs claimed to have 'high brightness' and 'narrow beam angle' were selected. The LEDs were measured to determine the semi-cone angle at which the integrated luminous intensity of the LED output is half of the maximum (hereafter referred to as luminous flux half angle). The aim was to form RGB triads that are matched in angle, to facilitate uniform mixing of the light sources.

5.2.1 Luminous flux half angle measurements

An Oriel 70491 integrating sphere was mounted on an optical rail, and a Hagner S3 photometer detector was positioned at the integrating sphere's output port. The LED to be measured was mounted on a holder, positioned with its beam at normal incidence to the entry port. Current through each tested LED was set at 20 mA. Firstly, the LED was positioned so that the entrance aperture of the integrating sphere received the total light emitted from LED, and this maximum integrated luminous intensity reading was recorded. The distance between the integrating sphere's support stand and that of the LED was recorded using a vernier calliper. The LED was then moved along the optical rail an additional distance d until the photometer reading was at 50% of the maximum reading. The

radius of the entrance aperture is known, hence the semi-cone angle can be calculated. The diameter of the integrating sphere entrance port was measured as 25.25 ± 0.05 mm. Measurement uncertainty of the distance *d* was taken to be 1 mm. The procedure was repeated to obtain the angle at which the integrated intensity was 25% of maximum.

5.2.2 Luminous flux half angle results

The results showing the luminous flux half angle measurements are given in Figure 5-1, for each LED in the original 'pool'. Each measured LED is a unique type, with its own serial number. Notice the large variation in beam angle between the different LEDs, particularly within the red group. The angle at which the integrated light intensity is at 25% of maximum is included here to illustrate the large variation in individual beam profiles.

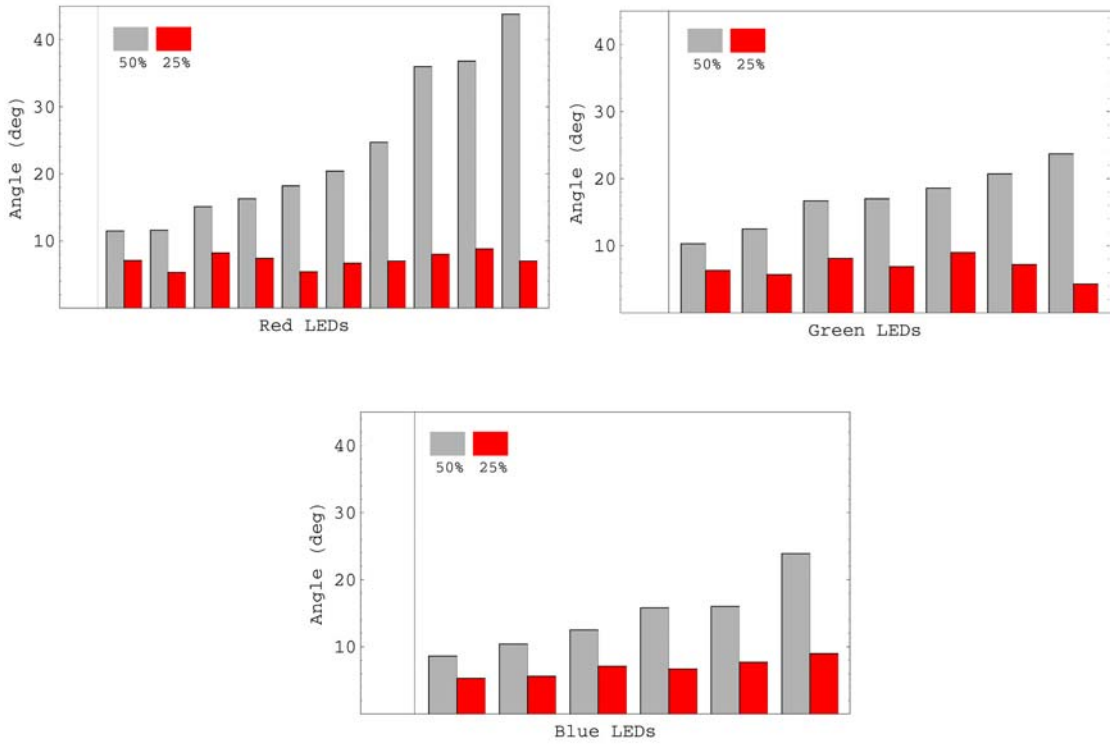

Figure 5-1. LED semi-cone angles at which integrated light output is 50% and 25% of maximum.

Two sets of 5 mm LEDs, designated "Alpha" and "Beta" were selected from the main group, judged to be well matched in angle based on the luminous flux half angle measurements. Detailed results for these six LEDs are given in Table 5-1. These LEDs were selected from the larger group because they have smaller luminous flux half angles.

Table 5-1. LED luminous flux half angle results

LED Group, Colour	*Relative integrated luminance*	*Angle(°) for 50% integrated light output*	*Angle for 25% integrated light output*
Alpha Red	63	11.5 ± 0.2	7.1 ± 0.1
Alpha Green	44	12.5 ± 0.3	5.7 ± 0.1
Alpha Blue	31	12.5 ± 0.3	7.1 ± 0.1
Beta Red	35	11.6 ± 0.2	5.3 ± 0.1
Beta Green	100	6.3 ± 0.1	6.3 ± 0.1
Beta Blue	17	5.3 ± 0.1	5.3 ± 0.1

5.2.3 Photogoniometer measurements

The LEDs that were selected to form the Alpha and Beta RGB triads were measured using a photogoniometer (Smith *et al.* 2001). The source-to-detector distance was 30 cm. The LEDs were scanned in a raster pattern over a semi-cone angle of 20 degrees, where the detector was moved in one-degree increments in the ω and σ photogoniometer scanning directions (refer Figure 5-2).

Measurements were also taken for 0.5 degree increments across a single line for $-80 < \sigma < 80°$, at $\omega = 0$. The LED measurement-based source profiles used in computer simulations are based on these data.

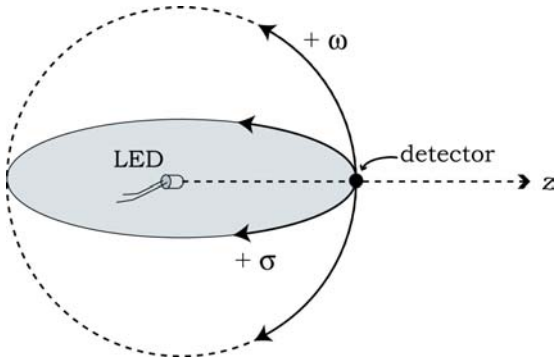

Figure 5-2. Photogoniometer measurement geometry

5.2.4 Photogoniometer Results

The 20° semi-cone raster angular intensity measurements of the selected 'Alpha' and 'Beta' group LEDs are plotted in Figure 5-3.

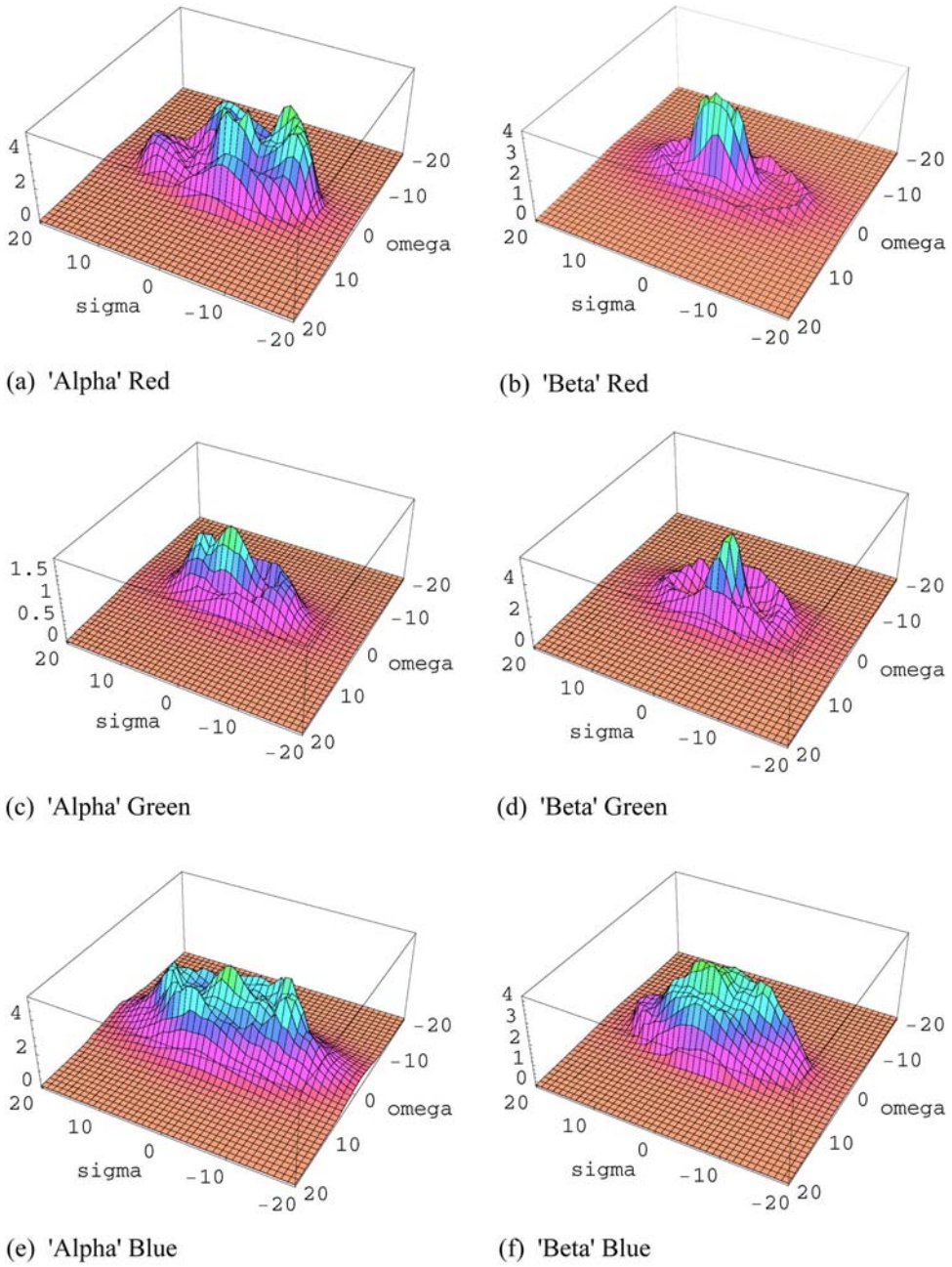

Figure 5-3. Photogoniometer measurements of intensity with angle (arbitrary units, from photo-detector output), from normal (0°) to 20°, for 'Alpha' and 'Beta' triads of RGB LEDs.

Corresponding 'single line' scans for $-80 < \sigma < 80°$, at $\omega = 0$ are shown in Figure 5-4. These are essentially a cross-section of the 3D scans of Figure 5-3.

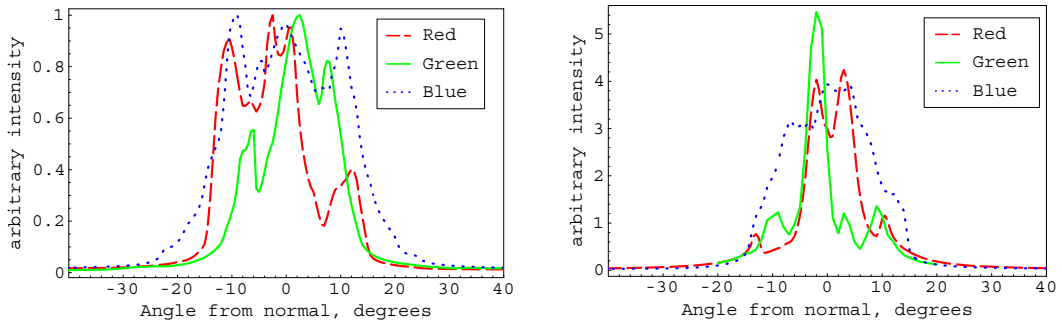

Figure 5-4. Measured angular distribution of the source LEDs. a) Alpha group. b) Beta group.

It can be seen that, for LEDs with similar luminous flux half angles, the photogoniometer profiles of light output with angle are quite different. Notice also that the individual profiles are not rotationally symmetric. The patterns are elongated in the σ direction, having an overall shape similar to an ellipse. Repeat measurements of Alpha blue and Beta green LEDs at a later date resulted in very similar beam patterns, verifying that the evident asymmetry is not due to a mounting or alignment problem. Similarly, for Alpha Blue, a closely matched profile was obtained from measuring an extra LED with the same product code. This suggests that the beam pattern of LEDs within a particular batch do not vary to a significant extent, but two different commercially available LEDs with similar specifications on the product sheet can be vastly different.

5.3 LED source models

5.3.1 Empirical LED source model

An intensity profile that decreases smoothly with angle is the basis of the empirical source model used in some of the Monte Carlo computer ray tracing simulations. This profile was generated before the luminous flux half angle measurements were undertaken. It is based on data from 'single line' scans of 2 LEDs, measured using the UTS photogoniometer at 0.5° increments, as described in Section 5.2.3. This gives a single line scan of the LED θ cone angle along a line perpendicular to the z-axis, as shown in Figure 5-5.

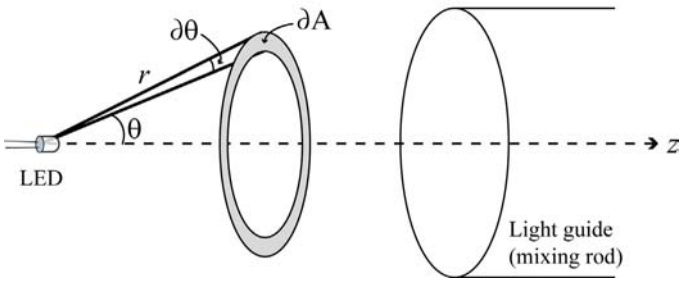

Figure 5-5. Geometry of source emission from source LED

It was initially assumed that the light intensity emanating from an LED, with manufacturer specified viewing angle θ_{diode}, has a distribution that can be approximated by a Guassian, of a similar form to

$$I(\theta) = ke^{\frac{-\theta^2}{\theta_{diode}^2}} \qquad \textbf{(5-1)}$$

The empirical model was based on measured LED profiles of two 5 mm LEDs, one of which was the 'Beta red' LED. θ_{diode} was taken as 16°, as both LEDs had a viewing angle of 16° specified by the manufacturer. The aim was to create a modelled intensity profile based on a smooth, Guassian curve. An empirical fit for the measured profiles is expressed by four equations:

$$\begin{aligned} I &= 1 - 0.0300\theta \\ I &= 70\sin\theta e^{\left|\frac{\theta}{16}\right|^{-7.7}} \\ I &= 25\sin\theta e^{\left|\frac{\theta}{16}\right|^{-5.0}} \\ I &= 0.15\sin\theta e^{\left|\frac{\theta}{16}\right|^{-0.9}} \end{aligned} \qquad \textbf{(5-2)}$$

Figure 5-6(a) shows the empirical *I(θ)* profile given in eqn 5-2 compared with the measured profile of the 'Beta red' LED. (The other LED profile is omitted, because it is not featured in any of the modelling.) Figure 5-6(b) shows the empirical *I(θ)* profile compared with the measured profiles of the 3 mm RGB LEDs. This empirical profile was the basis of the source model used for the TRIMM-doped rod ray tracing (Section 6.4.1), for comparison with experiment when the 3 mm LEDs were the source triad. It can be seen

that the empirical profile fits the 3 mm red LED measured profile fairy closely, but is not an accurate representation of the green and blue measured profiles.

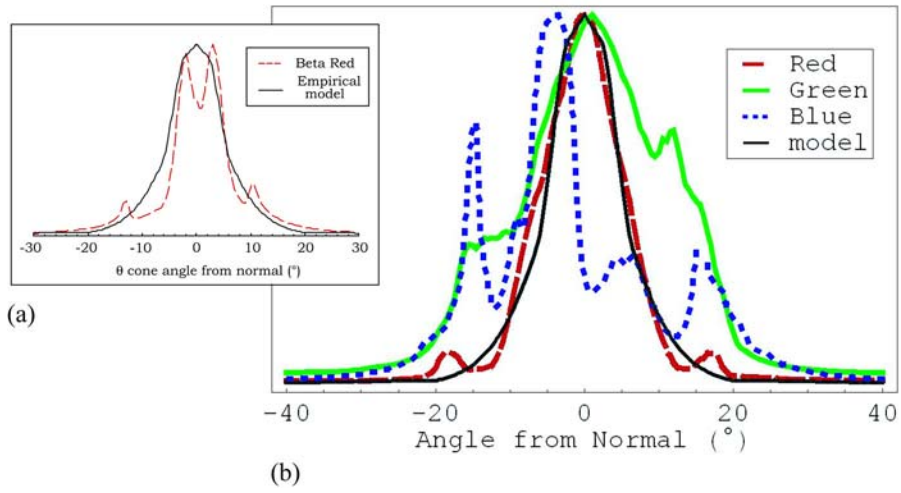

Figure 5-6. (a) Empirical model of LED intensity profile *I(θ)*, shown with the measured photogonometer intensity profile on which it is based, that of the 5 mm 'Beta red' LED. (b) Empirical model of LED intensity profile *I(θ)*, compared with photogoniometer angular intensity scans of 3 mm red green and blue LEDs

5.3.2 Cumulative probability density distributions for LED sources in Monte Carlo modelling

Monte Carlo ray tracing in polymer light guides using Mathematica® was described in Section 4.2. Launch ray source direction is described by the angle θ with the light guide axis *z*, and an azimuth angle randomly selected between 0 and 2π. The cone angle θ is chosen according to a previously calculated cumulative probability distribution *P(θ)*, by selecting a random number between 0 and 1. θ is calculated inversely, using the relevant function according to the value of *P(θ)*. The cumulative probability functions used in the Monte Carlo modelling are based on the source LED measurements.

The LED profiles are expressed as cumulative probability density distributions, in order to select individual launch angles for each ray in the Monte Carlo ray tracing. Given an angular intensity distribution *I(θ)*, the probability of a ray being emitted within an angular range θ to $\partial\theta$ is

$$\partial p = \frac{2\pi r^2 I(\theta)\sin\theta\partial\theta}{\int_0^{\pi/2} 2\pi r^2 I(\theta)\sin\theta\partial\theta} \qquad \textbf{(5-3)}$$

(refer Figure 5-5). The cumulative probability density function is

$$P(\theta) = \int_0^{\theta} \partial p \text{ where } \int_0^{\pi/2} \partial p = 1 \qquad \textbf{(5-4)}$$

The probability ∂p for bins of $I(\theta)$ was calculated using eqn 5-3. The cumulative probability density, $P(\theta)$, for each bin was calculated using the Reimann sum as an approximation of eqn 5-4. A fit was made to these points, using a series of functions (mostly polynomials).

5.3.3 Empirical cumulative probability density function

$I(\theta)$ for the empirically modelled LED profile was given in eqn 5-2. The probability ∂p for each 0.25° bin of $I(\theta)$ was calculated using eqn 5-2 and eqn 5-3. Then the cumulative probability density was calculated using Reimann sums to approximate eqn 5-4. Eleven separate equations were needed to obtain curves to closely fit the calculated points over the whole range of $P(\theta)$, $0 < \theta < \pi/2$. These curves are given in Appendix 3.1, and plotted in Figure 5-7.

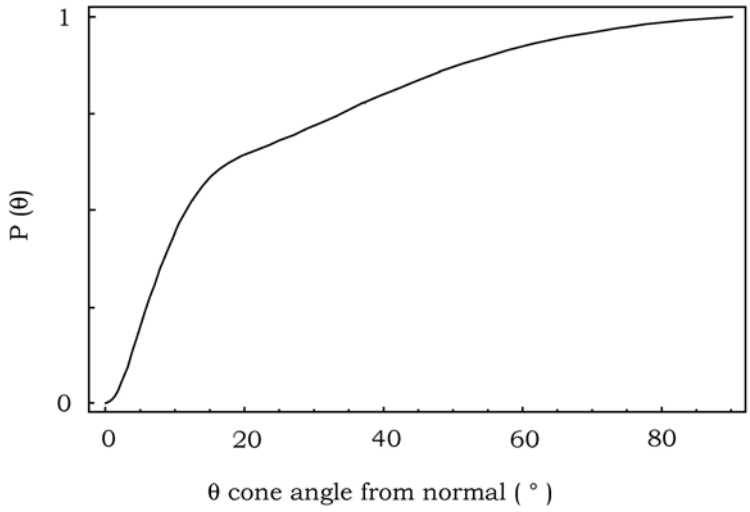

Figure 5-7. Cumulative probability density function $P(\theta)$ for the empirical LED model.

5.3.4 Individual LED measurement-based cumulative functions

Luminous intensity with angle had been measured in 0.5° increments using the photogoniometer for each LED in each of the Alpha and Beta triads (Figure 5-4). These profiles are not symmetrical about the normal. For a particular LED profile, an average of the two readings for each measured cone angle on each side of the normal was taken. The resulting data set is $I(\theta)$ for that LED, used for calculating its cumulative probability density distribution. The same method as described in Section 5.3.2 was applied for each LED

data set to obtain an individual $P(\theta)$ distribution for each, using 0.5° bins of $I(\theta)$. Fitting functions to the $P(\theta)$ points was much simpler for these profiles than for the empirical model. Only 4 or 5 functions were needed to get a very close fit for each of the Alpha group LED's cumulative probability density distributions, and 6 to 8 for each in the Beta group (compared with 11 for the empirical source model).

The cumulative probability density distributions calculated for each of the LEDs in the Alpha and Beta groups are shown in Figure 5-8 and Figure 5-9. The empirical model, included for comparison, is the same as shown in Figure 5-7. The equations used as a fit for the Alpha red $P(\theta)$ are given in Appendix 3.2.

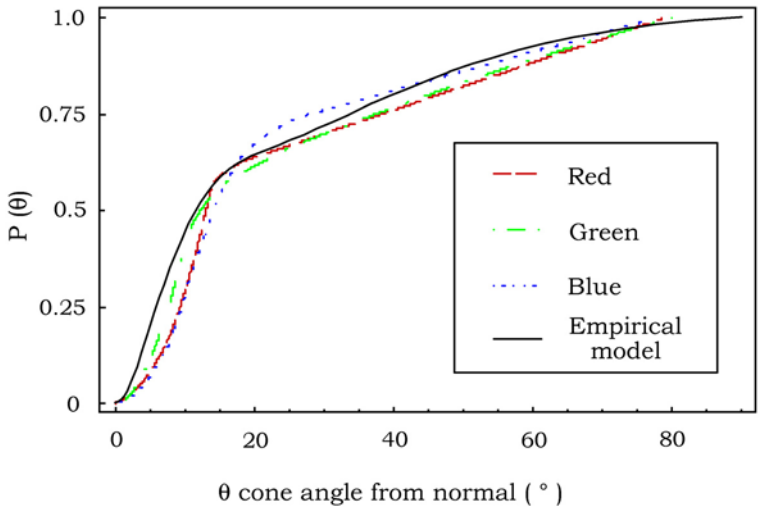

Figure 5-8. Cumulative probability density function: Alpha group LEDs

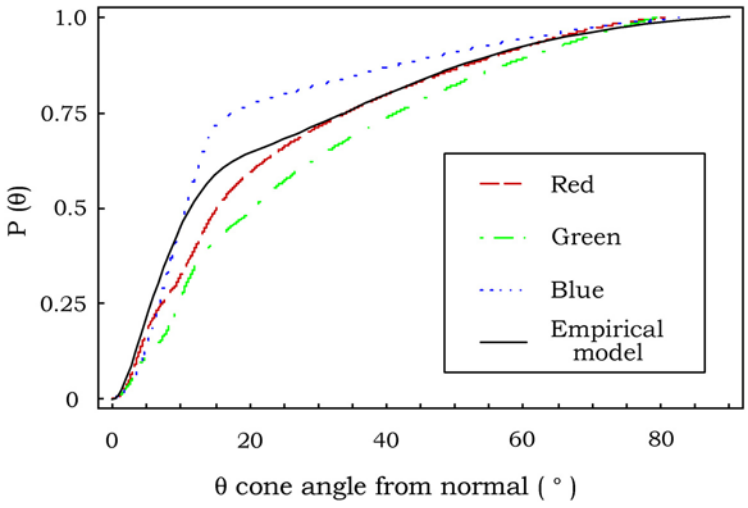

Figure 5-9. Cumulative probability density function: Beta group LEDs

5.4 Discussion

It is clear from Figure 5-3 that the LED beam patterns are not rotationally symmetrical. Firstly, the profiles are elongated along the axis containing the electrode 'pins'. Similar published data has not been found, although Radiant Imaging have a downloadable 3D LED profile on their web-site with a similar elongated shape (Radiant Imaging inc 2004). Secondly, the bright spots in the angular profile are not rotationally symmetric either, and the profiles do not smoothly decrease with cone angle. Similar large light fluctuations with azimuth angle have been recently reported (Boher *et al.* 2004). It is evident that modelling an LED using a rotationally symmetric smooth profile is not an accurate representation of the source. This will be discussed further in Chapter 7.

It is acknowledged that the LED cumulative probability distributions presented here, although based on actual source measurements, contain approximations. The Monte Carlo model selects launch semi-cone angles using the $P(\theta)$ distributions (Figure 5-8 and Figure 5-9). The azimuth angle is selected randomly, so the resultant simulated sources are rotationally symmetric, whereas the measured profiles are not. The bright spots evident in Figure 5-3 are accounted for, not in a precise spatial sense, but in an averaged sense around the azimuth direction. The elongation of the profiles (in the 'sigma' direction, see Figure 5-3) has also not been taken into account. However, it will be seen in Section 7.2 that it is the general large fluctuations in cone angle that have the greatest effect on output light distribution from a light guide.

6 Colour mixing LEDs with TRIMM-doped PMMA rods

6.1 Introduction

Mixing rods are used to homogenize light from single or multiple sources in devices such as backlit liquid crystal displays and data projectors, as well as for general illumination applications. Mixing rods that rely entirely on total internal reflection (TIR), such as plain PMMA rods, have the disadvantage that undesirable patterns are produced due to caustic effects. It was reported in a previous study that acrylic light guides that utilised TIR only provided no significant improvement in illuminance, colour, or beam uniformity compared to a bare LED array. A diffuser at the output end significantly improved the output light distribution, but with an additional loss of 6% (Zhao *et al.* 2002). These systems also require long mixing lengths, particularly when the number of LEDs in the source array is small (Martynov *et al.* 2003). Shorter lengths are desirable as the size of devices is steadily decreasing; designers want high efficiency and output uniformity in the minimum possible size. TRIMM-doped mixers homogenize the light output with low loss, because the micro-sphere particles deviate the light rays by a small amount each interaction, with low backscatter (Smith *et al.* 2003). Shorter rod lengths can also be used for TRIMM-doped light mixers, compared with undoped rods.

In this chapter, the combined output of red, green and blue (RGB) LEDs using clear, undoped PMMA rods is compared with the mixing performance of TRIMM-doped systems. Output light projected from the ends of the rods is measured and modelled. Two systems were studied:

1. TRIMM-doped PMMA rods, using 3 mm LEDs as light sources, and the empirical LED model in the simulations;
2. Clear PMMA rod with TRIMM diffuser sheet at the output end, using 5 mm LEDs as light sources, with measurement-based LED profiles used in the simulations. Results are presented for the Alpha group of LEDs.

For the TRIMM-doped rods (system 1), quantitative measurement of colour output was made using a photometer. These rods were not of sufficient optical quality to ascertain experimentally the loss of transmitted 'end-light' associated with the TRIMM particles alone. In addition, the diameter of these rods was too small to use 5 mm LED triads as light sources, and extruded larger diameter rods were not available. The PMMA rod with added diffuser sheet (system 2) was prepared in order to perform additional transmittance measurements and to have a mixing rod of good optical quality. It is also of interest to see how the particles perform as end diffusers, instead of having TRIMM dispersed evenly throughout the rods. For both TRIMM mixing systems, photographs of output light were taken and computer ray tracing simulations performed, to compare the output and losses of doped with undoped mixing rods. This chapter presents the colour mixing calculations and results, and end-light output distributions. Transmittance results and side-scattered distributions are discussed in Chapter 8.

6.2 Colour space

Colour spaces are systems which describe the connection between the radiant energy entering the eye of a person, and the colour which the person perceives (Tastl *et al.* 1994). The standard chromaticity diagram adopted by the Commission Internationale de L'Eclairage (*CIE*) in 1931 remains in widespread use (Wyszecki *et al.* 1967). Colour of light sources and output light are represented in this report using *CIE x* and *y* chromaticity values. The *RGB* colour space is commonly used for computer graphics, as colours are produced on a computer monitor by the addition of different levels of RGB phosphors (Foley *et al.* 1995, Durret 1987). Here *RGB* colour space is used for the display of output distributions on a computer monitor. An ideal colour space should assign the same value for all colours that are indistinguishable to the observer, and encompass all possible colours. However, not all colours can be displayed on a computer monitor because of the reduced colour gamut (Orava *et al.* 2004). This can be seen in Figure 6-1(b), by comparing the plotted *CIE* coordinates of the 3 mm RGB LEDs with those of a computer monitor RGB phosphors.

6.3 Experiment

6.3.1 TRIMM-doped PMMA rods

As stated in Section 3.1.1.2, TRIMM-doped PMMA rods 12.7 mm in diameter were extruded by combining plain PMMA granules with TRIMM-doped granules in a com-

mercial extruder. Rods with two different TRIMM concentrations were studied. Low concentration rods contain 0.45% TRIMM particles (15K) and high concentration rod contain 3.0% TRIMM particles (100K). All measured rods are 10 cm long, except one 100K rod is 8.84 cm long.

The experimental set up is shown in Figure 6-1(a). A triad of red, green and blue 3 mm LEDs were mounted as close as possible to one end of the mixing rod. (3 mm LEDs were used because of the limited diameter of the available mixing rods.) The centre point of the LED array was aligned with the rod's axis. A frosted glass screen was positioned 10 cm from the exit end of the light guide. Photographs of the output light distributions transmitted through the screen were taken with an Olympus C-4000 ZOOM digital camera. For quantitative observations, the screen was removed and replaced with a translational stage, carrying the detector of a Hagner S3 photometer. The detector size was reduced to ~1 mm diameter with a cover. The illuminance of each LED was measured every millimetre in a horizontal direction through the centre axis of the guide, to form a strip 80 mm long. Each measurement corresponds to one pixel.

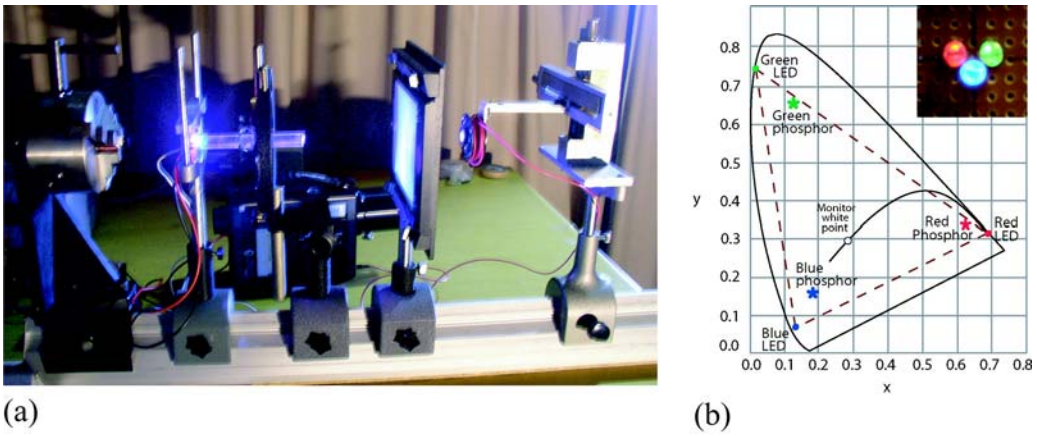

Figure 6-1. a) Experimental setup, showing (from left): alignment laser, LED array, acrylic mixing rod, frosted glass screen and the translational stage with photometric detector. b) 1931 CIE diagram showing the 3 mm LED source chromaticity coordinates, and the coordinates of the computer monitor's phosphors. Inset: 3 mm LED array.

The source luminous flux of each of the LEDs was measured using the Hagner meter coupled to an Oriel 70491 integrating sphere. Spectra for each LED were obtained via an Ocean Optics SD2000 fibre optic spectrometer coupled to the Oriel 70491 integrating sphere, and associated software. The spectral power distributions for the red, green and blue 3 mm LEDs are shown in Figure 6-2.

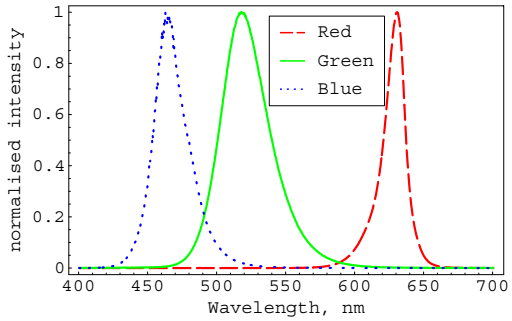

Figure 6-2. 3 mm LED spectral power distributions (normalised to maximum intensity values)

CIE coordinates for each LED (x_{LED}, y_{LED}, z_{LED}) were derived from the respective spectral power distributions,

$$x_{LED} = \frac{\int [x_{(\lambda)} S_{(\lambda)}] \partial\lambda}{\int [S_{(\lambda)}(x_{(\lambda)} + y_{(\lambda)} + z_{(\lambda)})] \partial\lambda} \qquad \textbf{(6-1)}$$

where $S_{(\lambda)}$ is the spectral power distribution for a particular LED and $x_{(\lambda)}$, $y_{(\lambda)}$, $z_{(\lambda)}$ are the 1931 *CIE* colour matching functions. The *CIE* chromaticity coordinates for each of the 3 mm LEDs, and for a DELL computer monitor's phosphors, are shown in Table 6-1.

Table 6-1. 1931 CIE coordinates of the 3 mm source LEDs, and of the Dell computer monitor phosphors

3mm LED group	*CIE x*	*CIE y*	*Monitor Phosphors*	*CIE x*	*CIE y*
Red (630.5 nm)	0.690	0.310	Red	0.625	0.340
Green (518.2nm)	0.166	0.707	Green	0.275	0.650
Blue (465 nm)	0.131	0.070	Blue	0.150	0.065

6.3.2 PMMA rod with TRIMM diffuser sheet

Two transparent PMMA rods 25.55 mm in diameter were used in this experiment. A 2.94 mm thick TRIMM diffuser sheet was glued to an end of a 58.95 mm long rod using Loctite IMPRUV® 34931 glue. No air bubbles or defects were visible at the interface, which is indicative of a good optical joint. Thus the total length of the rod with TRIMM sheet diffuser is 59.8 mm. The plain PMMA rod (referred to as 'clear') is 61.9 mm long.

The sources that are mixed are two sets of 5 mm RGB LEDs, denoted as Alpha group and Beta group. Each group consists of a triad of 3 LEDS, as described in Chapter 5. Spectra and *CIE* coordinates for the LEDs were obtained in the same manner as for the 3 mm

LEDs. The spectral power distributions of the RGB LEDs of the Alpha and Beta groups are shown in Figure 6-3. The corresponding source *CIE* coordinates and the LED peak spectral wavelengths are given in Table 6-2.

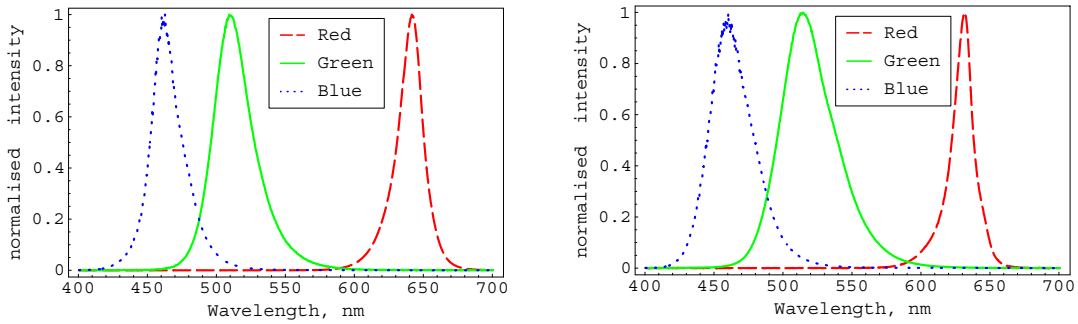

(c) (d)

Figure 6-3. Spectral power distribution of selected 5 mm LEDs, normalised to arbitrary maximum intensity. a) Alpha group b) Beta group

Table 6-2. 1931 CIE coordinates and peak wavelength of the source LEDs, as measured using a spectrometer.

Alpha Group	*CIE x*	*CIE y*	*Beta Group*	*CIE x*	*CIE y*
Alpha Red (641.6 nm)	0.701	0.294	Beta Red (631.5 nm)	0.691	0.301
Alpha Green (509.4 nm)	0.114	0.681	Beta Green (512.8 nm)	0.162	0.674
Alpha Blue (461.5 nm)	0.135	0.058	Beta Blue (460.4 nm)	0.138	0.062

The Alpha group LEDs are better matched in angle than the Beta group, as can be seen from inspection of Figure 5-4, but the Beta group is superior in terms of colour for RGB mixing, as the spectra of the Beta peaks are more widely spread. (The spectral peaks of Alpha green and blue are closer together, as can be seen from Table 6-2.)

The experimental setup for measurements is shown in Figure 6-4(a), and is similar to that of the previous section. The frosted glass screen (dimensions 120 mm x 95.5 mm) was positioned 4 cm or 15 cm from the exit end of the rod. Photographs of the transmitted output distributions were taken as before. Transmittance measurements were performed using the Alpha LED source array and the 'clear' and 'clear + TRIMM diffuser sheet' rods with the output end coupled to the entrance port of an Oriel 70491 integrating sphere. A BPW21 photo-diode was attached to the detector port of the integrating sphere, and readings taken with a Data Precision DP 100 Multimeter. The ratio of the transmitted to

incident readings were taken using measurements of the bare LED array as the total incident light.

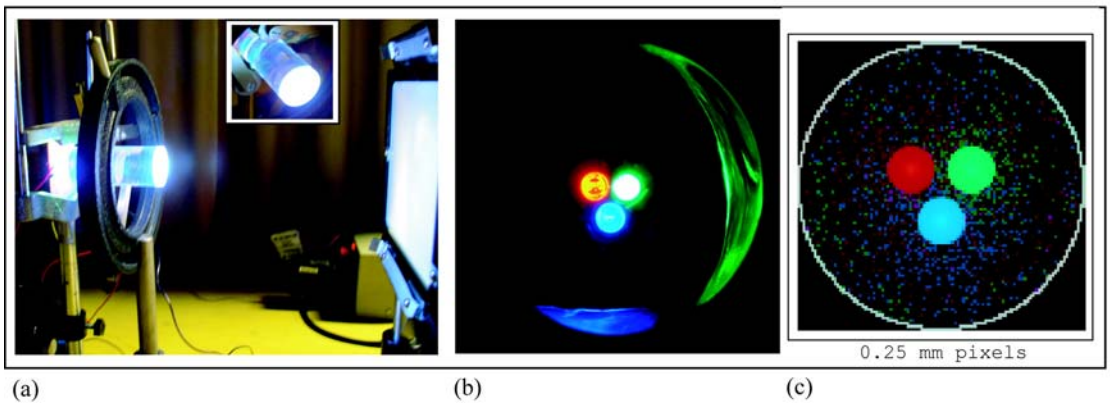

Figure 6-4. a) experimental setup: LED array, mixing rod, frosted glass screen. b) photograph of Beta LEDs and clear PMMA rod, ~20 cm from the rod exit surface, at an off-axis angle to avoid excessive overexposure. TIR from the rod surfaces is visible. c) modelled clear rod exit end surface illumination of modelled Beta LEDs.

6.4 Computer modelling simulations

6.4.1 Source models: Trimm-doped PMMA rods

Ray tracing simulations involving TRIMM particles have been described in Chapter 4. For the 3 mm LED source simulations, rays originate from a circular source area 2 mm in diameter, the centre of which is a specified coordinate for each LED corresponding to its position in the array (see Figure 6-5(a)). The axial launch angle θ is randomly selected using the empirical cumulative probability density function, as described in Section 5.3.3. Figure 5-6(b) shows the empirical angular intensity profile compared to that of the measured angular profiles of the red, green and blue 3 mm LEDs. Note that the angular profile of the empirical source closely follows the profile of the red 3 mm LED, and is somewhat narrower and more symmetric than that of the other 3 mm LEDs. This will affect the distribution of the simulated green and blue projected output, and hence the total computed colour output distribution.

6.4.2 Source models: PMMA rod with TRIMM diffuser sheet

The rays were emitted uniformly over a 4 mm diameter area, the centre of which is a specified coordinate for each 5 mm LED corresponding to its position in the array (see Figure 6-5(b)). Measurement-based algorithms were used to simulate the LED light output, as outlined in Section 5.3.4. Transmittance and loss data is modelled by counting the number of rays exiting or reflecting from the relevant rod surfaces.

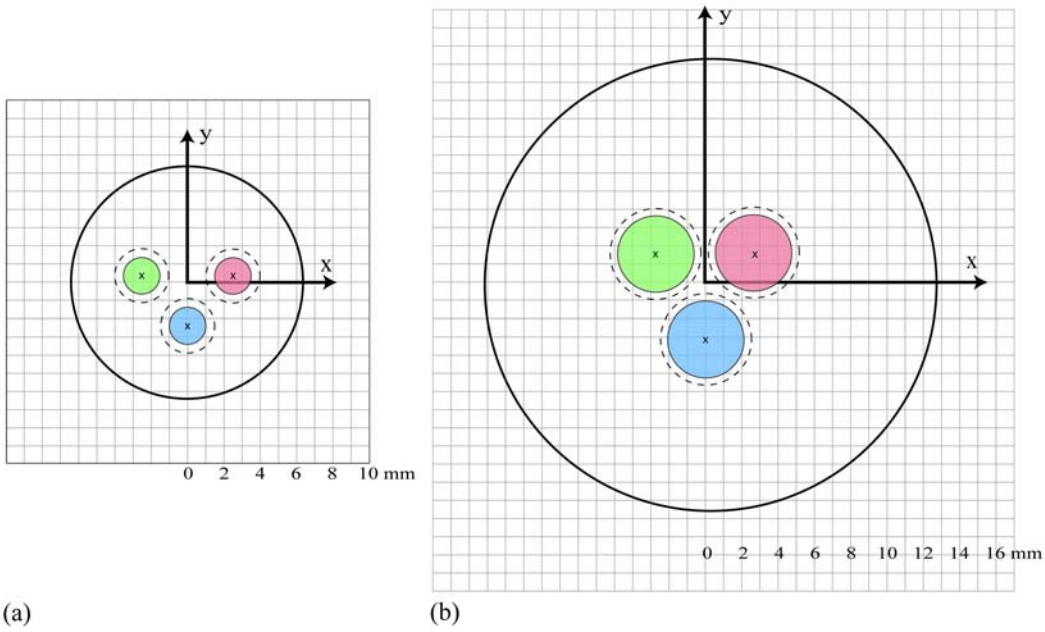

Figure 6-5. Source configurations for ray tracing simulations, to scale. a) 3 mm triad set-up b) 5 mm (Alpha and Beta) triad set-up. 'x' marks the coordinates of source points, using same coordinate system as for Figure 4-1 and Figure 4-3 (z-axis into the page). The filled circles correspond to the modelled source area for each LED. The dotted circles correspond to actual lens diameter of the LEDs used in experiments. The outer circle is the perimeter of the light guide in each case.

6.4.3 Modelling method for projected combined RGB light output

Ray tracing simulations using 1 million initial rays for each source LED were carried out to model the experimental conditions. A separate simulation was carried out for each LED, and the RGB results combined to obtain the simulated output intensity and colour distribution. Rays exiting the end of a rod are traced to predefined detector planes which simulate square 'screens'. Each screen is divided into a matrix of pixels, and each pixel is incremented when hit by a ray. This is illustrated in Figure 6-6. Each pixel in the matrix for each of the RGB LED simulations is normalised to the photopic response of the eye by dividing by y_{LED}, and is weighted by the intensity fraction of the source LED. The RGB matrices for a simulated screen are then added together to form a complete colour map, using eqn 6-2 and eqn 6-3. This is described in detail in the following section.

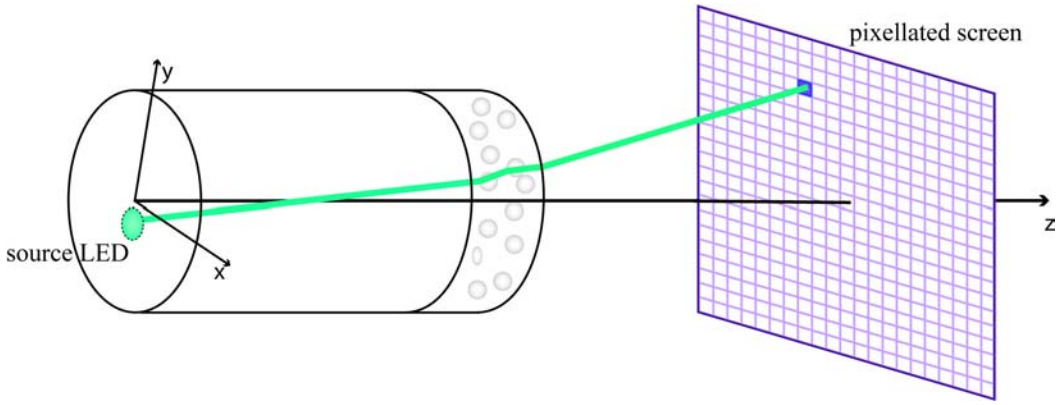

Figure 6-6. Projected light distribution onto a predefined screen for ray tracing model. This creates pixellated data from a single LED after ray trace through a mixing rod.

6.5 Colour mixing calculations

When considering the calculation of colour output, it is helpful to refer to Figure 6-7, which shows a flowchart of the entire process.

A modelled source LED is defined by probability functions describing its angular ray distribution. Other source variables are the coordinates with respect to the input face of the light guide, and the area over which the rays are launched. The pixellated output distribution of light hitting a modelled screen is dubbed a 'LED diffusion map', and is simply a matrix of the number of rays which strike each pixel. This light distribution is dependent on the geometrical position and size of the screen, and light guide parameters such as length to diameter aspect ratio and TRIMM concentration, as well as the parameters previously mentioned pertaining to the LED source. The LED diffusion map is now converted to photometric units by weighting each pixel by the colour and intensity corresponding to the measured LED. This is dubbed a 'Single LED colourised map'. For a RGB LED source triad, three such maps are generated to obtain modelled combined colour output.

The red, green and blue luminance at each pixel point (I_{Ri}, I_{Gi}, I_{Bi}) is measured directly using the photometer for experimental data (Section 6.3.1). The pixellated triplets of RGB data, both measured and modelled, are added together as a weighted sum to calculate the pixels' 1931 CIE xyz components of colour from the 3 LEDs:

$$x_i = (I_{Ri}x_R + I_{Gi}x_G + I_{Bi}x_B)/(I_{Ri} + I_{Gi} + I_{Bi}) \quad \textbf{(6-2)}$$

and similarly for y and z. The tristimulus values (X_i , Y_i , Z_i) are calculated by

$$(X_i = (x_i / y_i) Y_i) \qquad (Z_i = (z_i / y_i) Y_i) \tag{6-3}$$

where firstly $Y_i = I_{Ri} + I_{Gi} + I_{Bi}$ are normalised so that the Y_i maximum is equal to 1. This gives a combined colour map in *CIE* coordinates.

To display the resultant colour map on a computer screen, the *X, Y, Z* data is converted to *R, G, B* using a matrix (Foley *et al.* 1995):

$$\begin{bmatrix} X \\ Y \\ Z \end{bmatrix} = \begin{bmatrix} x_r C_r & x_g C_g & x_b C_b \\ y_r C_r & y_g C_g & y_b C_b \\ (1 - x_r - y_r) C_r & (1 - x_g - y_g) C_g & (1 - x_b - y_b) C_b \end{bmatrix} \begin{bmatrix} R \\ G \\ B \end{bmatrix} \tag{6-4}$$

This matrix requires the white point of a computer monitor, (C_r, C_g, C_b) which was calculated from photometer measurements (Y_r, Y_g, Y_b) of the RGB primaries displayed filling a monitor screen, along with the *CIE* coordinates of the RGB monitor phosphors obtained from the monitor manufacturer (x_r, y_g, z_b):

$$C_r = \frac{Y_r}{y_r} \qquad C_g = \frac{Y_g}{y_g} \qquad C_b = \frac{Y_b}{y_b} \tag{6-5}$$

A calculated RGB component of a colour map pixel occasionally falls outside of the colour gamut of the monitor (refer Figure 6-1(b)), and exceeds 1. If this occurs, the relevant matrix is scaled so that its maximum component is 1. For colour map display, the final values are converted to a log (base 10) scale.

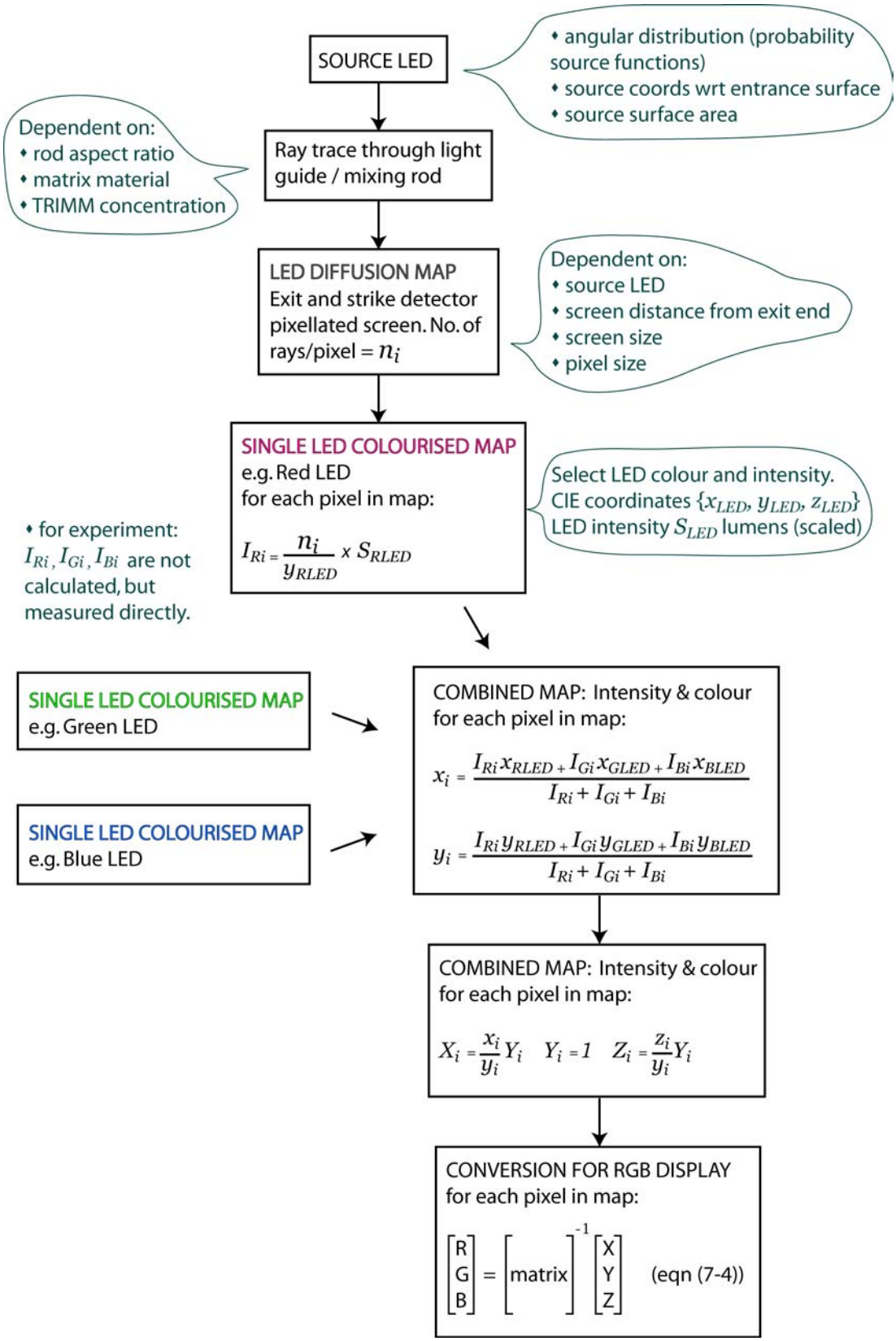

Figure 6-7. Flowchart describing the calculation of colour output from RGB LEDs and a mixing rod.

6.6 Results

6.6.1 TRIMM-doped PMMA rods

6.6.1.1 undoped rod

Coloured patterns are formed due to caustic effects dependent on rod aspect ratio, LED size, LED radial distance from the centre of the rod, and screen distance from the rod's end. Figure 6-8 shows modelled, photographed and measured colour distributions at a distance 10 cm from the exit end of the rod. Notice the excellent qualitative agreement between modelled data (Figure 6-8(a)) and photograph of experiment (Figure 6-8(d)), although some colour in the white, slightly overexposed parts of the photographs may be hidden. It is interesting to note that the visual pattern is strongly dependent on the viewing angle: Figure 6-8(b), (c), (d) and (e) are the same set up photographed from slightly different angles. This considerable colour variation with viewing angle shows that undoped PMMA light guides are not suitable as LED mixers.

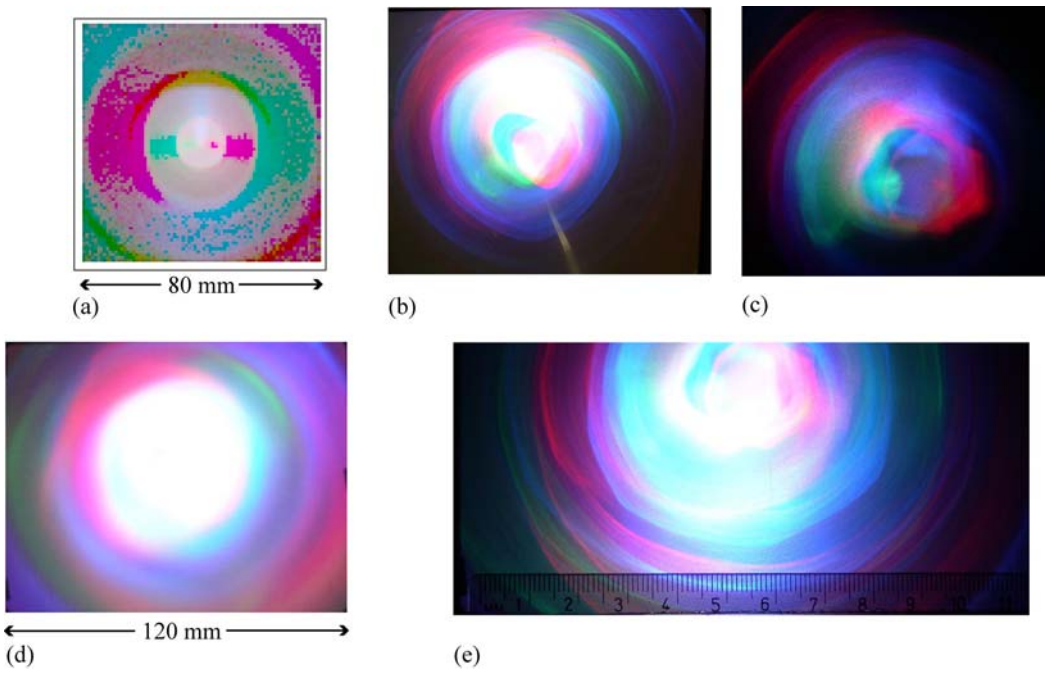

Figure 6-8. a) Modelled output colour mix falling on detector 10 cm from end of 10 cm acrylic rod. Pixel size is 1 mm. Source diameter is 2 mm. b-e) Photographs of experimental results modelled in a), taken at varying viewing angles.

Figure 6-9(a) shows the modelled illuminance of the light falling on a detector 10cm from the end of the undoped PMMA rod. Figure 6-9(b) shows a cross-section through the centre of Figure 6-9(a), showing the individual red green and blue components of the

modelled illuminance. Figure 6-9(c) shows the measured red, green, blue and total illuminance corresponding to Figure 6-9(b).

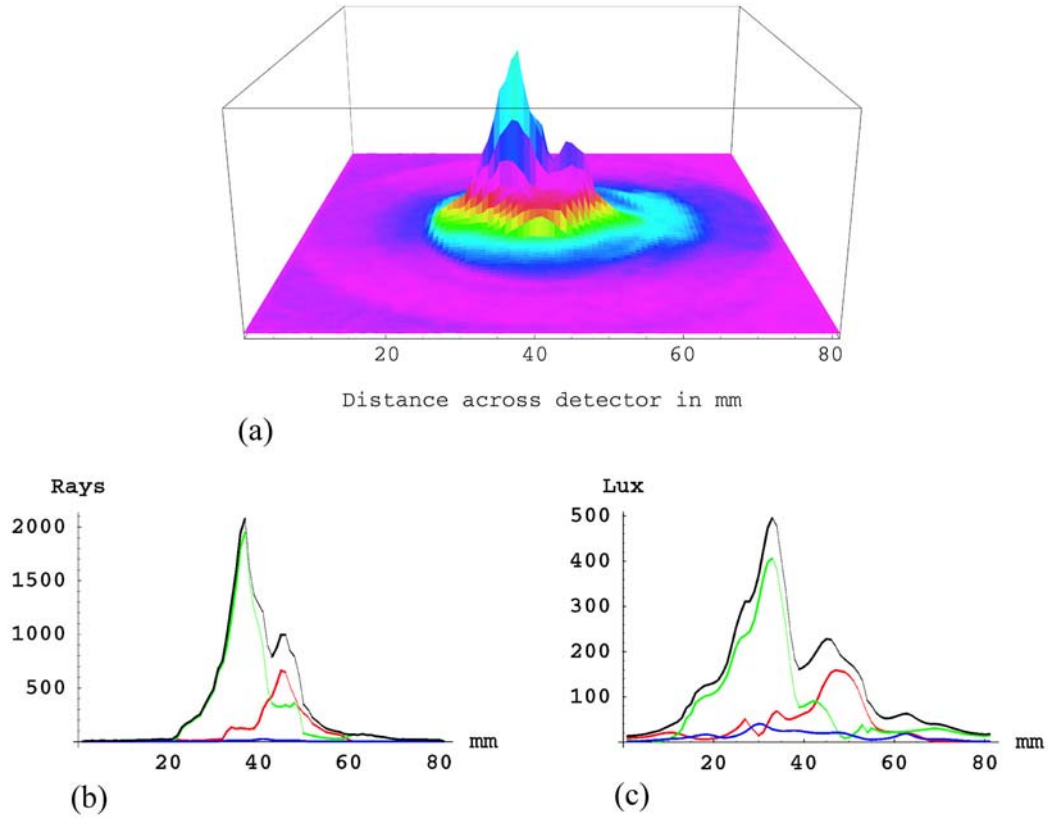

Figure 6-9. a) Modelled illuminance falling on detector 10 cm from end of the undoped 10 cm acrylic mixing rod. Source diameter is 2 mm. b) Cross-section through the centre of a), showing computed R, G and B components, and the total in black. c) Corresponding measured illuminance.

6.6.1.2 Doped rods

Measurements and simulations performed for the 15K 10 cm rod (axial particle number $a = 25$) were made using the same ratio of luminous fluxes as for the undoped rod (R:G:B = 1 : 1.24 : 0.379). It can be seen that the mixing is nearly complete for this configuration, although the relative intensity of the red has been set too high (Figure 6-10).

Figure 6-10. Output colour falling on detector 10 cm from end of 10 cm long 15K rod. Pixel size is 1 mm. a) Measured horizontal strip through the centre, converted to *RGB* colour space. b) modelled strip, using source diameter of 2 mm.

The relative amount of red source light was reduced for the 100K 10 cm rod measurements. Source luminous flux ratios were (R:G:B = 1 : 1.66 : 0.462). The photographed and simulated results are shown in Figure 6-11(a), (b) and (c). For Figure 6-11(a) the camera was positioned about 1 cm from the screen while for Figure 6-11(b) the distance was ~30 cm.

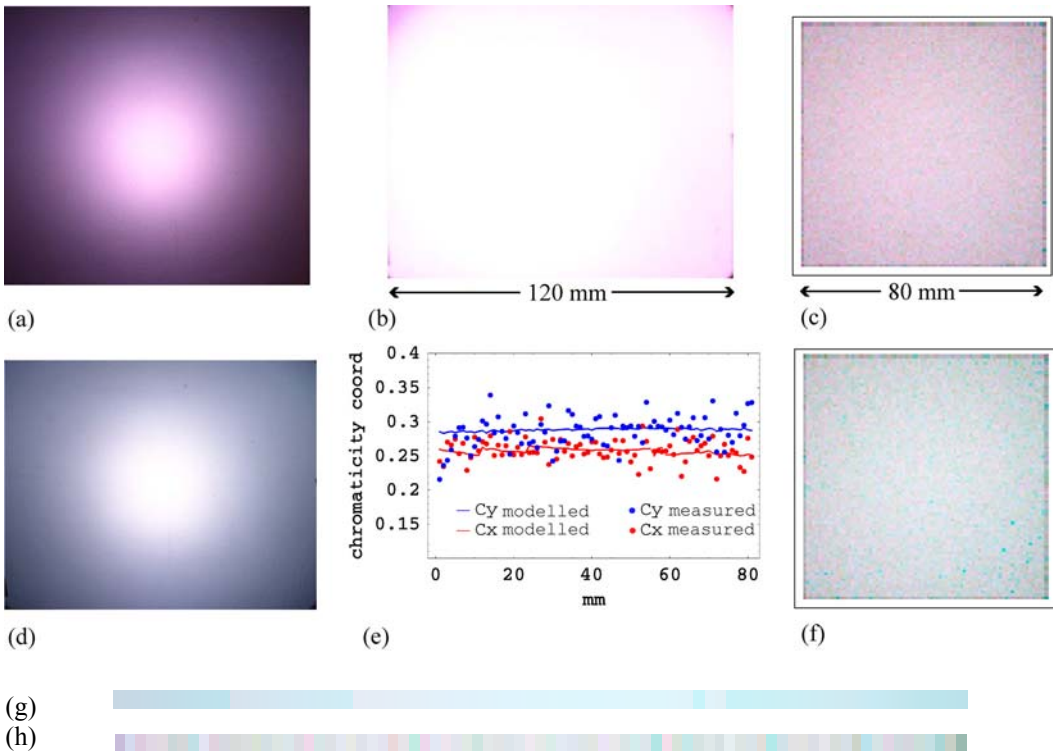

Figure 6-11. Projected light 10 cm from the end of 100K rods. a-c) 10 cm rod length. a, b) photographed results, c) computer simulation. d-h) 8.84 cm rod length. d) photographed results. f) computer simulation. g, h). measured and modelled strips through center cross-section. e) CIE coordinates corresponding to g) and h).

Figure 6-11(d), (f-h) show the output 10 cm from the end of a 8.84 cm 100K rod. Source luminous flux ratios were (R:G:B = 1 : 2.77 : 0.569). Uniform mixing is achieved with a shorter rod for higher TRIMM particle concentration. (a = 133 for the 10 cm 100K rod: a = 117 for the 8.84 cm 100K rod.) The computer simulation shows uniform colour across a 80 cm detector width. Although the measured and modelled appear blue (Figure 6-11(f), (g) and (h)), the actual appearance of the light output is white with a blue halo (Figure 6-11(d)). This is not surprising, as the blue LED source angular profile is the widest (Figure 6-9(b)). The colour variance across the centre of the screen are represented as *CIE* coordinates, and measured and modelled values compared quantitatively, in Figure 6-11(e).

6.6.1.3 Modelled varying screen distance

Simulated colour projected onto screens 1 cm and 100 cm from the output end of the 10 cm mixing rods are shown in Figure 6-12. The source intensities are the same as for Figure 6-11(a-c), so the output is pinkish/white, nevertheless it is clear that very good mixing is achievable. The colour variation across the screen 1 cm from the end is shown quantitatively in the form of *CIE x* and *y* coordinates in Figure 6-13.

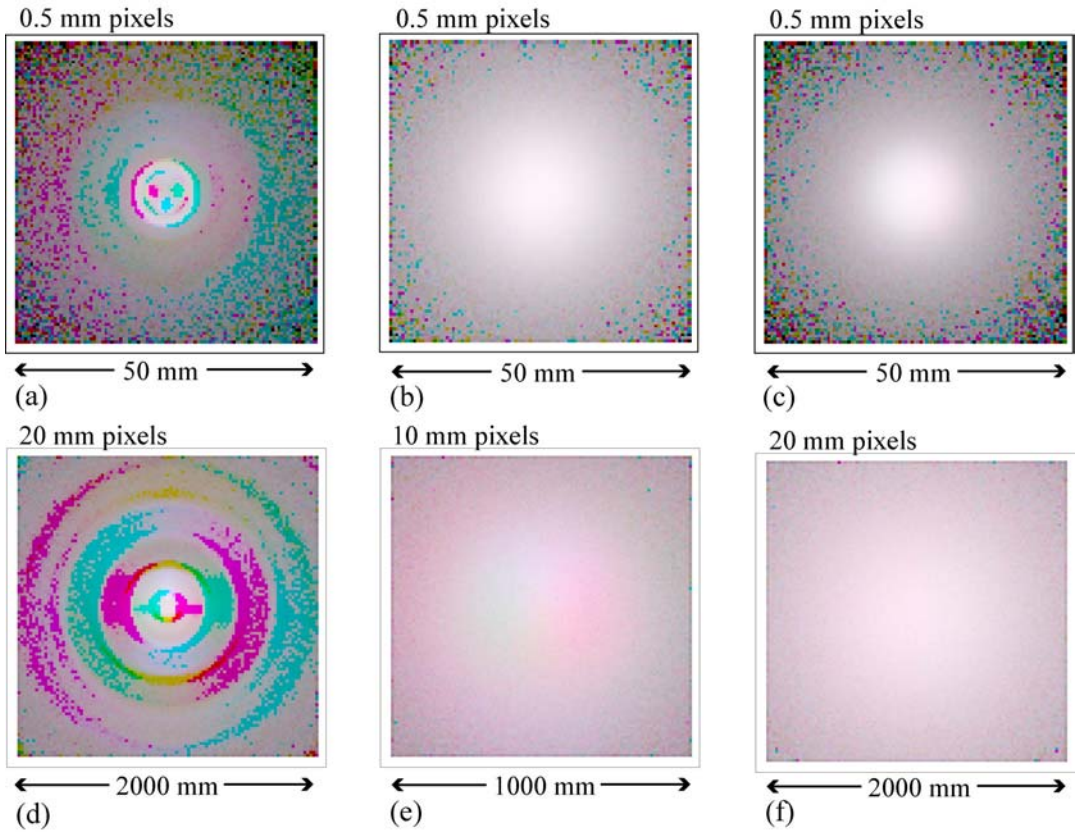

Figure 6-12. Modelled colour distribution for 10 cm mixing rods. a-c) 1 cm from the rod's end. a) PMMA, b) low concentration, c) high concentration TRIMM. d-f) 100 cm from the rod's end. d) PMMA, e) low concentration (15K) TRIMM, f) high concentration (100K) TRIMM.

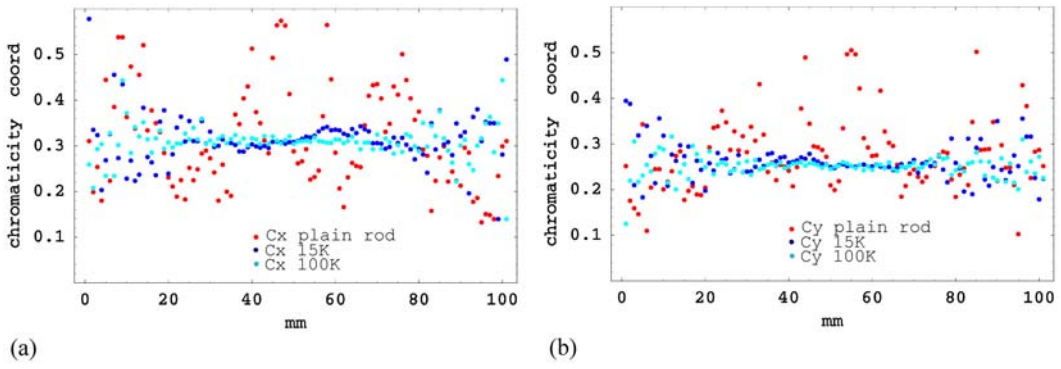

Figure 6-13. Chromaticity coordinates; a) CIE x, b) CIE y for simulations 1 cm from the end of the three 10 cm mixing rods shown in Figure 6-11(a-c)

6.6.2 PMMA rod with TRIMM diffuser sheet

Modelled and photographed results of the output light from the Alpha group LED triad, projected onto a screen 15 cm from the end of the mixing rods, are shown in Figure 6-14 and Figure 6-15. Figure 6-14 shows the colour distribution when using the clear PMMA rod only as the mixer. Figure 6-15 shows the distribution from the rod with TRIMM diffuser sheet.

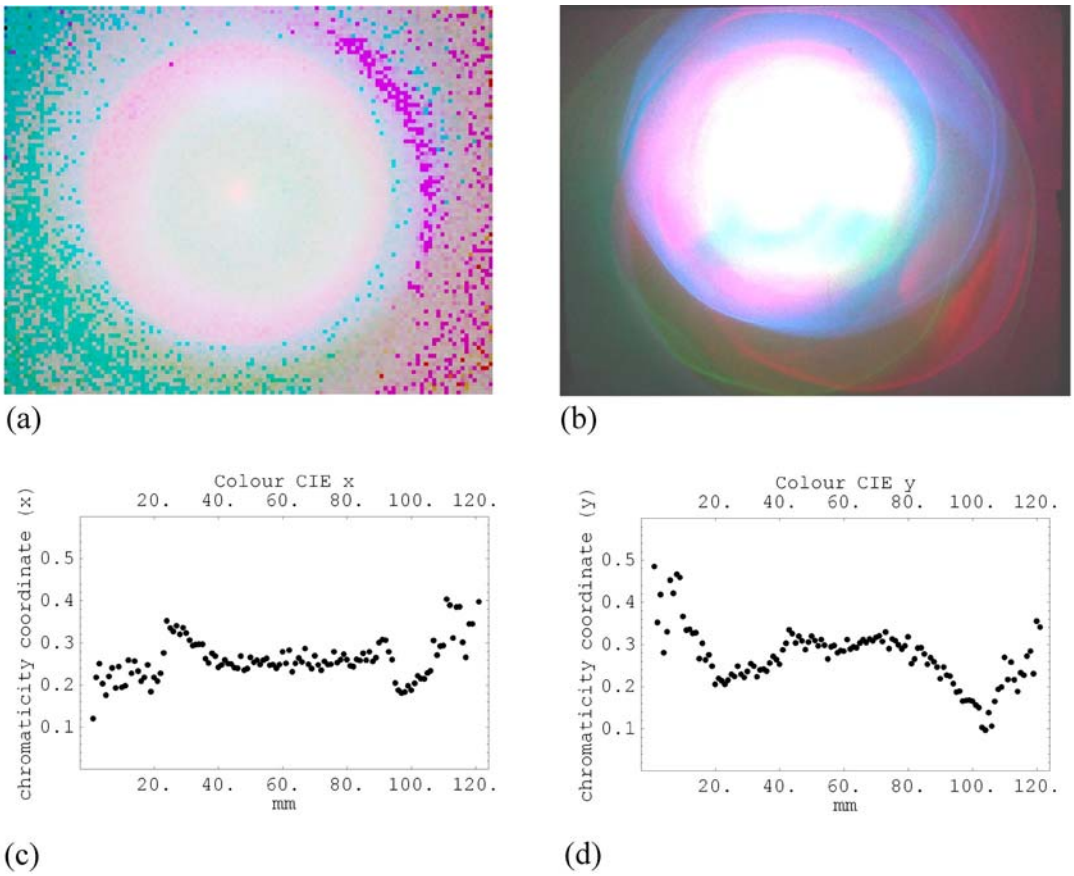

Figure 6-14. a,b) Output colour distribution transmitted through the frosted glass screen 15 cm from the end of the clear PMMA rod. a) modelled. b) photographed. c,d) Modelled *CIE* coordinates of a horizontal strip through the centre of the screen. c) *CIE x* d) *CIE y*

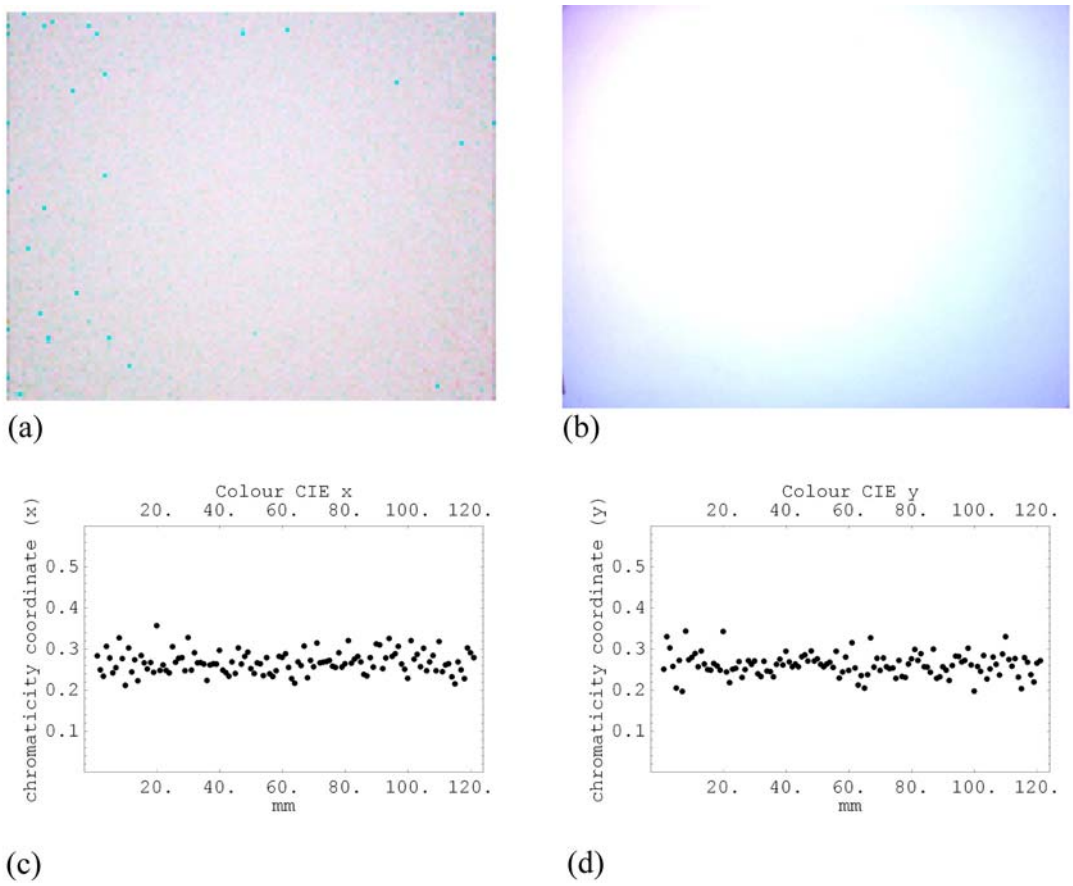

Figure 6-15. a,b) Output colour distribution transmitted through the frosted glass screen 15 cm from the end of the PMMA rod +TRIMM diffuser sheet. a) modelled. b) photographed. c,d) Modelled *CIE* coordinates of a horizontal strip through the centre of the screen. c) *CIE x.* d) *CIE y.*

The photographed and modelled images are both 120 mm x 95.5 mm. Each pixel in the modelled screens represents 1 mm^2. Excellent quantitative agreement between the measured and modelled *CIE x* and *y* coordinates derived from colour output from mixing rods, and from corresponding modelled colour output, was demonstrated in the previous section for the TRIMM-doped rods. *CIE* coordinates from modelled results only are shown for the rods + diffuser sheet.

An artefact of the photographs is the inability to display colour over a large brightness range. The colours on the outer periphery of Figure 6-15(b) actually appear brighter when viewed with the eye. Similarly, the blue halo in Figure 6-14(b), although slightly visible in the experimental system, appears much lighter to the eye. In addition, it was difficult to generate a sufficiently high intensity from the green LED to achieve a desirable colour balance, as is evident in both the modelled and photographed results. It can be seen, how-

ever, that a uniform colour is obtained across the screen, because, as Figure 6-14(c) and Figure 6-14(d) indicate, the *CIE* plots of the rod + diffuser sheet are constant.

6.7 Discussion: colour mixing

The measured and modelled colours of Figure 6-11 appear to differ because of display differences between camera and simulated images. Transformations between *XYZ* and *RGB* spaces include viewing and display conditions, and the CCD chip in the digital camera is not adaptive to colour balance as is the human eye (Orava *et al.* 2004). Measured and modelled output colour are compared using *CIE* coordinates, avoiding artifacts due to factors such as limited camera contrast range. Figure 6-11(e) shows the agreement. Scatter in the modelled data is from statistical fluctuations.

Variation of refractive index with wavelength was not taken into account for this modelling, and is discussed in Section 7.1. Preliminary modelling trials have shown that there is little visual effect on the colour mixing results within the variation of refractive index that is expected. This is because for the 'end-light' configuration used in mixing, almost no light is lost via the side wall.

The modelled results for the TRIMM-doped PMMA rods indicate that transmittance including Fresnel end loss is ~ 0.93, therefore nearly all the loss is due to Fresnel reflectance. The extruded samples used here gave lower transmittance as they contain small air bubbles. Larger diameter or longer rods make mixing easier, but TRIMM doped systems allow a much wider variety of geometrical configurations than for undoped rods.

7 Variables affecting uniform colour mixing

This chapter analyses factors which impact on the distribution of end-light from TRIMM mixing rods, particularly when combining the light from red, green and blue LEDs. Section 7.1 illustrates the effect of varying μ with wavelength on the visual colour output. Section 7.2 shows the impact of using individual measured profiles as LED source models, compared to adopting a common smoothed empirical source. Geometrical effects, as influenced by both the rods and source distributions, are discussed in Section 7.3. A statistical method aiding speed of optimisation of colour mixing is given in Section 7.4. A comparison of round and square mixing rods is presented in Section 7.5, and an example of a TRIMM mixer for multiple LEDs is given in Section 7.6. This includes analysis of optimisation of the configuration for best mixing.

7.1 Effect of varying μ with wavelength on colour mixing

In Section 3.4.2 it was noted that μ is not constant with wavelength, and hence the propagation paths of rays with differing wavelengths may vary in TRIMM-doped rods. The effect of using varying values of μ for each of the RGB LEDs was tested by computer ray tracing and colour mixing output simulations.

The simulations were performed using the 3 mm LED triad configuration shown in Figure 6-5(a), the empirical source model outlined in Section 6.4.1, and the 15K 10 cm TRIMM-doped rod with p = 4mm and a = 25. For the purposes of this investigation, a value of a was selected such that the light mixing is not quite complete, to facilitate the qualitative comparison between the output of TRIMM systems with μ constant and μ varied. A single wavelength was selected for each source LED as given in Table 6-1: 630 nm for red, 518 nm for green, and 465 nm for blue. The μ values corresponding to these wavelengths were read from the μ vs λ graph of TRIMM in PMMA given in Figure 3-7(c).

The luminous flux ratios R:G:B = 1 : 2.21 : 0.515 were selected for the source LEDs in the simulations. This is midway between the two ratios used in experiment (refer

Section 6.6.1.2, Figure 6-11(a) and Figure 6-11(d)) and was chosen to obtain a good colour balance. Table 7-1 shows the refractive index values of the TRIMM and matrix selected for each corresponding LED colour, along with the corresponding μ values. For the constant μ simulations, the refractive index of the matrix was set at 1.49, and the refractive index of TRIMM at 1.507, for each of the LEDs. These values are the same as those adopted for the colour mixing simulations presented in Chapter 6.

Table 7-1. Values of matrix and TRIMM refractive index adopted for the 3 mm RGB LEDs, for constant and varied μ

	LED	*matrix RI*	*TRIMM RI*	μ
Constant μ	R,G,B	1.49	1.507	0.01141
Varied μ	R	1.489	1.505	0.01075
	G	1.493	1.513	0.01340
	B	1.496	1.520	0.01604

Figure 7-1 shows the simulated colour output at the exit end of the rod, and projected onto screens 1 cm, 10 cm and 100 cm from the rod end, for constant μ vs λ (μ = 0.114 for each of the red, green and blue LEDs). Figure 7-2 shows the corresponding outputs for μ that is varied with LED peak wavelength, according to Table 7-1.

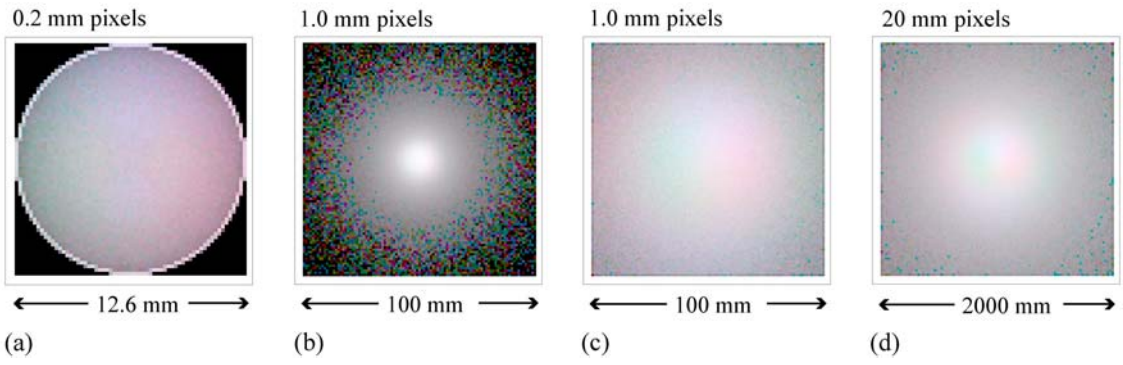

Figure 7-1. Simulated colour output for μ **constant with LED wavelength**. a) at the exit surface (0 cm from the end of a 10 cm 15K TRIMM-doped rod). b) 1 cm from the rod's end. c) 10 cm from the rod's end. d) 100 cm from the rod's end.

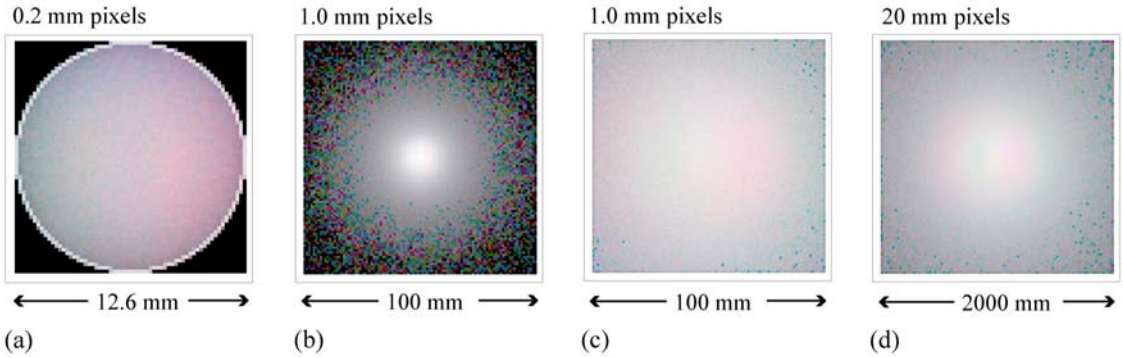

Figure 7-2. Simulated colour output for μ **varied with LED wavelength**. a) at the exit surface (0 cm from the end of a 10 cm 15K TRIMM-doped rod). b) 1 cm from the rod's end. c) 10 cm from the rod's end. d) 100 cm from the rod's end.

It can be seen by comparison of Figure 7-1 and Figure 7-2 that the total angular spread is higher for the blue coloured rays. This is particularly evident for the far field projection (1 metre from the rod's end: Figure 7-2(d)). It should be noted, however, that this screen size is 2 metres square, and that the blue halo is obvious only on the periphery. It is more difficult to obtain homogenous output as the angle from the mixing rod axis increases. Manufacturers of commercial diffusers do not deny this problem: "Of course, the insertion of a simple diffuser cannot correct for the color banding observed outside of the mixed white region, caused by the spatial separation of the sources" (Sales *et al.* 2004). In the example shown in this section, the colour mixing is not quite complete, and yet the effect of varying μ for the different LED wavelengths has low visual impact. For slightly higher TRIMM concentration and more complete mixing, differences in output colour distribution due to wavelength dependence are negligible for this type of application. Hence, most simulations were carried out using a common μ value for each LED.

7.2 Colour mixing modelling: smoothed vs measured LED profiles

7.2.1 Introduction

In this section, the effect of using an empirical, common smooth model for each RGB source in a colour mixing simulation, is compared with that of using individual measurement-based LED source models.

As mentioned in Section 5.4, the modelled empirical angular profile decreases smoothly with cone angle. A problem with using a smooth LED profile is that LED patterns frequently have distinct bright spots at particular cone angles. These are evident in the profiles shown in Figure 5-6. The individual beam pattern is greatly influenced by the shape

of the lens as light is directed outwards from the semiconductor chip (Decker 2000). When diffusing elements are not present in the light mixing system, this effect is amplified, so when light from LEDs with different emission profiles is combined using a clear light guide, caustic ring-shaped patterns are formed. This was seen in the results in the previous chapter (Figure 6-8). If a single measured source profile is used to simulate the combination of light from several LEDs, the simulated output will almost certainly not show as many caustic ring patterns as are present in the physical system. It appears that bright spots in the angular profile have a significant effect on the projected light distribution, so using a smooth empirical model has limited accuracy.

7.2.2 Colour mixing of LEDs: comparison of empirical and measurement-based source distributions

These simulated light output patterns have been performed using Monte Carlo ray tracing through the 6 cm long, 25.55 mm diameter clear PMMA light guide of Section 6.3.2. Two sets of Monte Carlo ray tracing illumination results were compared. Simulation 1 uses an identical, smooth empirical source model for each of the 3 LEDs. Simulation 2 uses individual measured profiles of the 'Alpha' LED triad, taking into account differences in the beam patterns between the LEDs. (Simulation 2 results appeared in Figure 6-14, and are reproduced here for comparison.) Both sets of simulated ray tracing results were compared with a photograph of the experimental light output.

7.2.3 Results

The modelled colour maps of LED output from a clear, undoped mixing light guide are shown in Figure 7-3(a) and Figure 7-3(b). Simulation 1 results, using only the empirical LED source model, show 3 bands of cyan, magenta and yellow each taking up about one-third of a circle around a fairly uniform whitish disc in the centre (Figure 7-3(a)). This ring pattern is rotationally symmetric, because the LEDs are distributed in a triangle about the light guide axis, as was shown in Figure 6-5(b), and each has the same modelled source distribution. Simulation 2 results, which are based on individual measured source profiles, show distinct complete rings of individual colours, particularly pink and blue around a smaller central disc (Figure 7-3(b)). These rings are also visible in the photographed result (Figure 7-3(c)).

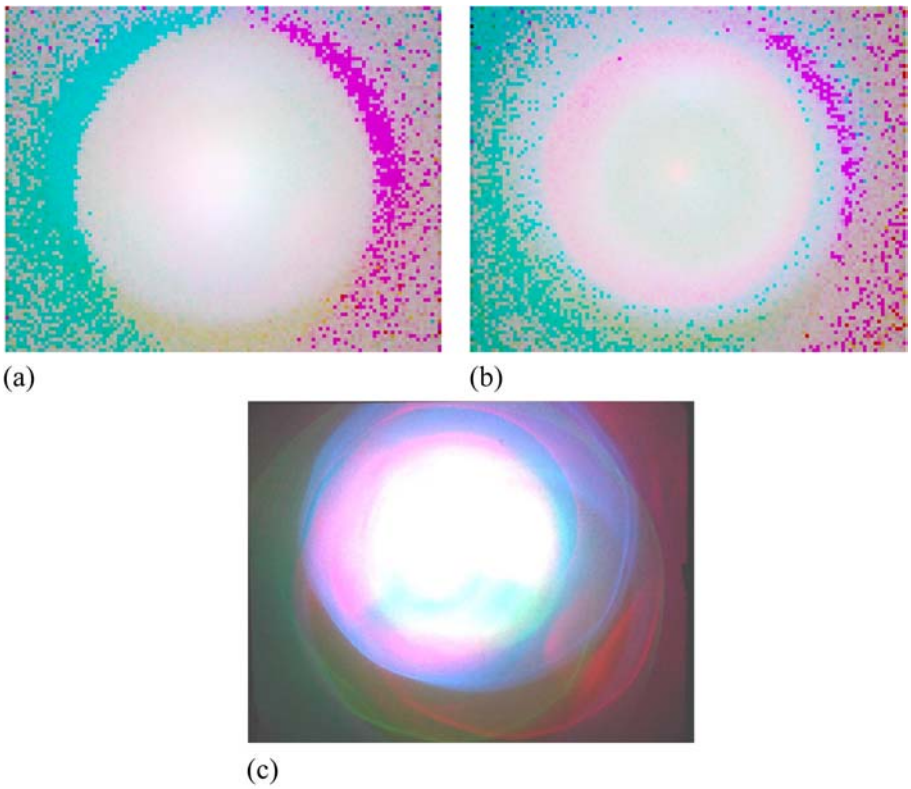

Figure 7-3. Light output from polymer mixing rod. a) Simulation 1, using a common empirically modelled LED source. b) Simulation 2, using individual measurement-based LED sources. c) Photographed experimental result. (Screen widths are 120 mm.)

7.2.4 Discussion

It was stated in Section 5.4 that the measured LED beam patterns are not rotationally symmetrical. In contrast, the modelled LED sources are rotationally symmetrical, because the azimuth angle is randomly selected for each ray launch. Ideally, one would have a measurement-based representation for each source that takes azimuth variations into account, as (Guo *et al.* 2003) did using Radiant Imaging software (Radiant Imaging inc 2004). The crucial aspect, however, is the sharp variations of intensity with cone angle. Creating a rotationally symmetrical modelled source by averaging the higher intensity sections of the individual profiles in the azimuth direction, and disregarding the elongation along the axis containing the electrode pins, does not have a large effect on the visual accuracy of the output pattern. This is evident when comparing Figures 7-3(b) and (c). Assuming a distribution decreasing smoothly with cone angle for each LED, creates a higher level of visual discrepancy, as can be seen by comparing Figures 7-3(a) and (c).

It is also worth noting that when sufficient TRIMM particles are incorporated into a mixing rod, then individual differences in the source LED beam patterns are not critical.

The TRIMM particles tend to homogenise the light, and the caustics are smoothed out. Suitable diffusers can reduce or eliminate these problems associated with mixing LEDs, but it is undesirable to add an excess amount of diffuser into a mixing system. Excessive scattering and lowering of light throughput would result. One purpose of performing simulations is to estimate the threshold amount of scatterers needed for adequate mixing. The effectiveness of a certain concentration of diffuser cannot be assessed if source characteristics are not incorporated into the simulation in sufficient detail. *If the source profiles are too smooth to start with, an insufficient amount of diffuser will be estimated, and light output will not be homogenised.*

In Figure 5-8 and Figure 5-9, the empirical $P(\theta)$ model is plotted along with the individual RGB LED $P(\theta)$ functions. At first glance, it appears that the empirical model fits reasonably closely with the Alpha group's measured profiles (Figure 5-8), particularly when compared with the Beta Group (Figure 5-9). One might assume that a common empirical LED source model would be sufficiently accurate for lighting simulation purposes. Upon closer inspection of Figure 5-8, it is evident that the empirical model does not fit the 0-15° angular range closely. This is because the empirical model follows a smooth curve, shaped similar to a Guassian, and does not account for the bright rings in the intensity profiles of the alpha LEDs at a semi-cone angle of approximately 12° (compare the alpha group profiles with those of the Beta group, in Figure 5-4). As has been mentioned, use of the empirical source model causes significant error in the visual colour distribution of the output light. This is because the angles near normal incidence are crucial to the mixing output in this case. (Wider-angle rays are coupled into the light guide, but they also exit at wide angles. They may miss the target screen, or strike it near the edges.)

7.3 Geometrical effects: source distribution and size, and rod aspect ratio

It has been shown that when light is combined from LEDs with different emission profiles using a non-diffusing light guide mixer, caustic ring-shaped patterns result. This is partly due to the relationship between the aspect ratio of the mixing rod and the angles at which the peaks in light intensity occur. This was tested by Monte Carlo ray tracing using a source model of uniform intensity distribution which cuts off sharply at angle θ_{max} (a 'flat-top' source model). If θ_{max} and the light guide aspect ratio are chosen such that, for each ray, a single reflection occurs inside the light guide at approximately half way along the rod, then an intensity 'spike' would be expected at the output surface. The output light falling on modelled screens positioned at various distances from the output end of the rod

would be expected to form bright ring patterns, dependent upon the screen positions and the cone angle of the output light. Another reason for performing test simulations with a 'flat-top' source model with undoped mixing rods was to confirm that the observed intensity spikes are geometrically based, and not an artifact of programming errors.

7.3.1 Angle of incidence and rod aspect ratio

The 'flat-top' model is described as a light source distribution with constant illuminance upon the light guide surface, from normal incidence ($\theta = 0°$) to a certain angle θ_{max}, after which the illuminance abruptly drops to zero.

To generate such a source model for the ray tracing program, the same method was employed as for the LED source models, described in Section 5.3.2. $I(\theta)$ is set to 1 for $0 > \theta \geq \theta_{max}$, and to 0 for $\theta_{max} > \theta$. $I(\theta) \sin\theta \partial\theta$ is computed, and a curve fitted to the cumulative probability density. A test simulation was performed using θ_{max} of 16.85° relative to the light guide axis in air, which is 11.3° upon refraction into POF material. Rays incident at θ_{max} will intercept, and reflect from, the guide wall half way along a guide 10 cm in length with a 2 cm diameter. The cumulative probability density function is $P(\theta) = 11.888 \sin\theta^2$ (θ in radians). As expected, a spike in intensity occurs at the centre of the exit surface of the guide as evidenced by Figure 7-4.

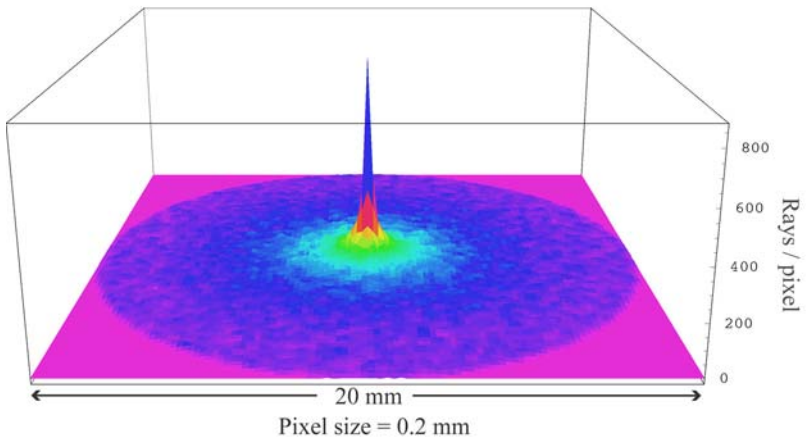

Figure 7-4. Illuminance (rays per pixel) modelled at the exit end of an undoped light guide 10 cm in length and 2 cm in diameter. A 'flat-top' source model with θ_{max} set to launch rays that reflect half way along the light guide was used. A spike results in the output intensity. 100,000 initial rays were launched from a point source located at the centre of the guide input end.

7.3.2 LED model: geometrical effects from aspect ratio, and source size effects

A similar case using the smoothed empirical LED source model of Figure 5-7 will now be considered. Rays launched from a point source, located off-centre with respect to the

axis of the same 10 cm x 2 cm POF guide as for the previous example, forms an asymmetrical illuminance pattern at the exit surface of the guide (Figure 7-5). The location of the source relative to the guide end surface is shown as the red cross in Figure 7-10(e). Mixing several LEDs of different colours using a similar undoped light guide results in visually striking coloured patterns due to the lack of uniformity of the output light distributions from the individual sources.

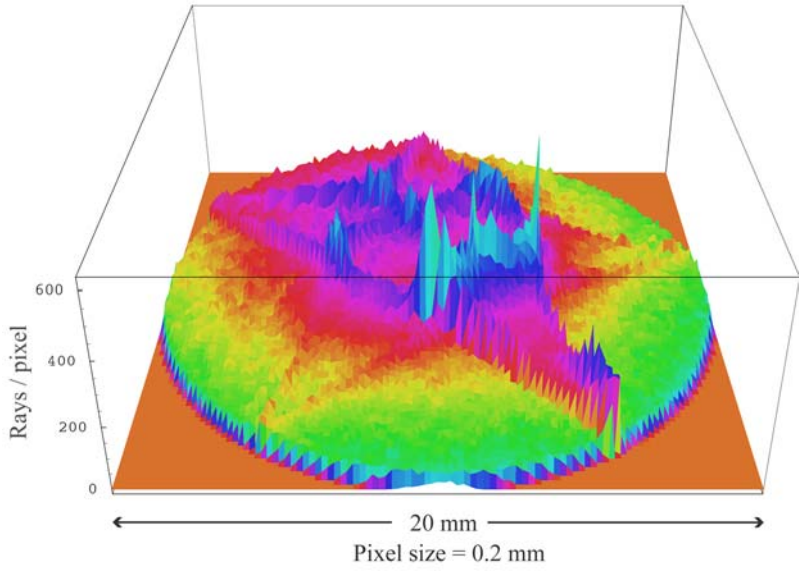

Figure 7-5. Illuminance in rays per pixel (LED diffusion map) modelled at the exit end of an undoped POF light guide 10 cm in length and 2 cm in diameter, using the LED smoothed empirical source model (Figure 5-7) from a point source off centre with respect to the guide axis. 1 million initial rays were launched.

Another important geometrical consideration is the relationship between the angular distribution of the transmitted end-rays and the location of the detector plane. There can be marked variation in illuminance distributions over the 'LED diffusion maps' as the distance of the target surface from the rod end is increased. This is clearly illustrated in Figure 7-6(a), which shows the same angular distribution of end-light as for Figure 7-5, but striking a modelled 'screen' located 10 cm from the end of the light guide.

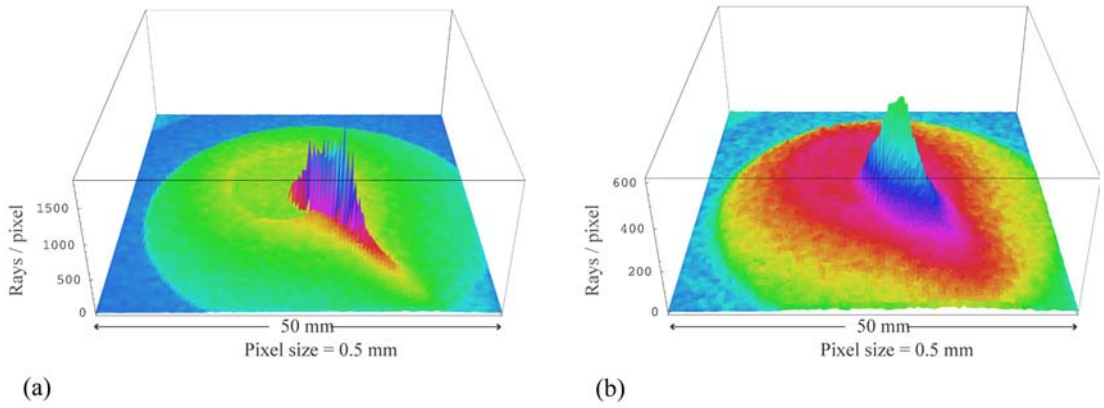

Figure 7-6. LED diffusion maps modelled 10 cm from the exit end of an undoped POF light guide 10 cm in length and 2 cm in diameter, using the LED smoothed empirical source model. 1 million initial rays were launched. a) point source b) 3 mm diameter source.

Another factor fundamental to the simulated output light patterns is the area over which the source rays are launched. Figure 7-6(a) is the LED diffusion map, located 10 cm from the guide end, that results when all of the source rays originate from a single point. Figure 7-6(b) shows the result when the source rays originate from points that are randomly distributed over a circular area, 3 mm in diameter. The asymmetrical pattern remains, but the maximum intensity is much lower and the sharpness of the intensity maximum is smoothed out. This is important for two reasons:

1. accuracy of LED source models is dependent on the area over which the source distribution originates, and
2. varying the physical size of the light source coupled into light guides will affect the end lighting result (for example, swapping a 5 mm LED for a 3 mm LED).

7.3.3 Effect of modelled source size on colour maps

The effect of changing the size of the modelled sources on the final combined colour map is illustrated in Figure 7-7. The coloured strip labelled (a) shows the measured output colour falling on a detector 10 cm from the output end of an undoped PMMA rod. The strips labelled (b), (c) and (d) show the corresponding modelled output, using source sizes of 1, 2 and 3 mm in diameter respectively. (See Section 6.6.1.1 for experimental and simulation details.) There is some discrepancy between the measured results and the simulated results, regardless of the modelled source size, due to the use of the smoothed empirical LED source model for each of the red, green and blue LED ray tracing simulations, instead of individual source profiles.

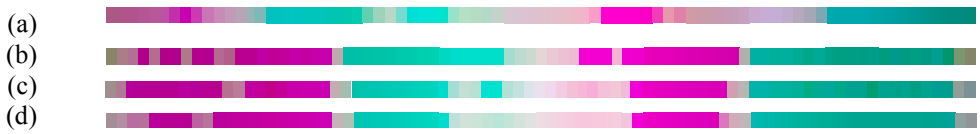

Figure 7-7. a) Measured colours in a horizontal strip through the centre of screen 10 cm from the end of the TRIMM-doped rod shown in Figure 6-8, which has been converted to RGB via calculations. b-d) modelled strip, using source diameters of 1, 2 and 3 mm, respectively.

Variations in modelled output with size of the modelled source are evident in Figure 7-7(b), (c) and (d). This is significant because although the angular distribution is known, it is difficult to determine exactly over what area the light originates. Sensitivity to slight variations in source distribution is amplified by the small diameter of these PMMA rods.

7.4 Rotational symmetry and statistical analysis of end-light distribution

The caustics that are often formed when light mixing is performed using clear undoped PMMA rods can be removed by adding a TRIMM diffuser to the end of a clear rod, or having TRIMM dispersed within the mixing rod. There may be cases where it is desirable to keep the TRIMM concentration low to avoid side loss, for instance, if the TRIMM/ matrix combination gives a larger μ value, thus making δ_m larger (eqn 2-9). High angular spread of the source distribution can be another reason for keeping the TRIMM particle concentration as low as possible. In such cases, it is desirable to select geometries which minimise caustics, hence lower concentrations of TRIMM are needed. The chief geometrical factors affecting the degree of caustics formation in a clear rod, apart from the source distribution, are:

1. rod length to diameter aspect ratio, and
2. the 'source radial fraction' (SRF): the relative radial source distance of the LEDs from the rod axis (illustrated in Figure 7-8(a)).

Computer modelling is useful for optimising these factors to minimise caustics formed purely due to system geometry, and for determining the optimal TRIMM concentration needed to homogenize the light output. It is desirable to minimise the long simulation times necessary to generate the several high resolution LED diffusion maps required to combine into a complete colour map. A statistical method was devised to analyse the output of a single map for elements of rotational symmetry. If the modelled mixing rod

output intensity from a single LED diffusion map is not rotationally symmetric, as in the case of Figure 7-5, then the final colour mixing will be uneven. This type of analysis aids in system design, as aspect ratio and source radial fraction can be optimised to give uniform light distribution for a given μ and TRIMM concentration. An advantage is that for this analysis, fewer rays need to be traced to obtain an adequate estimate of output light homogeneity, obviously shortening computer simulation times.

Figure 7-8(b) shows the concept of arranging the pixels of an LED diffusion map into 'bins' of equal radial intervals from the centre of the simulated screen. The average number of rays per pixel, and the standard deviation, is calculated for each 'radial bin'. This data, plotted against the radial distance from the centre of the 'screen', is a good measure of the rotational symmetry of the light output.

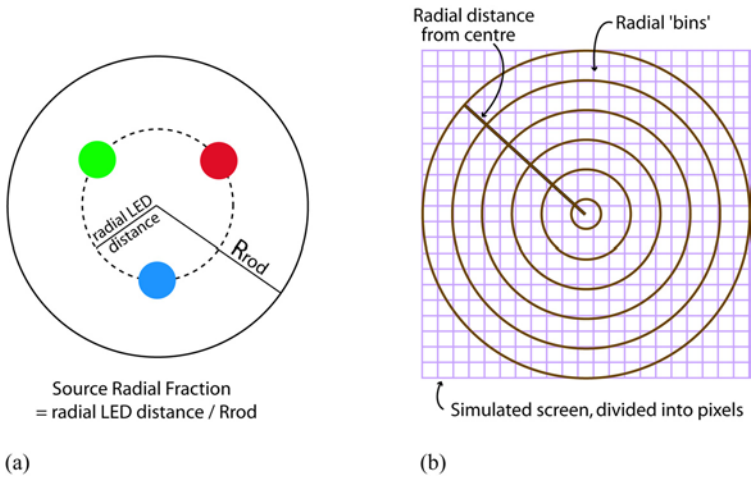

Figure 7-8. a) Schematic showing entrance end of mixing rod, with relative positions of the LEDs to the rod axis (centre) and rod radius. b) Pixels in a simulated 'screen' are sorted into radial 'bins' for analysis of rotational symmetry of output light distribution**.**

7.4.1 Rotational symmetry results for PMMA rod + diffuser sheet

As an example, consider a single LED diffusion map resulting from rays that have been traced through the 6 cm undoped PMMA rod described in Section 6.3.2. The screen was modelled at 15 cm away from the end of the clear rod for the Alpha red LED. The average number of rays per pixel for each radial 'bin' is plotted against the radial distance from the centre of a modelled screen in Figure 7-9(a). If 3 matrices of different colour are to be 'mixed', there must be no sudden 'spikes' or variations in the intensity of the individual LED outputs with screen radius, for uniform colour mixing to be obtained. Figure 7-9(b) shows the standard deviation divided by the average rays per pixel for the same data as

Figure 7-9(a). The 'expected' values are those expected purely due to statistical fluctuations within the data due to the finite number of rays traced. It is evident that the light distribution is not uniform across the screen, and that if colour mixing were attempted with distributions such as these, caustics would be formed. This is supported by the final calculated colour distribution results for the Alpha LED triad, shown in Figure 6-14. Figure 7-9(c) and Figure 7-9(d) show the analysis of the same system modelled through the rod with TRIMM diffuser sheet. It can be seen that the light distribution has been smoothed, and caustics will not result in this case. This is confirmed by the calculated combined colour distribution of the RGB Alpha triad after transmission through the PMMA rod + TRIMM diffuser sheet, as shown in Figure 6-15.

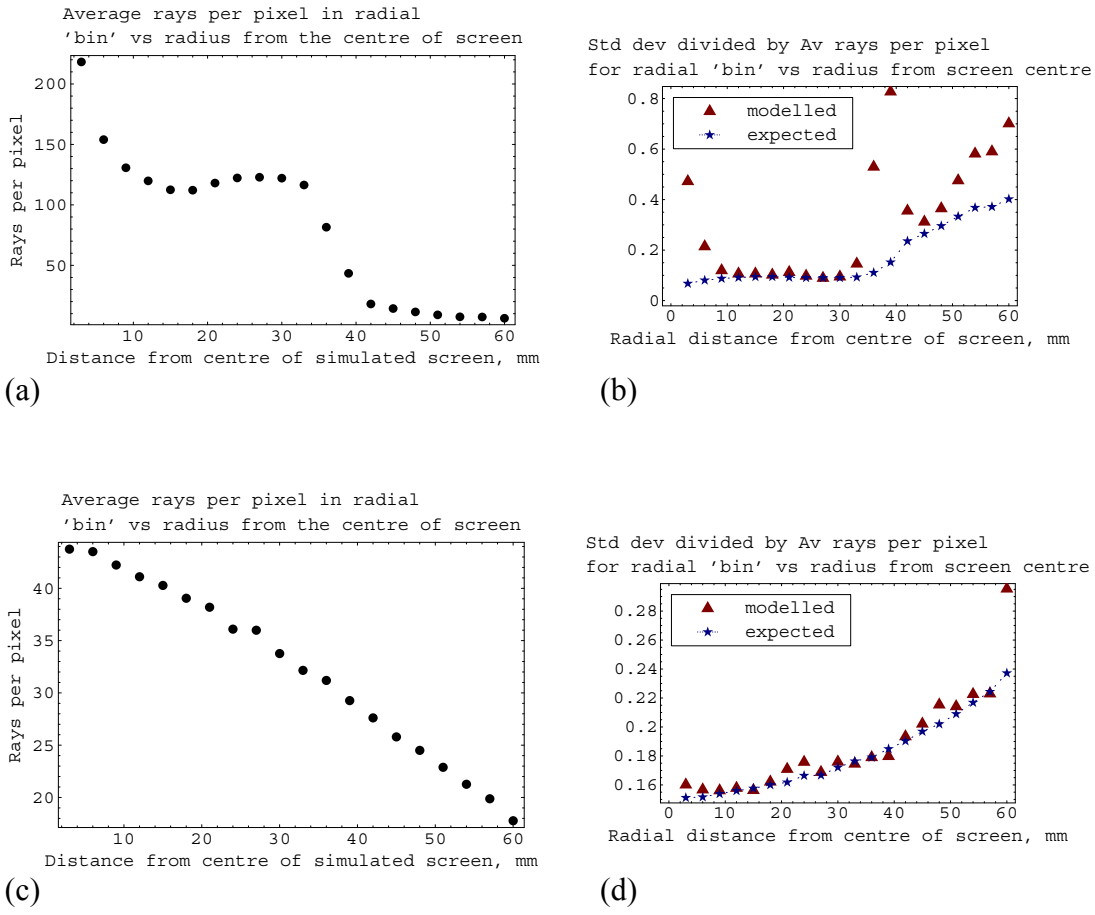

Figure 7-9. a,b) analysis of simulated ray tracing data projected onto a screen 15 cm from the end of the 6 cm clear PMMA rod, with Alpha Red LED as the source. a) Average rays per pixel in a 'radial bin' vs radial distance from the centre of the screen (see Figure 7-9(b)). b) std deviation/average rays per pixel in a 'radial bin' vs radial distance from screen centre. c,d) similar analysis for PMMA rod with TRIMM diffuser sheet. Outlying point in modelled data is due to the very small number of rays hitting screen edge.

Similar analyses of different modelled data have shown that to obtain uniform colour mixing of 3 RGB LEDs, it is important to position the LEDs so each has a similar source

radial fraction (SRF) relative to the rod entrance end, as shown in Figure 7-8(a). It is not necessary to have the LEDs evenly spaced to get good mixing, as long as they lie on a circle of the same radius from the centre of the rod. It has also been found that different source radial fractions produce optimum results for different rod aspect ratios.

7.5 Comparison: square and round mixers

A comparison was made between the mixing performance of TRIMM-doped guides of circular and square cross-section, using two RGB triad sources of different SRF. The modelled 'square' guides are 2 cm x 2 cm in cross-section, and 10 cm long. The cylindrical guides are 2 cm in diameter and 10 cm long. For both guides, the average path length between spheres is p = 2 mm, and the matrix material is unclad POF, so μ = 0.0182.

For each simulation, 1 million rays were traced for each of the RGB sources to predefined 'screens', and the resultant LED diffusion maps combined as described in Section 6.5. Two source configurations were investigated:

1. 'Inner' configuration, with a SRF of 0.36 for the red source and 0.32 for the green and blue[1],
2. 'Outer' configuration, with a SRF of 0.86 for each of the RGB sources.

(Strictly speaking SRF only applies to guides of circular cross-section, although in this example the side length of the square cross-section is equal to the diameter of the circular cross-section, and the configuration of the source triads are the same for both shapes).

These comparisons were performed early during the research project, before all of the final features had been incorporated into the computer programs. The sources are profiles of uniform luminance across a θ cone range of 0-5°, originating from a point. Fresnel reflection had not yet been incorporated, so internal wall and end reflections are a result of TIR only. Rays exiting via the guide walls are recorded in a forward direction only. Experience has shown, however, that these factors do not noticeably affect the projected end-light distributions.

Figure 7-10 shows the results for the Inner configuration, at a distance of 1 cm and 1 metre from the end of the light guide. Figure 7-11 shows corresponding results for the Outer configuration.

1. There is a slight difference in the SRF values of the red, compared to the green and blue, for the Inner configuration. This occurred because cartesian coordinates were used, and precise radii calculated later.

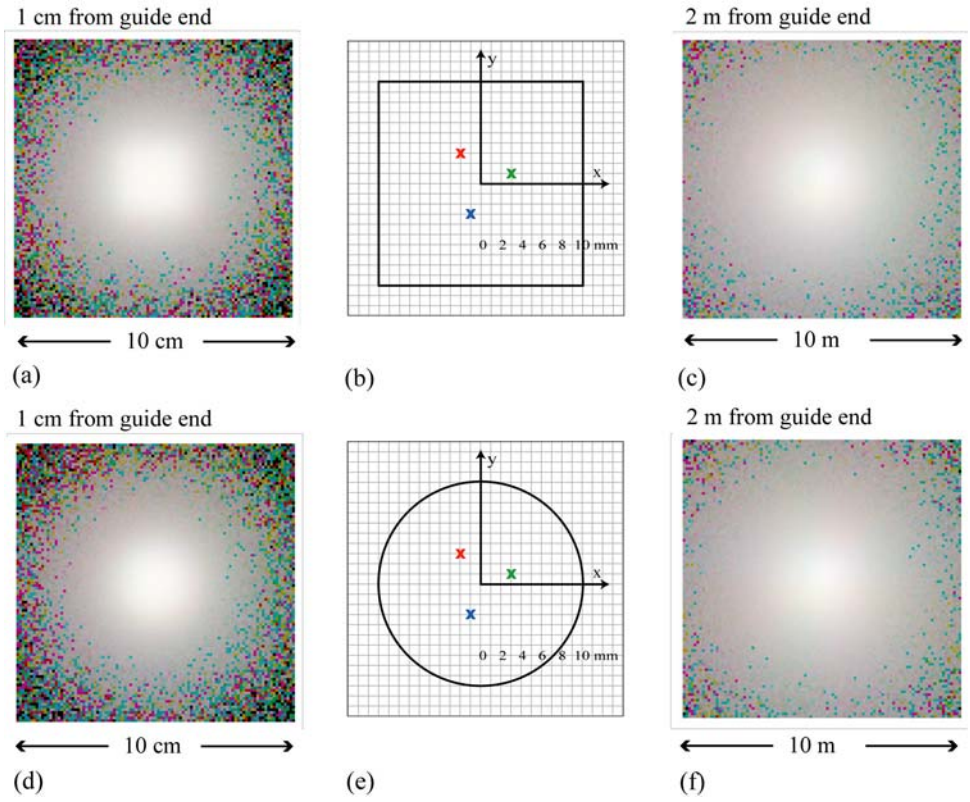

Figure 7-10. RGB source inner configuration. a-c) square. d-f) round SRF: 0.32, 0.36

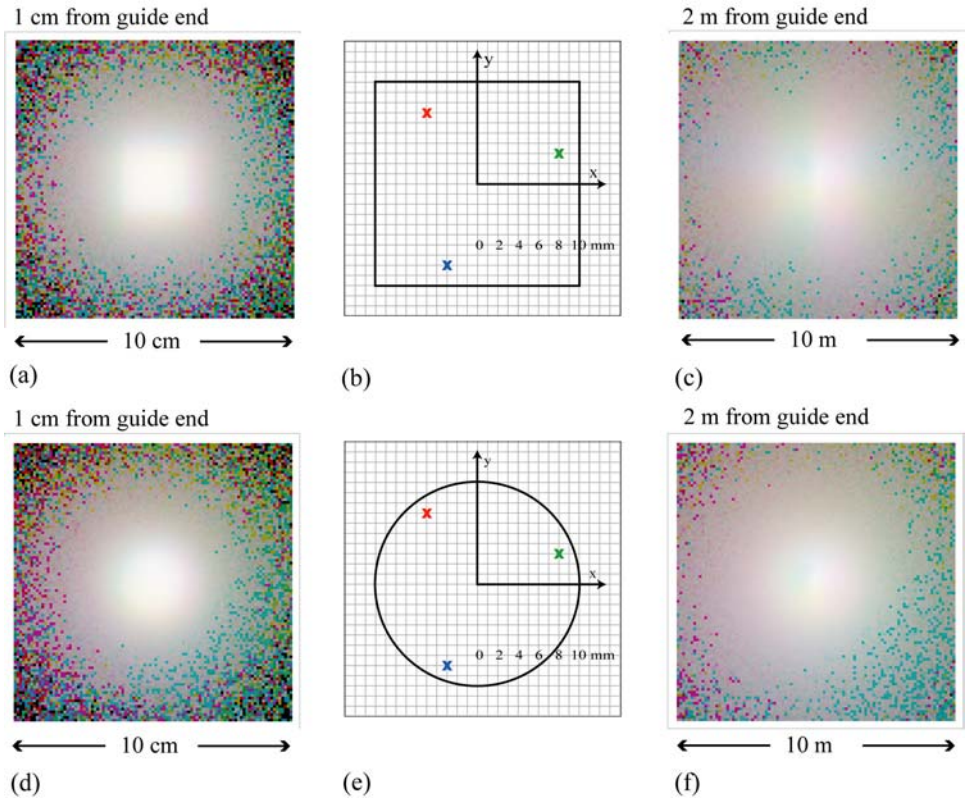

Figure 7-11. RGB source outer configuration. a-c) square. d-f) round. SRF: 0.85

7.5.1 Discussion

7.5.1.1 High SRF vs low SRF

It is clearly evident from comparing Figure 7-10 and Figure 7-11 that when the RGB sources are placed near the periphery of the source end of a light guide, i.e. the SRF is high, that the visual homogeneity is inferior to when the SRF is below ≈ 0.5. (The colour mixing systems presented in Chapter 6 have SRF = 0.4 for the 3 mm LEDs with TRIMM-doped PMMA rods, and SRF = 0.24 for the 5 mm LEDs with PMMA rod with TRIMM diffuser sheet.)

7.5.1.2 Circular vs square cross-section

It can be seen from comparing Figure 7-11(c) and Figure 7-11(f) that for the square guide, inhomogeneities in colour appear to the eye as 'bands' radiating from the centre. These appear in many simulations involving square light guides. They are more visually distracting than the patterns from circular guides, which are generally peripheral. Comparing Figure 7-11(a) and Figure 7-11(d), it can be seen that for large SRF, the output distributions projected onto a screen close to the exit end of the guide will show the cross-sectional shape of the guide.

For small SRF (Figure 7-10), it is noted that for an output target close to the guide end, the circular guide gives more directional light than the square. The reverse is true for a distant target, i.e. the circular guide gives an even, diffuse illuminance over a wide area, whereas the square guide is more directional.

7.6 LED array

RGB mixing of LEDs using TRIMM-doped PMMA has been demonstrated in Chapter 6 for triads. Consider now a mixed colour source of a larger scale. How many 5 mm LEDs can be arranged at the input end of a 3 cm diameter PMMA mixing rod? What geometrical configuration gives optimum uniformity of colour mixing with low light loss via the walls?

7.6.1 Configuration of source LED array

Considering that three colours are to be mixed, some possible geometrical configurations of LEDs are shown in Figure 7-12. LEDs with the same SRF (the same radial distance from the centre) are displayed with the same colour.

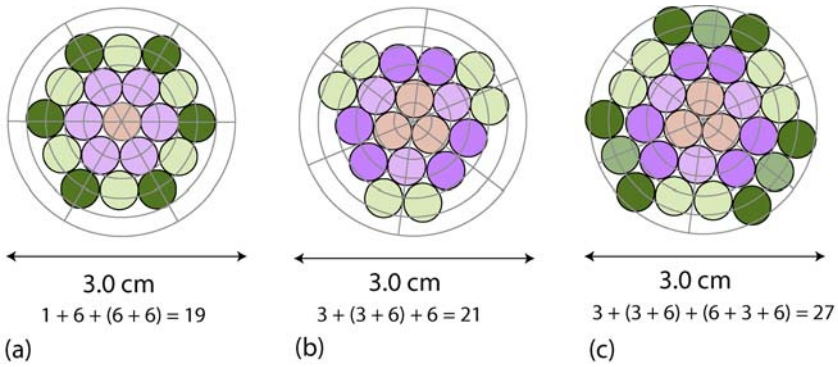

Figure 7-12. Possible configurations of 5 mm LEDs positioned at the entrance of a 3 cm diameter TRIMM mixing rod. a) single central LED, total = 19 LEDs. b) innermost ring of 3 LEDs, total = 21 LEDs. c) innermost ring of 3 LEDs, total = 27 LEDs.

It can seen that configuration (a) has the highest rotational symmetry, because each group of 6 LEDs sharing the same SRF are evenly spaced around the circumference of their relevant circle. This is in contrast to configs. (b) and (c). Configuration (c) was rejected because the outermost LEDs protrude slightly over the outer edge of the mixer. Configuration (a) was selected due to uniformity of spatial distribution of the LEDs over the area of the entrance end of the mixing rod, and for simplicity of the radial structure (circles of different SRF are fairly evenly spaced).

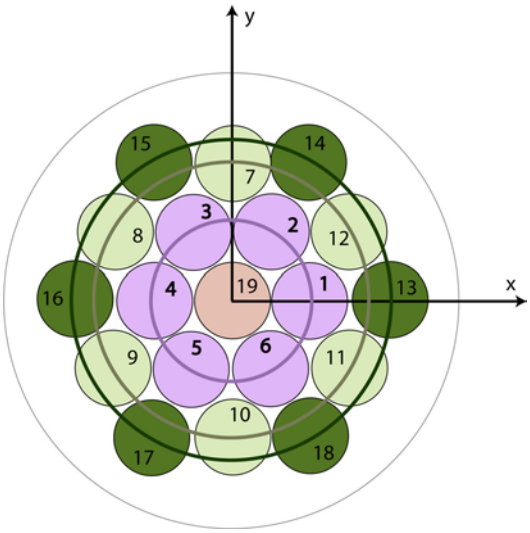

Figure 7-13. Geometrical configuration of source LEDs for mixing, showing inner, middle and outer rings of LEDs sharing the same SRF.

7.6.2 Ray tracing simulations

In the light of previous colour mixing experiments and computer simulations, it was judged that a TRIMM concentration of about ≈ 33K and a length of 6 cm would be suitable as a multi-LED TRIMM mixer. An average sphere separation of $p = 2$ mm gives ≈ 33K granule concentration, or ≈ 1% sphere concentration. For a 6 cm rod length, this corresponds to an axial particle number of $a = 30$.

The 'Alpha red' profile was used as the source for all LEDs in the computer simulations (Figure 5-4, Figure 5-8). This profile was selected as being fairly typical of many LEDs, and preferable to using the empirical smooth profile. The modelled source diameter was 4 mm.

To perform a final colour map of the output from the array, it is necessary to combine the individual LED diffusion maps of all 19 LED sources shown in Figure 7-13. I therefore first utilised the statistical approach outlined in Section 7.4 to check the rotational symmetry of the output from one LED in each SRF circle, before embarking on a full analysis.

7.6.2.1 Rotational symmetry check

Ray tracing simulations of 10,000 rays were performed to conduct rotational symmetry tests. Source coordinates were chosen to fall on the y-axis at 0, 5.5 mm 8.8 mm and 10.5 mm from the centre of the array, to lie on the rings of constant SRF shown in Figure 7-13. Rays were launched from a source area of 4 mm diameter, the source coordinate being in the centre of the launching area in each case. Rotational symmetry statistical analysis was performed for each of the simulated LED diffusion maps, as explained in Section 7.2. The results for the LEDs which lie on the inner and middle circles of LEDs, repetitively are shown in Figure 7-14.

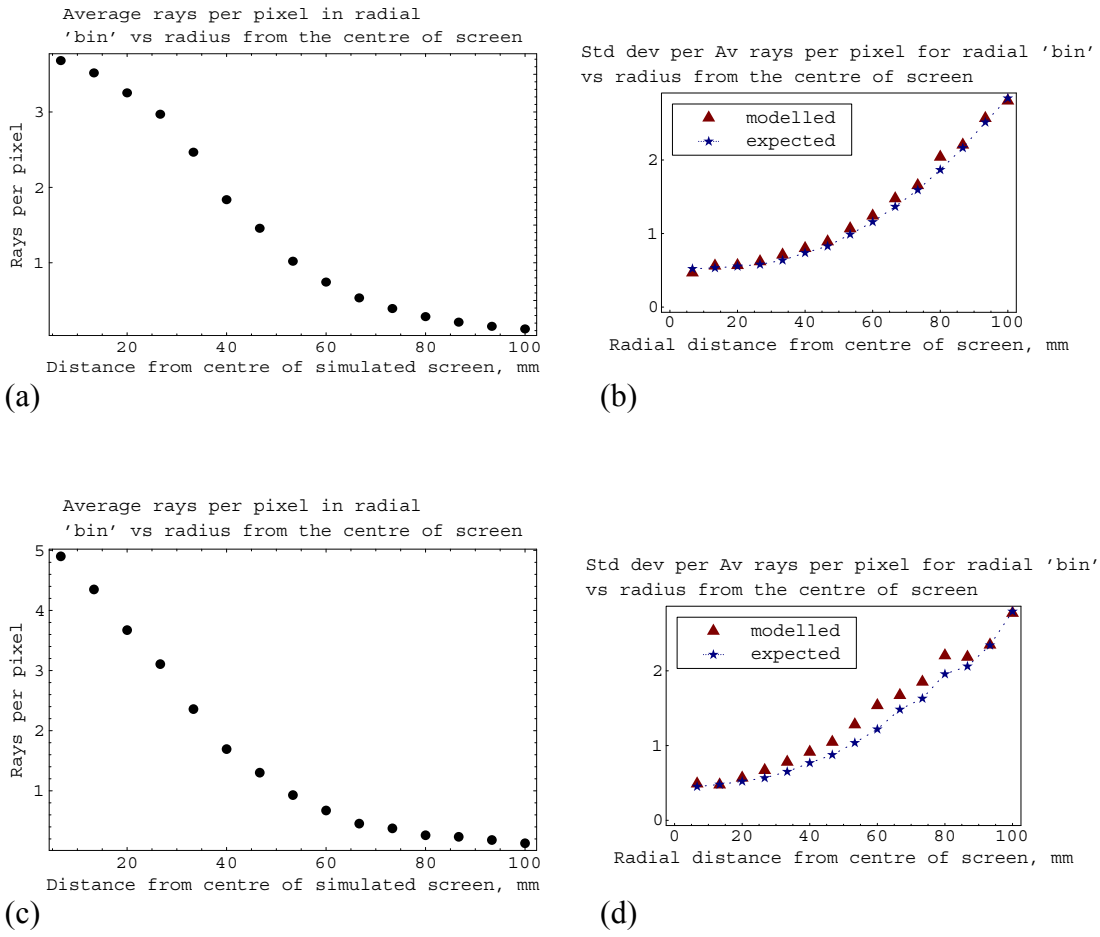

Figure 7-14. Rotational symmetry check of detector output of LEDs from the array pictured in Figure 7-13, 10 cm from the output end of TRIMM mixing rod. a-b) An LED from the inner ring of the array, 5.2 mm radially from the rod axis (coloured purple in Figure 7-13). c-d) An LED from 2nd ring of the array, 8.8 mm radially from the rod axis (coloured light green in Figure 7-13).

It is evident from Figure 7-14 that there are no sudden spikes in the LED diffusion maps for each of the inner and middle rings. The same SRF gives the same rotational symmetry pattern, so only one LED in each ring needed to be tested.

7.6.2.2 Individual rings colour mixing

For each ring of 6 of constant SRF, simulations were run for each of two LEDs, using their specific $\{x, y\}$ source coordinates. LED diffusion maps were recorded for each LED at four detector planes, located at 0, 1 cm, 10 cm, and 100 cm from the mixing rod output end. Maps for the other LEDs of the same SRF were obtained by reflection about the x or y axis. As an example, consider the inner most ring in Figure 7-13 (the purple coloured group of LEDs, numbered 1-6). The source point (in mm) for LED1 is $\{5.2, 0\}$. The source point for LED2 is $\{3.6, 4.6\}$. Ray tracing simulations were performed for each of these two sources, and a set of diffusion maps, one for each screen distance, recorded for

each LED. The set of diffusion maps for LED4 were obtained by reflecting the diffusion maps from LED1 about the *y*-axis; LED6 diffusion maps were obtained by reflecting the diffusion maps of LED2 about the *x*-axis; and so on. Ray tracing simulations were performed and sets of diffusion maps obtained for the LEDs numbered 1, 2, 7, 8, 13, 14 and 19 in Figure 7-13. The maps corresponding to the remaining LEDs were obtained by reflection.

Initially, combined colour output maps were prepared for groups of 6 LEDs with the same SRF. The subset of these located 10 cm from the end of the TRIMM mixer are shown in Figure 7-15, along with the colour allocation of the individual LEDs in each ring.

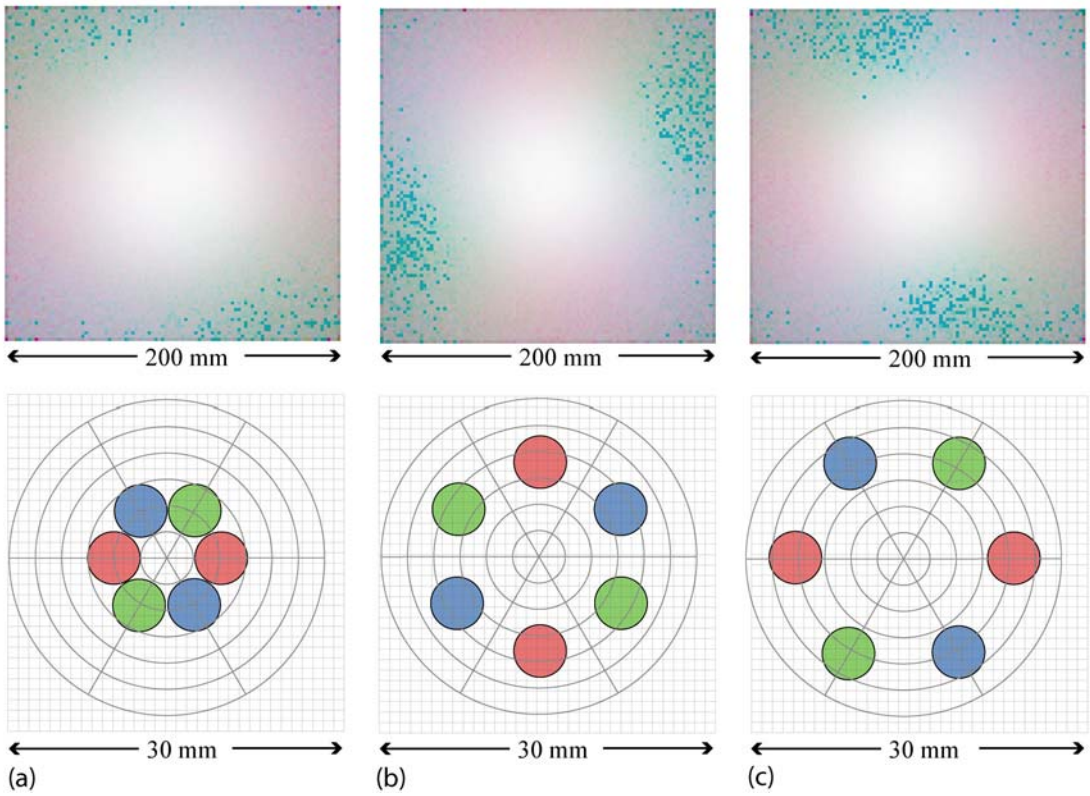

Figure 7-15. Simulated colour output 10 cm from TRIMM mixer rod end, for individual rings of the LED mixer array shown in Figure 7-13. a) inner ring, SRF = 0.35 b) middle ring, SRF = 0.59 c) outer ring, SRF = 0.7. LED arrays and colour output are displayed as viewed with the *z*-axis into the page.

It can be clearly seen that the mixing is uniform in the central section of the detector screen in each case. Patches of individual colour appear around the periphery, especially for the outer ring, so care needs to be taken in the placement of RGB LEDs for the overall array, to avoid the coincidence of similar coloured peripheral patches from rings of different SRF overlapping.

7.6.2.3 Total LED array colour mixing

The allocation of red, green and blue over the entire array that gives the most uniform colour mixed output is shown in Figure 7-16. The combined colour maps corresponding to the exit surface of the TRIMM mixer and the 3 modelled detector distances are presented in Figure 7-17. Each of the red LEDs was set to the same flux output, and similarly for the green and blue LEDs. This is an important practical point, as different coloured LEDs have different threshold voltages, and all LEDs of similar colour are usually controlled by common electronics. The ratio of luminous fluxes was R:G:B = 1 : 2.44 : 0.43 for the individual LEDs, although it should be noted that the array contains 7 green LEDs and only 6 each of red and blue.

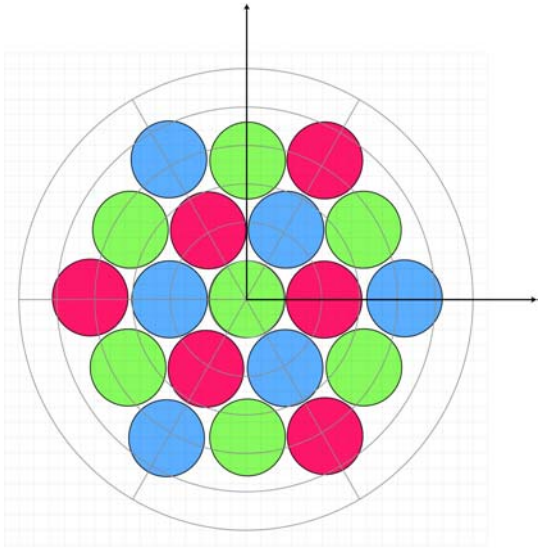

Figure 7-16. Configuration of RGB in the 19 LED array for uniform colour output from the TRIMM-doped mixer.

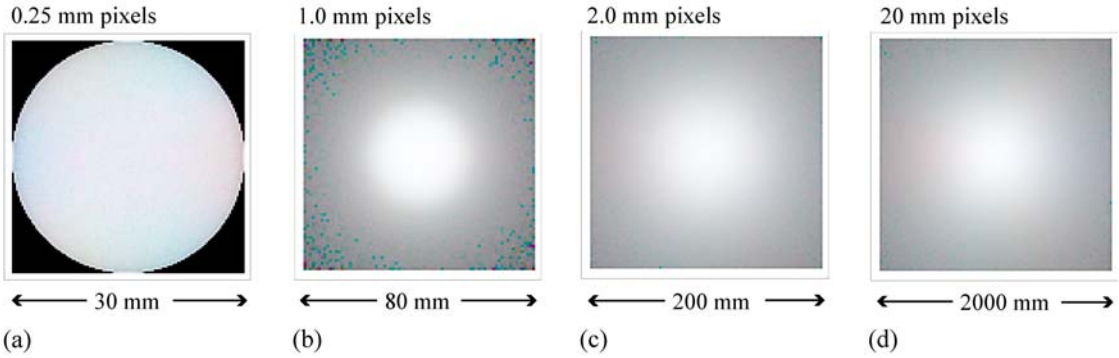

Figure 7-17. 19 LED array simulated colour output after ray tracing through the TRIMM mixer. a) exit surface of rod. b) 1 cm from rod end. c) 10cm from rod end. d) 100 cm from rod end.

It can be concluded that TRIMM mixing rods are highly suited for mixing larger numbers of LEDs, especially if the geometrical configuration of the array is optimised. The mixing shown in this example can be further enhanced by slightly increasing the TRIMM concentration.

8 Fresnel losses, wall transmittance and side-light distributions

TRIMM-doped mixing rods and diffuser sheets offer high forward transport of visible light with low loss due to backscatter. In this chapter, measured and modelled transmittance results are presented, and the effect of Fresnel reflectance on the outcomes is considered.

8.1 Fresnel reflectance and ray propagation in light guides

Theoretical treatments of light propagation in light guides are often made without considering Fresnel losses (Van Derlofske *et al.* 2003, 2004, Leutz *et al.* 2003, Gupta *et al.* 2001, Li *et al.* 2004). This is because for rays of near-normal incidence, the Fresnel reflection losses are constant at ~ 4% per interface. In TRIMM-doped systems, the angle of propagation changes with each particle interaction, and Fresnel effects can be very significant as angles of incidence increase.

Another simplification that is commonly made in light pipe modelling is the meridional ray approximation (Van Derlofske *et al.* 2003, 2004, Li *et al.* 2004, Narendran *et al.* 2000). This can be a valid approximation for square light guides relying on TIR only. As was discussed in Chapter 4, ray tracing geometry is more complicated for cylindrical guides than for rectangular. If the light source covers a significant portion of the guide entrance face, numerous skew rays invalidate the meridional approximation to some extent (Mildner et al. 1994). For rays of increasing skewness, TIR from the wall of a cylindrical guide increases due to an increase of the incident angle of the ray with the normal to the guide wall, so assuming all the rays are emitted from the centre of the guide leads to erroneous results (Saraiji et al. 1996).

8.1.1 Fresnel reflection curves for the PMMA/air boundary

Fresnel reflectance from the boundary between media can be calculated using the familiar equations (Hecht 1998);

$$R_{\perp} = \left(\frac{n_i \cos\theta_i - n_t \cos\theta_t}{n_i \cos\theta_i + n_t \cos\theta_t}\right)^2 \qquad R_{\parallel} = \left(\frac{n_t \cos\theta_i - n_i \cos\theta_t}{n_i \cos\theta_t + n_t \cos\theta_i}\right)^2 \qquad \textbf{(8-1)}$$

$R_{\perp}$ and $R_{\parallel}$ refer to the reflectance for perpendicular and parallel polarisation states respectively. Every time a ray intersects a light guide/air boundary in the ray tracing simulations, $R_{\perp}$ and $R_{\parallel}$ are calculated and averaged since it is assumed that the light is unpolarised. The ray is reflected or transmitted based on this probability value.

There are three interfaces for which Fresnel reflection must be considered:

1. source ray coupling from air into the light guide. Fresnel reflectance curves for the ray angle-of-incidence in air, when intersecting a PMMA rod of $n_1 = 1.49$, are shown in Figure 8-1(b). The probability of reflectance becomes increasingly significant for angles of incidence > 60°.

2. reflectance of propagating rays from the light guide wall. It can be seen from Figure 8-1(a) that Fresnel reflectance increases near the matrix/air critical angle. This needs careful consideration in circular light guides. As a result of Fresnel reflectance and the high number of skew rays, fewer rays escape via the side walls.

3. reflectance of rays from the end of the light guide (at the matrix/air interface). It is well known that a ray that enters an undoped light guide by refraction, and propagates to the far end by TIR, will not be totally internally reflected at the exit end. However TRIMM spheres in PMMA cause a mean ray deviation of 1.8° per interaction. Some rays, after encountering several spheres, have θ sufficiently large to undergo TIR at the end surface. A significant number of those rays not turned back by TIR will be Fresnel reflected, since the coefficient of Fresnel reflection increases with increasing angle from the normal.

The net effect expected from incorporating Fresnel reflection into ray tracing simulations, compared to simulations that ignore Fresnel reflection, is that coupling efficiency from the source into the guide will be decreased, particularly if the source angular spread is large; transmittance through the guide walls will be decreased; and reflection from the guide ends will be increased.

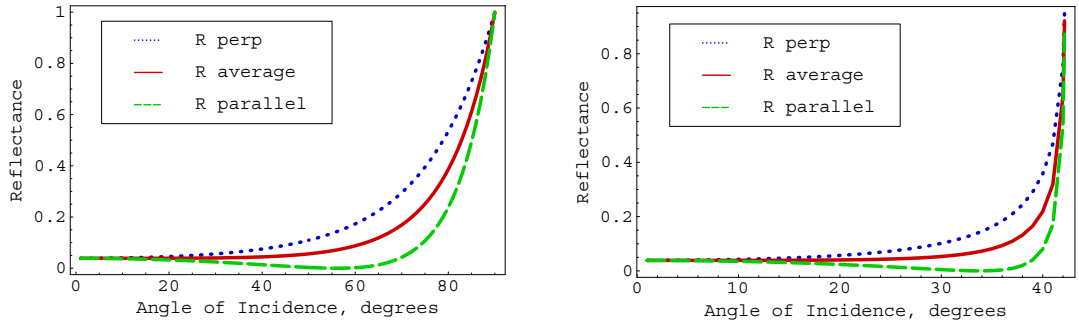

(a) (b)

Figure 8-1. Fresnel reflection with angle-of-incidence, for a) rod to air (affecting ray transmittance out of rod), b) air to rod (affecting coupling of LED source rays into rod) for PMMA matrix. (n_1 = 1.49)

8.2 Modelling: Fresnel reflectance vs Fresnel neglected

Ray tracing simulations were carried out to investigate the impact of Fresnel reflection on the guide wall transmittance, and on the amount of light reflected at the exit end of the rod. Simulations were performed for 10,000 rays using a 2 cm diameter, 10 cm long unclad POF guide, with p = 2 mm. For the same reasons as described for the round guide simulated in Section 7.5, only rays propagating in a forward direction are considered, and the point source function is spread across a θ cone of 0-5°. The source point is located at the green cross shown in Figure 6-5(b). Comparisons were made between simulations when Fresnel reflection was applied to the internal surfaces of the light guide, and those when the reflection was due to TIR only. For all simulations described in this section, no Fresnel reflection was applied when coupling source rays into the entrance face of the light guide.

When TRIMM-doped guides are to be used as mixers for purposes of 'end-light', it is desirable to maximise the transmittance at the exit face at the end of the guide. Therefore rays that are reflected backward from the exit face are considered a loss. Similarly, rays that are transmitted through the wall during propagation are also considered as a loss. Table 8-1 shows the comparison between

1. no Fresnel reflection incorporated,
2. Fresnel reflection applied to guide end face only, and
3. Fresnel reflection applied to end face and the side wall,

on the light losses via side wall transmittance and end-reflected rays.

Table 8-1. Effect of applying Fresnel reflection to the internal surfaces of a TRIMM-doped light guide (POF; $\mu = 0.0182$, $p = 2$ mm, length = 10 cm, diameter = 2 cm) used as a mixer.

	No Fresnel	*Fresnel end only*	*Fresnel end + side wall*
Side wall transmittance (as % of initial rays)	3.7%	3.7%	3.4%
End-reflected rays (as % of rays reaching guide end)	6.0%	10.9%	11.7%
Wall + end loss (as % of initial rays)	9.5%	14.2%	14.2%

It can be seen from Table 8-1 that applying Fresnel reflection to the end surface of the light guide increases the end-reflected rays (as a percentage of the rays that reach the guide end) from 6.0% to 10.9%. Adding Fresnel reflection to the side wall as well as the end surface increases this end-reflected loss by only a small amount.

Adding Fresnel reflection to TIR for the side wall reduces the wall transmittance from 3.7% to 3.4%. This small increase in forward propagation that occurs is compensated for by an increase in the number of end-reflected rays. Therefore, Fresnel reflectance from the end of the guide makes a far greater contribution to the TRIMM mixing rod losses than Fresnel reflectance from the wall. It is clearly of benefit to reduce this end-reflectance by reshaping or coating the exit end, to increase the mixing rod transmittance.

8.2.1 Effect of TRIMM concentration on wall and end losses

Simulations (as outlined above) were also performed for increasing sphere separation distance, p. The relationship between end-reflected loss, with and without Fresnel effects, and increasing inter-particle distance is shown in Figure 8-2. End-reflected rays are shown as a percentage of the rays remaining when the end of the light guide is reached. It can be seen that the effect of Fresnel reflection on the percentage of end-reflected rays is significant and should not be ignored. It is also noteworthy that the fraction of rays that are totally internally reflected at the guide end increases exponentially as the TRIMM concentration increases.

A plot of rays transmitted via the wall (as a percentage of rays launched) vs p is also shown in Figure 8-2. Only the simulated results including Fresnel reflection are shown, as the difference between the number of wall exited rays including and excluding Fresnel reflection is small.

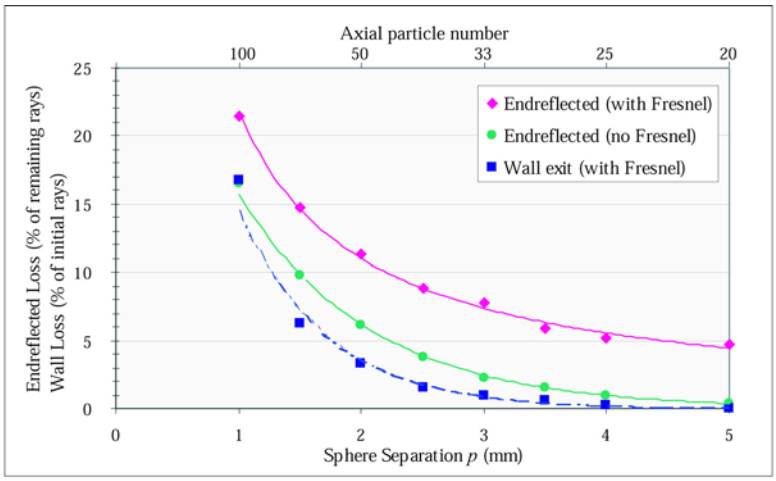

Figure 8-2. Comparison of percentage of end-reflected rays, with and without Fresnel reflection, for a 10 cm long, 2 cm diameter POF guide, with varying TRIMM separation (p). Percentage of wall-exited rays (with Fresnel reflection included) are also shown ($\mu = 0.0182$).

8.2.2 Effect of angle-of-incidence variation on wall and end losses

The effect of varying the angle-of-incidence (in air) of initial rays on the amount of wall loss and end-reflected loss is shown in Figure 8-3, for various values of TRIMM separation p. Simulations were performed using a unclad POF guide 10 cm long and 2 cm in diameter, as before, and only rays propagating in a forward direction were considered. The results shown have the source point located off-axis (SRF = 0.32). When the source point is located at the centre of the guide entrance face, the wall losses are slightly greater, and the number of end-reflected rays slightly lower, than if the point source is located slightly off-axis.

Not surprisingly, the percentage of rays transmitted through the guide wall increases steadily with increasing angle-of-incidence, particularly for rays with initial angle > 20° with respect to the guide axis. The effect of increasing TRIMM concentration is primarily an increase in total wall transmittance. The end-reflected loss with angle-of-incidence, shown in Figure 8-3(b), shows an interesting pattern with changing TRIMM concentration for the higher angles-of-incidence. This is because the data are expressed as a percentage of the rays remaining at the end of the light guide. For low concentration (i.e. high p) the end-reflected loss increases with angle-of-incidence, as one would expect, but for high concentration, the end-reflected loss decreases with increasing angle-of-incidence. For higher concentrations, a greater number of ray/particle interactions occur, so for rays launched at normal incidence the mean half angular spread $\bar{\Sigma}$ increases with axial

particle number (see eqn 2-15). Conversely, rays launched with high angle-of-incidence can have a small θ angle with respect to the guide axis upon reaching the end of the guide. Hence the TIR and Fresnel reflectance is lower for these rays.

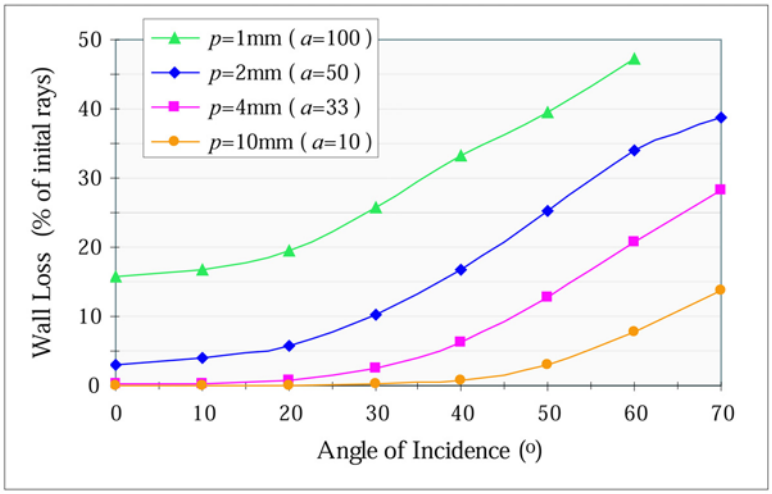

(a)

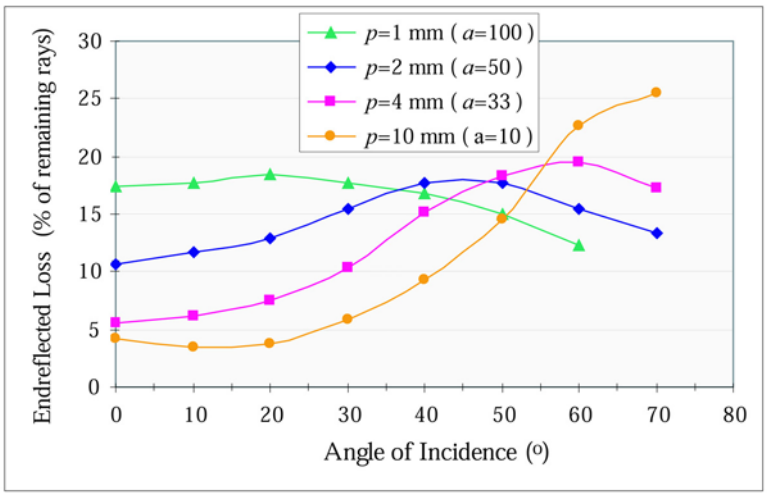

(b)

Figure 8-3. Effect of varying angle-of-incidence of launched rays (in air), for varying TRIMM concentration, on (a) wall loss (as a percentage of initial rays), (b) end-reflected loss (as a percentage of rays remaining in the light guide) (μ = 0.0182).

8.3 Effect of varying μ on wall and end loss

8.3.1 μ and TRIMM concentration

Simulations were performed to investigate the effect of changing μ on the relationship between light losses and TRIMM concentration. Similarly to the previous section 10,000 rays were traced through a 2 cm diameter, 10 cm long guide, only forward propagating rays are considered, and the point source function is spread across a θ cone of 0-5°, with SRF = 0.32.

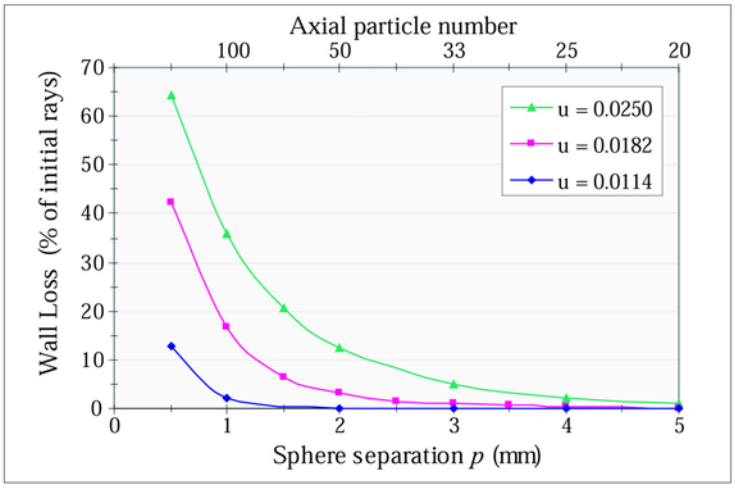

(a)

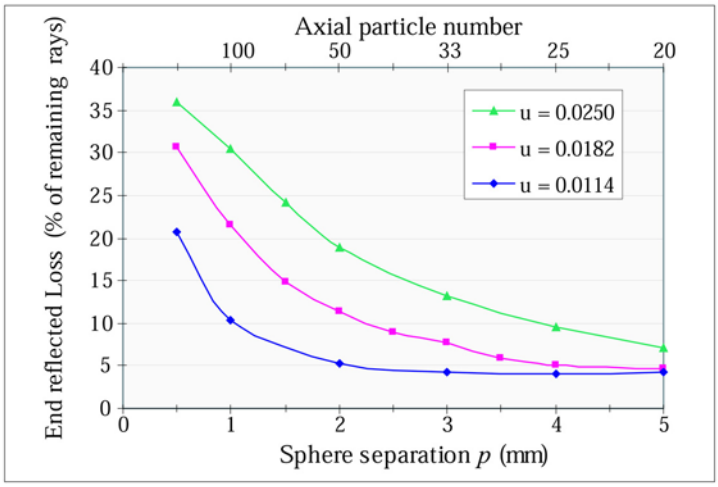

(b)

Figure 8-4. Effect of TRIMM sphere separation p on (a) wall loss, (b) end-reflected loss, for 3 different values of μ.

Figure 8.4 shows that for μ = 0.0114, which is the case for TRIMM in PMMA, wall transmittance and end-reflected losses start to increase significantly when the axial particle number approaches 100. For μ = 0.0182, which applies to TRIMM in POF, this increase occurs at an axial particle number of about 40. It can also be seen from Figure 8.4 that increasing μ and TRIMM concentration causes a dramatic increase in the side loss, with a corresponding more gradual increase in the end-reflected loss. For μ = 0.025 with p = 0.5 mm (a = 200) almost no light exits the guide end. This suits a design purely for side-light.

8.3.2 Wall transmittance of PMMA rod: constant μ vs varied μ

In Section 7.1 the effect of varying μ with wavelength on RGB colour mixing was investigated, via simulations using the LED empirical model with the 15K 10 cm TRIMM-doped PMMA rod. Table 8-2 summarises the wall transmittance, in forward and reverse directions, for each of the RGB LEDs for both constant and varied μ. (Rays exiting in the reverse direction are primarily due to backward propagating end-reflected rays.) It can be seen that the transmittance through the rod wall is increased for the blue peak wavelength for higher values of μ, predominantly in the forward ray propagation direction.

Table 8-2. Rays 'lost' by refraction out of the light guide wall as a percentage of the number of rays initially entering the rod, for ray tracing modelling shown in Figure 7-1 and Figure 7-2.

Loss through wall: Constant μ				*Loss through wall: Varied μ*			
LED	*Side loss (fwd)*	*Side loss (rev)*	*Total*	*LED*	*Side loss (fwd)*	*Side loss (rev)*	*Total*
R $\mu = 0.01141$	2.61%	2.01%	4.62%	*R* $\mu = 0.01075$	2.42%	1.91%	4.33%
G $\mu = 0.01141$	2.64%	1.98%	4.61%	*G* $\mu = 0.01340$	3.33%	2.38%	5.71%
B $\mu = 0.01141$	2.68%	1.99%	4.67%	*B* $\mu = 0.01604$	4.55%	2.40%	6.94%

It was shown in Figure 7-2 that the differences in angular propagation characteristics caused by the slight increase in angular deviation angle with increasing μ does not critically alter the appearance of the projected light output for the TRIMM mixers. Previous spectral measurements performed on TRIMM diffuser sheets (Smith *et al.* 2003) have also found that there is very little variation with wavelength in transmittance and reflectance measurements.

8.4 TRIMM losses, measured and modelled, for rod + diffuser sheet

Transmittance measurements made of the light from the 'Alpha' RGB LED triad through the PMMA + diffuser sheet were described in Section 6.3.2. The fate of rays can be categorized as detailed in Figure 8-5 in terms of key surfaces and ray directions at the surface. Results are given in Table 8-3 for measured and modelled mixing of the Alpha LED array with clear 6 cm rod, and for PMMA rod with TRIMM mixer. 'Input Fresnel' refers to the fraction of rays incident on the entrance end of the rod that are Fresnel reflected. 'Output end Fresnel' is the fraction of incident light (I_0) reflected from the end surface which is 'lost', most of which is transmitted out through the source end of the mixer. 'Forward' is the percentage of I_0 transmitted out of the end surface. Light transmitted out of

the side edges of the diffuser TRIMM sheet, in any direction, is given by 'Lateral'. (For a clear rod, 'Lateral' is negligible.) The reduction in forward output of the rod + TRIMM diffuser sheet, compared to the clear rod, is compensated for by the lateral output from the TRIMM diffuser sheet (see Table 8-3).

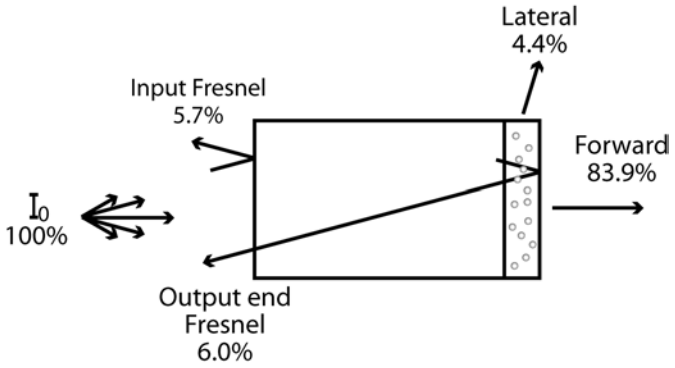

Figure 8-5. Schematic of PMMA rod + TRIMM diffuser sheet, showing surfaces at which transmittance is recorded, or reflected losses occur. The values shown are the simulated results shown in Table 8-3.

Table 8-3. Simulated and measured transmittance results and reflected losses, as a percentage of the incident light, for Alpha group LEDs, for 6 cm PMMA mixing rod with and without TRIMM diffuser. *measurement has higher uncertainty (see text).

	Clear PMMA rod		*Clear rod + TRIMM diffuser sheet*	
	Simulated	*Measured*	*Simulated*	*Measured*
Input Fresnel reflection losses	5.7	-	5.7	-
Output end Fresnel losses	4.7	-	6.0	-
Forward useful output	89.6	87	83.9	83*
Lateral useful output	N/A	N/A	4.4	6.0

Transmittance measurements made for the individual red, green and blue LEDs were averaged, and compared with similarly averaged transmittances obtained from simulation data. The measured output from the TRIMM sides ('Lateral') was obtained by difference, by taking readings with the diffuser in and out of the integrating sphere. The transmitted end light for the rod + TRIMM mixer has a higher uncertainty than the other measurements. This is because measurements using integrating spheres can only be accurately compared when the angular spread of the light is comparable. According to eqn 2-15, the TRIMM diffuser sheet produces an additional half-cone angular spread of about 12° compared to the clear rod, so a correction factor was estimated to account for the effect that this difference has on readings obtained using the integrating sphere. This correction

factor was obtained by making measurements of the transmitted light from the LED array through a diffuser sheet alone, compared with estimates based on previous measurements with two spectrophotometers using a narrow collimated beam (Smith *et al.* 2003).

8.4.1 Discussion

In a previous study of RGB colour mixing it was reported that clear PMMA mixing rods made no significant improvement to illumination and colour uniformity compared to a bare LED array. The addition of an end diffuser improved the output light distribution, but gave rise to a 6% loss (Zhao *et al.* 2002) in addition to Fresnel losses. That loss was primarily caused by backscatter. The losses shown here are almost entirely due to Fresnel reflection, since backscatter is negligible from the TRIMM particles. The output end Fresnel reflectance for the PMMA + TRIMM diffuser sheet is slightly higher than that from the clear rod, due to the additional angular spread of light imposed by the particle deviations, as was described in Section 2.3.1. Much of this exits via the sides of the TRIMM sheet and can be utilised for lighting by the addition of reflectors. The remainder of this end-reflected light is transmitted through the source end; for the rod + TRIMM diffuser sheet this loss is 1.3% higher than for the clear PMMA rod. The loss imposed by the diffuser sheet is much lower than the 6% loss reported above (Zhao *et al.* 2002), and furthermore can be reduced by minimising the Fresnel reflection at both input and output ends.

Input Fresnel loss increases as the LED source angular distribution increases, as there are a greater number of oblique rays. One way to minimise Fresnel reflectance from source coupling is to choose directional LEDs in preference to higher angle ones, for example the Beta blue LED in preference to the Alpha blue (refer to Figure 5-4). Further simple reduction in Fresnel losses would make these systems exceptionally efficient.

8.5 TRIMM-doped rods: side-emitting ray modelling

Measured and simulated colour output of RGB LEDs coupled into TRIMM-doped rods was presented in Chapter 6. When TRIMM rods are utilised as colour ‘mixers’, it is desirable to achieve adequate homogenisation of the light from the individual sources. Simultaneously, it is aimed to transmit the maximum amount of source light along the rod and through its exit end (i.e. maximise the ‘end-light’), while transmitting the minimum amount of light through the side wall (i.e. minimise the ‘side-light’). Study of the distribution of wall-exited light is important; both the quantity of light that escapes through the wall before the rod end is reached, and the nature of the side light distribution, is of inter-

est. The latter is especially important from the viewpoint of visual appearance, since TRIMM rods can also be used as side-emitting light sources. The distribution of output light along the length of the guide, and the angular distribution of the side light, are important considerations for TRIMM rods used as 'side-light' sources. The actual quantity that escapes is important both in 'side-light' and 'end-light' applications.

Simulation results of the distribution of wall-exited rays are given in this section. The variation of emitted intensity along the rods with distance from the source, and the angular distribution of these exited rays relative to the wall normal are considered. The conditions are the same as for the TRIMM-doped rods of Section 6.3.1, with the exception that only one LED of the RGB triad is modelled for each rod. An additional simulation has been performed for the 15K TRIMM concentration, for a rod 20 cm long, for purposes of comparison. For each rod, a modelled LED source is situated at $(x_0, y_0, z_0) = (0, 2.4, 0)$, i.e. the blue LED in Figure 6-5(a). One million rays were traced through each rod.

Simulated rays refracted out of a rod's wall are binned in 1 cm intervals along the length of a rod from its source end. For example, the total number of rays that exit in the interval 3 cm to 4 cm from the source end of a guide is recorded at 4 cm. The rays propagating in forward and reverse directions are recorded separately; reverse rays are those that are travelling towards the source end of the rod after reflection from the end surface.

Figure 8-6 shows the change in the relative intensity of the wall-exited light with distance along the light guides, expressed as a percentage of the initial number of rays launched. Forward and reverse totals are shown for each 1 cm interval. The final interval of each of the 15K rods (i.e. the 10 cm bin of Figure 8-6(b), and the 20 cm bin of Figure 8-6(c)) show higher numbers of wall-exited rays in the reverse direction than the forward direction. This is an 'end effect', resulting from Fresnel reflection at the rods' ends.

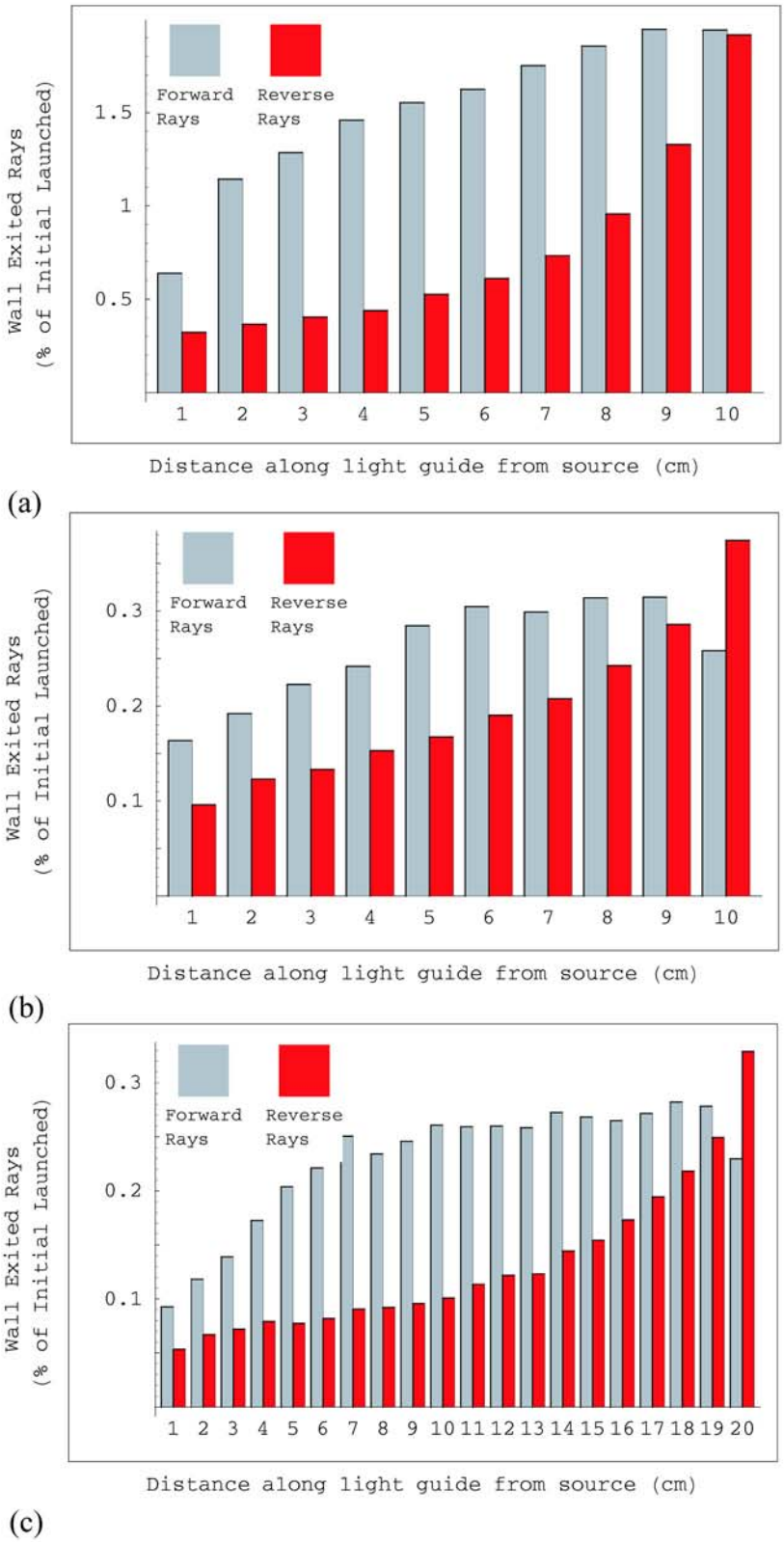

Figure 8-6. Simulated wall-exited rays from TRIMM mixing rods, in forward and reverse directions, binned into 1 cm increments along the length of the light guides. a) 100K 10 cm light guide. b) 15K 10 cm light guide. c) 15K 20 cm light guide.

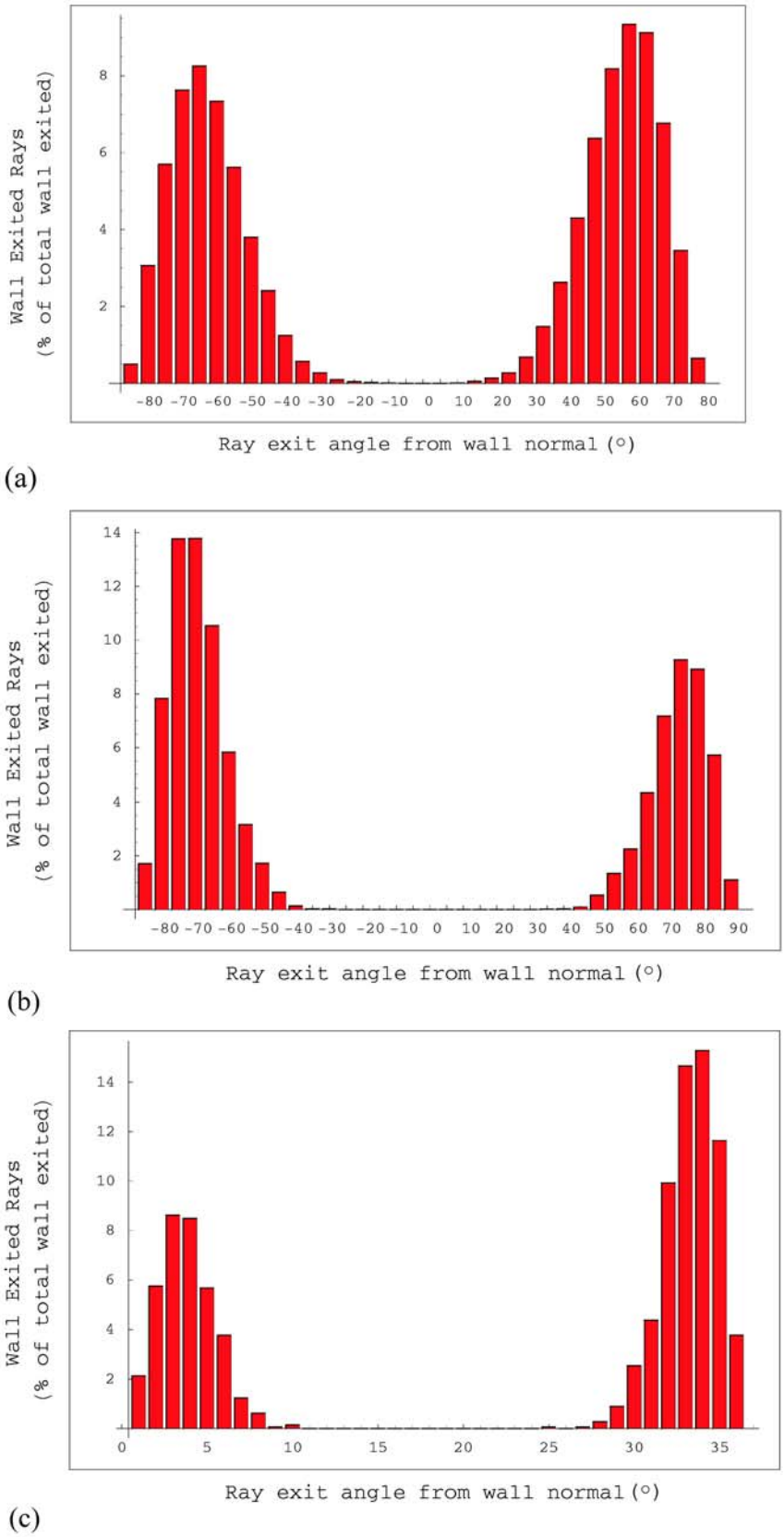

Figure 8-7. Simulated angular distribution of wall exited rays from TRIMM mixing rods, for a 1 cm interval, sorted into 5° bins. 0° corresponds to the wall normal. a) 100K 10 cm light guide, 10th interval. b) 15K 10 cm light guide, 10th interval. c) 15K 20 cm light guide, 12th interval.

For each 1 cm interval along the rods, the rays transmitted through the wall are binned according to their angle with the wall normal. A positive sign associated with an angle indicates a positive *Z* direction cosine for the exiting ray, and a negative sign associated with an angle indicates a negative *Z* direction cosine for the exiting ray. The bin sizes are in 5° intervals. Ray azimuth direction around the wall normal was not recorded. Figure 8-7 shows the angular distribution results for a 1 cm interval for each of the 3 light guide simulations. Figure 8-7(a) and Figure 8-7(b) show the distribution of the 100K and 15K rods respectively, at the 9 to 10 cm interval. Figure 8-7(c) shows the angular side-light distribution for the 15K 20 cm rod, at the 11 to 12 cm interval. The angular distribution of rays exiting the walls are very similar for each 1 cm interval along a particular light guide. The results show a bimodal distribution due to the 'forward' and 'reverse' binning, but as the azimuth direction was not taken into account, it is anticipated that the actual distribution is spread as a cone in the azimuth direction around the wall normal.

8.5.1 Simulation results

There are two main points of interest when considering wall-exited light from TRIMM light guides: the total amount of wall-exited light, and the evenness of its distribution. The evenness of distribution can be subdivided into the evenness of intensity along the rod length, and uniformity of the angular distribution.

It can be seen from Figure 8-6 that the amount of side-loss reaches a steady state within a few centimetres from the source end of the light guide. This is verified by the longer 15K simulation in Figure 8-6(c). At the light guide end, the number of wall-exited rays in the forward direction decreases, corresponding with an increase in the number of reverse exit rays. This is an effect caused by reflection of rays from the exit end surface of the rod. Figure 8-8 shows how a ray that would exit the wall in a forward direction (Ray 1) can be reflected and exit in the reverse direction if it encounters the guide end (Ray 2). This effect is more pronounced for the 15K rods, since the TRIMM concentration is low (p = 4 mm). In the 100K case, there are sufficient particle interactions to further randomise the ray direction (p = 0.75 mm).

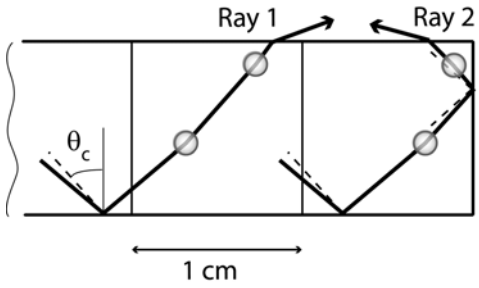

Figure 8-8. 2D schematic illustrating the 'end effect' for a 15K rod. Critical ray angles are marked with dotted lines.

The simulated angular distribution results in Figure 6 show data for one 1 cm interval for each rod. Each rod has a consistent wall-exited angular distribution over its entire length, irrespective of ratio of forward to reverse exit rays. The peak angles of the distributions are concentration dependent. In the 100K rod, a ray encounters a higher number of particles before reaching the wall than in a 15K rod. The peak angular range for the 100K rod is ~60-70° from the wall normal, and for the 15K rod ~70-80° from the wall normal. Thus, this highly directional effect decreases with increasing concentration. The 15K rod is designed for 'end-light' applications: the total side loss of the modelled LED through the rod is 4.6%, which is not useful for side-light. This side loss in the forward direction can be useful for short TRIMM rods for general lighting, as it is essentially added to the end-transmitted output distribution. It is anticipated that high concentration TRIMM rods designed for side-light applications would have an acceptable angular distribution of wall-exited light, although this would need to be verified by further study.

8.6 Other TRIMM system losses

8.6.1 Square vs circular cross-section

In Section 7.5, the performance of square and circular guides as colour 'mixers' was compared, for low and high source radial fractions (SRF). The total losses were comparable for both circular and square, for both SRFs, but the proportion of end-reflected rays differed.

For the square guide, the recorded losses were 3.2% wall loss, and 6.4% end-reflected loss, for both high and low SRF configurations. It should be noted, however, that the colour mixing was inferior for the high SRF.

For the circular guide, the lower SRF configuration had 2.4% wall loss, but 7.1% end-reflected loss. This lower wall loss, and higher end-reflected loss of the circular guide compared to the square is due to the effect of skew rays. This was discussed in Section 4.3.1; a ray with angle θ will give varying ray/wall intercept angles with varying distances from the guide axis. The circular guide high SRF configuration had slightly greater (0.4%) wall loss than for the low SRF, with correspondingly lower end-reflected loss.

The total wall and end-reflected 'loss' is comparable for the guides of square and circular cross-section, for this example. However, when the guides are designed to produce 'side-light', the end-reflected rays are 'lost' only if they propagate the entire length of the light guide (in the reverse direction) and are transmitted out of the source end. It was shown in Section 8.5 that end-reflected rays can be refracted out via the light guide walls and thus become useful light in side-scattered systems. So, for many side-light applications, guides that are circular in cross-section are preferable to those with square cross-section.

8.6.2 LED array

The simulated TRIMM mixing rod used to combine the output of the 19 LED array described in Section 7.6 is 6 cm long and 3 cm in diameter, and has an axial particle number of 30. The 'end-light' forward transmittance for the array through the TRIMM rod, obtained by ray tracing, is 83.9%. The simulated results of the LED array and TRIMM-doped mixer are remarkably similar to the simulated results for the Alpha LED triad and PMMA rod + diffuser sheet, as shown in Table 8-4.

Table 8-4. Comparison of transmittance and loss between LED array and Alpha triad array mixers

	19 LED Array + TRIMM-doped PMMA	*Alpha triad with PMMA+diffuser sheet*
Forward Transmittance (%)	83.9	83.9
Wall Transmittance (%)	5.1	4.4
Input Fresnel loss (%)	5.9	5.7
Source end transmitted loss (%)	5.1	6.0
Axial particle no (a)	30	39
Rod aspect ratio (length:diameter)	2	3

The wall transmittance for the LED mixer is higher than for the rod + diffuser sheet. This could be due to the outer rings of the LEDs possessing a high SRF. It is noteworthy, how-

ever, that the increased wall loss is complemented by reduced source end transmission. The rays transmitted at the source end are a direct consequence of the end-reflected rays.

9 Flexible polymer optical fibre

9.1 Introduction

Recent developments in the forward light transmitting capability and production techniques of single core polymer optical fibres (POF) have resulted in increased potential for their use in diverse lighting applications. The flexible POF studied here are manufactured by Poly Optics Australia Pty Ltd by casting of a monomer mixture (mostly acrylates, plus plasticisers) in Teflon® tubing. Lateral illumination is achieved by the addition of TRIMM to the matrix material.

9.1.1 Applications of flexible polymer light guides

9.1.1.1 End-light

Undoped POF, that is fibre that has been polymerised with no TRIMM added, is useful for 'end-light' applications. Source light coupled into the fibres is transported by total internal reflection and transmitted at the exit end. The output light distribution is determined by the angular and spatial distribution of the input light. Uses of end-light POF include decorative lighting (such as chandeliers), inspection lighting (such as illumination for jewellers, dental, and medical workers) and transporting light from a single source to several output points (e.g. for car headlights). A small amount of TRIMM can be incorporated to homogenise 'end-light' distribution.

9.1.1.2 Side-light

Side-scattering guides have the potential to be a replacement for fluorescent lighting systems, and to be used for new applications. For example, TRIMM-doped POF can be used as safety lights for steps and aisles, and for decorative lighting. The guides distribute the input light: the actual light source and electricity supply are separate. This can be useful from the viewpoint of safety; in the case of swimming pool lighting, for example. The light source (along with its generated heat) is remote from the area being lit, which aids energy efficiency in applications such as display lighting inside shop fridges.

9.2 Research aims: initial investigation of POF

Flexible POF were the first type of TRIMM light guides studied during this project. Poly Optics Ltd supplied a commercially available illuminator, along with POF in 5 mm, 9 mm and 14 mm diameters, containing various concentrations of TRIMM granules. Investigations were made to find:

- change of side-scattered intensity with propagation distance along a light guide
- internal and external angular light distributions (relative to the light guide)
- the effect of change in wavelength of incident light
- the causes of a visible 'colour shift' over long propagation distances
- the influence of TRIMM concentration on the above factors
- the role of the Teflon® jacket on external light distributions and colour shift

The remainder of this chapter covers these research efforts. Illuminator characterisation measurements are reported in Section 9.3. Section 9.4 records the investigation of side-scattered light intensity with distance of propagation along a fibre. External angular distribution measurements are described in Section 9.5, and computer modelling of internal angular distributions in Section 9.6.

9.3 Illuminator and filter characterisation

The illuminator supplied by Poly Optics consists of a black metal box, in which is mounted a metal halide discharge light source, a glass ultraviolet (UV) and infra-red (IR) blocker, a rotating colour wheel containing five plastic coloured filters (including 'clear') and manifolds with various sized apertures, designed to hold the end of the fibres in place (Figure 9-1). The geometry of the reflector is chosen such that the light exiting the filament is focussed on the input end of the POF.

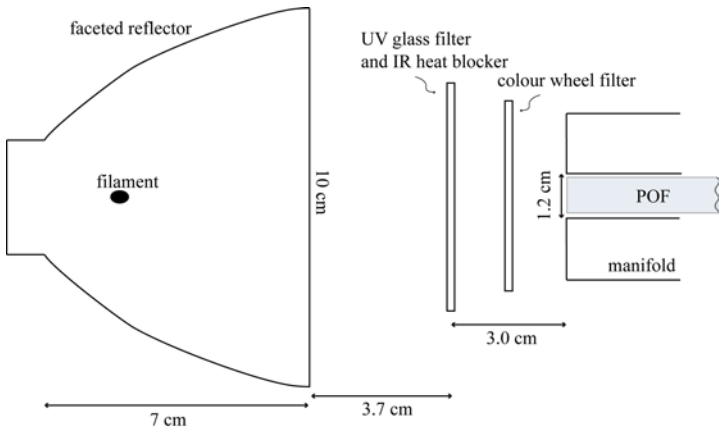

Figure 9-1. Illuminator configuration, showing metal halide light source, UV / IR blocker, coloured filters, and manifold positions.

9.3.1 Spectral response of filters

The transmittance over the visible wavelength range was measured for the five coloured filters, and for the glass filter, using a CARY 5E UV-VIS-NIR Spectrophotometer. The transmittance of the coloured filters is shown in Figure 9-2.

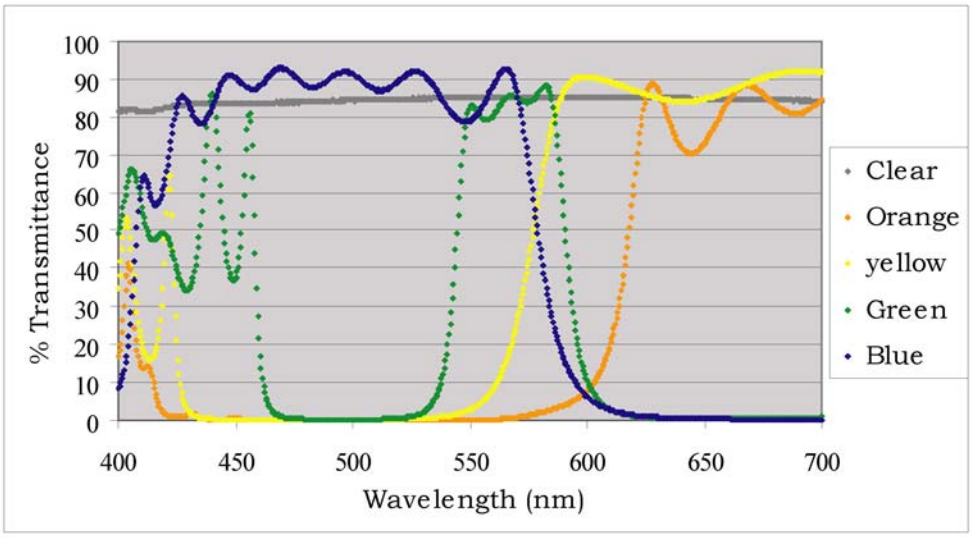

Figure 9-2. Transmission spectra of the coloured filters for the illuminator (halide discharge source).

The UV / IR filter is necessary to prevent fibre damage, as the halide lamp gets very hot. Measurements made using the CARY spectrophotometer show that the glass effectively blocks transmission of radiation below 310 nm. However, transmittance of visible light ranges between 70% and 75% between 500 and 700 nm, and is only 60% at 400 nm. This

transmitted light then passes through one of the coloured filters, which reduces the amount of light by a further 10 - 20%, as is evident from Figure 9-2.

Figure 9-2 shows that each of the filters transmits light over a large bandwidth. In addition, when the illuminator was operated using the clear filter without the manifold attached, the output light distribution contained some light that had been transmitted through the adjacent red and yellow filters. These problems illustrate the advantages of using LEDs as light sources for the colour mixing experimental work described in Chapter 6. Illuminators are used as POF light sources for applications where high brightness is required, especially for POF several metres in length.

9.3.2 Light distribution exiting illuminator manifold

The angular distribution of the light from the illuminator that is incident on a fibre end was not known. This was estimated by measuring the distribution of light exiting the illuminator manifold, without POF, in a single horizontal plane at the height of the centre of the manifold aperture. Measurements were taken in an arc at a constant distance of 39.5 cm from the manifold, using a BPW21 photo-diode detector mounted on a metal rotating arm. The rotation point of the arm was mounted at the centre of a protractor, and detector voltage output readings taken in 1° increments to ± 30° from the normal direction, then in larger increments to ± 60°. The results for two commonly used aperture diameters are shown in Figure 9-3.

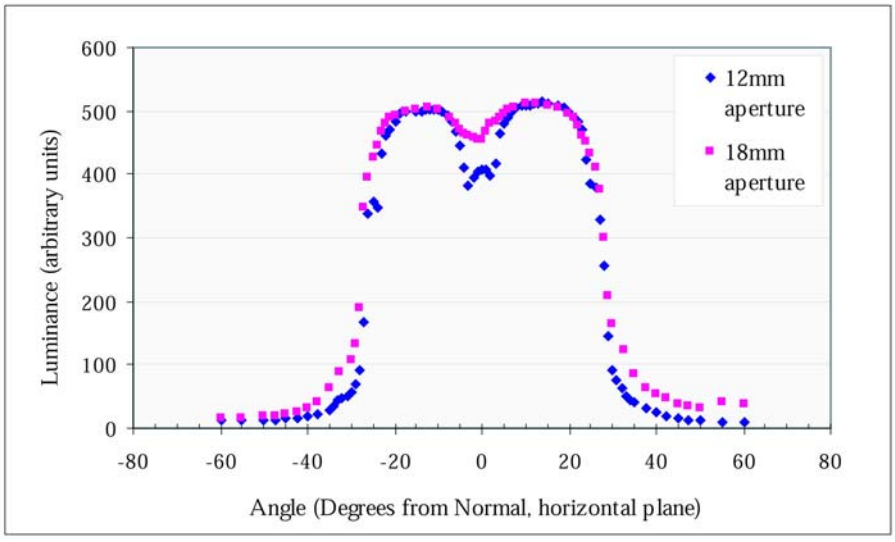

Figure 9-3. Angular distribution of light exiting the Poly Optics POF illuminator manifold, for 12 mm and 18 mm aperture sizes.

It can be seen that the angular light distributions from the illuminator manifolds can be approximated by square wave functions, or a 'top hat' shape, as the luminance drops suddenly at approximately 21°. For this reason, initial computer ray tracing simulations were performed using source rays randomly selected from a semi-cone angular range of 0 - 20°.

9.4 Side-scattered integrated luminance with propagation distance

9.4.1 Falloff of side-scattered light with propagation distance

Measurements of side-scattered integrated luminance of POF were made by passing the fibre through an Oriel 70491 integrating sphere, with a BPW21 photo-diode as a detector. The experimental set-up is shown in Figure 9-4. A 1 cm wide strip of thin diffuse white card was used as a baffle for the detector to prevent light from the fibres directly striking the detector. The linearity of the BPW21 photo-detector over the measured range was first tested by measuring, then plotting, the detector voltage output of HeNe light transmitted through crossed polarisers, against the square of the sine of the angle between the polarisers.

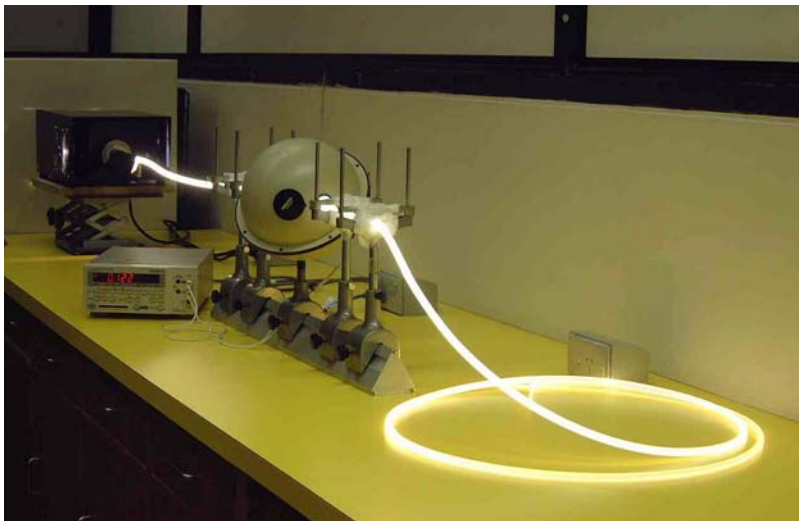

Figure 9-4. Measurements of side-scattered integrated luminance from POF using Oriel integrating sphere and photo-diode detector. The light source is the Poly Optics illuminator.

Relationship of side-scattered integrated luminance with distance from the light source was examined. Measurements were taken at various distances along a length of POF by moving the integrating sphere relative to the fibre. The integrating sphere is 20 cm in diameter, which means that total output light is measured for a 20 cm section of light guide. The validity of this method as a measurement of variation of side-light with dis-

tance was cross-checked by measurements using a spot photometer (Section 9.4.6). Measurements were made of 9 mm diameter POF, with TRIMM granule concentrations of 2000, 390, 200, and 20 ppm. The measurements were performed using each of the four coloured filters mounted in the illuminator: yellow, orange, blue and green.

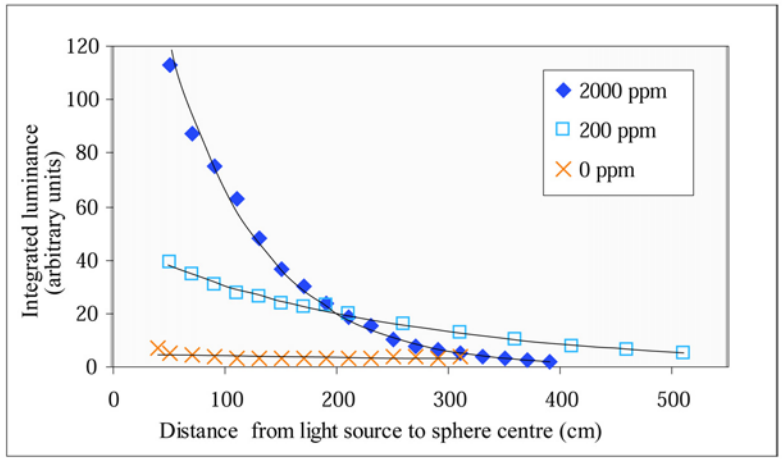

(a)

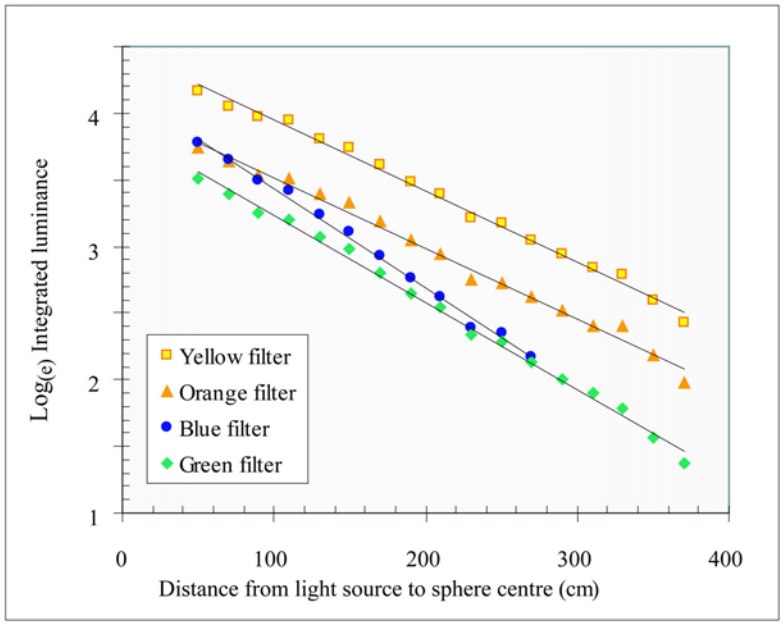

(b)

Figure 9-5. a) Integrated luminance vs distance along the light guide for 2000 ppm, 200 ppm and undoped 9 mm diameter POF, showing an exponential falloff of side-scattered intensity with distance from the (orange) light source. b) $Log_{(e)}$ integrated luminance vs distance along light guide to the centre of the integrating sphere, for 390 ppm 9 mm diameter POF. Results are shown for each of the illuminator's coloured filters.

The results show that there is an exponential 'falloff' of integrated side-light output with distance along the light guides from the source. Figure 9-5(a) illustrates this relationship for 2000 ppm and 200 ppm POF, compared with an undoped POF of similar diameter (the

orange filter was used). A plot of $Log_{(e)}$ of the side-light luminance vs length along the guide gives a straight line, for all measurement sets taken. (Similar measurements that were made of 14 mm diameter POF with 50 ppm and 100 ppm concentrations, and of 5 mm diameter POF with 50 ppm TRIMM granule concentration, evidenced the same relationship). This relationship of side-light 'falloff' with propagation distance is shown for each of the source colours in Figure 9-5(a), for the 390 ppm POF.

If S is the integrated luminance at each measurement point, then the relationship of S with distance along the light guide (z) from the source, can be expressed as:

$$S(z) = S(0)\, e^{-Fz} \qquad \textbf{(9-1)}$$

where $S(0)$ is the side-scattered brightness at the input end, F is the exponential decrease of side-scattered output and z is the propagation length along a light guide. If $Log_{(e)}S$ is plotted against z, as in Figure 9-5(b), then the resultant slope is rate of 'falloff' of output intensity with propagation distance along the light guide, i.e. F.

Table 9-1 gives F for POF containing four different concentrations of TRIMM, using the illuminator source with each of the four coloured filters in turn. It can be seen that the rate of falloff F is concentration dependent and, to a lesser extent, wavelength dependent. The uncertainty in F is higher for the 20 ppm fibre; partly because the falloff rate is lower, which makes slope determination more difficult, and partly because the 20 ppm fibre is shorter in length than the higher concentration fibres.

Table 9-1. 'Falloff slope' F (x 10^3 cm^{-1}) for 9 mm diameter TRIMM-doped POF.

		TRIMM granule concentration			
		20 ppm	*200 ppm*	*360 ppm*	*2000 ppm*
	Orange	-3.12	-4.26	-5.31	-12.0
lluminator filter	*Yellow*	-2.94	-4.53	-5.33	-12.5
colour	*Green*	-2.61	-5.49	-6.55	-14.6
	Blue	-2.74	-5.48	-7.44	-14.7

9.4.2 Relationship of falloff with TRIMM concentration

A graph of $Log_{(e)}$ of detector output voltage vs propagation distance for 9 mm POF was plotted using each of the coloured light filters. Each graph showed data for each of the four TRIMM concentrations available, obtained using one particular coloured filter.

Analysis of these graphs showed that there is a relationship between the rate of falloff of side-scattered integrated luminance with TRIMM concentration. Figure 9-6 shows the graphed results obtained using the green filter.

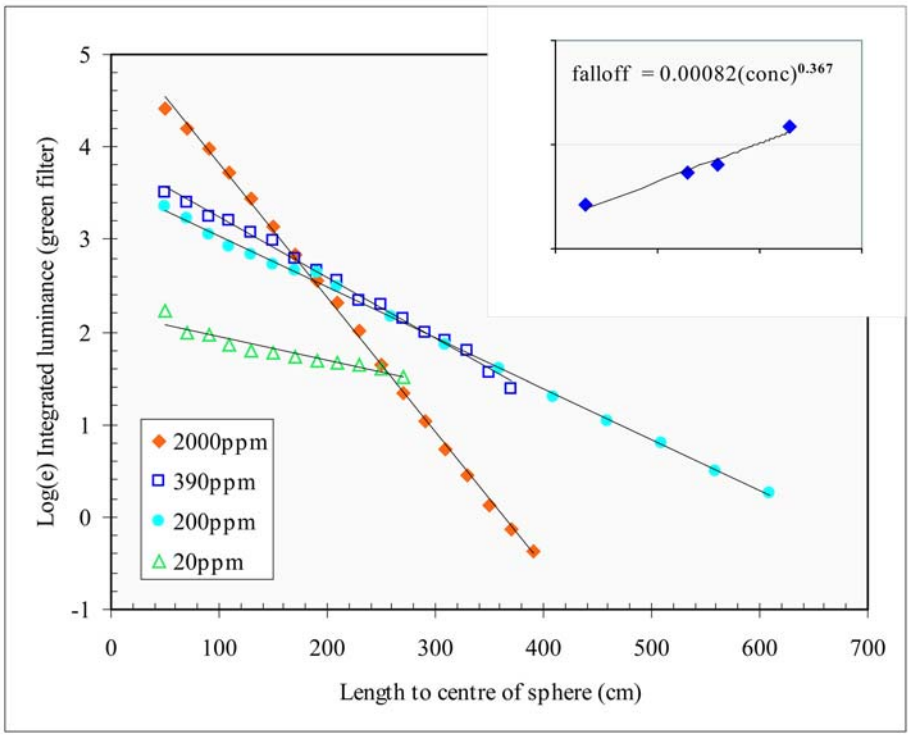

Figure 9-6. $\text{Log}_{(e)}$ integrated luminance vs propagation distance for 9 mm POF, for four TRIMM granule concentrations, using the green illuminator filter. Inset: Relationship of falloff F with TRIMM concentration for the same data.

The inset of Figure 9-6 shows the proportionality of the slope F to TRIMM granule concentration, for the illuminator with the green filter. For the 9 mm TRIMM-doped POF illuminated using the green filter, F is proportional to the concentration raised to the power of approximately one third, so

$$F \propto C^{\kappa} \qquad \textbf{(9-2)}$$

where C is the concentration of TRIMM granules in the matrix (in ppm) and $\kappa \approx 0.37$ for the green filter. This same analysis was performed for the other filter colours, and Table 9-2 shows that the exponent κ increases with decreasing wavelength.

Table 9-2. Power relationship of 'Falloff slope' with TRIMM granule concentration for 9 mm diameter POF.

Illuminator filter colour	*exponent of TRIMM granule concentration (κ)*
Orange	0.283
Yellow	0.303
Green	0.367
Blue	0.363

9.4.3 Colour variation with propagation distance

It is evident from examination of Table 9-1 and Figure 9-5(b) that, with the exception of the 20 ppm TRIMM-doped fibre, the rate of exponential falloff is slightly higher for the green and blue filters than for the yellow and orange. This loss of shorter wavelength light with propagation distance was also visible to the eye. Incident light that was transmitted through the clear filter at the illuminator, appeared faint yellow to the eye at the exit end of the guide, for undoped POF lengths of ≈ 10 m. For the TRIMM-doped guides, the blue source light appeared green at the exit end, for a guide length of ≈ 3 m for the 2000 ppm POF, and for a guide length of ≈ 5 m for the 200 ppm POF. The data presented in this chapter was performed early during the research project, before later improvements to the POF production process were made. It was initially unknown if this colour dependence was due to chemical impurities in the matrix material, or caused by the TRIMM particles. The role of the Teflon® cladding on the propagation processes was also unclear.

At a later time it became evident that the shorter wavelengths were being highly attenuated due to presence of chemical impurities. Improvements in the colour constancy with propagation distance in POF occurred when attention was given to removing these impurities during the production process. Subsequent undoped samples transmitted white light for ≈ 30 m without visible 'yellowing' of the output light. Hence, although it has been shown in Section 3.4 that TRIMM scattering exhibits some wavelength dependence, much of the colour shift described in the current section was not caused by the TRIMM particles. The interplay between guide quality and TRIMM scattering is work for the future.

9.4.4 Effect of fibre bending on side-light variation

The POF are packaged in coils, and as a result of storage are difficult to straighten completely when working with them. It was found that bending and twisting of the guides, including rotation of the source end of the guide in the manifold of the illuminator, caused small variations in side-light output. Care was taken to minimise this by clamping the guides as straight as possible.

If the longer lengths of POF are coiled, and the coils are allowed to touch during measurement, the side-light output readings decrease. This shows that light transfer can occur from one part of the guide to another via the Teflon®, if the relevant sections are in contact.

9.4.5 Diameter variation

Upon close inspection of Figure 9-5(b) and Figure 9-6, it can been seen that the measured output luminance varies in a periodic fashion with propagation distance along each light guide, falling variously above and below the plotted straight line. A similar phenomenon is evident in POF measurement data by another group (Narendran *et al.* 1998). Investigations were made to ascertain if this feature was material dependent, guide length dependent, or somehow connected to the source light distribution. Several previously measured long lengths of POF were cut into shorter, even lengths, and side-scattered integrated luminance measurements repeated. The variations persisted, and it was evident that the cause was linked to the material. The variations occurred at different distances along different cut sections, and, as the length of the sections were equal, the variation could not be due to guide length or light distribution. Similar variations, spaced ≈ 140-160 cm apart, were found in all data, for all POF diameters and concentrations.

At the suggestion of a colleague, detailed diameter measurements of several POF light guides were made. Measurement points along the guides were the same as for the previous side-scattered measurements. Two readings of diameter, orthogonal to each other, were made at each measurement point, using a micrometer. The average of these two measurements, av_i, was calculated at each measurement point. An average diameter for the entire length of the light guide, av_t, was then calculated, and the diameter variation for each measurement point expressed as $av_t - av_i$.

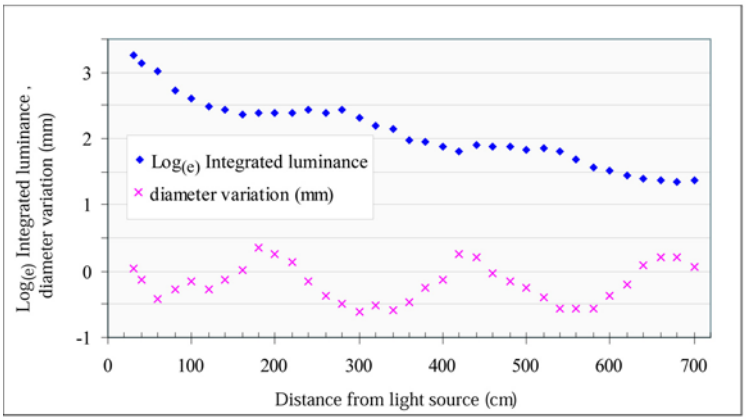

Figure 9-7. Comparison of the $\log_{(e)}$ integrated luminance measurements of 14 mm diameter 100 ppm POF, with the corresponding diameter variations of the fibre from average.

The lower trace in Figure 9-7 shows the diameter variation (in mm) as a function of distance along the guide for a 14 mm diameter TRIMM-doped POF. The upper trace shown is the $\log_{(e)}$ of side-scattered luminance as measured using the integrating sphere. It can be seen that the pattern of side-light output variation is directly related to the diameter variation with distance along the light guide. Variation in POF diameter corresponds to variations in light output because the critical angle with respect to the pipe axis changes as the diameter changes. When the light guide diameter is decreasing, one expects more light to escape, as some rays that would have been totally internally reflected, if the wall was parallel to the guide axis, can now escape (e.g. Ray 1 of Figure 9-8). Conversely, when the diameter is increasing, one expects a build-up of light internally within the light guide (see Ray 2 of Figure 9-8). It can be seen from Figure 9-7 that when the light guide diameter is decreasing, the side-scattered light is higher than expected if F was constant.

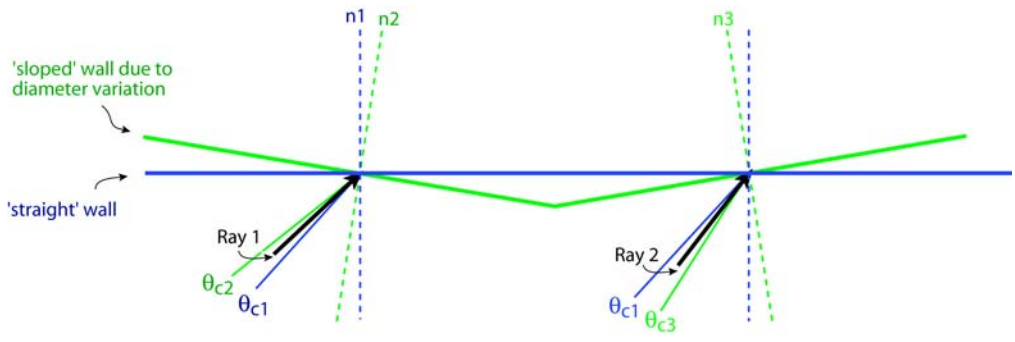

Figure 9-8. Schematic showing how diameter variation along a light guide can cause additional light to escape through the wall (Ray 1) or cause a decrease in side-light output (Ray 2). θ_{c1} is the critical angle for a light guide with uniform diameter; θ_{c2} is the critical angle for a wall sloped due to decreasing fibre diameter; θ_{c3} is the critical angle for a wall sloped due to increasing fibre diameter.

In addition, it was found that the variation of the side-scattered output is the most pronounced when the ovality of the guides is greatest. One 5 mm diameter light guide showed similar variation of av_i with length as for the guide shown in Figure 9-7, but in addition showed a marked increase in ovality with distance along the light guide. The difference between the two orthogonal diameter measurements increased from very close to zero at the source end of the guide (i.e. circular cross-sectional shape), to ≈ 30% of av_t at the exit end of the guide (i.e. oval cross-sectional shape). As the ovality of the cross-sectional shape increased, the variations in F increased. As a result of these findings, Poly Optics subsequently used Teflon® that expands isotropically as the cladding material for their light guides. This resulted in POF with close to uniform diameter and cross-sectional shape for the entire length of the guides.

9.4.6 Photometer measurements and addition of end reflector

As mentioned in Section 9.4.1, each side-scattered integrated luminance measurement of POF was measured over a 20 cm interval of the light guide, as constrained by the diameter of the integrating sphere. Is this a valid method of measuring, and presenting, the relationship of the side-scattered light with distance along the light guide from the source? To test this, luminance readings were made using a Hagner Universal Model S3 Photometer set to take 'spot' measurements, along a 2 m length of 9 mm 200 ppm TRIMM-doped POF. These were compared with corresponding measurements using the photo-diode and integrating sphere.

The illuminator, set on the green filter, was the light source for both types of measurements. The light guide was fixed at a constant height upon blocks, which were covered with a black cloth to minimise reflections. Two sets of readings were taken at intervals along the guide using the photometer; one at ≈ 40° from the horizontal, and one at ≈ 25° from the vertical. There was very little difference between the two sets of readings.

The same 2 m length of POF was also used to test the effect of an added end reflector on side-scattered distribution, using the integrating sphere. If a POF is to be used in a side-lighting application, it is desirable to have a constant side-scattered light distribution along the entire length of the light guide. Thus the aim to reduce 'falloff' rate F as much as possible. The effect of adding a reflector to the end of fibres was tested because it was noticed that the side-scattered integrated illuminance readings near the output end of the

light guides are dependent on the end orientation, and on the presence of any nearby reflecting surfaces.

A double layer of self-adhesive 3M® SilverLux® tape was affixed to the end of the guide, to form a reflecting surface. For this POF sample, using the green illuminator filter, the addition of a reflector to the guide end reduced *F* to approximately one half of *F* obtained without the reflector. For the same POF sample using the orange illuminator filter, adding the reflector reduced *F* to about one third of *F* without the reflector.

Figure 9-9 shows a graph of the photometer and integrating sphere readings (the latter with and without end reflector) performed on the same sample of 9 mm 200 ppm POF, using the green filter. The profile of the photometer readings is similar to that of readings obtained using the integrating sphere, as can be seen by comparing the blue coloured traces in Figure 9-9. The integrating sphere gives an 'averaged' reading over an extended length, so the output fluctuations that occur as a result of diameter variation along the guide are less pronounced than for the photometer data, which gives 'spot' readings. The integrating sphere measurements of the fibre with the added end reflector are shown in red; the resultant reduced falloff in slope of *F* is evident.

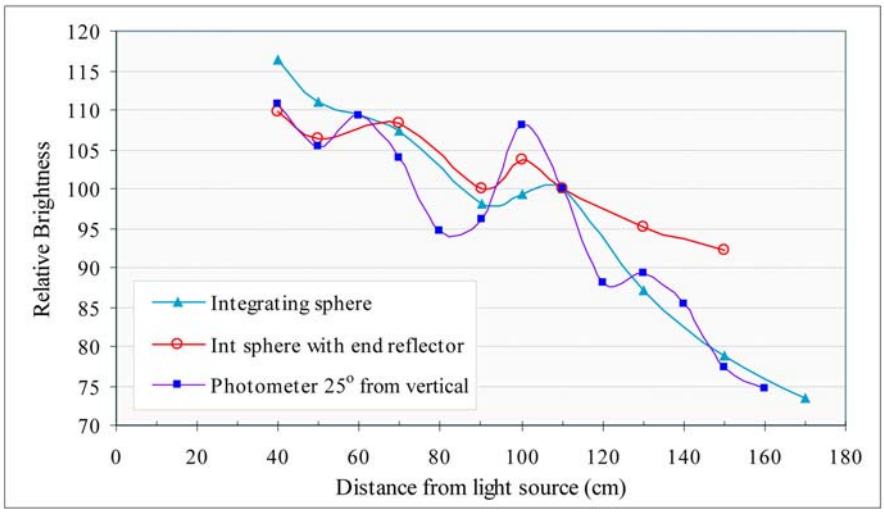

Figure 9-9. Comparison of integrating sphere and photometer illuminance measurements of a 2 m long 9 mm diameter 200 ppm POF; source is the illuminator with the green filter. Integrating sphere measurements with an end reflector are also shown. Measurements are normalised at a distance of 110 cm from the source end of the guide.

The optimum configuration required to obtain close to uniform side-scattered light output along a 9 mm diameter POF guide, using this illuminator light source, is approximately 2 metres in length, with a relatively low concentration of TRIMM scatterers. For POF

with a high concentration of added TRIMM, the addition of an end reflector only affects the falloff rate near the exit end of the guide. For example, the side-scattered luminance of a 2000 ppm length of POF ≈ 4.3 m in length was unchanged by addition of an end reflector up until a distance of ≈ 2.75 m along the light guide from the source. *F* for the end section of the guide (≈ 2.9 - 3.9 m from the source) was reduced by ≈ 13%.

9.5 Photogoniometer illuminance measurements of side-light

A photogoniometer built at UTS (Smith *et al.* 2001) was used to measure the angular distribution of side-scattered illuminance of a 9 mm diameter 200 ppm TRIMM-doped POF light guide. The section to be measured is aligned in the centre of the sphere of rotation of the measurement arm of the photogoniometer, with the aid of a peephole and a laser. A BPW21 photo-diode detector, mounted on the end of the 30 cm rotating arm, can take readings over a raster pattern following the profile of a sphere. (The photogoniometer scanning geometry was shown in Figure 5-2.)

Photogoniometer measurements of side-scattered light were carried out for 9 mm cylindrical light guides, with and without Teflon® cladding. The fibre was mounted on a custom-made holder, as shown in Figure 9-10. All of the fibre except for a short exposed length was covered with sleeves made from heavy black cloth. The exposed lengths were 5 cm, 2.5 cm, and 1 cm.

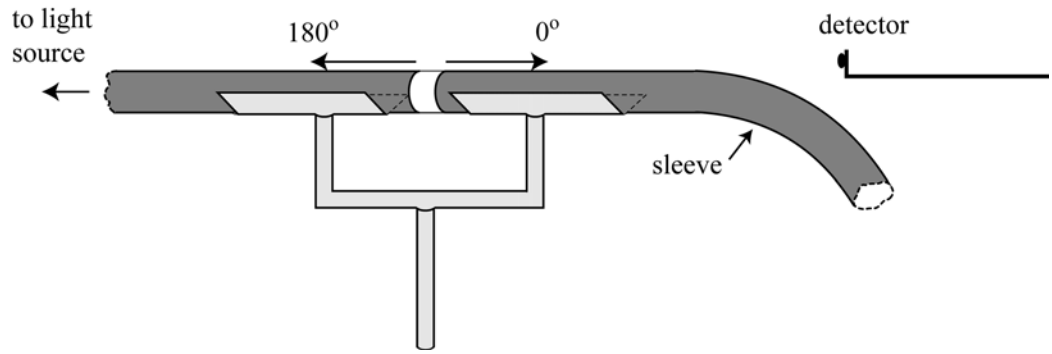

Figure 9-10. Photogoniometer set-up for POF directional scattering measurement.

9.5.1 Side-light scattered in the general propagation direction ('forward scattering')

Photogoniometer measurements of POF were made for the 3 different exposed strip lengths as described above, at distances of 80, 110 and 150 cm along the guide from the illuminator light source. Results for exposed sections at 80 cm along the light guide, with and without the Teflon® cladding, are shown in Figure 9-11. Measurements were taken

from 0° to 180° in 1° increments, 0° being the direction of forward light propagation.The signal reaching the detector near zero and 180° was blocked for some sample measurements as the cloth sleeves were not completely flat and flush with the light guide surfaces. It was difficult to reproduce the intensity of POF exactly between different runs because, as mentioned in Section 9.4.4, the side-scattered output of POF is very sensitive to movement. However, the profile of intensity with angle was consistent between experiments.

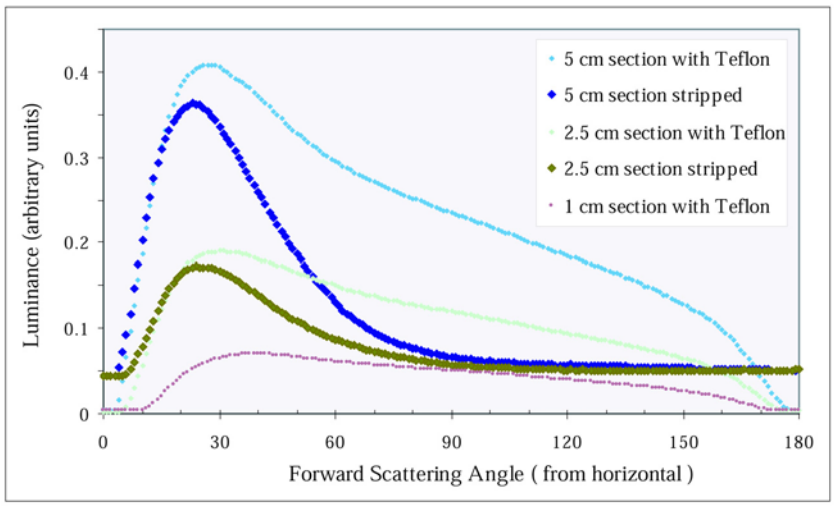

Figure 9-11. 'Side scattered' luminance (light escaped through the guide walls) of 200 ppm 9 mm diameter POF, at 80 cm along the guide from the source. 0° is the forward propagation direction. Measurements are shown for Teflon®-clad and Teflon®-stripped exposed sections of 5 cm, 2.5 cm and 1 cm in length. The light source was the illuminator with the clear filter.

The forward scattering caused by the TRIMM spheres is apparent, with the maximum scattering angle occurring at $\theta_{max} \approx 25°$ (from the horizontal) after refraction out of the light guide wall. This corresponds to an angle inside the core material of $\theta_{matrix} \approx 52.5°$. For meridional rays, the matrix-to-air critical angle corresponds to $\theta_{matrix} = 48°$ (with respect to the light guide axis). So for a ray to escape the wall at angle θ_{max}, a meridional ray travelling at the critical angle would be deviated by ≈ 4.5° before exit.

It is evident when comparing the 'Teflon®-stripped' POF side-scattered measurements shown in Figure 9-11, with the simulated distribution of wall exited rays from TRIMM-doped PMMA rods shown in Figure 8-7, that the agreement between simulated and measured side-light angular distributions is very good. (Note that the angle for the experimental distributions is measured from the horizontal, whereas the modelled distribution angles are measured from the vertical.)

The angle corresponding to maximum side-scattered luminance for the three exposed strip lengths, at 3 different distances along the measured Teflon®-clad light guide, are shown in Table 9-3.

Table 9-3. Angle (from horizontal forward direction) of maximum luminance, θ_{max}, for 200 ppm, 9 mm diameter POF, as measured by a photogoniometer. Light source is illuminator with clear filter.

		Distance along fibre from source			
		(Teflon® stripped) 80cm	*80cm*	*110cm*	*150cm*
Exposed fibre length	1.0cm	28°	37°	34°	33°
	2.5cm	24°	30°	25°	23°
	5.0cm	23°	27°	26°	26°

It is noted that:

1. The angle of maximum side-scattered luminance increases as the length of the exposed section decreases. (That is, θ_{max} shifts towards the normal to the guide wall.) It can be seen from Figure 9-11 that the maximum peak also becomes less pronounced. As a consequence, the forward scattering is more apparent when viewing a long exposed section; that is, the maximum luminance for long sections occurs closer to the horizontal axis of the light guide. The TRIMM and matrix material alone are highly forward scattering, whereas the Teflon® jacket tends to disperse the light, increasing the component of the total emitted light in the reverse direction.
2. The maximum side-scattered angle (from the horizontal) decreases with increasing propagation distance along the fibre. High angle rays from the source distribution are out-coupled after few TRIMM interactions, closer to the source end of the fibre.

9.5.2 Side-light scattered perpendicular to the general propagation direction

Measurements were also made around the circumference of the guide, at a distance of 110 cm from the source. The detector was set at the 90° position relative to the forward direction (refer Figure 9-10), and rotated in the plane normal to the exposed 1 cm POF section. Even though the TRIMM spheres are concentrated along one edge of the guide for these samples (as discussed in Section 3.2.1), side-light intensity measurements taken around the circumference of the guide were constant within ≈ 5%.

9.6 Internal light distribution model

The internal angular distribution of rays within POF were studied using Monte Carlo ray tracing modelling. Changes in these distributions with propagation along the light guides were recorded. The general ray tracing method for TRIMM-doped guides was described in Chapter 4.

Rays were launched in air from a point source located at the centre of the guide end, at a 0 - 20° incident angular spread, as an approximation of the light exiting the illuminator used for experimental measurements (Section 9.3.2). After launch, each ray was refracted into the fibre. Angular data, θ with respect to the light guide axis z, were recorded for each ray passing through planes perpendicular to the z-axis at predetermined distances from the source. The data has been normalised by dividing the number of rays by the number remaining within the interior of the light guide for each recording plane. Normalised angular distribution data is shown for a 1 cm square light guide in Figure 9-12. Here $\mu = 0.0182$ (as for POF), and the average path length $p = 3.5$ mm, corresponding to ≈ 20K TRIMM granule concentration. Angular distributions were recorded for rays travelling in a forward direction only.

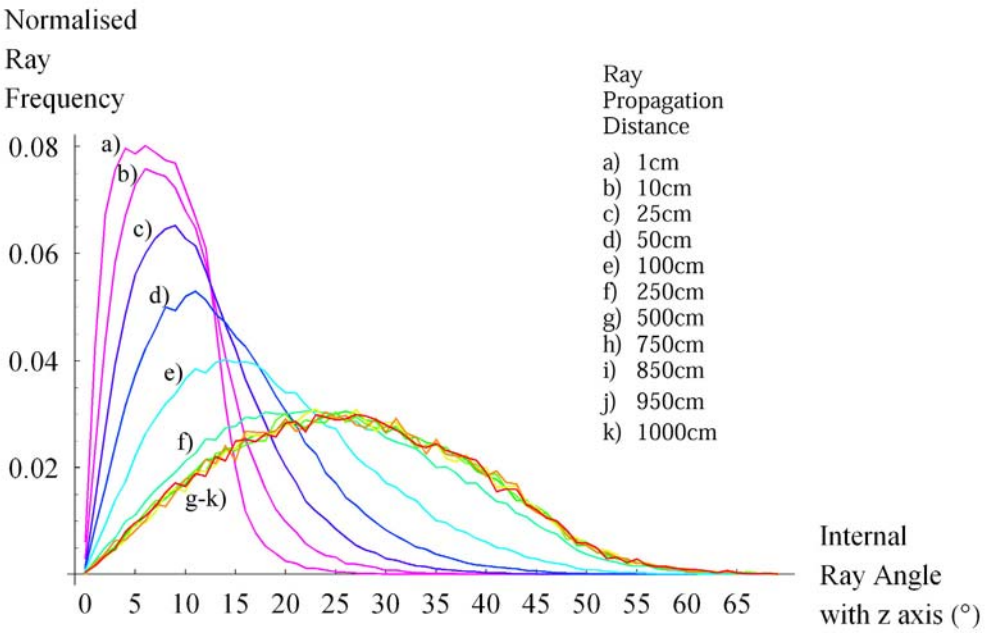

Figure 9-12. Normalised ray frequency vs θ for various distances along a 1 cm x 1 cm square light guide. The internal angular distribution becomes constant beyond 250 cm. Average path increment between spheres, $p = 3.5$ mm. Initial incidence angle 0 - 20° in air. 100,000 rays were launched.

Steady-state angular distribution occurs at ≈ 250 cm along the guide for the example shown in Figure 9-12, as the TRIMM concentration is relatively low. High concentrations of TRIMM result in a very similar distribution, although the steady state is reached at much shorter distances from the source. At the steady-state point, the intensity of side-scattered rays exiting the guide follows the exponential pattern of decay discussed in Section 9.4.1. The steady-state distribution is independent of incident angle.

Modelling of these parameters for a cylindrical guide with a diameter of 1 cm gave very similar results to Figure 9-12. The 'tail' at higher angles extends to 85° for the cylindrical guide, compared with the 65° for the square guide, due to the effect of skew rays in a cylindrical system, as explained in Chapter 4. Also, the angular peak region for curves (a - f) in Figure 9-12 are about 5° wider for the cylindrical guide model than for the square model.

10 Further Work and Applications

10.1 Applications of TRIMM

10.1.1 Mixing rods

TRIMM-doped mixing rods are ideal for homogenising light output, removing caustics that appear at the output end of 'clear' mixing rods, and combining light sources of different colours. There are many recent reports of technologies and systems where TRIMM could be incorporated to improve the light mixing.

The ends of clear PMMA rods have been roughened by researchers in order to mix RGB LEDs, or transport daylight, with a caustic-free output distribution (Shao *et al.* 2003, Zhao *et al.* 2002). TRIMM-doped rods are a superior alternative, as surface roughening results in losses from backscattering. Similarly, side-light has previously been produced by roughening of the sides of clear PMMA rods. The addition of TRIMM would result in a side-light with an improved light emission control rate, variable according to the TRIMM concentration.

For light guides used for backlighting, it is required that the variation of brightness across the screen be kept within 10% (Perduijn *et al.* 2000). In configurations where light is coupled directly into a light guide, paint or microstucture arrays have been used to out-couple the light, in addition to wedge shapes or aspheric geometry to obtain an even light distribution. An alternative to direct coupling is to use a mirror or diffuse reflector as part of the coupling process to scatter light and increase uniformity (Van Derlofske 2001, Martynov *et al.* 2003). The disadvantages of these approaches are the complicated manufacturing processes, high cost, and reflection and backscattering losses. The use of TRIMM is superior to the above designs, because homogenisation can be achieved with the use of simple light guide and source coupling geometries, with negligible backscattering loss.

Light guides are also used for light transport and uniform illumination in data projectors. Commonly, light from source LEDs is coupled into a mixing rod via a parabolic or cylindrical reflector (Martynov *et al.* 2003, Lee *et al.* 2004). For mixing rods relying only on TIR, a length to width aspect ratio of 10:1 is currently required, and even longer lengths

are needed for very high levels of uniformity (Krijn *et al.* 2004, Irving 2003, Li *et al.* 2004). TRIMM-doped mixing rods have reduced this aspect ratio to about 3:1 or lower. Furthermore, LEDs can be coupled directly into a TRIMM mixer, eliminating the losses induced by using a coupling reflector.

Lumileds™ have contrasted 3 types of ultra compact projectors, each using different source LEDs (Keuper *et al.* 2003);

1. Single white LED source. The projector efficacy is low because 2/3 of the light is wasted in colour filters.
2. RGB source in a single package. Duty cycling of the individual RGB chips reduces the projector efficacy.
3. 4 x white LEDs. A 3 cm mirror light pipe was needed to achieve a uniform illumination pattern on the display.

A preferable alternative to all of the above is to use separate RGB LEDs as sources, and adopt a TRIMM-doped mixing rod to combine their outputs for uniform, low-loss light display. Research aimed at facilitating the adoption of TRIMM in backlighting and projector displays should yield fruitful results for these developing technologies.

10.1.2 Step safety lights

TRIMM-doped rods with an LED mounted at each end were installed on steps in a UTS lecture theatre during the course of this research. They can be lit for long periods of time with very low energy consumption. They serve as safety lighting for people entering or leaving the theatre when the main room lights are turned off. Further research could be undertaken to study the lighting distributions resulting from different source configurations and TRIMM concentrations, the optimum position for the lights to be placed on the steps, and so forth.

10.1.3 Refrigerators

Fluorescent lights are commonly used for refrigerator lighting for shop display. Fluorescent lights convert only 25% total energy consumed into light; the remainder is converted to heat. This is obviously a double disadvantage if they are used in refrigeration units. The luminous efficacy of fluorescents decreases with decreasing temperature, and furthermore, only 60% of the light emitted is in the direction useful for lighting, as the light emitted 'backwards' towards the refrigerator wall is wasted. It has been estimated that, if white

LEDs are used as an alternative to fluorescents, there would be a 70% reduction in energy consumption of these fridges by 2010 (Raghavan *et al.* 2002). The use of RGB LEDs and TRIMM mixing rods would increase these energy savings still further, since the light sources would be positioned exterior to the fridge, so no heat from the light sources enters the refrigerated compartment. In addition, light that exits the TRIMM mixer in a 'reverse' direction can, unlike fluorescent lights, be transmitted through the mixer after reflection from the wall.

10.1.4 Recently patented RGB mixer

A patent for a "color-mixing lighting system" has been filed recently (Koninklijke Philips Electronics 2005). Essentially, blue and green leds are embodied in a reflector, along with a luminescent red material to provide the red colour for RGB colour mixing. The idea was conceived to circumnavigate the problems of flux and colour variation with temperature induced by the use of red LEDs, since small variations in the peak wavelength of red LEDs can cause relatively large changes in colour rendering index. This design uses a reflector to mix the colours in air. It is evident that several reflections would be necessary to achieve adequate spatial and angular uniformity of mixing, hence the efficacy of the system is lowered. A solid TRIMM mixer would be an energy efficient alternative to the reflector in this case.

10.1.5 Spectrally tunable solid state calibration source

A spectrally tunable solid state light source is currently being constructed at the National Institute of Standards and Technology (NIST) in the United States of America (Fryc *et al.* 2004). Measurement errors increase dramatically if the relative spectral power distribution (SPD) of a test source differs from that of a calibration source. Variation in the SPD between LEDs to be measured has prompted the design of this calibration source consisting of 80, 40 or 20 LEDs, depending on the resolution required. Clearly, a requirement for this source is the homogenous mixing of the light from many LEDs. The author of this thesis was approached by Dr Ohno, a project leader at NIST, about the possibility of using a TRIMM mixer to combine the light from the LEDs.

10.1.6 Commercial interest

A patent has been lodged for the use of TRIMM-doped materials as light mixers (Smith *et al.* 2004). The author received enquiries regarding the state of commercialisation of TRIMM mixers as a result of a published paper (Deller *et al.* 2004), magazine article

(Overton 2004) and a conference presentation (Deller *et al.* 2004). Representatives from Lawrence Berkley National Laboratory, Coherent, and OSRAM, as well as a private designer, contacted me requesting samples, scientific collaboration, bulk quantities or information regarding licensing. The various interests of these, and similar groups could later generate new projects.

10.2 Further improvements in efficiency

Almost all light loss in a TRIMM mixer is due to Fresnel reflection at the input and exit ends. At the input end of a mixing rod, this can be reduced by an anti-reflection surface, or by optically integrating the LED chips with the rod. At the output end, Fresnel reflection can be reduced by an anti-reflection coating, or by using a specially shaped end. With such additional measures, TRIMM mixers should deliver homogeneous complete colour mixing in a compact system with transport efficiency of greater than 92%. A luminaire or reflector integrated with the clear PMMA rod with TRIMM diffuser sheet would also capture the small amount of side-emitted light, and this could be directed forward to add to the useful forward light output.

10.3 Optimising colour and efficacy of RGB LEDs

The work in this thesis considers combining the light of coloured LEDs to obtain uniform illumination on a projected surface, using light guides that are low in material cost and high in light transport efficiency. It does not consider balancing the desired output colour with maximum flux, minimum cost, maximum efficacy, and maximum colour rendering index of the source LEDs. This has been considered by Ries and Leike (Ries *et al.* 2004) who gave guidelines for choosing the correct number of LEDs of various colours, and the corresponding drive currents, but did not consider "various optical means to mix the light in the phase space of radiation".

If the amount of flux, the efficacy or the colour rendering index is optimised in a multi-chip LED colour mixing system, performance may be very poor in the other aspects. Optimisation of CRI usually leads to low luminous flux values. One problem with specifying CRI is that often an abbreviated version, R_a, is calculated. R_a consists of 8 colour samples that are low in saturation. Two different 3-chip RGB LED sources may have the same value of R_a, but one may have very poor colour rendering of bright red, or of red/green contrast for example (Ohno 2004). In certain applications a lamp with relatively low CRI

may be preferred by a human observer over a lamp with high CRI. These are matters that should be considered in further work of mixing RGB LEDs for illumination purposes.

10.4 μ vs λ dependence and side-scattering POF

It was demonstrated in Section 7.1 that the dependence of μ on λ does not impact visually on the colour output for short rods. This may not be the case when using long lengths of POF for side-lighting. The evolution of internal ray distributions with propagation distance along a POF light guide was studied with a constant value of μ. This work did not encompass the study of colour variations of side-scattered light with propagation distance along a light guide. Bends in the flexible POF were also not considered in the computer modelling.

10.5 Computer Simulations

The ray tracing computer program in its present form, although a useful tool, is not suited for studying light transport through high concentration TRIMM-doped light guides of long length. The practical limit is ray tracing simulations of 100 K 10 cm TRIMM-doped rods, due to long simulation times. With further development, the mathematical models for multiple scattering in TRIMM-doped rods given in Section 2.3 could be utilised to design TRIMM systems with reduced computing time. In addition, the rate of side-emission along a TRIMM-doped light guide can be predicted for the constant internal angular distribution region (as discussed in Section 9.6), thus eliminating the need for further simulations in long TRIMM systems.

10.6 Conclusion

Complete homogeneity in colour mixing can be achieved using short PMMA rods doped with TRIMM particles. The output is diffuse, which reduces source glare and creates uniform illuminance for good quality lighting. The TRIMM particle concentration, source arrays and screen distance from the output end of the rods can be tailored to suit the desired application. Forward transmittance of light is high, since almost all of the losses are due to Fresnel reflectance from the input and output surfaces. TRIMM-doped polymers are also useful as side-emitting sources, and long lengths of POF are suitable for light transport. LEDs are readily coupled into TRIMM-doped light guides, resulting in a simple, low-cost, energy efficient alternative for lighting.

Bibliography

Allan, W.B., (1973) "Fibre Optics: Theory and Practice", London, New York: Plenum Press.

Azzam, R.M.A., Bashara, N.M., (1977) "Ellipsometry and polarized light", Amsterdam; New York: North-Holland Pub. Co.

Barreneche, R.A., (1997) "Shedding light on fiber optics", Architecture **86**(4), 162-165.

Benítez, P., Miñano, J.C., Hernández, M., (2004) "On the analysis of microstructured surfaces", in *Proceedings of SPIE Vol 5529: Nonimaging Optics and Efficient Illumination Systems*, 186-197.

Berthet, R., Brun, G., Zerroukhi, A., et al., (2001) "Plastic optical fibers for lateral illumination: synthesis and scattering studies when polymer micro-particles are added", in *POF 2001: 10th Annual International Conference of the Polymer Optical Fibre Trade Organisation*, 361-367.

Biermann, A., Narendran, N., Maliyagoda, N., (1998) "How to report light loss values for optical fibers used in fiber-optic lighting applications", in *Proceedings of SPIE Vol 3428: Illumination and Source Engineering*, 62-72.

Bockstaele, R., Sys, C., Blondelle, J., et al., (1999) "Resonant Cavity LEDs Optimized for Coupling to Polymer Optical Fibers", IEEE Photonics Technology Letters **11**(2), 158-160.

Boher, P., Luet, M., Leroux, T., (2004) "Rapid Photo-goniometric Technique for LED Emission Characterization", in *Proceedings of SPIE Vol 5530: Fourth International Conference on Solid State Lighting*, 99-110.

Broehl, J., (Feb 2005) "Lighting Up the Road Ahead", in *Renewable Energy Access*, website: http://www.renewableenergyaccess.com/rea/news/story?id=22477 (accessed April 7th 2005).

Brown, D., Nicol, D., Payne, A., et al., (2004) "Investigation of the Spectral Properties of LED-based MR16s for General Illumination", in *Proceedings of SPIE Vol 5530: Fourth International Conference on Solid State Lighting*, 160 -164.

Budimir, M., (2004) "Bright Ideas", Machine Design **76**(4), 134-136.

Callow, J.M., Shao, L., (2003) "Air-clad optical rod daylighting system", Lighting Research and Technology **35**(1), 31-38.

Cassarly, W.J., (2002) "LED Modeling: Pros and Cons of Common Methods", in *Photonics Tech Briefs Online*, website: http://www.ptbmagazine.com/articles/April_2002_article.html (accessed 8th April 2005).

Cassarly, W.J., Davenport, J.M., Hansler, R.L., (1995) "Distributed Lighting Systems: Uniform Light Delivery", SAE Technical Paper Series **950904**, 1-5.

Cassarly, W.J., Davenport, J.M., Hansler, R.L., (1996) "Uniform Light Delivery Systems", SAE Technical Paper Series **960490**(1-4).

Cassarly, W.J., Davenport, T.L., Hansler, R.L., et al., (1997) "Comparison of Dual Focus Collector Schemes for Fiber Systems", SAE Technical Paper Series **970254**, 1-10.

Cayless, M.A., Marsden, A.M., eds. (1983) "Lamps and Lighting", 3rd ed. Edward Arnold: London.

CIE Publication No.127, (1997) "Measurement of LEDs", Available through the CIE web site: http://www.cie.co.at/framepublications.html.

CIE Publication No.13.3, (1995) "Method of Measuring and Specifiying Colour Rendering Properties of Light Sources".

Cozannet, A., Treheux, M., (1975) "Skew rays in optical fibers", Applied Optics **14**(6), 1345-50.

Craford, M.G., Holonyak, N., Kish, F.A., (2001) "In Pursuit of the Utimate Lamp", Scientific American **284**(2), 62-68.

CRC, (1991) "CRC Handbook of Chemistry and Physics", Cleveland, Ohio: CRC Press.

Cree inc, (2004) "Cree XLAMP™ LEDs achieve industry's highest white light brightness", website: www.cree.com/News/news210.asp (press release: accessed 13th May 2005).

Crist, B., Marhic, M.E., Raviv, G., et al., (1980) "Optical absorption in polymer glasses by laser calorimetry", Journal of Applied Physics **51**(2), 1160-2.

Davenport, J.M., Cassarly, W.J., (1998) "Advances in Fiber Optics: Fiber Applications Move into the Mainstream", in *The 8th International Symposium on the Science and Technology of Light Sources*, 61-69.

Decker, D., (Dec 2000) "High-flux LED light sources", Automotive Engineering International, 62-4.

Deller, C., Smith, G.B., Franklin, J., (2004) "Uniform white light distribution with low loss from coloured LEDs using polymer doped polymer mixing rods", in *Proceedings of SPIE Vol 5530: Fourth International Conference on Solid State Lighting*, 231-240.

Deller, C.A., Smith, G.B., Franklin, J., (2004) "Colour mixing LEDs with short microsphere doped acrylic rods", Optics Express **12**(15), 3327-3333.

Doyle, S., Corcoran, D., Connell, J., (1999) "Automated mirror design for an extended light source", in *Proceedings of SPIE Vol 3781: Nonimaging Optics: Maximum Efficiency Light Transfer V*, R. Winston, Editor, 94-102.

Driscoll, W.G., Vaughan, W., eds. (1978) "Handbook of Optics", McGraw-Hill.

Dugas, J., Sotom, M., Martin, L., et al., (1987) "Accurate characterization of the transmittivity of large-diameter multimode optical fibers", Applied Optics **26**(19), 4198-4208.

Durret, H.J., ed. (1987) "Color and the Computer", Academic Press, Inc.

Edmonds, I.R., Moore, G.I., Smith, G.B., et al., (1995) "Daylighting enhancement with light pipes coupled to laser-cut light-deflecting panels", Lighting Research and Technology **27**(1), 27-35.

Elmualim, A.A., Smith, S.J., Riffat, S.B., et al., (1999) "Evaluation of dichroic material for enhancing lightpipe/natural ventilation and daylighting in an integrated system", Applied Energy **62**, 253-266.

Feuermann, D., Gordon, J.M., Huleihil, M., (2001) "Light Leakage in Optical Fibers: Experimental Results, Modeling and the Consequences for Solar Concentrators", Solar Energy **72**(3), 195-204

Feuermann, D., Gordon, J.M., Ries, H., (1998) "Nonimaging optical designs for maximum-power-density remote irradiation", Applied Optics **37**(10), 1835-44.

Foley, J.D., van Dam, A., Feiner, S.K., et al., (1995) "Computer Graphics Principles and Practice", 2nd ed.: Addison-Wesley.

Fryc, I., Brown, S.W., Eppeldauer, G.P., et al., (2004) "A Spectrally Tunable Solid-State Source for Radiometric, Photometric and Colorimetric Applications", in *Proceedings of SPIE Vol 5530: Fourth International Conference on Solid State Lighting*, 150-159.

Garcia-Botella, A., Vazquez, D., Bernabeu, E., (2000) "A New Concentrator-Collimator Lighting System Using LED Technology", Journal of the Illuminating Engineering Society **29**(2), 135-140.

Green, D., Milanovic, M., (2003) "Solid-state lighting offers 'vices' as well as 'virtues'", Laser Focus World **39**(9), 99-103.

Grossman, S., (2000) "Color LEDs take on a new assignment - Backlighting LCDs", Electronic Design **48**(16), 30-31.

Guo, Z., Daly, S.R., Matson, J., (2003) "Optical Modeling of Cylindrical Light Sources within Tissue", in *Proceedings of SPIE Vol. 4961: Laser-Tissue Interaction XIV*, 114-121.

Gupta, A., Lee, J., Koshel, R.J., (2001) "Design of efficient lightpipes for illumination by an analytical approach", Applied Optics **40**(22), 3640-3645.

Hancock, J.J., Baker, D.J., Ware, G.A., (2004) "An optical source for characterizing CMOS imagers", in *Proceedings of SPIE Vol 5529: Nonimaging Optics and Efficient Illumination Systems*, 140-149.

Hecht, E., (1998) "Optics", 3rd ed.: Addison Wesley Longman.

Hemsley, D.A., ed. (1989) "Applied Polymer Light Microscopy", Elsevier Applied Science: London, New York.

Hopkins, G.W., Simons, T.D., (1999) "Cylindrical light pipes for collecting light scattered from a Gaussian beam", in *Proceedings of SPIE Vol 3781: Nonimaging Optics: Maximum Efficiency Light Transfer V*, 202-208.

Irvin, B.R., Nakamura, T., (1991) "Characterization of optical fibers for solar energy transmission", Journal of Solar Energy Engineering: Transactions of the ASME **113**, 359-366.

Irving, B., (2003) "Illumination Design Gets Faster, Easier", Photonics Spectra **37**(4), 109-112.

Jenkins, T.E., (2000) "Errors in the refractive indices of solids measured using a 45 degree angle-of-incidence technique", measurement science and technology **11**(6), 828-832.

Jonsson, J.C., Smith, G.B., Deller, C., et al., (2005) "Directional and angle-resolved optical scattering of high-performance translucent polymer sheets for energy efficient lighting and skylights", Applied Optics **44**(14), 2745-2754.

Kaino, T., Jinguji, K., Nara, S., (1982) "Low loss poly(methyl methacrylate-d5) core optical fibers", Applied Physics Letters **41**(9), 802-4.

Kaino, T., Jinguji, K., Nara, S., (1983) "Low loss poly(methylmethacrylate-d8) core optical fibers", Applied Physics Letters **42**(7), 567-9.

Kan, P., Whitehead, L.A., Pojar, S.J., et al., (2000) "Structure for Efficiently Coupling Large Light Sources into Prism Light Guides", Journal of the Illuminating Engineering Society **29**(2), 78-82.

Kerker, M., (1965) "Light Scattering from Colloidal Spheres and Cylinders", in *Electromagnetic Scattering*, R.L. Rowell and R.S. Stein, Editors, Gordon and Breach Science Publishers: New York, London, Paris.

Kerker, M., (1969) "The Scattering of Light and Other Electromagnetic Radiation", New York, London: Academic Press.

Keuper, M., Paolini, S., Harbers, G., et al., (2003) "Ultra-Compact LED based Image Projector for Portable Applications", SID 03 Digest.

Keuper, M.H., Harbers, G., Paolini, S., (2004) "RGB LED Illuminator for Pocket-Sized Projectors", SID 04 Digest, 943-645.

Knisley, J., (2002) "Understanding LED technology", Electrical Construction and Maintenance **101**(4), 54-6.

Knisley, J., (2003) "Lamp and Ballast Update", Electrical Construction and Maintenance **102**(10), C6,C8-9.

Knisley, J., (2003) "New strides in LED technology could be a sign of things to come", Electrical Construction and Maintenance **102**(11), 16-18.

Koninklijke Philips Electronics N.V., "Color-Mixing Lighting System", *World Intellectual Property Organisation* (2005), Patent: International Publication Number WO 2005/022030 A2.

Krijn, M.P.C.M., Salters, B.A., de Vaan, A.J.S.M., (2004) "Light guide based optical engine for light-valve-projection", in *Proceedings of SPIE Vol 5529: Nonimaging Optics and Efficient Illumination Systems*, 17-26.

Labsphere, (2001) "The Radiometry of Light Emitting Diodes", website: http://www.labsphere.com/applications.asp?appId=1&catId=14 (accessed 7th April 2005).

Latvala, J., (2003) "Lighting management for multimedia displays", Power Electronics Technology **29**(10), 30-33.

Lazarus, M.J., Ellarby, V., Campbell, D., (2001) "Enhanced Coupling of Light Emitters to Plastic Optical Fiber With the Use of Bulb-lens Antenna Systems", Microwave and Optical Technology Letters **33**(1), 6-9.

Lee, J., Greivenkamp, J.E., (2004) "Modeling of automotive interior illumination systems", Optical Engineering **43**(7), 1537-1544.

Lee, W.Y., Lee, Y.C., Sokolov, K., et al., (2004) "LED projection displays", in *Proceedings of SPIE Vol 5529: Nonimaging Optics and Efficient Illumination Systems*, 1-7.

Lee, W.Y., Lim, T.K., Lee, Y.W., et al., (2003) "Fast ray tracing method for LCD backlight simulation using area ratio function", in *Proceedings of SPIE Vol 5186: Design of Efficient Illumination Systems*, 175-182.

Leutz, R., Ries, H., (2003) "Squaring the circle - The Use of Microstructures for Converting and Homogenizing Beam Patterns", in *Proceedings of SPIE Vol 5186: Design of Efficient Illumination Systems*, 106-112.

Li, K., Sillyman, S., Inatsugu, S., (2003) "Etendue Efficient Illumination System using Dual Paraboloid Reflectors and Lensed Tapered Light Pipes", in *Proceedings of SPIE Vol 5186: Design of Efficient Illumination Systems*, 143-153.

Li, K.K., Sillyman, S., Seiji, I., (2004) "Optimization of dual paraboloidal reflector and polarization system for displays using a ray-tracing model", Optical Engineering **43**(7), 1545-1551.

Li, Y., Wang, T., (1996) "Distribution of Light Power and Optical Signals Using Embedded Mirrors Inside Polymer Optical Fibers", IEEE Photonics Technology Letters **8**(10), 1352-4.

Littlefair, P.J., (1989) "Innovative daylighting systems", Building Research Establishment Information Paper **IP 22/89**.

MacAdam, D.L., (1942) "Visual sensitivities to color differences in daylight", Journal of the Optical Society of America **49**, 1143-6.

Marcou, J., ed. (1997) "Plastic optical fibres: practical applications", John Wiley: Chichester, New York.

Martynov, Y., Konijn, H., Pfeffer, N., et al., (2003) "High-efficiency slim LED backlight system with mixing light guide", SID 03 Digest, 43.3.

Mathis, R.F., (1997) "Efficient Coupling of Noncoherent Light to Fiber Optic Light Guides", in *Proceedings of SPIE Vol 3139: Nonimaging Optics: Maximum Efficiency Light Transfer IV*, 165-169.

Mie, G., (1908) "Considerations on the optics of turbid media, especially colloidal metal sols", Annalen der Physik **25**, 377.

Mildner, D.F.R., Chen, H., (1994) "The Neutron Transmission through a Cylindrical Guide Tube", Journal of applied Chrystallography **27**, 316-325.

Miller, C.C., Zong, Y., Ohno, Y., (2004) "LED photometric calibrations at the National Institute of Standards and Technology and future measurement needs of LEDs", in *Proceedings of SPIE Vol 5530: Fourth International Conference on Solid State Lighting*, 69-79.

Morrison, D., (Dec 2000) "Brighter LEDs Signal Longer Life and Lower Power for Lighting Applications", Electronic Design, 79-88.

Mueller-Mach, R., Mueller, G.O., (2000) "White light emitting diodes for illumination", in *Proceedings of SPIE Vol 3938: Light-Emitting Diodes: Research, Manufacturing, and Applications IV*, 30-41.

Mueller-Mach, R., Mueller, G.O., Trottier, T., et al., (2002) "Green Phosphor-Converted LED", in *Proceedings of SPIE Vol 4776: Solid State Lighting II*, 131-136.

Murdoch, J.B., (1985) "Illumination Engineering - From Edison's Lamp to the Laser", New York: Macmillan.

Narendran, N., Bullough, J.D., Maliyagoda, N., et al., (2001) "What is Useful Life for White LEDs?", Journal of the Illuminating Engineering Society **30**(1), 57-66.

Narendran, N., Deng, L., (2002) "Color Rendering Properties of LED Light Sources", in *Proceedings of SPIE Vol 4776: Solid State Lighting II*, 61-67.

Narendran, N., Gu, Y., Freyssinier, J.P., et al., (2004) "Solid-state lighting: failure analysis of white LEDs", Journal of Crystal Growth **268**, 449-456.

Narendran, N., Maliyagoda, N., (1998) "Characterizing fiber-optic illuminators for lighting applications", in *Proceedings of SPIE Vol 3428: Illumination and Source Engineering*, 45-55.

Narendran, N., Maliyagoda, N., Levin, R., (2000) "Propagation Characteristics of Polychromatic Light Through Polymer Optical Fibers", Journal of the Illuminating Engineering Society **29**(1), 81-89.

Oakley, G., Riffat, S.B., Shao, L., (2000) "Daylight Performance of Lightpipes", Solar Energy **36**(2), 89-98.

Ohno, Y., (2004) "Color Rendering an Luminous Efficacy of White LED Spectra", in *Proceedings of SPIE Vol 5530: Fourth International Conference on Solid State Lighting*, 88-98.

Okumura, T., Ishikawa, T., Tagaya, A., et al., (2003) "Optical design of liquid crystal display backlighting with high scattering optical transmission polymer", Journal of Optics A: Pure and Applied Optics **5**, S269-S275.

Optical Research Associates, (2004) "LED Product Database Files", website: http://www.opticalres.com/ltdownloads_f.html (accessed April 7th 2005).

Orava, J., Jaaskelainen, T., Parkkinen, J., (2004) "Color Errors of Digital Cameras", Color Research and Application **29**(3), 217-221.

Overton, G., (2004) "Microsphere-doped acrylic rods mix colors", Laser Focus World **40**(10), 17-18.

Pelka, D.G., Patel, K., (2003) "An Overview of LED Applications for General Illumination", in *Proceedings of SPIE Vol 5186: Design of Efficient Illumination Systems*, 15-26.

Perduijn, A., de Krijger, S., Claessens, J., et al., (2000) "Light Output Feedback Solution for RGB LED Backlight Applications", SID 00 Digest.

Poly Optics Australia Pty Ltd, see http:\\www.fiberopticlight.com.

Poppendieck, M., (1998) "Test Methods for Optical Fiber", in *Proceedings of SPIE Vol 3428: Illumination and Source Engineering*, 90-97.

Pritchard, D.C., (1985) "Lighting", 3rd ed. Essex: Longman Group Limited.

Rabl, A., Gordon, J.M., (1994) "Reflector design for illumination with extended sources: the basic solutions", Applied Optics **33**(25), 6012-6021.

Radiant Imaging inc, (2004) "ProSource", website: http://www.radiantimaging.com/dloverview.htm (accessed 7th April 2005).

Raghavan, R., Narendran, N., (2002) "Refrigerated Display Case Lighting with LEDs", in *Proceedings of SPIE Vol 4776: Solid State Lighting II*, 74-81.

Remillard, J.T., Everson, M.P., Weber, W.H., (1992) "Loss mechanisms in optical light pipes", Applied Optics **31**(34), 7232-40.

Ries, H., (1997) "Performance limitations of rotationally symmetric nonimaging devices", Journal of the Optical Society of America **14**(10), 2855-2862.

Ries, H., Leike, I., (2004) "Optimized additive mixing of colored light-emitting diode sources", Optical Engineering **43**(7), 1531-1536.

Robinson, G.W., Cho, C.H., Gellene, G.I., (2000) "Refractive Index Mysteries of Water", Journal of Physical Chemistry B **104**, 7179-7182.

Ryde, J.W., Cooper, B.S., (1931) Proceedings of the Royal Society **A131**, 451.

Saddlers, J., (2001) "Light Fantastic: the automotive industry turns to fibre optics", Engineering **242**(12), 45-46.

Sales, T.R.M., Chakmakjian, S., Schertler, D.J., et al., (2004) "LED illumination control and color mixing with engineered diffusers", in *Proceedings of SPIE Vol 5530: Fourth International Conference on Solid State Lighting*, 133-140.

Saraiji, R.M.N., Mistrick, R.G., Modest, M.F., (1996) "Modeling Light Transfer through Optical Fibers for Illumination applications", Journal of the Illuminating Engineering Society **25**(2), 128-138.

Savage, N., (2000) "LEDs light the future", Technology Review **103**(5), 38-44.

Saxe, S., Whitehead, L.A., Cobb, S.J., (1986) "Progress in the development of prism light guides", in *Proceedings of SPIE Vol 692: Materials and Optics for Solar Energy conversion and Advanced Lighting Technology*, 235-40.

Schiebener, P., Straub, J., (1990) "Refractive Index of Water and Steam as Function of Wavelength, Temperature and Density", Journal of Physical and Chemical Reference Data **19**(3), 677-717.

Shakir, I., Narendran, N., (2002) "Evaluating white LEDs for outdoor lighting applications", in *Proceedings of SPIE Vol 4776: Solid State Lighting II*, 162-170.

Shao, L., Callow, J.M., (2003) "Daylighting performance of optical rods", Solar Energy **75**, 439-445.

Shatz, N., Bortz, J., Ries, H., et al., (1997) "Nonrotationally symmetric nonimaging systems that overcome the flux-transfer performance limit imposed by skewness conservation", in *Proceedings of SPIE Vol 3139: Nonimaging Optics: Maximum Efficiency Light Transfer IV*

Sillyman, S., Li, K., Inatsugu, S., (2004) "Source numerical aperture control for efficient light emission from notched, side-lighting fiberoptics", in *Proceedings of SPIE Vol 5529: Nonimaging Optics and Efficient Illumination Systems*, 70-78.

Smith, G.B., Deller, C.A., Swift, P.D., et al., (2002) "Nanoparticle-doped polymer foils for use in solar control glazing", Journal of Nanoparticle Research **4**, 157-165.

Smith, G.B., Green, D.C., McCredie, G., et al., (2001) "Optical Characterisation of Materials and Systems for Daylighting", Renewable Energy **22**(1), 85-90.

Smith, G.B., Jonsson, J.C., Franklin, J., (2003) "Spectral and global diffuse properties of high-performance translucent polymer sheets for energy efficient lighting and skylights", Applied Optics **42**(19), 3981-3991.

Smith, G. B., Franklin, J. B., Joseph, E. K, "A light emitting device", *World Intellectual Property Organisation* (2004), Patent: International Publication Number WO 2004/027474.

Swift, P.D., Smith, G.B., (1995) "Cylindrical mirror light pipes", Solar Energy Materials and Solar Cells **36**, 159-168.

Talbot, D., (2003) "LEDs vs the light bulb", Technology Review **106**(4), 30-36.

Tastl, I., Purgathofer, W., (1994) "Color Spaces and Human Color Perception", in *Photo-realistic Rendering in Computer Graphics*, P. Brunet and F.W. Jansen, Editors, Springer-Verlag: Berlin. 219-226.

Teijido, J.M., Herzig, H.P., Dandliker, R., (1996) "Design of a non-conventional illumination system using a scattering light pipe", in *Proceedings of SPIE Vol 2774: Design and Engineering of Optical Systems*, 747-756.

Teijido, J.M., Herzig, H.P., Dandliker, R., et al., (1996) "Illumination light pipe using micro-optics as diffuser", in *Proceedings of SPIE Vol 2951: Holographic and Diffractive Techniques*, 146-155.

Teijido, J.M., Herzig, H.P., Fuhrer, C., et al., (1998) "Design methods for illumination light pipes", in *Proceedings of SPIE Vol 3428: Illumination and Source Engineering*, 34-44.

Ungut, A., Grehan, G., Gouesbet, G., (1980) "Comparisons between geometrical optics and Lorenz-Mie theory", Applied Optics **20**(17), 2911-2918.

van de Hulst, H.C., (1981) "Light Scattering by Small Particles", New York: Dover Publications.

Van Derlofske, J., Hough, T.A., (2003) "Flux Propagation in Light Pipe Illumination Systems", in *Proceedings of SPIE Vol 5186: Design of Efficient Illumination Systems*, 44-55.

Van Derlofske, J., Hough, T.A., (2004) "Analytical model of flux propagation in light-pipe systems", Optical Engineering **43**(7), 1503-1510.

Van Derlofske, J., McColgan, M., (2002) "White LED sources for vehicle forward lighting", in *Proceedings of SPIE Vol 4776: Solid State Lighting II*, SPIE: Bellingham, WA. 195-205.

Van Derlofske, J.F., (2001) "Computer modeling of LED light pipe systems for uniform display illumination", in *Proceedings of SPIE Vol 4445: Solid State Lighting and Displays*, 119-129.

Wall, J., (Jan 2000) "Geometry boosts visible LED efficiency", Laser Focus World **36**(1), 18-20.

Whitaker, G., Zarian, J., (1997) "Commercial Vehicle Applications Using Linear Emitting Fiber Optics", SAE Technical Paper Series **970257**, 1-4.

Whitehead, L.A., (1982) "Simplified ray tracing in cylindrical systems", Applied Optics **21**(19), 3536-8.

Whitehead, L.A., (1998) "High-efficiency prism light guides with confocal parabolic cross sections", Applied Optics **37**(22), 5227-33.

Whitehead, L.A., (1998) "Method for Estimating the Efficiency of Prism Light Guide Luminaires", Journal of the Illuminating Engineering Society **27**(2), 13-20.

Whitehead, L.A., (1998) "New Simplified Design Procedures for Prism Light Guide Luminaires", Journal of the Illuminating Engineering Society **27**(2), 21-27.

Wild, C.J., Seber, G.A.F., (1995) "Introduction to Probability and Statistics", Auckland: Department of Statistics, University of Auckland.

Winston, R., (1970) "Light Collection within the Framework of Geometrical Optics", Journal of the Optical Society of America **60**(2), 245-7.

Winston, R., O'Gallagher, J.J., (2004) "Nonimaging solar concentrator with uniform irradiance", in *Proceedings of SPIE Vol 5529: Nonimaging Optics and Efficient Illumination Systems*, 237-239.

Wriedt, T., Schuh, R., (2002) "The inclusion-concentration measurement of suspension droplets based on Monte Carlo ray tracing", Measurement Science and Technology **13**(3), 276-279.

Wyszecki, G., Stiles, W.S., (1967) "Color Science", New York: John Wiley & Sons, Inc.

Wyszecki, G., Stiles, W.S., (2000) "Color Science", 2nd ed. New York: John Wiley & Sons, Inc.

You, C., (2004) "LED White Light Visual Equivalence", in *Proceedings of SPIE Vol 5530: Fourth International Conference on Solid State Lighting*, 80-87.

Zhao, F., Narendran, N., Van Derlofske, J., (2002) "Optical elements for mixing colored LEDs to create white light", in *Proceedings of SPIE Vol 4776: Solid State Lighting II*, 206-214.

Zhao, F., Van Derlofske, J., (2003) "Side-Emitting Illuminators Using LED Sources", in *Proceedings of SPIE Vol 5186: Design of Efficient Illumination Systems*, 33-43.

Zukauskas, A., Vaicekauskas, R., Ivanauskas, F., et al., (2002) "Optimization of white polychromatic semiconductor lamps", Applied Physics Letters **80**(2), 234-236.

Appendix

Appendix 1 Principles of the Abbe Refractometer

No. 2002 ATAGO Abbe Refractometer

This type of refractometer is used for examination of concentration and purity of various chemicals in the fields of petroleum, resin, sugar, fuel and food industries, Also it is adequate for the experiment of refraction in physics, chemistry and biology. Small samples of lipuid powder or solution can be applied. Constructed and tested according the Japan Industrial Standard JIS Machinary 3201.

N_D range=1.3000～1.7000

Range of sugar concentration=0～90%

Minimum scale unit=0.5%

Precision of refractive index=0.0002

Precision of dispersion=0.0005

Temperature range=0°C～50°C

Instruction for Use

The refractometer is equiped two large prisms, the lower of which has a ground glass diagonal face and is used to illuminate and confine the sample, while the upper prism is the refracting prism. The prism mount is connected to an arm extending at right angle to upper face of the upper prism. This arm is used to rotate the prisms with respect to the telescope, so as to set the critical boundary on the cross hair in the eyepiece. The position of the arm is read on a curved scale which is graduated directly in refractive indices. The reproducibility of the individual readings on the scale is 0.0002 refractive-index unifs.

Light from a frosted electric lamp is reflected into the lower prism, where it is scattered at the ground-glass surface. Some of the scattered light passes into the liquid held between the prisms at nearly grazing incidence (i=90°) and produces a critical boundry

in the telescope. When white light is used, the critical boundary is diffuse and colored because of the dispersion by the sample and prism of critical rays having different wave lengths. The color of the critical boundary is removed by means of two identical Amici prisms. which may be adjusted to introduce a dispersion which is equal and opposite to that caused by the sample plus prism. When this has been done, the critical boundary is sharp and colorless.

Although white light is used, N is obtained for the sodium D line because the Amici prisms are constructed so that rays for the sodium D line are not deviated, but all other wave lengths are deviated.

The prisms are opened like jaws after turning the lock nut to the right, and they are wiped with lens tissue, care being taken not to scratch them. A few drops of liquid are placed on the face of the lower prism, and the prism jaws are then closed and locked. The instrument is turned back until the telescope is in a convenient position, and the mirror is adjusted to reflect the light from a frosted electric lamp into the refractometer. The prism is rotated by means of the arm until the border between the dark and light fields passes exactly through the intersection of the cross hairs. The telescope eyepiece is adjusted until the cross hairs are in good focus, and the eyepiece on the movile arm is adjusted to give a sharp focus on the scale.

Thermostat for the refractometer

The refractive index of a substance varies with minute change of temperature. The prisms are jacketed, so that the temperature may be controlled to within 0.2° with a stream of water from a thermostat. In this case, the refractometer should be connected to the water supply from the thermostat, which could be regulated to keep certain adequate temperature.

Appendix 2 Cosine Rule for sides. (a) spherical triangles (b) planar triangles

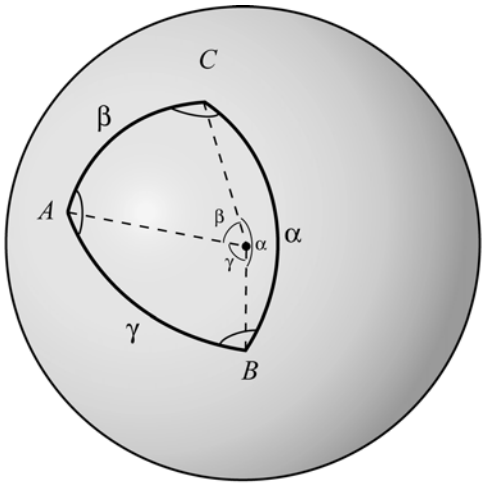

$$\cos\alpha = \cos\beta\cos\gamma + \sin\beta\sin\gamma\cos A$$

(a)

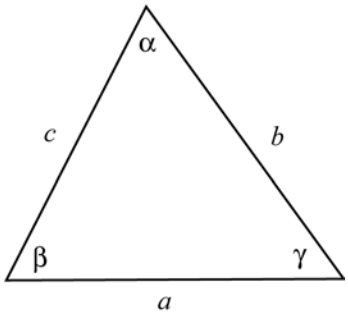

$$a^2 = b^2 + c^2 - 2bc\cos\alpha$$

(b)

Appendix 3 Cumulative probability density functions

Appendix 3.1 Functions for cumulative probability curve for empirical LED fit

$$P(\theta) = 32.5\sin\theta \qquad 0 > P(\theta) > 0.0618$$
$$P(\theta) = 2.64055\theta - 0.05388 \qquad 0.06180 \geq P(\theta) > 0.0733$$
$$P(\theta) = -38\theta^3 + 7.8\theta^2 + 2.7\theta - 0.07 \qquad 0.07330 \geq P(\theta) > 0.3994$$
$$P(\theta) = -18.5\theta^3 + 4.5\theta^2 + 2.47\theta - 0.028 \qquad 0.39940 \geq P(\theta) > 0.4786$$
$$P(\theta) = -8.5\theta^3 + 0.8\theta^2 + 2.47\theta - 0.035 \qquad 0.47860 \geq P(\theta) > 0.58315$$
$$P(\theta) = -4.15\theta^3 + 0.8\theta^2 + 1.35\theta - 0.25 \qquad 0.58315 \geq P(\theta) > 0.6353$$
$$P(\theta) = -0.13\theta^3 + 0.33\theta^2 + 1.22\theta - 0.53 \qquad 0.63530 \geq P(\theta) > 0.77963$$
$$P(\theta) = -0.3\theta^3 + 0.48\theta^2 + 0.21\theta - 0.52 \qquad 0.77963 \geq P(\theta) > 0.9076$$
$$P(\theta) = -0.14\theta^3 + 0.36\theta^2 + 0.03\theta - 0.72 \qquad 0.90760 \geq P(\theta) > 0.9375$$
$$P(\theta) = -0.1201\theta^3 + 0.2905\theta^2 + 0.0035\theta - 0.741 \qquad 0.93750 \geq P(\theta) > 0.99306$$
$$P(\theta) = -0.1152\theta^3 + 0.29\theta^2 + 0.0058\theta - 0.74 \qquad 0.99306 \geq P(\theta) > 0.99994$$

Appendix 3.2 Functions for cumulative probability curve based on LED measurements

Appendix 3.2.1 "Alpha Red" LED functions

$$P(\theta) = 7\theta^2 + 0.35\theta \qquad 0 > P(\theta) > 0.1789$$
$$P(\theta) = 10\theta^2 + 0.06\theta \qquad 0.17890 \geq P(\theta) > 0.571$$
$$P(\theta) = 0.351\theta + \sqrt{-0.11 + \theta - \theta^2} \qquad 0.57100 \geq P(\theta) > 0.6260$$
$$P(\theta) = 0.351\theta + 0.515 \qquad 0.62608 \geq P(\theta) > 1.0$$

Appendix 3.2.2 "Alpha Green" LED functions

$$P(\theta) = 16\theta^2 + 0.05\theta \qquad 0 > P(\theta) > 0.065625$$
$$P(\theta) = 12\theta^2 + 0.3\theta \qquad 0.065625 \geq P(\theta) > 0.4000$$
$$P(\theta) = 0.333\theta + \sqrt{-0.127 + 0.94\theta - \theta^2} \qquad 0.4000 \geq P(\theta) > 0.5831$$
$$P(\theta) = 0.56\theta + 0.419 \qquad 0.5831 \geq P(\theta) > 0.6609$$
$$P(\theta) = 0.47\theta + 0.47 - 0.065\theta^2 \qquad 0.6609 \geq P(\theta) > 1.0$$

Appendix 3.2.3 "Alpha Blue" LED functions

$$P(\theta) = 5.8\theta^{1.8} \qquad 0 > P(\theta) > 0.1535$$
$$P(\theta) = 44\theta^3 + 0.05 \qquad 0.1535 \geq P(\theta) > 0.3\dot{0}661$$
$$P(\theta) = -20.3\theta^3 + 8\theta^2 + 2.31\theta - 0.25 \qquad 0.30661 \geq P(\theta) > 0.6475$$
$$P(\theta) = 0.378 + \sqrt{-0.214 + 1.21\theta - \theta^2} \qquad 0.6475 \geq P(\theta) > 0.7584$$
$$P(\theta) = 0.30\theta + 0.605 - 0.008\theta^2 \qquad 0.7584 \geq P(\theta) > 1.0$$

Appendix 3.2.4 "Beta Red" LED functions

$$P(\theta) = 23\sin^2\theta \qquad 0 > P(\theta) > 0.153$$
$$P(\theta) = 27\sin^2\theta + 0.15\sin\theta - 0.0065 \qquad 0.1530 \geq P(\theta) > 0.0\dot{5}28$$
$$P(\theta) = 2.96\theta - 0.078 \qquad 0.0528 \geq P(\theta) > 0.1772$$
$$P(\theta) = 0.2\log(\theta) - 0.605\theta + 0.673 \qquad 0.1772 \geq P(\theta) > 0.2976$$
$$P(\theta) = 2\theta - 0.025 \qquad 0.2976 \geq P(\theta) > 0.471$$
$$P(\theta) = 0.135 + \sqrt{-0.155 + 1.1\theta - 0.08\theta^2} \qquad 0.2976 \geq P(\theta) > 0.5585$$
$$P(\theta) = 0.295\log(\theta) + 0.903 \qquad 0.5585 \geq P(\theta) > 0.845$$
$$P(\theta) = -0.113\theta^{0.35} + 0.36\theta^2 + 0.66 \qquad 0.8450 \geq P(\theta) > 1.0$$

Appendix 3.2.5 "Beta Green" LED functions

$$P(\theta) = 11.8\sin\theta^{1.81} \qquad 0 > P(\theta) > 0.0560$$
$$P(\theta) = 0.121\log(\theta) - 0.12\theta + 0.42 \qquad 0.0560 \geq P(\theta) > 0.1\dot{4}93$$
$$P(\theta) = 17.7\theta^{2.5} + 0.008\theta^{-1} - 0.006 \qquad 0.1493 \geq P(\theta) > 0.2\dot{7}34$$
$$P(\theta) = 0.09 + \sqrt{-0.18 + 1.4\theta - 1.1\theta^2} \qquad 0.2734 \geq P(\theta) > 0.3737$$
$$P(\theta) = 0.05 + \sqrt{-0.115 + 1.15\theta - 0.79\theta^2} \qquad 0.3737 \geq P(\theta) > 0.4837$$
$$P(\theta) = 1.11\theta + 0.1 \qquad 0.4837 \geq P(\theta) > 0.5270$$
$$P(\theta) = \sqrt{-0.125 + 1.17\theta - 0.32\theta^2} \qquad 0.5270 \geq P(\theta) > 0.7089$$
$$P(\theta) = 0.41\log(\theta) - 0.025\theta + 0.9 \qquad 0.7089 \geq P(\theta) > 1.0$$

Appendix 3.2.6 "Beta Blue" LED functions

$$P(\theta) = 18.5\theta^2 \qquad 0 > P(\theta) > 0.1574$$

$$P(\theta) = 14\theta^3 + 3.1\theta - 0.14 \qquad 0.1574 \geq P(\theta) > 0.3918$$

$$P(\theta) = 3.5\theta - 0.15 \qquad 0.3918 \geq P(\theta) > 0.5500$$

$$P(\theta) = 2.5\theta^3 + 5\theta^2 + 4.9\theta - 0.25 \qquad 0.5500 \geq P(\theta) > 0.6960$$

$$P(\theta) = 0.592 + \sqrt{-0.112 + 0.699\theta - 0.822\theta^2} \qquad 0.6960 \geq P(\theta) > 0.7758$$

$$P(\theta) = 0.33\theta + 0.66 - 0.055\theta^{2.5} \qquad 0.7758 \geq P(\theta) > 1.0$$

Appendix 4 Simplified ray tracing flow chart

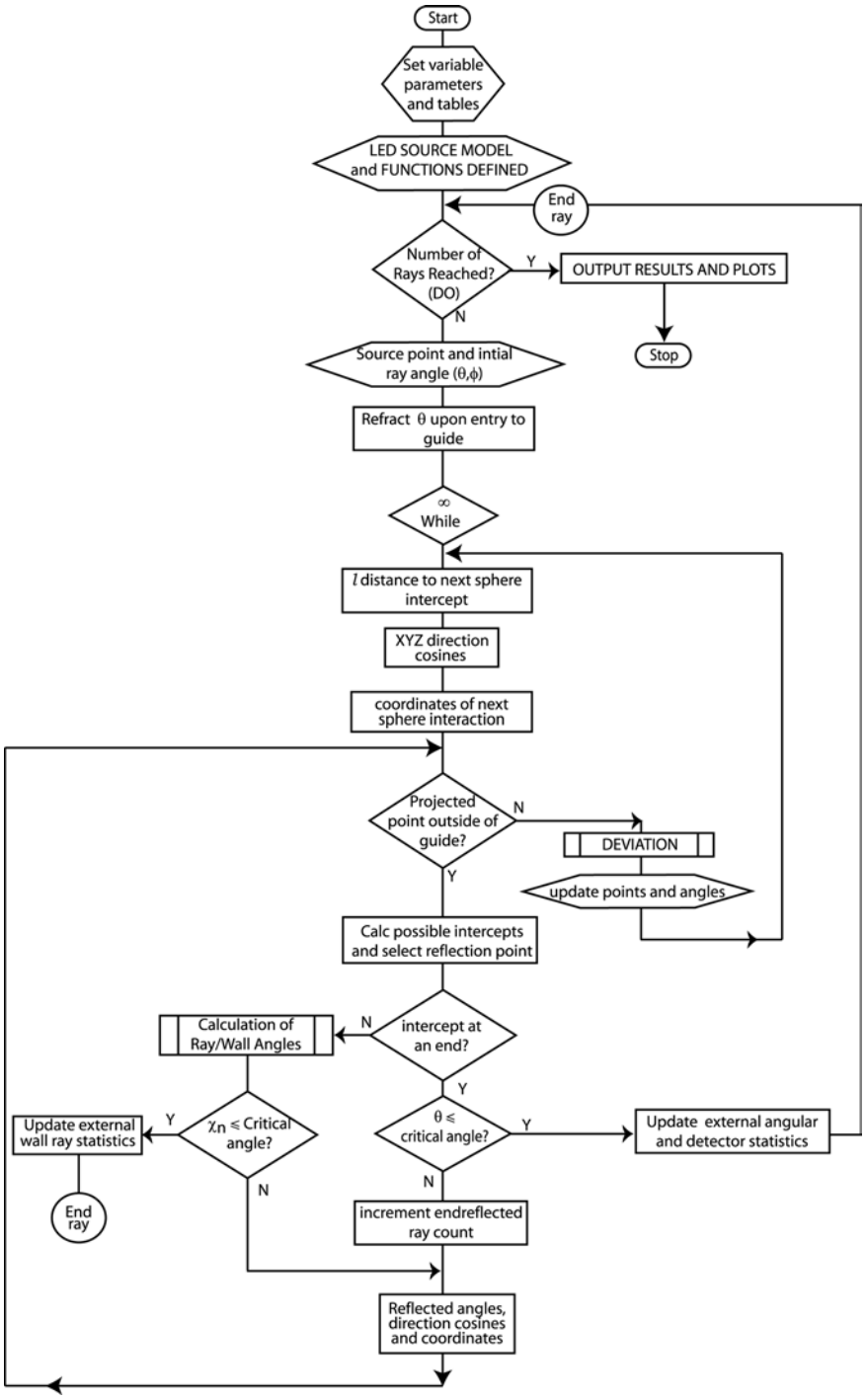

Appendix 5 Computer Program

```
(* Put in actual LED CIE coords used in expt,
 and intensities of 'redhagner', etc meas of LED using
  int sphere. Normalise intensity fractions so that they
  are not photopically weighted. This version also plots
  CIE coodinates in 2 D and 3 D, plus total intensity *)


(* Diode Source CIE coords: GROUP 4 LEDs *)
xR = 0.690; yR = 0.310; zR = 1 - xR - yR; (* 630 nm *)
xG = 0.166; yG = 0.707; zG = 1 - xG - yG; (* 518 nm *)
xB = 0.131; yB = 0.070; zB = 1 - xB - yB; (* 465 nm *)

matrix = {{3.7138671918964556`, -1.5732009003939227`, -0.5793911086100169`},
   {-1.0264973178789916`, 1.8828007016174415`, 0.04024528926970065`},
   {0.054525961963197644`, -0.18163744017039715`, 0.7908000980267578`}};
(* to convert XYZ to RGB *)

(* plain acrylic rod simulation 1.5 mm rad source pt (constant mu) *)
redmap = Import@"C:\Deller C\Modelling\Mathematica\
     Model 7cB Data\\meas1c(10mil)\\meas1cRmid.dat", "Table";
greenmap = Import@"C:\Deller C\Modelling\Mathematica\Model
     7cB Data\\meas1c(10mil)\\meas1cGmid.dat", "Table";
bluemap = Import@"C:\Deller C\Modelling\Mathematica\Model
     7cB Data\\meas1c(10mil)\\meas1cBmid.dat", "Table";
param = Import@"C:\Deller C\Modelling\Mathematica\Model 7cB
     Data\\meas1c(10mil)\\meas1cRdetpmid.dat", "Table";
parameters = Import@"C:\Deller C\Modelling\Mathematica\Model 7cB
     Data\\meas1c(10mil)\\meas1cRpmtrs.dat";(* only need one *)

rays = parameters[[8]];
reccount = parameters[[1]];
reclengths = parameters[[2]];
anglerange = parameters[[3]];
pipelength = First@parameters[[4]];
radius = parameters[[5]];
avpath = First@parameters[[6]];
initialthetarange = parameters[[7]];
n1Matrix = parameters[[10]];
n2Spheres = parameters[[11]];
nRatio = parameters[[12]];
ledradius = parameters[[15]];

dim = IntegerPart@First@param[[1]][[1]]; (* number of pixels along side *)
zplane = First@param[[2]][[1]];
pixelsize = First@param[[3]][[1]];
detectorsize = First@param[[4]][[1]];

Off@Power::"infy"
Off@∞::"indet"
redhagner = 51.3 ê 0.31;
(* input measured LED source lux, then divided by y to make unweighted,
 same as the imported data. The other way to do it is to
  multiply all the imported data by y, to change to lux *)
greenhagner = 75.6 ê 0.707;
```

```
bluehagner = 25.2 ê 0.07;
sumhagner = redhagner + greenhagner + bluehagner;
fr = redhagner ê sumhagner;
fg = greenhagner ê sumhagner ;
fb = bluehagner ê sumhagner;

diodeintmap = Apply@Plus, 8fr  redmap, fg  greenmap, fb  bluemap<D;
H Totals rays from R, G, B diode sources L

H weighted sum of CIE xyz components
  of colour from the 3 source LED colours L

    Hfr  redmap  xR + fg  greenmap  xG + fb  bluemap  xBL
x = ii...ii ê.
                          diodeintmap
   8Indeterminate → 0<;
    Hfr  redmap  yR + fg  greenmap  yG + fb  bluemap  yBL
y = ii...ii ê.
                          diodeintmap
   8Indeterminate → 0<;
    Hfr  redmap  zR + fg  greenmap  zG + fb  bluemap  zBL
z = ii...ii ê.
                          diodeintmap
   8Indeterminate → 0<;

xyzmixmap =
  Partition@MapThread@List, 8Flatten@x, 1D, Flatten@y, 1D, Flatten@z, 1D<D,
   dimD; H forms matrix of 8xyz< for each pixel element,
 ie Cie colour coordinates of added maps L

intmax = Max@diodeintmapD;H maximum total ray value L

Y = N@diodeintmap ê intmaxD;
H Intensity normalised to a maximum of 1 L

    x
X = ii Y ê. 8Indeterminate → 0<;
    y
    z
Z = ii Y ê. 8Indeterminate → 0<;
    y
XYZmixmap =
  Partition@MapThread@List, 8Flatten@X, 1D, Flatten@Y, 1D, Flatten@Z, 1D<D,
   dimD; H forms matrix of 8XYZ< for each element L


H Conversion of XYZ map to RGB map L
RGBmixmap = 8<;
Do@
  XYZrow = XYZmixmapPjT;
  RGBrow = Map@Apply@Dot, 8matrix, #<D &, XYZrowD ê. 8Hx_ ê; x < 0L → Hx = 0L<;
  H range kept ≥0  L
  AppendTo@RGBmixmap, RGBrowD;
  ,
  8j, Length@XYZmixmapD<
 D;
RGBmixmap ê= Max@RGBmixmapD;H So never exceeds 1 L
```

```
logRGB = Log@10, RGBmixmapD;
zerolevel = Round@Min@Select@Flatten@logRGBD, NumberQDD - 1D
logRGB = Log@10, RGBmixmapD ê. 8Indeterminate → zerolevel<;
logRGB = % ê. 8-∞ → zerolevel<;

               logRGB - zerolevel
scaledRGB = ¡¡¡¡¡¡¡¡¡¡¡¡¡¡¡¡¡¡¡¡¡¡¡¡¡¡¡¡¡¡¡¡¡¡¡¡¡¡¡¡ ;
                   -zerolevel

H COLOUR MIX PLOT - LOG, in transmission L
mixplot4 = 8<;
Do@row = Reverse@Part@scaledRGB, jDD;
 Do@AppendTo@mixplot4, 8RGBColor@rowPi, 1T, rowPi, 2T, rowPi, 3TD,
    Rectangle@8i, j<, 8i + 1, j + 1<D<D, 8i, dim<D,
 8j, dim<
D
plot4 = Show@Graphics@mixplot4D, AspectRatio → Automatic,
  Frame → True, FrameTicks → False, PlotLabel →
   "Log Colour Mixing Map" Hzplane - pipelengthL " cm from guide end\n",
  FrameLabel → 8pixelsize "mm pixels", None,
    detectorsize "mm detector size", None<D

Print@"\nTotal Rays= ", raysP1TD;
Print@"Recording Planes are: \n z=", reclengths, "cm",
  "\nLightguide length is ", pipelength, "cm", " \nradius ", radius "cm",
  "\nAverage Path Increment length between sphere interactions is ",
  avpath, "cm", "\nLED θ range is ", initialthetarangeP1T,
  " degrees\nLED radius is ", ledradiusP1T, " degrees\nNo. rays= ",
  raysP1T, " \nn1 HmatrixL= ", n1MatrixP1T, "\nn2 HspheresL= ",
  n2SpheresP1T, "\nn HRatioL= ", nRatioP1TD;
```

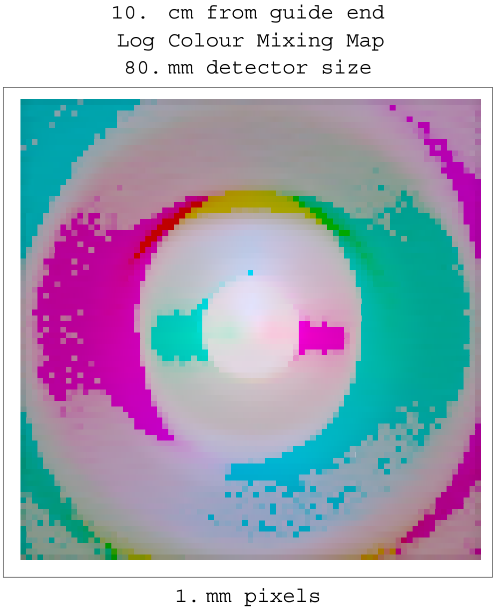

```
Out[56]= ⁝ Graphics ⁝
```

```
Total Rays= 10000000
```

```
Recording Planes are:
 z=81, 2, 3, 4, 5, 6, 7, 8, 9, 10<cm
Lightguide length is 10.cm
radius 80.63 cm<
Average Path Increment length between sphere interactions is
 200000000000000000000000000000000000000000000000000000000000000000000000000000000000000000000000000000000000¥
  0000000000cm
LED θ range is 16 degrees
LED radius is 0.15 degrees
No. rays= 10000000
n1 HmatrixL= 1.49
n2 HspheresL= 1.491
n HRatioL= 1.00067
```

```
xcie = 8<;
ycie = 8<;
Do@
  line = Transpose@xyzmixmapPiTD;
  AppendTo@xcie, First@lineDD;
  AppendTo@ycie, Part@line, 2DD;
  ,
  8i, 1, Length@xyzmixmapD<
 D;
ListPlot@Reverse@xciePi, 1TD, PlotRange → 80, 0.6<,
 Frame → True, PlotStyle → PointSize@0.015D,
 FrameTicks → 888Hdim − 1L ê 5, Hdim − 1L ê 5  pixelsize<,
    82  Hdim − 1L ê 5, 2  Hdim − 1L ê 5  pixelsize<,
    83  Hdim − 1L ê 5, 3  Hdim − 1L ê 5  pixelsize<, 84  Hdim − 1L ê 5,
     4  Hdim − 1L ê 5  pixelsize<, 8Hdim − 1L, Hdim − 1L  pixelsize<<, Automatic<,
 FrameLabel → 8"mm", "chromaticity coordinate HxL", "Colour CIE x", None<D
```

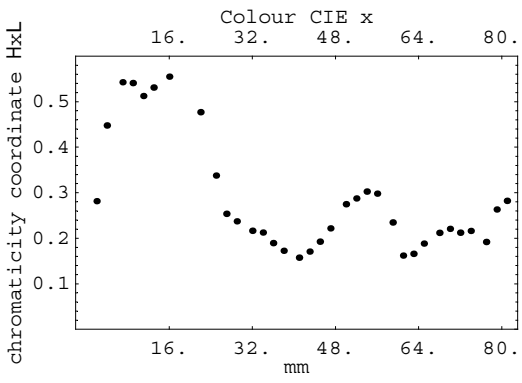

Out[62]= ¦ Graphics ¦

```
In[63]:= ListPlot@Reverse@ycieP51TD, PlotRange → 880, 0.6<,
          Frame → True, PlotStyle → PointSize@0.015D,
          FrameTicks → 888Hdim − 1L ê 5, Hdim − 1L ê 5  pixelsize<,
             82  Hdim − 1L ê 5, 2  Hdim − 1L ê 5  pixelsize<, 83  Hdim − 1L ê 5,
              3  Hdim − 1L ê 5  pixelsize<, 84  Hdim − 1L ê 5, 4  Hdim − 1L ê 5  pixelsize<,
             8Hdim − 1L, Hdim − 1L  pixelsize<<, Automatic<,
          FrameLabel → 8"mm", "chromaticity coordinate HyL", "Colour CIE y", None<D
```

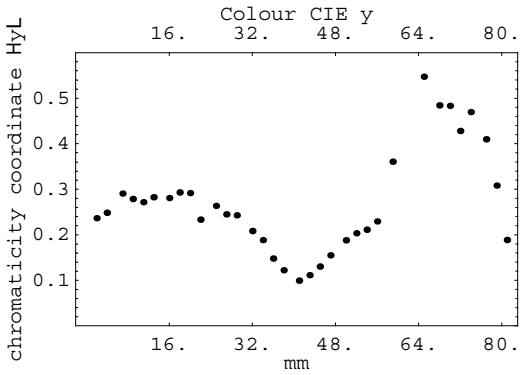


```
Out[63]= ¦ Graphics ¦
```

```
In[64]:= ListPlot3D@Map@Reverse, diodeintmapD, PlotRange → 8825, 55<, 825, 55<, All<,
          ViewPoint → 80, −2, 0.3<D H total intensity, in TRANSMISSION L
```

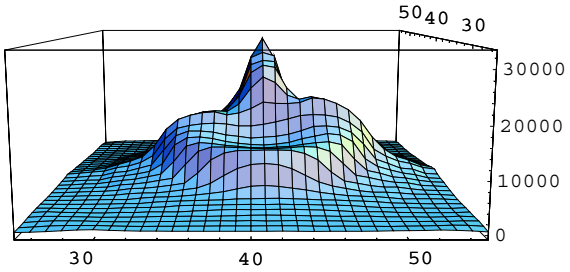


```
Out[64]= ¦ SurfaceGraphics ¦
```

```
In[65]:= ListPlot@Reverse@diodeintmapP51TD, PlotRange → AllD
         H cross-section total intensity in TRANSMISSION L
```

```
Out[65]= ¦ Graphics ¦
```

```
In[66]:= row = Reverse@Part@scaledRGB, 40DD;H Transmission L
         mixplot5 = 8<;
         Do@AppendTo@mixplot5, 8RGBColor@rowPi, 1T, rowPi, 2T, rowPi, 3TD,
             Rectangle@8i − 1, 0<, 8i, 1.5<D<D, 8i, dim<D;
         Show@Graphics@mixplot5D, AspectRatio → AutomaticD;
```